

Micromechanics of multiphase flow in fractured porous media

Author:

Yin, Peijie

Publication Date:

2015

DOI:

<https://doi.org/10.26190/unsworks/18582>

License:

<https://creativecommons.org/licenses/by-nc-nd/3.0/au/>

Link to license to see what you are allowed to do with this resource.

Downloaded from <http://hdl.handle.net/1959.4/55261> in <https://unsworks.unsw.edu.au> on 2024-05-05

MICROMECHANICS OF MULTIPHASE FLOW IN FRACTURED POROUS MEDIA

Peijie Yin

A thesis submitted in partial fulfillment of the requirements

for the degree of DOCTOR of PHILOSOPHY



SCHOOL OF CIVIL AND ENVIRONMENTAL ENGINEERING

FACULTY OF ENGINEERING

November 2015

ORIGINALITY STATEMENT

‘I hereby declare that this submission is my own work and to the best of my knowledge it contains no materials previously published or written by another person, or substantial proportions of material which have been accepted for the award of any other degree or diploma at UNSW or any other educational institution, except where due acknowledgement is made in the thesis. Any contribution made to the research by others, with whom I have worked at UNSW or elsewhere, is explicitly acknowledged in the thesis. I also declare that the intellectual content of this thesis is the product of my own work, except to the extent that assistance from others in the project's design and conception or in style, presentation and linguistic expression is acknowledged.’

Signed 

Date November 2015.....

ABSTRACT

The micromechanics of multiphase flow in fractured porous media are explored through the construction of microstructures to the modelling of micro-physics and macro-behaviors. Accordingly, four parts of studies are conducted so as to give a scientific explanation about the mechanism of two phase flow in fractured porous media.

The quantitative characterization of the microstructure and statistical description of the porous media are discussed in the first part. The microstructure reconstruction of sandstone from limited surface images is carried out by using simulated annealing method. The effectiveness of the reconstructed sandstone microstructure is tested and verified by comparing with available X-ray computed tomography (CT) experimental data.

The characterization of the multiphase distribution in fractured porous media is investigated in the second part. The single component multiphase (SCMP) lattice Boltzmann method (LBM) is selected among three commonly used numerical approaches through a comparison against the available results of micro X-ray CT. The two-phase fluid distribution in porous media and the effect of fracture are investigated.

In the third part, the single phase flow in natural fracture network is numerically investigated. The influence of fracture roughness and deformation on the fracture transmissivity/permeability is numerically studied. Meanwhile, the ability of LBM in the study of fluid flow in fracture network is validated through the comparison to the pipe network model. The influence of fracture length, fracture density, and deformation

on the fluid flow is also studied preliminarily from coupling LBM with the Discrete Fracture Network (DFN) model and Discrete Element Model (DEM).

The multiphase flow through fractured porous media is studied in the fourth part. The SCMP LBM is found effectively in simulating the two phase flow problems through the comparison with the multi-component multiphase (MCMP) LBM. Moreover, the body force for the simulation is calibrated and effect of wettability on two phase flow is studied. After that, the influence of fracture on two phase flow is investigated. The trial of two phase flow in 3D reconstructed porous media is conducted and some suggestions are given at the end.

Based on the comprehensive studies and numbers of numerical simulations, a clear understanding of macroscopic behaviors and their dependence on microstructure and microscopic physics process at pore scale are obtained.

ACKNOWLEDGEMENTS

The work described in this thesis was carried out as research into the micromechanics of multiphase flow in fractured porous media in the School of Civil and Environmental Engineering at the University of New South Wales (UNSW), Sydney, Australia.

I would like to thank many members of staff in the School of Civil and Environmental Engineering. I am enormously grateful to my supervisor Senior Lecture Dr. Gaofeng Zhao and co-supervisor Professor Nasser Khalili for sparking their invaluable guidance and encouragement.

I am extremely grateful to my wife, Jiao Liu, who provided so much support during the last four years, especially the hectic months prior to completion.

Peijie Yin

Sydney, Australia

November 2015

TABLE OF CONTENTS

1 INTRODUCTION	1
1.1 BACKGROUND	1
1.2 OBJECTIVE, METHOD AND SCOPE	2
1.3 THESIS STRUCTURE	3
2 LITERATURE REVIEW	5
2.1 PROBLEM STATEMENT	5
2.2 CHARACTERIZATION OF POROUS MEDIA	5
2.2.1 Sphere packing	6
2.1.2 Process based model	7
2.1.3 Pore network model	7
2.1.4 Local porosity theory based stochastic model	8
2.3 CHARACTERIZATION OF FRACTURE NETWORKS	9
2.4 THE FLOW MODEL	11
2.5 REFERENCES	13
3 STOCHASTIC RECONSTRUCTION OF GOSFORD SANDSTONE FROM SURFACE IMAGE	20
3.1 INTRODUCTION	20
3.2. STOCHASTIC RECONSTRUCTION	24
3.2.1 Two-point probability function	24

3.2.2 Stochastic reconstruction based on the simulated annealing method	25
3.3. QUANTITATIVE MORPHOLOGICAL MEASUREMENTS OF POROUS MEDIA	28
3.3.1 Porosity and specific surface	28
3.3.2 Local porosity distribution	29
3.3.3 Local percolation probability	29
3.4 MORPHOLOGICAL DESCRIPTION OF THE GOSFORD SANDSTONE	31
3.4.1 Relationship between the 2D and 3D morphological description	31
3.4.2 Surface image of the Gosford sandstone	36
3.5 STOCHASTIC RECONSTRUCTION OF THE GOSFORD SANDSTONE	38
3.5.1 Reconstruction based on the X-ray micro CT model	38
3.5.2 Reconstruction based on the surface images	41
3.6 CONCLUSIONS	44
3.7 REFERENCES	44
4 NUMERICAL STUDY OF TWO-PHASE FLUID DISTRIBUTIONS IN FRACTURED POROUS MEDIA	48
4.1 INTRODUCTION	48
4.2 NUMERICAL METHODS	52
4.2.1 Simulated Annealing Method (SAM)	52
4.2.2 Lattice Boltzmann method (LBM)	56

4.3 VERIFICATION	67
4.4 TWO-PHASE FLUID DISTRIBUTION IN FRACTURED POROUS MEDIA	72
4.4.1 Periodic boundary effect and initial configurations	72
4.4.2 Fluid distribution in porous media	79
4.4.3 Fluid distribution in fractured porous media	81
4.5 CONCLUDING REMARKS	88
4.6 REFERENCES	89
5 NUMERICAL FLUID FLOW THROUGH DEFORMABLE NATURAL FRACTURE NETWORK	95
5.1 INTRODUCTION	95
5.2 SINGLE PHASE INCOMPRESSIBLE LBGK MODEL	99
5.2.1 Basic concept	99
5.2.2 Boundary conditions	101
5.3 FLUID FLOW IN SINGLE FRACTURE	102
5.3.1 Validation	102
5.3.2 Fluid flow through 3D synthetic fracture	106
5.3.3 Effect of displacement	115
5.4 FLUID FLOW THROUGH FRACTURE NETWORK	120
5.4.1 Pipe network model (PNM)	120

5.4.2 Pipe model generation	122
5.4.3 Fluid flow in natural fracture network	123
5.5 FLUID FLOW IN DISCRETE FRACTURE NETWORK MODEL (DFN) UNDER DEFORMATION	128
5.5.1 Fluid flow in DFN	128
5.5.2 Indirect coupling between LBM and DEM	133
5.6 CONCLUDING REMARKS	136
5.7 REFERENCES	137
6 NUMERICAL STUDY OF MULTIPHASE FLOW IN FRACTURED POROUS MEDIA USING LATTICE BOLTZMANN METHOD	144
6.1 INTRODUCTION	144
6.2 COMPARISON OF THE SHAN-CHEN SCMP AND MCMP MODEL IN TWO PHASE FLOW PROBLEMS	147
6.2.1 The two phase pattern in single fracture	148
6.2.2 Validations of co-current flow	152
6.2.3 Bubble flow around a solid surface	159
6.3 TWO PHASES FLOW IN POROUS MEDIA	161
6.3.1 Setup of the simulation	161
6.3.2 The effect of wettability	167
6.3.3 The effect of hydraulic aperture	171
6.4 FLOW IN FRACTURED POROUS MEDIA	175

6.5 TRIAL OF TWO PHASE FLOW IN NATURAL MATERIAL	183
6.6 CONCLUDING REMARKS	187
6.7 REFERENCES	187
7 SUMMARY AND CONCLUSIONS	190

LIST OF FIGURES

Figure 3.1 Illustration of the stochastic reconstruction for Gosford sandstone.	23
Figure 3.2 Sample drilled for x-ray CT scanning and region of interests selected for analysis.	32
Figure 3.3 Areal porosity distribution of the X-ray micro CT model	32
Figure 3.4 Morphological description curves of different CT slices.	34
Figure 3.5 Derived morphological description curves of the CT slices (method 1).	35
Figure 3.6 Derived morphological description curves of the CT slices (method 2).	36
Figure 3.7 Process of the surface image acquisition for the Gosford sandstone.	37
Figure 3.8 Obtained surface images of the Gosford sandstone specimen.	38
Figure 3.9 Stochastic reconstructed models based on the 3D morphological description curve from the micro X-ray CT model.	39
Figure 3.10 Quantitative measures of the reconstructed models based on the X-ray micro CT model.	40
Figure 3.11 Quantitative measures of the reconstructed models based on the surface images.	43
Figure 3.12 Computational time of reconstructed models with different sizes.	44
Figure 4.1 Flowchart of the simulated annealing method for modeling two-phase distributions.	55
Figure 4.2 Anti-aliasing to produce a smooth interface after equilibrium is obtained.	56
Figure 4.3 Correlation between $G_{ads,\sigma}$ and the contact angle in the MCMP LBM ($G=0.9$; $G_{ads,2}=-G_{ads,1}$).	65
Figure 4.4 Correlation between G_{ads} and the contact angle in the SCMP LBM ($G=-120$)	66
Figure 4.5 Comparison between micro X-ray CT and three numerical methods.	69

Figure 4.6 Wetting-phase linear-path functions of different fluid distributions by the different methods in Figure 4.5.	70
Figure 4.7 Dependence on the initial configuration in the MCMP Shan-Chen model.	71
Figure 4.8 Dependence on the initial configuration in the SCMP Shan-Chen model.	71
Figure 4.9 Geometry of a porous medium generated from DEM.	73
Figure 4.10 Influence of buffer size on the macroscopic properties in the region of interest.	75
Figure 4.11 Fluid distributions in the region of interest from simulations of different buffer sizes.	76
Figure 4.12 Investigation of the boundary conditions and the initial configuration.	77
Figure 4.13 Fluid distributions in regular geometry from different random initializations.	78
Figure 4.14 Fluid distributions in irregular geometry from different random initializations.	78
Figure 4.15 Multiphase distributions at different degrees of saturation in a porous medium.	79
Figure 4.16 Correlation between the degree of saturation and the specific surface area of the fluid interface.	81
Figure 4.17 Influence of fractures on multiphase distributions ($S_r = 0.4$, Fracture width = 100 l.u., Fracture length = 1000 l.u.).	82
Figure 4.18 Macroscopic description of differences between Figures 17(a) and 17(b) ($S_r = 0.4$, Fracture width = 100 l.u., Fracture length = 1000 l.u.)	84
Figure 4.19 Influence of the degrees of saturation on the coincident ratio (Fracture width = 50 l.u.; Fracture length = 1000 l.u.).	84

Figure 4.20 Influence of the fracture widths on the coincident ratio ($S_r = 0.4$; Fracture length = 1000 l.u.).	85
Figure 4.21 Influence of fracture lengths on the coincident ratio ($S_r = 0.4$; Fracture width = 100 l.u.).	87
Figure 4.22 Influence of the fracture length on the disturbance ratio at different degrees of saturation.	88
Figure 5.1 The D2Q9 model and D3Q15 model.	99
Figure 5.2 Bounce back scheme.	101
Figure 5.3 Impact of parameter choice.	104
Figure 5.4 The simulation results based on the relationship $\delta t = \delta x^2$.	105
Figure 5.5 Fracture generator (Ogilvie et al. 2006).	107
Figure 5.6 Effect of fractal dimension on fracture profile (standard deviation = 2 mm).	110
Figure 5.7 Effect of standard deviation on fracture profile (fractal dimension = 1.6).	112
Figure 5.8 Geometry for the fracture and velocity distributions at slices from LBM simulation.	113
Figure 5.9 Dependence of coefficients on fractal dimension and standard deviation of fracture surfaces.	114
Figure 5.10 Assumptions made to implement shear displacement.	117
Figure 5.11 Geometry of the fracture and the aperture change induced by displacement.	118
Figure 5.12 Relationship between the aperture changes and shear displacement under two assumptions.	119
Figure 5.13 Relationship between the transmissivity and mean aperture.	120

Figure 5.14 Process of implement the fracture network in pipe network model and LBM simulation.	122
Figure 5.15 Generation of fracture network with roughness.	124
Figure 5.16 Velocity distribution of fluid flow in fracture network under different maximum amplitude through LBM simulation.	126
Figure 5.17 Simulation results of fluid flow in fracture network involving roughness.	127
Figure 5.18 DFN models with different fracture densities and lengths.	129
Figure 5.19 Velocity distributions in DFN from LBM simulations.	130
Figure 5.20 Dependence of flow rate on mean fracture length and density.	131
Figure 5.21 Relationship between LD and flow rate.	132
Figure 5.22 Relationship between fracture density and flow rate under different LD.	132
Figure 5.23 Implementation of "indirect" hydro-mechanical coupling.	134
Figure 5.24 Conductivity of flow region with different orientation and axial strain.	135
Figure 5.25 Transmissivity of flow region with different orientation and axial strain.	136
Figure 6.1 Effect of body force on two phase distribution at different degree of saturation using Shan-Chen SCMP model.	151
Figure 6.2 Flow patterns at different degree of saturation using Shan-Chen MCMP model.	152
Figure 6.3 Flow pattern of two phase co-current flow.	153
Figure 6.4 Equation of state from Shan and Chen (1994).	154
Figure 6.5 Implementation of the co-current flow in SCMP model.	155
Figure 6.6 Velocity profile from SCMP model.	156

Figure 6.7 Velocity profile from MCMP model with viscosity ratio = 1.	157
Figure 6.8 Velocity and density distribution from MCMP model with viscosity ratio = 3.	158
Figure 6.9 Setup of the bubble flow.	159
Figure 6.10 Time evolution of bubble flow across the solid bar.	160
Figure 6.11 The isotropic and homogeneous porous media.	162
Figure 6.12 Density and velocity profile for the distribution at static condition.	164
Figure 6.13 Effect of body force on velocity profile at $X = 220$.	166
Figure 6.14 Two phase in porous media at perfect wetting condition (Left-density distribution; Right-velocity distribution).	169
Figure 6.15 Relative permeability-Saturation relationships with different contact angle.	170
Figure 6.16 Illustration of the change of aperture in the porous media.	171
Figure 6.17 Relationship between the hydraulic aperture and absolute permeability.	172
Figure 6.18 Density and velocities distribution at different hydraulic aperture.	174
Figure 6.19 Relative permeability-saturation relationships with different hydraulic aperture.	175
Figure 6.20 Geometry of the fractured porous media.	176
Figure 6.21 Density distribution and velocity profile in the fractured porous media at different degree of saturation and different fracture orientation.	181
Figure 6.23 Relative permeability-saturation relationships of the fractured porous media.	182
Figure 6.24 Geometry of different material from CT.	184
Figure 6.25 3D reconstructed Ceramics.	185

Figure 6.26 Density and velocity distribution of two phase flow in 3D reconstructed porous media.	186
---	-----

LIST OF TABLES

Table 3.1 Difference between the morphological descriptions obtained from surface images and that of the micro X-ray CT model.	38
Table 3.2 Quantitative morphological description of the stochastic reconstructed models based on the micro X-ray CT model.	41
Table 3.3 Quantitative morphological description of the stochastic reconstructed model based on the surface images using method 1 and method 2 ("A,B,C,D" refers to the image, "1,2 "means the method id).	42
Table 4.1 Parameters used in the SCMP LBM simulations.	72
Table 5.1 Parameters used in the simulation of fluid flow in single fracture	103
Table 5.2 Parameters used to generate fracture for different fractal dimension, standard deviation and aperture.	107
Table 5.3 Parameters in the fluid flow under shear displacement.	116
Table 5.4 Coefficients of rough fracture.	125
Table 5.5 Parameters of DFN models.	129

CHAPTER 1 INTRODUCTION

1.1 BACKGROUND

Multiphase flow in fractured porous media can be very complex due to the simultaneous presence of different phases, which has been the subject of great interest related to unsaturated soil mechanics, hydrology, petroleum engineering, mining engineering, geothermal energy plants, CO₂ sequestration and radioactive waste storage. For example, in the subject of unsaturated soil, the soil-water characteristic curve and the relative permeability is of significant importance for the determination of mechanical property. The hysteresis, the air entry value, and the residual saturation have been the research interests over several decades. In petroleum engineering, the efficiency of the recovery is determined by a number of factors including the permeability of the rocks and the property of the fluids. The hydraulic fracturing is often utilized as an effective means to increase the production by creating number of intersected fractures. The storage of CO₂ via geologic carbon sequestration is being developed to solve the greenhouse problems. The characterization of the multiphase flow properties, such as relative permeability and residual CO₂ trapping of CO₂/water system, is of high importance in CO₂ storage project. The two-phase flow of water and gas mixture is also common in mining engineering and other underground engineering. On opposite, the main problem of nuclear installation is often the isolation of radioactive waste from biosphere. The isolation requires the minimization of the flow through discontinuities which is also the most significant mechanism of pollutant migration.

Reliable estimate of the hydraulic conductivity is difficult to obtain for its extensive variability in the field and the measurement of the parameters is time-consuming.

Numerous attempts have been made to predict empirically the permeability function. Recently, the physics of multiphase flow through fractured porous medium directly related to the microstructure and pore scale process has been recognized by numerous researchers based on experiments and theoretical analysis in the past three decades. However, the micromechanics of two phase flow in fractured porous media are still not clearly understood. Therefore, it is significant to develop a thorough understanding of the mechanism of multiphase flow in fractured porous media.

1.2 OBJECTIVE, METHOD AND SCOPE

The objective of this research is to provide a more scientific and more convincing methodology to illustrate the mechanism of two phase flow in fractured porous medium based on the micro-structural information of the media and complex physical or chemical process at pore scale. Applying the microstructure of fractured porous medium into the analysis of multiphase flow behavior encounters great challenge for the requirement of both statistical characterization of the fractured porous microstructure and the numerical method that could cope with the two phase flow in complex microstructure.

Therefore, three steps are required in the study of micromechanics of multiphase flow in fractured porous media:

- 1) Quantitative characterization of the microstructure, statistical description of the porous media and fracture network;
- 2) Characterization of the multiphase distribution in microstructure and clear understanding of the chemical and physical phenomenon at the pore scale;

3) Exact or approximate solution of the transport phenomena and prediction of the multiphase flow in fractured porous media.

1.3 THESIS STRUCTURE

In order to complete three research steps and approach the research goals, extensive works are conducted. Chapter 2 reviews the researches on characterization of porous media and fracture networks as well as the numerical methods related to fluid flows. Chapter 3 and chapter 4 give clear picture on static distribution of pore space, solid phase, wetting phase and non-wetting in porous media. Moreover, these two parts provide the boundary condition and initial condition in the study of the two phase flow problems. The dynamic fluid flows are investigated in chapter 5 and chapter 6. To this end, chapter 5 focuses on the single phase flow in fracture networks and chapter 6 extend the single phase flow to two phase flow problems. The research topics of each chapter are provided as follows.

Chapter 3 presents the method to reconstruct the porous media of sandstone from surface image; a good agreement between the reconstructed model and X-ray CT is obtained through the comparison of the quantitative measurements.

Chapter 4 compares the two phase fluid distribution of X-Ray CT with three different numerical methods, from which, the single component multiphase (SCMP) lattice Boltzmann method (LBM) is used to investigate the mechanism of fluid distribution in fractured porous media. The effect of degree of saturation and geometry of fracture on distribution pattern is studied.

Chapter 5 investigates the single phase fluid flow in rock fractures by using single phase LBM. The roughness and displacement on fluid flow is numerically studied and the empirical equation is proposed to predict the hydraulic conductivity under complex geometry, which is extended to the fracture network with roughness. The LBM is then coupled with Discrete Fracture Network (DFN) model and Discrete Element Model (DEM) to investigate flow in fracture networks under deformations.

Chapter 6 investigates the effect of body force, wettability and hydraulic aperture on two phase flows in porous media, the relative permeability-degree of saturation relationship is obtained at different scenarios. Meanwhile, the effect of fracture on two phase flows is explored. The trial of two phase flow in 3D reconstructed porous media is also conducted.

Chapter 7 provides summary and conclusions.

CHAPTER 2 LITERATURE REVIEW

2.1 PROBLEM STATEMENT

During the past four decades, the multiphase flow through fractured porous media has become a very popular research topic for its widely application in many engineering projects such as petroleum engineering, hydrology, mining industries as well as the isolation of radioactive waste. Generally, the study of two phase flow in fractured porous media is classified into two directions: the macroscopic approach and microscopic approach (Bear 1972, Khalili 1991). In the macroscopic approach, the single porosity and double porosity model are widely used in applications for its large scale description and easy implementation. However, the macroscopic approach cannot capture the phenomenon at pore scale, the influence of microstructure on fluid flow cannot be readily considered and the capillary force cannot be included in the model easily. Therefore, to have a more accurate and more scientific understanding of the multiphase flows in fractured porous media, the microscopic approach is employed in this thesis. To this end, the study of multiphase flow in fractured porous media requires both the microstructure information as well as the fluid flow model that could characterize the microscopic process.

2.2 CHARACTERIZATION OF POROUS MEDIA

Fluid flow in porous medium is critically dependent on the geometry and topology of the pore space. The accurate description of fluid properties requires the geometry and topology of the pore space, such as the hydraulic radius and connectivity of pores. A common approach is to represents the detail of pore structure as a distribution of pores

of different size. Information about the pore structure was usually obtained from mercury injection and image analysis Yanuka et al. (1986). Generally, the reliable method to obtain the microstructure information would be the 3D microstructure measurement. However, direct measurements of the 3D microstructures are usually difficult and expensive in practice. Alternatively, there are several numerical approaches that produce the microstructure of porous media, such as sphere packing model, process based model, pore network model and stochastic reconstruction model.

2.2.1 Sphere packing

The sphere packing is one of the earliest models which are used to study the fluid flow through porous media. The difficulties of accurate describe the fluid flow in complexity of pore geometry of sphere packs is recognized by Kozeny, who proposed an equation which related permeability to porosity and internal surface area of a sphere packing model. The equation was modified by Carman (1937), which is called Kozeny-Carman equation. However, the difficulty in analyzing the flow through in the sphere packing is still the prevention of its development for its complex shape of pores. Bernal (1964) stressed the need of “statistical geometry” and advocated it to describe the complex geometry of sphere packing model which rapidly accelerate the progress in such fields and others. The accurate description of the fluid flow in complex porous media becomes possible. Bernal’s concept was adopted in Finney’s study (1968, 1970) on fluid flow in random packing. The statistics of random packing is described, which is used to characterize the relatively simple geometrical entities and their statistical distribution. The statistical geometry is suggested as a powerful tool to describe the complete character of random sphere packing.

2.2.2 Process based model

Øren and Bakke (2003) proposed a process based method to reconstruct the 3-D microstructure of porous media. Image analysis technique is used to extract the microstructure information for generating realistic and fully characterized 3-D pore network model based on numerical modeling of geological processes which can representative the pore space of sandstone. The attempt has been done to reconstruct the 3-D sandstone by simulating the results of the main sandstone-forming processes: sedimentation; compaction; diagenesis. In the process based model, the microstructure generated as a result of complex physical, chemical and geological processes. However, this method required a lot of physical information, such as porosity, grain size distribution, a visual estimate of the degree of compaction, and parameters related to cementation. And the general geometrical characteristics does not necessary match with natural sample.

2.2.3 Pore network model

The pore network model originates from the bundle of tube model. In the early stage, the description of the geometry in fractured porous medium is simplified by applying the bundle of tube model where the mathematical operations get comparatively simple. The equation of the permeability and geometry of porous structure is derived from the tube radius frequency distribution of the equivalent bundle of tubes. However, the oversimplified bundle of tube model cannot represent accurately real fractured porous media for its absence of cross-connections between the tubes which is a major structural feature of these porous media. Alternatively, Fatt (1956) proposed the network of tubes to represent the real porous media which is more accurate than the bundle of tubes and more easier to complemented than sphere packing model. The vast majority of network

models consist of pore bodies and throats, along with a description of how the pore bodies are connected via the pore throats. The pore bodies are meant to represent the larger void spaces found in the natural porous medium, the narrow openings that connect the adjacent pore bodies are modeled by the pore throats (capillary tubes). Quantitative characteristic lies in choosing the geometric shape, sizes, location, and orientations of the pore bodies and throat so that the amount of detail in the description of the pore geometry is sufficient to be modeled. Moreover, the capillary pressure curves are derived from the network model and the pore size distribution is also calculated based on capillary pressure curves. Bryant et al. (1993) applied the network model to represent the real random sphere packing with no assumption invoked for the well characterized geometry and topology of the void space. More recently, the coupled image technique and network model method is applied to reflect the pore structure. The network work skeleton is represented by the center line of the pore space from the binarized image and the statistical spatial information is used to generate the topology and geometry of the network which can represent the real structure of the pore structure. However, various assumptions concerning with the pore network model which oversimplify the structure of void space. For example, the pore space is often idealized to simple geometries such as uniform circular or square cross-sectional shapes.

2.2.4 Local porosity theory based stochastic model

Local porosity theory and its application to the analysis of stochastic reconstruction models for porous media was reviewed and discussed by Hilfer (1991). Typical geometric observation such as porosity and specific internal surface area are not sufficient to distinguish the fractured porous microstructure. The stochastic

reconstruction models are found not only match the porosity and specific internal but also other geometric quantities such as correlation functions and linear and sphere contact distributions.

The reconstruction of the microstructure of 3D random heterogeneous media from the information obtained from a 2D micrograph has manifold potential applications especially only 2D images are available for analysis. It is desirable that a reconstruction procedure has the ability to incorporate as much crucial microstructure information as possible to capture the remarkable feature of the reference structure. Jacques (1984) proposed a 3D modeling technique of fractured porous media. The choice of two functions of probability distribution function and correlation function for characterizing a fractured porous medium had been discussed by Joshi (1974, PHD thesis) and Quiblier(1984), and they are remain unchanged from 2D to 3D among the few characteristics of fractured porous medium. Alder (1990) suggested that the fractured porous media share the same statistical property of porosity and the autocorrelation function measured on thin section of the sandstones, which can be used to reconstruct artificial media with the same average geometrical properties. Yeong and Torquato (1998) formulated a procedure to reconstruct the structure of general random heterogeneous media from limited morphological information where any type and numbers of correlation function are incorporated in order to reconstruct accurately.

2.3 CHARACTERIZATION OF FRACTURE NETWORKS

The characterization of flow in fracture network has been a research focus in the past half century. Conventional models to characterize the flow in fracture network including single equivalent continuum model (Pruess et al. 1990), dual continuum model

(Barenblatt et al. 1960, Huyakorn et al. 1983), multiple interacting continua model, multi-permeability model (Bai et al. 1993, Bear et al. 1993). However, most of the conventional methods do not explicitly model the geometry of discrete fractures that control the flow pathway.

Alternatively, the discrete fracture network (DFN) model is a more realistic model which considers both the physical property and geometrical property. DFN models have been used for a wide variety of exploration and production purposes since the mathematical studies and experimental works by Snow (1965, 1969). Beacher et al. (1967) developed a fracture model with all the joints simplified as circular disks randomly distributed in space based on the geological statistics. Methods for characterizing fractures can be found in Pointe and Hudson (1985) and Singhal and Gupta (1999). Long et al. (1985) developed a numerical code to generate random fracture systems in two dimensions. It was found that the fracture network do not necessarily behave like a equivalent porous medium only if the fracture system is of high density and non-uniform orientation distribution. The fluid flow in fracture network is affected by the degree to which the fractures are interconnected. The relationship between the fractures interconnectivity and permeability was by investigated Long and Witherspoon (1985). It was found that, the fracture connectivity increases with increasing fracture length and fracture density, as the chance of fracture intersection increases. Later on, Long and Billaux (1987) developed a technique to process field data into fracture network model, in which, a geo-statistical simulation was used to predict the average geometric parameters of the network. Similar work was also conducted by Andersson and Dverstorp (1987). The permeability of anisotropic fracture

network was studied by Chen et al. (1999), the solution of anisotropic flow within the fracture plane was derived.

Dershowitz et al. (2004) highlighted the advances in the discrete fracture network approaches to flow and transport modeling and analysis for fracture rock. Recently, the DFN model is adopted to establish the hydro-geological site descriptive model in relation to design and construction of subsea tunnels (Kim et al. 2007), to investigate the contaminated sites on fractured rock (Parker et al. 2007), and to investigated the directivity of permeability of fractured rock masses with varying flow directions and different aperture distribution (Liu et al. 2014). However, in most of the aforementioned researches, the flow in individual fracture is characterized by the cubic law based on the assumption that the fracture is smooth with constant aperture. The directly simulation of roughness effect on fluid flow through fractured network is rarely reported (Zhao et al. 2014).

2.4 THE FLOW MODEL

Theoretically, the fluid flow is governed by the Navier-Stokes equation and a set of coupled and nonlinear partial equation are derived from the conservation of mass, momentum and energy. However, the analytical solution is impossible especially in the system of complex geometry and boundary condition. Alternatively, there are several numerical methods are proposed such as finite difference method, finite element method, finite volume method and spectral method, which are class of conventional computational fluid dynamics (CFD). However, the conventional numerical methods for fluid flow are based on grid or element, and the computational cost is high and is not

easy for implementation of simulation at pore scale. Moreover, the tracking of the interface in multiphase system is always a challenge for conventional methods.

In contrary , the Lattice Boltzmann method (LBM) is a “bottom-up” method for simulation of fluid flow which is quite distinctive from molecular dynamics (MD) on the one hand and “top-down” methods based on the discretization of partial differential equations on the other hand (Wolf-Gladrow 2000). The fundamental idea of LBM is to construct the kinetic model with the essential physics of microscopic processes incorporated so that the macroscopic averaged properties can be derived directly. The difficulties to solve the complicated Boltzmann equation and trace the path of particles in molecular dynamics simulation were simplified by solving the kinetic equations.

In the past two decades, comprehensive investigations have been done to improve the accuracy and efficiency of Lattice Boltzmann Method in the treatment of boundary conditions (Skordos 1993; Noble et al. 1995; Inamuro et al. 1995; Maier et al. 1996; He & Zou et al. 1997; Filippova & hänel, 1998; Mei et al., 1999; Guo et al. 2002; Latt et al. 2008) and interfacial physics among multi-phases (Swift et al. 1996; Zhang, he & Chen 2000; He & Doolen 2002; Yu et al. 2003; Yan & Zu 2007; Sukop et al. 2008; Sarkar et al. 2009; Zu et al. 2010). Applications of LBM in the simulation of single and multiphase flow in porous medium were investigated by numerous researchers (Hill et al. 2001; Pan et al. 2004; Chai et al. 2008; Walsh et al. 2010; Yan et al. 2011; Ghassemi et al. 2011).

In order to explore the mechanism of multiphase flow and its dependence on microstructure, the LBM is adopted in this research for its appealing features of

programming simplicity, intrinsic parallelism, straightforward implementation of complex boundaries and multiple fluid species.

2.5 REFERENCES

Adler P.M., Jacquin C.G., Quiblier J.A. (1990) Flow in simulated porous media. *International Journal of Multiphase Flow* 16(4): 691-712.

Andersson J., Dverstorp B. (1987) Conditional simulations of fluid flow in three-dimensional networks of discrete fractures. *Water Resources Research* 23(10): 1876-1886.

Bai M., Elsworth D., Roegiers J.C. (1993) Multiporosity/multipermeability approach to the simulation of naturally fractured reservoirs. *Water Resources Research* 29(6):1621-1633.

Barenblatt G.E., Zheltov I.P., Kochina I.N. (1960) Basic concept in the theory of seepage of homogeneous liquids in fissured rocks. *Journal of Applied Mathematics (USSR)* 24(5): 1286-1303.

Batchelor G.K. (1967) *An introduction to fluid dynamics*. Cambridge University Press, New York.

Bear J. (1972) *Dynamics of fluids in porous media*. American Elsevier.

Bear J., Tsang C.F., Marsily G. de (1993) *Flow and contaminant transport in fractured rocks*, Academic Press, New York.

Bryant S.L., King P.R., Mellor D.W. (1993) Network model evaluation of permeability and spatial correlation in a real random sphere packing. *Transport in Porous Media* 11(1): 53-70.

Carman P.C. (1937) Fluid flow through granular beds. *Transactions of the Institution of Chemical Engineers* 15: 150-166.

Chai Z., Guo Z., Zheng L., Shi B. (2008) Lattice Boltzmann simulation of surface roughness effect on gaseous flow in a microchannel. *Journal of Applied Physics* 104(1): 014902.

Chen M., Bai M., Roegiers J.C. (1999) Permeability tensors of anisotropic fracture networks. *Mathematical Geology* 31(4): 335-373.

Dershowitz W.S., La Pointe P.R., Doe T.W. (2004) Advances in discrete fracture network modeling. In: *Proceedings, US EPA/NGWA fractured rock conference, Portland*, pp.882–894.

Fatt I. (1956) The Network Model of Porous Media. *Petroleum Transactions* 207: 144-181.

Filippova O. and Hänel D. (1998) Grid Refinement for Lattice-BGK Models. *Journal of Computational Physics* 147(1): 219-228.

Ghassemi A., Pak A. (2011) Pore scale study of permeability and tortuosity for flow through particulate media using Lattice Boltzmann method. *International Journal for Numerical and Analytical Methods in Geomechanics* 35(8): 886-901

Guo Z., Zheng C. Shi B. (2002) An extrapolation method for boundary conditions in lattice Boltzmann method. *Physics of Fluids* 14(6): 2007-2010.

He X., Doolen D.G. (2002) Thermodynamic Foundations of Kinetic Theory and Lattice Boltzmann Models for Multiphase Flows. *Journal of Statistical Physics* 107(1): 309-328

He X., Zou Q. Luo L., Dembo M. (1997) Analytic solutions of simple flows and analysis of nonslip boundary conditions for the lattice Boltzmann BGK model. *Journal of Statistical Physics* 87(1): 115-136.

Hilfer R. (1991) Geometric and dielectric characterization of porous media. *Physical Review B* 44(1): 60-75.

Hill R.J., Koch D.L., Ladd Anthony J.C. (2001) The first effects of fluid inertia on flows in ordered and random arrays of spheres. *Journal of Fluid Mechanics* 448(01): 213-241

Huyakorn P.S., Lester B.H., Faust C.R. (1983) Finite element techniques for modeling groundwater flow in fractured aquifers. *Water Resources Research* 19(4):1019-1035.

Inamuro T., Yoshino M., Ogino F. (1995) A non-slip boundary condition for lattice Boltzmann simulations. *Physics of Fluids* 7(12): 2928-2930.

Khalili N. (1991) Numerical modeling of flow through fractured media. PhD thesis.

Kim H.M., Ryu D.W., Tanaka T., Ando K. (2007) Hydro-geological descriptive model using discrete fracture network (DFN) in a site characterization for subsea tunnels construction. *Chinese Journal of Rock Mechanics and Engineering* 26(11): 2217-2225.

Pointe L. Hudson J.A. (1985) Characterization and interpretation of rock mass joint patterns. Geological Society of America Special Paper 199: 1-37

Latt J., Chopard B., Malaspinas O., Deville M., Michler A. (2008) Straight velocity boundaries in the lattice Boltzmann method. Physical Review E 77(5): 056703.

Long J.C.S. Remer J.S. Wilson C.R., Witherspoon P.A. (1982) Porous media equivalents for networks of discontinuous fractures. Water Resources Research 18(3): 645-658.

Long J.C.S., Billaux D.M. (1987) From field data to fracture network modeling: an example incorporating spatial structure. Water Resources Research 23(7): 1201-1216.

Long J.C.S., Witherspoon P.A. (1985) The relationship of the degree of interconnection to permeability in fracture networks. Journal of Geophysical Research 90(B4): 3087-3098.

Maier R.S., Bernard R.S., Grunau D.W. (1996) Boundary conditions for the lattice Boltzmann method. Physics of Fluids 8(7): 1788-1801.

Mei R., Luo L., Shyy W. (1999) An Accurate Curved Boundary Treatment in the Lattice Boltzmann Method. Journal of Computational Physics 155(2): 307-330.

Noble D.R., Chen S., Georgiadis J.G., Buckius R.O. (1995) A consistent hydrodynamic boundary condition for the lattice Boltzmann method. Physics of Fluids 7(1): 203-209.

Øren P.E., Bakke S. (2003) Reconstruction of Berea sandstone and pore-scale modeling of wettability effects. Journal of Petroleum Science and Engineering 39(3-4): 177-199.

Pan C., Prins J.F., Miller C.T. (2004) A high-performance lattice Boltzmann implementation to model flow in porous media. *Computer Physics Communications* 158(2): 89-105.

Parker B.L. (2007) Investigating contaminated sites on fractured rock using the DFN approach. In *Proceedings of 2007 U.S. EPA/NGWA Fractured Rock Conference: State of the Science and Measuring Success in Remediation*, September 24-26, Portland, Maine, Westerville

Pruess K., Wang J.S.Y., Tsang Y.W. (1990) On thermohydrologic conditions near high-level nuclear wastes emplaced in partially saturated fractured tuff: 2. Effective continuum approximation. *Water Resources Research* 26(6):1249-1261.

Quiblier J.A. (1984) A new three-dimensional modeling technique for studying porous media. *Journal of Colloid and Interface Science* 98(1): 84-102.

Sarkar S., van der Hoef M.A., Kuipers J.A.M. (2009) Fluid-particle interaction from lattice Boltzmann simulations for flow through polydisperse random arrays of spheres. *Chemical Engineering Science* 64(11): 2683-2691.

Singhal B.B.S., Gupta R.P. (1999) *Applied Hydrogeology of Fractured Rocks*. Kluwer Academic Publishers, New York

Skordos P.A. (1993) Initial and boundary conditions for the lattice Boltzmann method. *Physical Review E* 48(6): 4823-4842.

Snow D.T. (1965) A parallel plate model of fractured permeable media. Ph.D. dissertation, 331 pp., Univ. of Calif., Berkeley.

Snow D.T. (1969) Anisotropic permeability of fractured media. *Water Resources Research* 5(6):1273-1289.

Sukop M.C., Huang H., Lin C.L., Deo M.D., Oh K, Miller J.D. (2008) Distribution of multiphase fluids in porous media: Comparison between lattice Boltzmann modeling and micro-x-ray tomography. *Physical Review E* 77(2): 026710

Swift M.R, Orlandini E., Osborn W.R., Yeomans J.M. (1996) Lattice Boltzmann simulations of liquid-gas and binary fluid systems. *Physical Review E* 54(5): 5041-5052

Walsh S.D.C., Saar M.O. (2010) Macroscale lattice-Boltzmann methods for low Peclet number solute and heat transport in heterogeneous porous media. *Water Resources Res* 46(7): W07517.

Wolf-Gladrow D.A. (2000) *Lattice-Gas Cellular Automata and Lattice Boltzmann Models: An Introduction*. Springer.

Yan Y., Zu Y. (2007) A lattice Boltzmann method for incompressible two-phase flows on partial wetting surface with large density ratio. *Journal of Computational Physics* 227(1): 763-775

Yan Y., Zu Y. (2007) A lattice Boltzmann method for incompressible two-phase flows on partial wetting surface with large density ratio. *Journal of Computational Physics* 227(1): 763-775

Yan Y., Zu Y., Dong B. (2011) LBM, a useful tool for mesoscale modelling of single-phase and multiphase flow. *Applied Thermal Engineering* 31(5): 649-655.

Yanuka M., Dullien F.A.L., Elrick DE (1986) Percolation processes and porous media: I. Geometrical and topological model of porous media using a three-dimensional joint pore size distribution. *Journal of Colloid and Interface Science* 112(1): 24-41.

Yeong C.L.Y., Torquato S. (1998) Reconstructing random media. II. Three-dimensional media from two-dimensional cuts. *Physical Review E* 58(1): 224-233.

Yu D., Mei R., Luo L., Shyy W. (2003) Viscous flow computations with the method of lattice Boltzmann equation. *Progress in Aerospace Sciences* 39(5): 329-367

Zhang R., He X., Chen S. (2000) Interface and surface tension in incompressible lattice Boltzmann multiphase model. *Computer Physics Communications* 129(1-3): 121-130

Zhao Z.H., Li B., Jiang Y.J. (2014) Effects of fracture surface roughness on macroscopic fluid flow and solute transport in fracture networks. *Rock Mechanics and Rock Engineering* 47(6): 2279-2286.

Zu Y., Yan Y., Li J., Han Z. (2010) Wetting behaviors of a single droplet on biomimetic micro structured surfaces. *Journal of Bionic Engineering* 7(2): 191-198.

CHAPTER 3 STOCHASTIC RECONSTRUCTION OF GOSFORD SANDSTONE FROM SURFACE IMAGE

To obtain the microstructure of material is one of the intrinsic interests for many researchers. The X-ray Computed Tomography (CT) and Scanning Electron Microscope (SEM) have been widely used to obtain the microstructure of materials for different purposes. However, there are some limitations of the SEM and X-ray CT. In this chapter, the stochastic reconstruction is adopted to obtain the microstructure model of Gosford sandstone, which may provide an alternative solution to obtain the microstructure of the Gosford sandstone and similar materials like cement. The main contributions of the present work are: employment of a digital microscope to obtain the surface image, the derivation of the 3D morphological distribution curve from the 2D surface image, and the verification of the reconstructed microstructure model. Our results show that the proposed method is able to reproduce a comparable microstructure model for the Gosford sandstone.

3.1 INTRODUCTION

Most rocks have complex microstructures which are regarded as the most important factor in determining their mechanical properties and transport behaviors (Alder et al. 1990, Hazor et al. 1997). Moreover, to obtain the microstructure of material is one of the intrinsic interests for scientists. For instance, two Nobel prizes were awarded for the inventions of X-ray Computed Tomography (CT) and Scanning Electron Microscope (SEM). In geosciences and geomechanics, these devices have been used to obtain the microstructure of geomaterials for different purposes, e.g. the study of fracturing in

granite by Ichikawa et al. (2001), the investigation of thermally induced microcracks in concrete by Wang et al. (2005), the characterization of shale rock properties by Josh et al. (2012), and the analysis of energy dissipation in Gosford sandstone by Sufian and Russell (2013). However, the SEM and X-ray CT are not perfect, besides being expensive and time consuming, there are limitations. The SEM can only get the surface image, and the X-ray CT is usually only applicable to small size specimen when the resolution is high.

Recently, a possible solution has been developed to reconstruct the microstructure model of a porous media based on its morphological information, and it is called stochastic reconstruction (Hazlett 1997). The stochastic reconstruction is capable to reproduce a large number of microstructure models for a material at little cost. Moreover, using the method, it is possible to generate a microstructure model of large size under high resolution. The principle of the stochastic reconstruction is straightforward and easy to understand. The reconstruction is treated as an optimization problem where the microstructure model is the target variable and the difference between the morphological description curves of the target material and the reconstructed microstructure model serves as the target function. The goal is to find the best solution to minimize the target function. The simulated annealing method has been widely used as an optimization method (Hazlett 1997, Yeong and Torquato 1998), and the two-point probability function, lineal path function, and multiple-point statistics function are commonly adopted as the morphological descriptor (Okabe and Blunt 2005, Politis et al. 2008, Hajizadeh et al. 2011, Tahmasebi and Sahimi 2012). Stochastic reconstruction has been used to generate microstructure models of different materials, e.g. the dispersions by Rintoul and Torquato (1997), the Berea and Fontainebleau

sandstones by Manwart et al. (2000), the chalk by Talukdar and Torsaeter (2002), and other heterogeneous materials by Jiao et al. (2008). However, in these work, the morphological description curve is simply obtained from 2D images of the corresponding material (Talukdar et al. 2002). Whether the morphological description curve can reflect the 3D morphological information of the target material is not verified. Moreover, the reconstructed microstructure models have not been validated against the real microstructure of the material.

In this chapter, the stochastic reconstruction is adopted to generate the microstructure model of the Gosford sandstone. The proposed method is illustrated in Figure 3.1. The surface image of the Gosford sandstone is captured using a digital microscope. The relationship between the morphological description curves of the 2D image and the 3D model is studied based on the X-ray micro CT data of the Gosford sandstone. Then, the simulated annealing method is used to generate the microstructure of the Gosford sandstone. The reconstructed models are compared with the X-ray micro CT model. The main contributions of the present work are: the employment of a digital microscope to obtain the surface image; the derivation of the 3D morphological distribution curve from the 2D surface image, and the verification of the reconstructed microstructure model. From our study, it is concluded that the stochastic reconstruction procedure is reasonably good to generate the microstructure model for the Gosford sandstone.

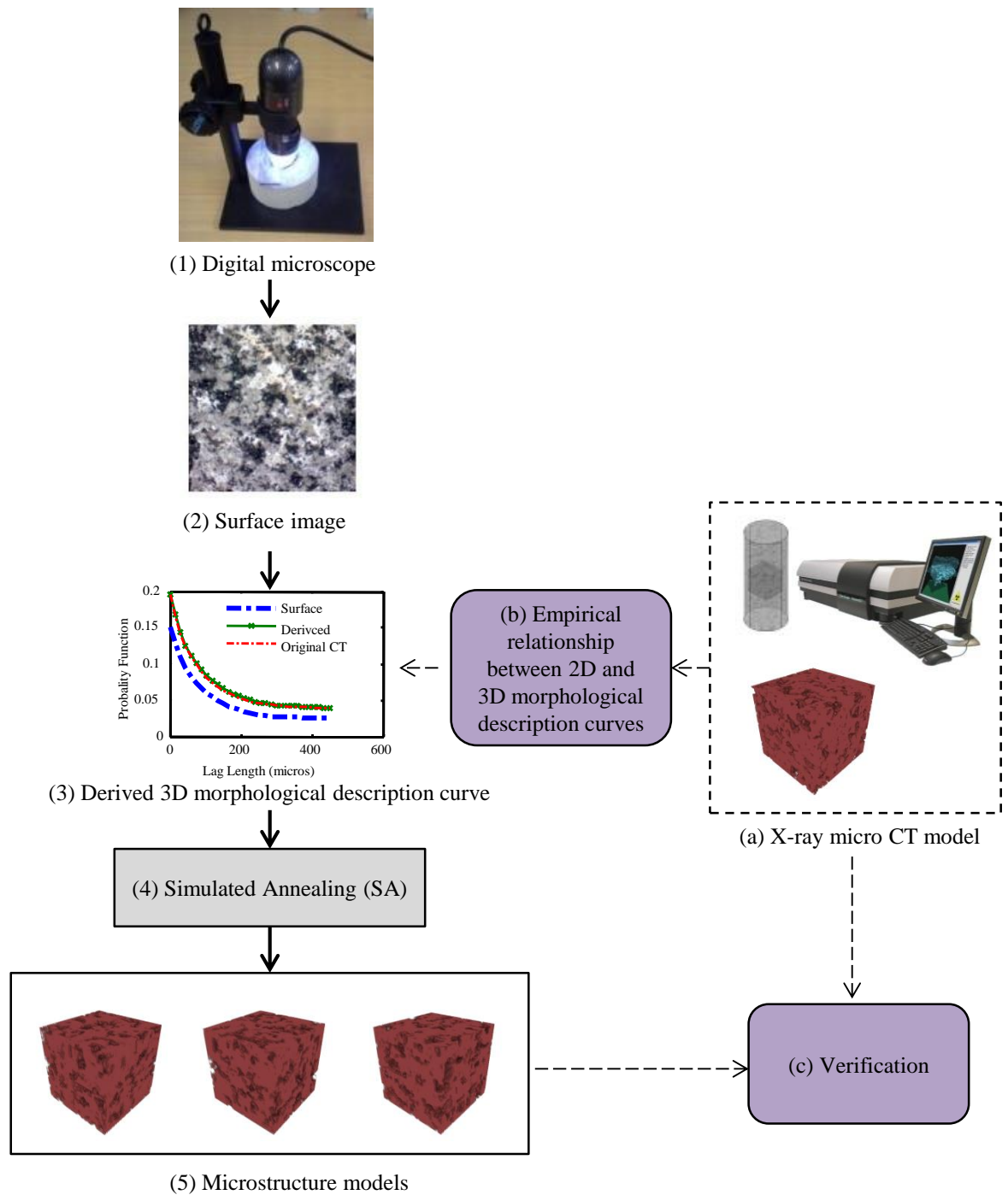


Figure 3.1 Illustration of the stochastic reconstruction for Gosford sandstone.

3.2. STOCHASTIC RECONSTRUCTION

3.2.1 Two-point probability function

In this paper, the porous media is considered as a two-phase mixture consisting of the solid and pores, and it is represented by a binary phase function $I(\vec{r})$ as

$$I(\vec{r}) = \begin{cases} 1, & \vec{r} \text{ is in the pore phase} \\ 0, & \vec{r} \text{ is in the solid phase} \end{cases} \quad (3.1)$$

where \vec{r} is the spatial position of a point in the porous media.

The two-point probability function is the most widely used morphological descriptor in the stochastic reconstruction, which is written as

$$S_2(\vec{r}_i, \vec{r}_j) = \langle I(\vec{r}_i) \cdot I(\vec{r}_j) \rangle \quad (3.2)$$

where the $\langle \rangle$ denotes the statistical average (probability) of two points in the pore phase at positions \vec{r}_i and \vec{r}_j . For a macroscopically homogeneous and isotropic porous media, $S_2(\vec{r}_i, \vec{r}_j)$ only depends on the length of the lag vector $\vec{u} = \vec{r}_j - \vec{r}_i$ between the two points. Thus, the two-point distribution function can be further simplified as

$$S_2(u) = \langle I(\vec{r}_i) \cdot I(\vec{r}_i + \vec{u}) \rangle \quad (3.3)$$

In the stochastic reconstruction, a porous media is usually represented by a digitalized model. The two-point distribution function of a digitalized model can be calculated as

$$S_2(u) = \frac{\sum \sum I(\vec{r}_i) \cdot I(\vec{r}_i + u\vec{e}_j)}{D \prod L_i} \quad (3.4)$$

where \vec{r}_i represents a pixel in the interested domain, u is length of the lag vector, \vec{e}_j is the unit vector, D is the dimension of the porous media, and L_i is the size of the domain (in pixels). It should be mentioned that when the periodic boundary condition is considered, the second pixel ($\vec{r}_i + u\vec{e}_j$) will return to the start boundary $(\vec{r}_i + u\vec{e}_j - L_{j*})|_{j=j*}$ when the point moves beyond the end boundary, with the same normal direction \vec{e}_{j*} .

The two-point probability function $S_2(u)$ can be viewed as a curve that represents certain morphological information for a porous media. In stochastic reconstruction, the two-point probability function is widely used due to its ease of implementation and high computational efficiency. In this paper, it is adopted as the morphological descriptor for the reconstruction. There are also other available morphological functions for stochastic reconstruction, and details can be found in the work of Yeong and Torquato (1998), Hajizadeh et al. (2011), and Tahmasebi and Sahimi (2012).

3.2.2 Stochastic reconstruction based on the simulated annealing method

The procedure of stochastic reconstruction based on the simulated annealing method is shown in Figure 3.3. The target function is defined as

$$E = \sum_{u=0}^{u_{\max}} (\tilde{S}_2(u) - S_2(u))^2 \quad (3.5)$$

where E is the system energy, $S_2(u)$ is the morphological distribution curve (two-point probability function) of the reconstructed model, $\tilde{S}_2(u)$ is the morphological distribution curve of the target material, and u_{\max} is the maximum lag length which can be determined by accounting the size of the interested domain, the accuracy of the morphological representation and the computational efficiency. In this work, it is taken as one to two tenths of the size of the domain.

There are two stages of iterations in the stochastic reconstruction. The first one is the internal phase exchange based on the Metropolis algorithm without updating of the system temperature:

$$p = \begin{cases} 1, & \Delta E \leq 0 \\ e^{-\Delta E/k_B T}, & \Delta E > 0 \end{cases} \quad (3.6)$$

where p is the probability of accepting the exchange, ΔE is the change of system energy due to the phase exchange, k_B is the Boltzmann's constant, and T is the temperature of the current system.

The second one is the Markov chain iteration which updates the system temperature according to

$$T = T_0 e^{(\lambda-1)(m+1)} \quad (3.7)$$

in which T_0 is the initial temperature of the system, λ is the reduction parameter of the system temperature and m is the current number of Markov chain. The reduction parameter λ is estimated by

$$\lambda = \text{Max} \left[\lambda_{\min}, \text{Min} \left(\lambda_{\max}, \frac{E_{\min}}{\bar{E}} \right) \right] \quad (3.8)$$

where $\lambda_{\min}=0.2$, $\lambda_{\max}=0.8$, and E_{\min} and \bar{E} are the minimum and average energy in each Markov chain, respectively.

The Markov chain number m is given by

$$m = N / Ne \quad (3.9)$$

where N is the total number of iterations, and Ne is Markov chain length which has significant influence on the convergence. For the reconstruction of geomaterials, Ouenes et al. (1994) suggest that Ne should be 100 to 300 (in this paper $Ne=200$).

Generation of the initial model is as described as follows. The first step is to generate a random model with the specific porosity. The phase properties of two pixels are randomly exchanged and the probability of accepting the exchange is p_0 . The exchange is repeated for N_0 times. Then, the initial temperature can be calculated as

$$T_0 = - \frac{\Delta E_{sum}}{N_0 \ln(p_0)} \quad (3.10)$$

With the initial model and its parameters ready, the model is iterated until the system energy is less than a specified value, e.g. $1e-5$. Therefore, the morphological curve of the reconstructed model approaches the target one, which guarantees that the reconstructed model has similar morphological information as the target material. More details on the implementation and determination of parameters in the stochastic

reconstruction based on simulated annealing method can be found in Talukdar and Torsaeter (2002).

3.3. QUANTITATIVE MORPHOLOGICAL MEASUREMENTS OF POROUS MEDIA

3.3.1 Porosity and specific surface

In stochastic reconstruction, the porosity φ is defined as the probability of finding a point in the pore phase. It also can be represented as the first statistical moment of the phase function $I(\vec{r})$ and equals to the two-point probability function when $u = 0$.

$$\varphi = S_2(0) \quad (3.11)$$

Another relationship between the porosity and the two-point probability function is

$$\varphi^2 = S_2(\infty) \quad (3.12)$$

The specific surface, s , is defined as the interfacial area per unit volume between the two phases. It can be used to evaluate how accurately the pore-solid interface has been reproduced. In the stochastic reconstruction, the specific surface is calculated as

$$s = \frac{-\frac{d}{du} S_2(u)|_{u=0}}{2D} \quad (3.13)$$

where D is the dimension of the reconstructed model.

3.3.2 Local porosity distribution

The local porosity of the reconstructed model is defined as the porosity within a cubic box of side length l centered at position \vec{r} . It is given as

$$\varphi(\vec{r}, l) = \langle I(\vec{r}) \rangle_M \quad (3.14)$$

where M refers to the operation domain, which is of the size $[i-l/2, i+l/2], [j-l/2, j+l/2], [k-l/2, k+l/2]$ when the measurement box is centered at $\vec{r} = (i, j, k)$. To achieve statistically accurate portrait of the local porosity distribution, the measurement box is moved from left top corner $(l/2, l/2, l/2)$ to right bottom corner $(L_x-l/2, L_y-l/2, L_z-l/2)$ by one pixel each time. Then, the local porosity distribution for a box with a side length of l is evaluated by dividing the number of boxes with porosity in a certain interval $(\varphi, \varphi + \Delta\varphi)$ by the total number of boxes. The local porosity distribution function can be described by the following equation

$$\mu(\varphi, l) = \frac{1}{n} \sum_{\vec{r}} \delta(\varphi - \varphi(\vec{r}, l)) \quad (3.15)$$

where,

$$\delta(\varphi - \varphi(\vec{r}, l)) = \begin{cases} 1, & \text{if } |\varphi - \varphi(\vec{r}, l)| \leq \Delta\varphi \\ 0, & \text{otherwise} \end{cases} \quad (3.16)$$

and n is the total number of measurement boxes.

3.3.3 Local percolation probability

In stochastic reconstruction, the local percolation probability is defined as the probability of finding a cubic measurement cell $M_o(\vec{r}, l)$ that percolates in orientation, o . It is expressed in the equation below (Hilfer 2000, Øren and Bakke 2003)

$$P_o(l) = \frac{1}{n} \sum_{\vec{r}} \Lambda_o(\vec{r}, l) \quad (3.17)$$

where

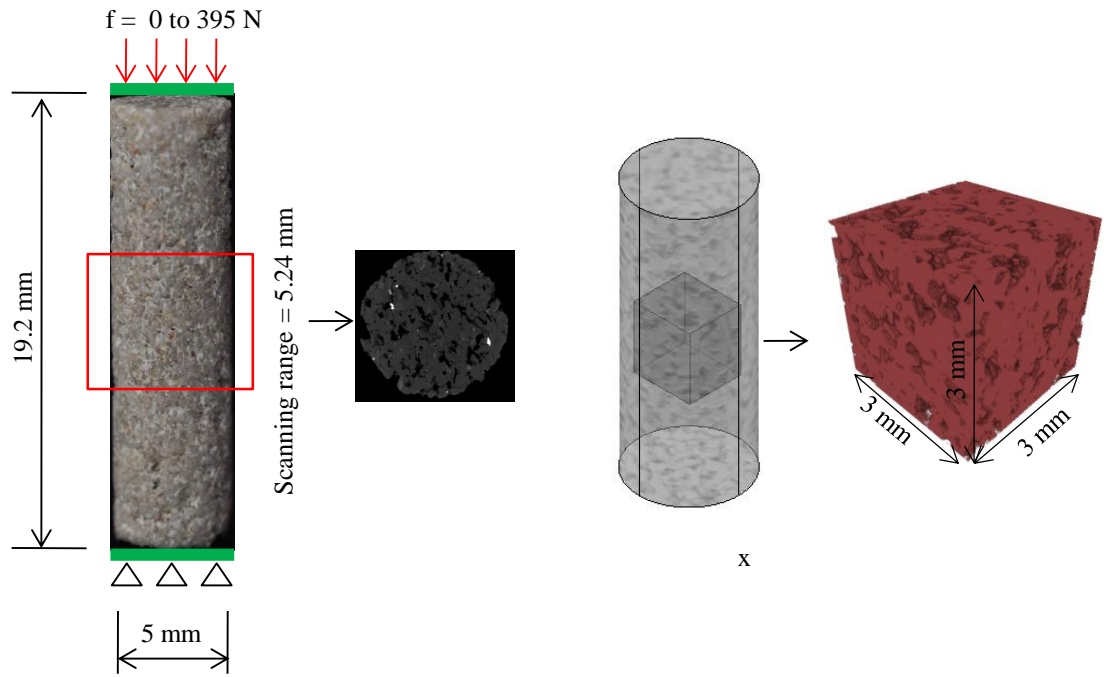
$$\Lambda_o(\vec{r}, l) = \begin{cases} 1, & \text{if } M_o(\vec{r}, l) \text{ percolates} \\ 0, & \text{otherwise} \end{cases} \quad (3.18)$$

The $\Lambda_o(\vec{r}, l)$ can be evaluated using a burning algorithm. First, a fire is set at the pore pixel; the fire then propagates to the neighboring pixel where pore pixel is presented; finally, the fire distinguishes until no neighboring pore pixel can be detected. The process is repeated until all the pore pixels are visited. When the burning process is completed, all the pore clusters are labeled with different fire numbers. The measurement cell is percolated in orientation o if the same cluster numbers are found on opposite sides of the measurement cell in direction o . It means that there exists a path within the cell along orientation o . After all the measurement cells have been visited, the local percolation probability can be measured by using equation (3.17).

3.4 MORPHOLOGICAL DESCRIPTION OF THE GOSFORD SANDSTONE

3.4.1 Relationship between the 2D and 3D morphological description

X-ray micro CT scanning with a spatial resolution of 5 micros was conducted on the Gosford sandstone by Sufian and Russell (2013). As shown in Figure 3.2, a spatial cube of $600 \times 600 \times 600$ pixels ($3 \times 3 \times 3 \text{ mm}^3$) is extracted from the original X-ray micro CT model, which is used to investigate the relationship between 2D and 3D morphological description curves of the Gosford sandstone. The binaryzation of the X-ray micro CT data is done by adjusting the threshold value based on the porosity of the Gosford sandstone which is reported as 19%. The areal porosity of each 2D CT slice image is shown in Figure 3.3. The areal porosity of the CT slice is mostly different from the 3D porosity. The morphological description curves of 2D and 3D models are also different (see Figure 3.7). It is found that the morphological description curve of a 2D slice image is close to that of the 3D model when the areal porosity is near the 3D porosity. Therefore, the specific surface image with areal porosity equal to the 3D porosity can be used to extract the 3D morphological description curve for the stochastic reconstruction. However, it is difficult to find this specific image in practice. One alternative solution is to modify the areal porosity by adjusting the threshold value if the surface image is in a gray format. The threshold value usually can be determined between two peaks of the



(a) Gosford sandstone specimen [6]

(b) X-ray micro CT model

Figure 3.2 Sample drilled for x-ray CT scanning and region of interests selected for analysis.

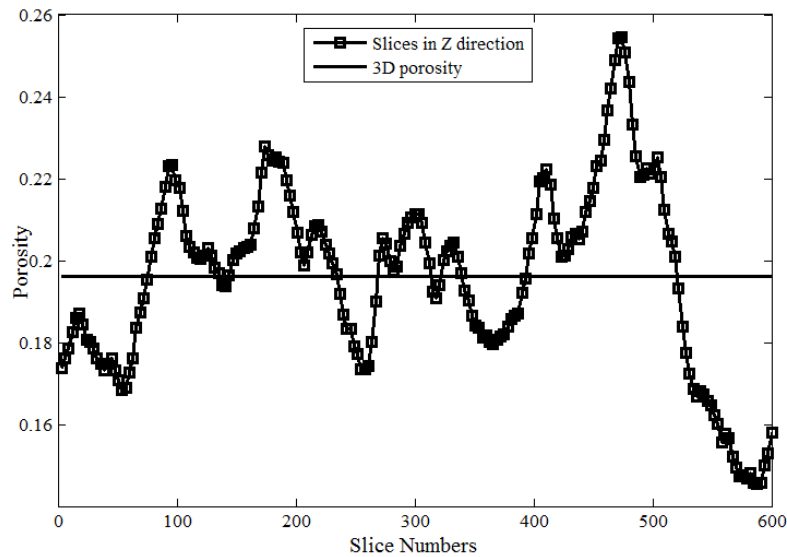


Figure 3.3 Areal porosity distribution of the X-ray micro CT model.

histogram of the gray values, Talukdar and Torsaeter (2002) adopted such method. However, in their work, the morphological description curve from the slice image is simply adopted for reconstruction without further comparison with the corresponding 3D one. To quantify the difference between the 2D and 3D morphological description curves, an index, Ω , in the same form as the system energy in the stochastic reconstruction is used.

$$\Omega = \sum_{u=0}^{u_{\max}} (S_2^{3D}(u) - S_2^{2D}(u))^2 \quad (3.19)$$

To verify the method, the original CT slice images with the highest and lowest porosities as shown in Figure 3.4 are processed. The results are presented in Figure 3.5, which prove the applicability of the method. In this method (named method 1), only the porosity and 2D image of the porous media are required, and they are easy to obtain. The shortcoming is that changing the areal porosity of a surface image may influence its original morphological information. For instance, if a surface image with low areal porosity is adjusted to a very high porosity binary image, more pores might be generated and connectivity between pores might be influenced as well. Moreover, the method is not applicable when the surface 2D image is already in the binaryzation form.

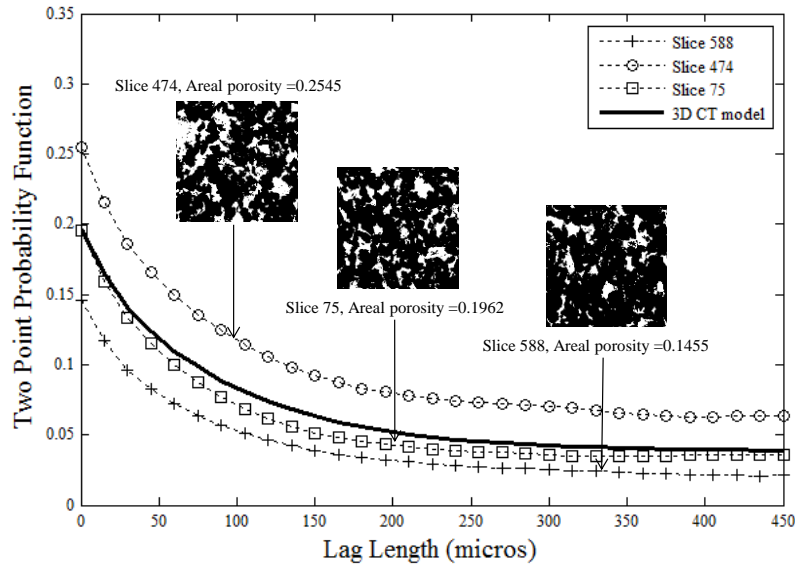


Figure 3.4 Morphological description curves of different CT slices.

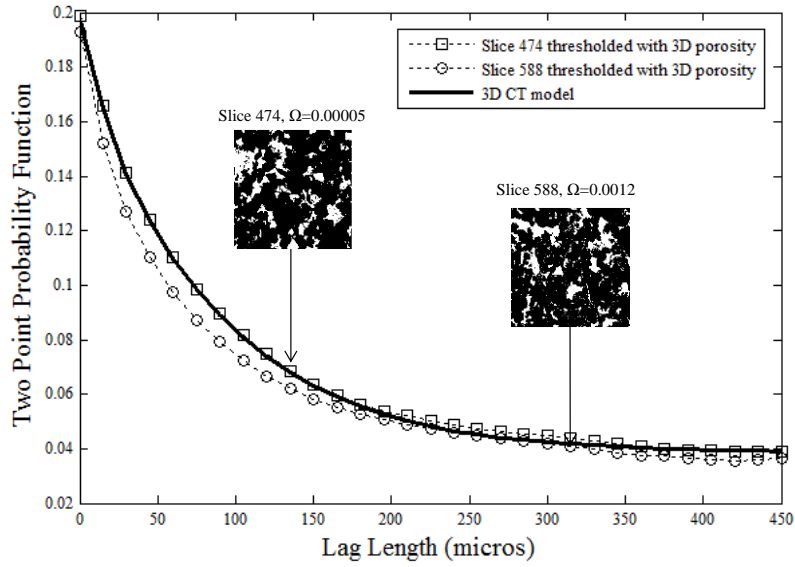


Figure 3.5 Derived morphological description curves of the CT slices (method 1).

Another solution is introduced, which is called method 2 in this paper. According to Equations (11) and (12), we have

$$S_2^{3D}(0) - S_2^{2D}(0) = \varphi_{3D} - \varphi_{2D} \quad (3.20)$$

$$S_2^{3D}(\infty) - S_2^{2D}(\infty) = \varphi_{3D}^2 - \varphi_{2D}^2 \quad (3.21)$$

If u_{\max} is large enough, the following relationship stands

$$S_2^{3D}(u_{\max}) - S_2^{2D}(u_{\max}) = \varphi_{3D}^2 - \varphi_{2D}^2 \quad (3.22)$$

Then, the relationship between 2D and 3D morphological distribution is assumed to satisfy the following equation

$$S_2^{3D}(u) = S_2^{2D}(u) + (\varphi_{3D} - \varphi_{2D})w(u) + (1 - w(u))(\varphi_{3D}^2 - \varphi_{2D}^2) \quad (3.23)$$

where $w(u)$ is the weight function which is estimated from the normalized 2D correlation function as

$$w(u) = \frac{S_2^{2D}(u) - S_2^{2D}(u_{\max})}{S_2^{2D}(0) - S_2^{2D}(u_{\max})} \quad (3.24)$$

Equation (3.23) can directly derive the 3D morphological distribution curve from the 3D porosity. The merit of method 2 is that no digital image processing is required, and the binarized slice image can also be used. Figure 3.6 shows that the derived 3D morphological distribution curves for the binarized slice images are close to the 3D one, which shows the effectiveness of method 2.

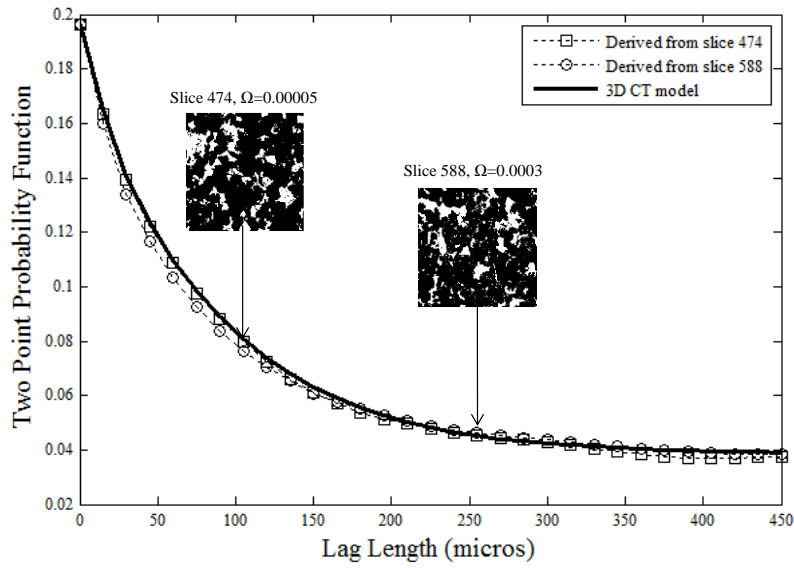


Figure 3.6 Derived morphological description curves of the CT slices (method 2).

3.4.2 Surface image of the Gosford sandstone

A digital microscope with a magnification ratio up to $600\times$ is used to capture the surface image of a Gosford sandstone specimen (see Figure 3.7a). The top surface of the specimen is milled into a flat plane. Carbon dust is poured to fill the pores, and redundancy dust is wiped off the surface to give a processed surface (see Figure 3.7c). The carbon dust treatment can decrease the influence of mineral components on pore identification and is necessary to obtain the 2D porosity structure. Figure 3.7e shows the surface image obtained from the digital microscope. The pixel resolution is 5.5 microns, which is fairly good compared to the X-ray micro CT scanning by Sufian and Russell (2013). It should be mentioned that the cost for a digital microscopy is only about fifty Australia dollars.

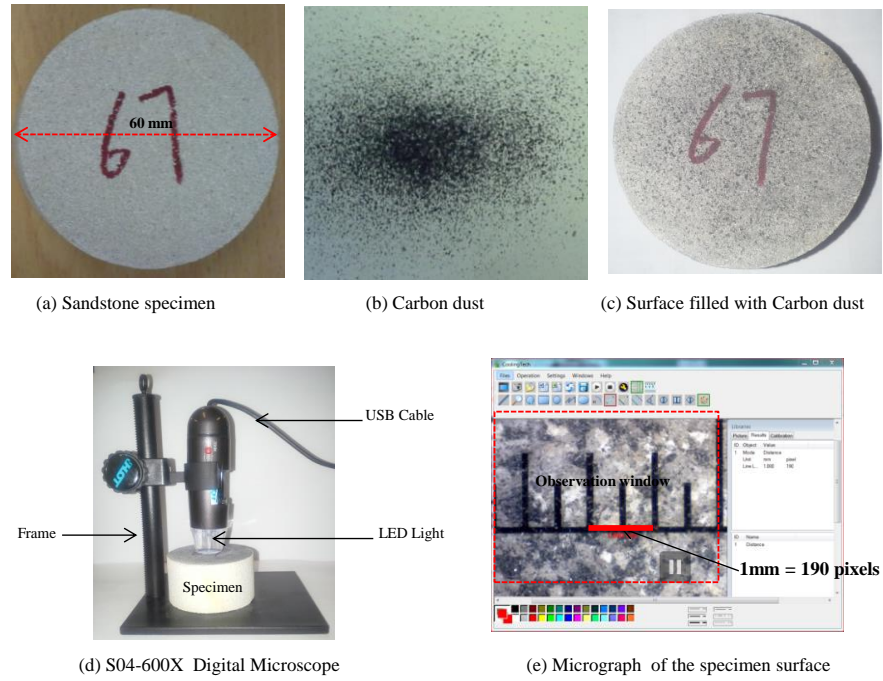


Figure 3.7 Process of the surface image acquisition for the Gosford sandstone.

Four surface images of the Gosford sandstone specimen are captured (see Figure 3.8). The region of interest is $3\text{ mm} \times 3\text{ mm}$. The 3D morphological description curves from these images are derived by using the two methods presented in Section 3.4.1. The discrepancies between the derived curve and that from the X-ray micro CT model are shown in Table 3.1. Both methods can provide a reasonable 3D morphological description for the Gosford sandstone. It should be mentioned that the surface of the Gosford sandstone specimen may be partially damaged during the milling process. The results in Table 3.1 show the robustness of the method in acquiring the morphological description of the Gosford sandstone.

Table 3.1 Difference between the morphological descriptions obtained from surface images and that of the micro X-ray CT model.

Ω	Image A	Image B	Image C	Image D
Method 1	0.00025	0.00090	0.00030	0.00034
Method 2	0.00050	0.00090	0.00026	0.00030

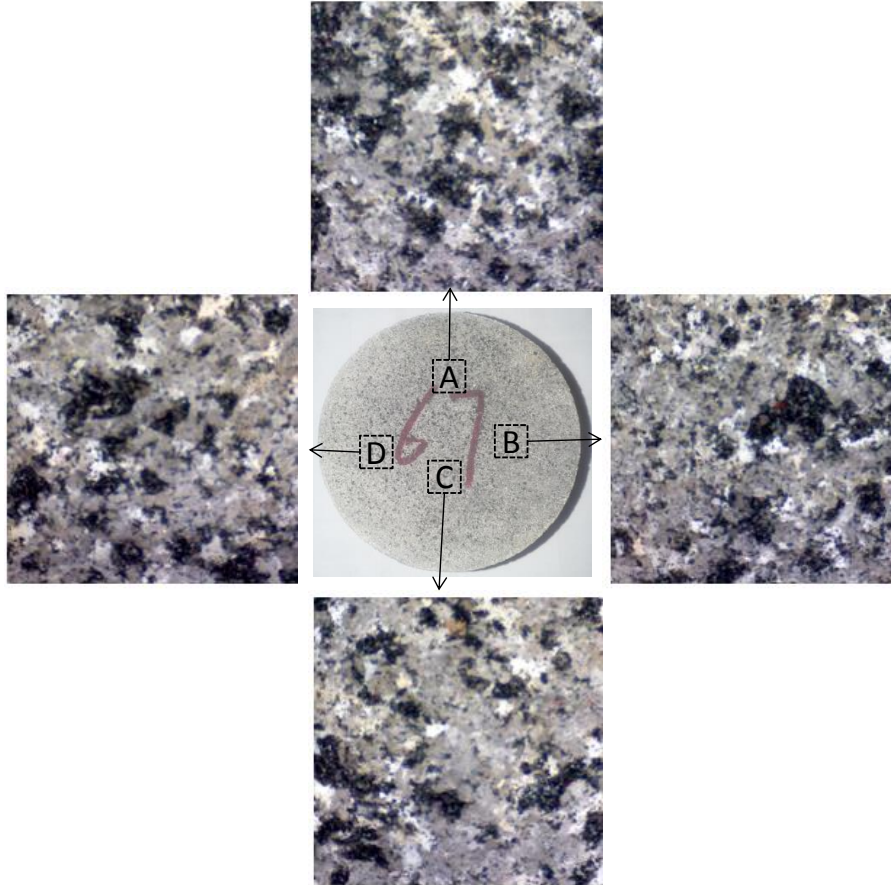


Figure 3.8 Obtained surface images of the Gosford sandstone specimen.

3.5 STOCHASTIC RECONSTRUCTION OF THE GOSFORD SANDSTONE

3.5.1 Reconstruction based on the X-ray micro CT model

In this section, the morphological distribution curve obtained from the X-ray micro CT model is used. Four reconstructed models are shown in Figure 3.9. The stochastic

reconstruction can reproduce models for different microstructures with local porosity distribution and local percolation probability close to the original X-ray micro CT model (see Figure 3.10). To quantify the difference between two curves, an error index is defined

$$Err = \frac{Max|CT - reconstructed|}{Max(CT)} \times 100\% \quad (3.25)$$

Results of the error analysis are listed in Table 3.2. It can be seen that, the morphological measurements of these reconstructed models are close to the X-ray micro CT model.

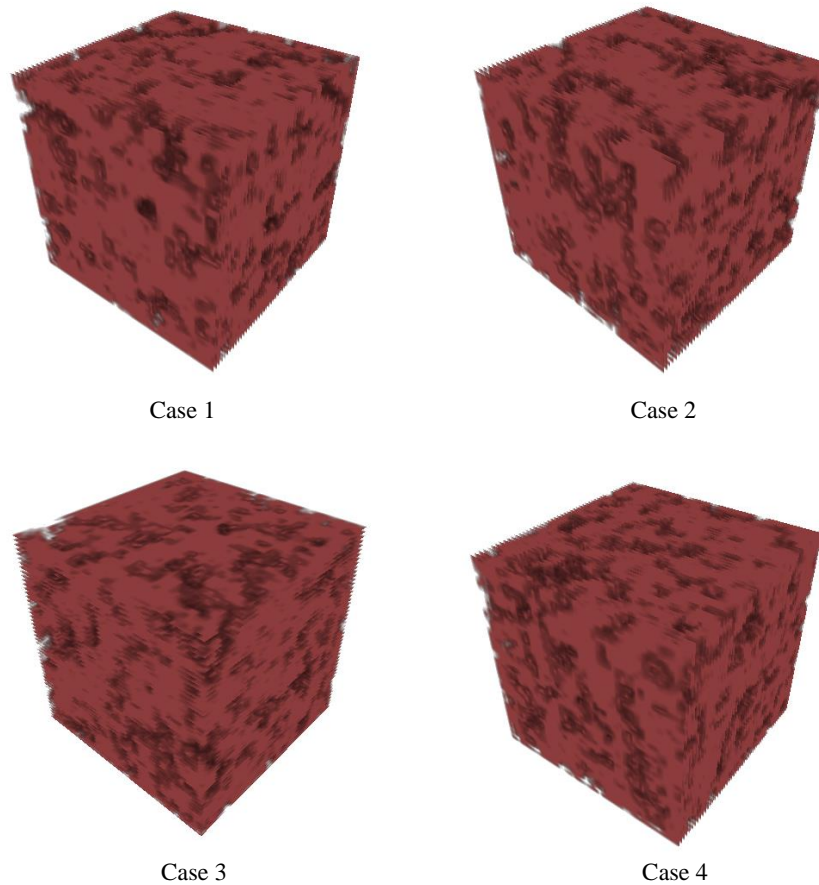
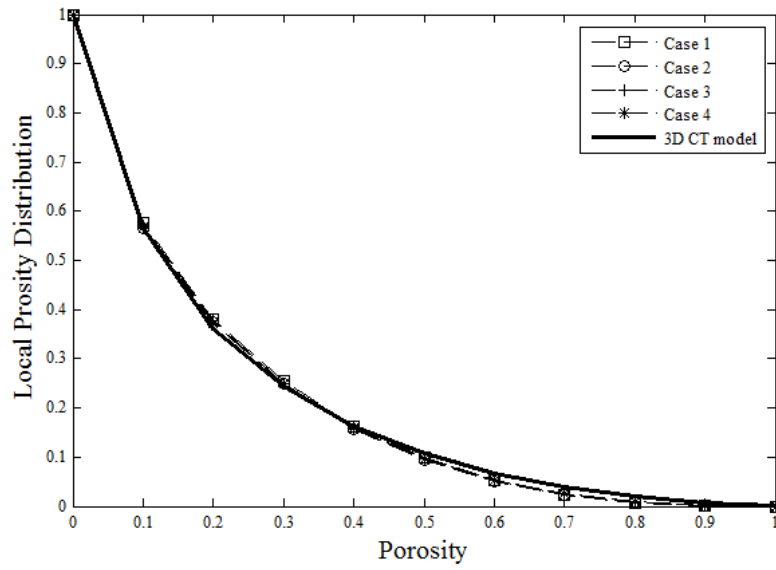
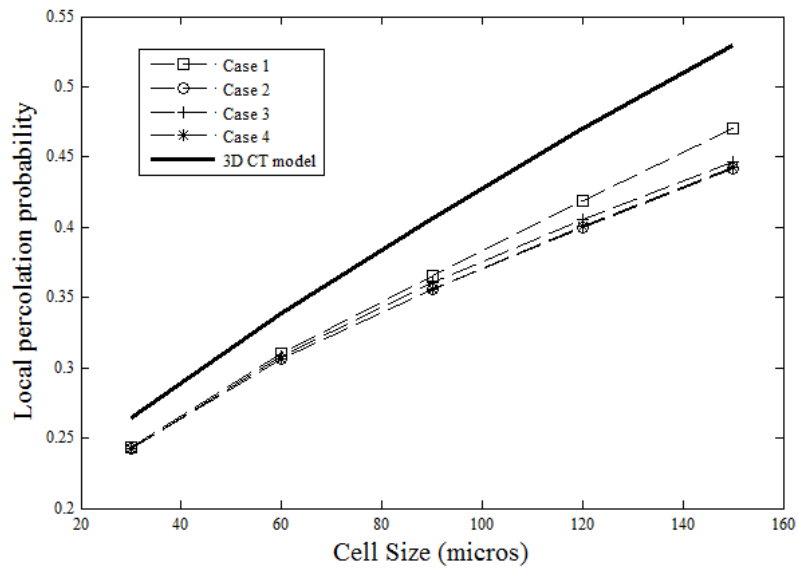


Figure 3.9 Stochastic reconstructed models based on the 3D morphological description curve from the micro X-ray CT model.



(a) Local porosity distribution at cell side length of 180 microns



(b) Local percolation probability

Figure 3.10 Quantitative measures of the reconstructed models based on the X-ray micro CT model.

Table 3.2 Quantitative morphological description of the stochastic reconstructed models based on the micro X-ray CT model.

Case No.	Specific area	Local porosity distribution	Local percolation probability
	Err (%)	Err (%)	Err (%)
1	5	2.07	11.13
2	5	1.59	16.48
3	5	1.64	15.59
4	5	1.19	16.26
Average	5	1.62	14.87

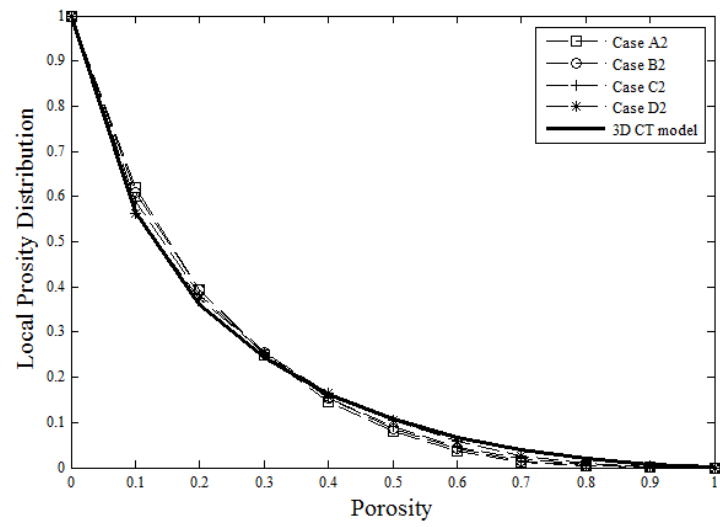
3.5.2 Reconstruction based on the surface images

In this section, the derived morphological distribution curves from the surface images captured by the digital microscopy are used. Figure 3.11 shows the local porosity distribution and local percolation probability of reconstructed models using method 2. It shows that the reconstructed microstructure models based on the surface images can also give reasonably good results. The results of error analysis performed on the reconstructed models from 4 surface images based on method 1 and method 2 are listed in Table 3.3. The average error of the local porosity distribution at cell side length of 180 micros is reported as less than 4% which shows the effectiveness of stochastic reconstruction from surface images. Meanwhile, an underestimation of 10% for the local percolation probability shows that the correlation functions do not capture some of the connected structures that present in the 3D model. In practice, the specific area can be an input value, obtained from other experiments. If the specific area is given, the distribution curve from surface images which gives the best fit can be used in the stochastic reconstruction (e.g. part D in this example).

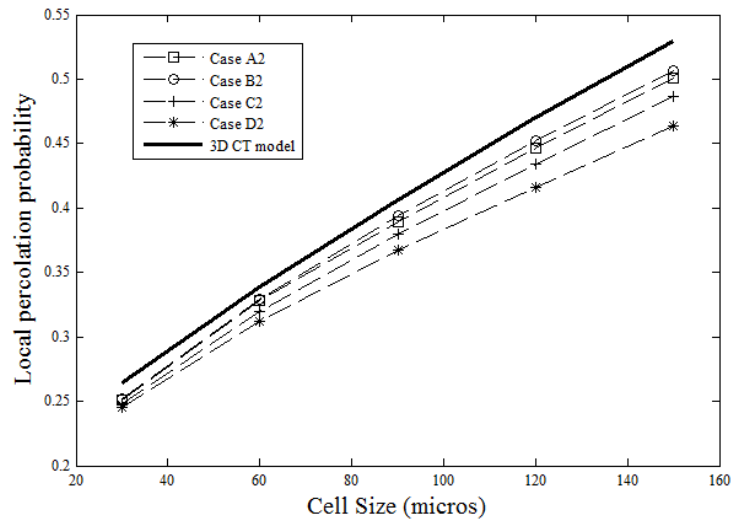
The stochastic reconstruction is also used to generate models with size of $3.75 \times 3.75 \times 3.75 \text{ mm}^3$, $4.5 \times 4.5 \times 4.5 \text{ mm}^3$, $5.25 \times 5.25 \times 5.25 \text{ mm}^3$ and $6 \times 6 \times 6 \text{ mm}^3$. In our test, a computer with Intel Core i7 960 3.20 GHz and memory of 8 GB is used. The program is run in 64-bit version of Windows 7 with Matlab 2012. The reconstructed models and the corresponding simulation time are summarized in Figure 3.12. This example demonstrates the capability of stochastic reconstruction in reproducing models of arbitrary large size with only small observation domain. However, the computational requirement is demanding when the model size becomes large. This issue will be addressed in future research.

Table 3.3 Quantitative morphological description of the stochastic reconstructed model based on the surface images using method 1 and method 2 ("A,B,C,D" refers to the image, "1,2 "means the method id).

Case No.	Specific area		Local porosity distribution		Local percolation probability	
	Err(%)	Average	Err(%)	Average	Err(%)	Average
A1	23.51		3.74		7.05	
B1	33.19	20.09	5.75	3.07	5.96	10.50
C1	13.31		1.62		15.00	
D1	10.35		1.17		14.00	
A2	30.82		5.56		5.37	
B2	31.86	24.12	4.45	3.50	4.33	7.53
C2	21.05		2.53		7.98	
D2	12.76		1.47		12.45	



(a) Local porosity distribution at cell side length of 180 micros



(b) Local percolation probability

Figure 3.11 Quantitative measures of the reconstructed models based on the surface images.

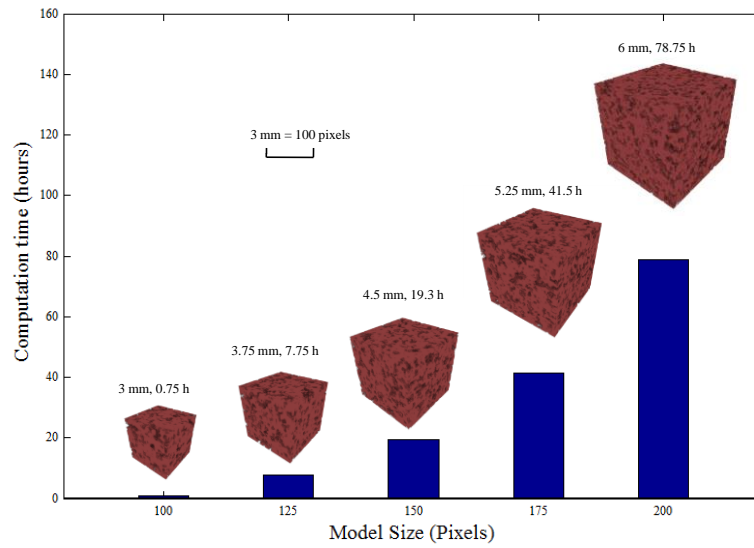


Figure 3.12 Computational time of reconstructed models with different sizes.

3.6 CONCLUSIONS

The stochastic reconstruction of Gosford sandstone from its surface image is conducted. A digital microscope is adopted to capture surface images of the Gosford sandstone specimen where the carbon dust treatment on the surface is introduced. The 3D morphological distribution curve is derived through a porosity adjustment of the 2D surface images. It is found that the derived morphological curves are close to that from the X-ray micro CT model. By comparing all the stochastic reconstructed microstructure models with the original X-ray micro CT model, it is shown that the reconstructed models can successfully reflect essential morphological information of the Gosford sandstone.

3.7 REFERENCES

Adler P.M., Jacquin C.G., Quiblier J.A. (1990) Flow in simulated porous media. International Journal of Multiphase Flow 16(4):691-712.

Hajizadeh A., Safekordi A., Farhadpour F.A. (2011) A multiple-point statistics algorithm for 3D pore space reconstruction from 2D images. *Advances in Water Resources* 34(10):1256-1267.

Hazlett R.D. (1997) Statistical characterization and stochastic modeling of pore networks in relation to fluid flow. *Mathematical Geology* 29(6): 801-822.

Hazor Y.H., Zur A., Mimran Y. (1997) Microstructure effects on microcracking and brittle failure of dolomites. *Tectonophysics* 281(3):141-161.

Hilfer R. (2000) Local Porosity Theory and Stochastic Reconstruction for Porous Media. In: *Statistical Physics and Spatial Statistics*, Springer Berlin Heidelberg. pp. 203-241.

Ichikawa Y., Kawamura K., Uesugi K., Seo Y.S., Fujii N. (2001) Micro- and macro behavior of granitic rock: observations and viscoelastic homogenization analysis. *Computer Methods in Applied Mechanics and Engineering* 191:47-72.

Jiao Y., Stillinger F.H., Torquato S. (2008) Modeling heterogeneous materials via two-point correlation functions. II. Algorithmic details and applications. *Physical Review E* 77(3): 031135.

Josh M., Esteban L., DellePiane C., Sarout J., Dewhurst D.N., Clennell M.B. (2012) Laboratory characterisation of shale properties. *Journal of Petroleum Science and Engineering* 88-89:107-124.

Manwart C., Torquato S., Hilfer R. (2000) Stochastic reconstruction of sandstones. *Physical Review E* 62(1):893-899.

Okabe H., Blunt M.J. (2005) Pore space reconstruction using multiple-point statistics. *Journal of Petroleum Science and Engineering* 46 (1-2):121-137.

Øren P.E., Bakke S. (2003) Reconstruction of Berea sandstone and pore-scale modelling of wettability effects. *Journal of Petroleum Science and Engineering* 39(3-4):177-199.

Ouenes A., Bhagavan S., Bunge P.H., Travis B.J. (1994) Application of Simulated Annealing and Other Global Optimization Methods to Reservoir Description: Myths and Realities. *Society of Petroleum Engineers* 28415.

Politis M.G., Kikkinides E.S., Kainourgiakis M.E., Stubos A.K. (2008) A hybrid process-based and stochastic reconstruction method of porous media. *Microporous and Mesoporous Materials* 110(1): 92-99.

Rintoul M.D., Torquato S. (1997) Reconstruction of the Structure of Dispersions. *Journal of Colloid and Interface Science* 186(2): 467-476.

Sufian A., Russell A.R. (2013) Microstructural pore changes and energy dissipation in Gosford sandstone during pre-failure loading using X-ray CT. *International Journal of Rock Mechanics and Mining Sciences* 57:119-131.

Tahmasebi P., Sahimi M. (2012) Reconstruction of three-dimensional porous media using a single thin section. *Physical Review E* 85(6):066709.

Talukdar M.S., Torsaeter O. (2002) Reconstruction of chalk pore networks from 2D backscatter electron micrographs using a simulated annealing technique. *Journal of Petroleum Science and Engineering* 33(4): 265-282.

Talukdar M.S., Torsaeter O., Ioannidis M.A., Howard J.J. (2002) Stochastic Reconstruction of Chalk from 2D Images. *Transport in Porous Media* 48(1):101-123.

Talukdar M.S., Torsaeter O., Ioannidis M.A., Howard J.J. (2002) Stochastic reconstruction, 3D characterization and network modeling of chalk. *Journal of Petroleum Science and Engineering* 35(1-2):1-21.

Wang X.S., Wu B.S., Wang Q.Y. (2005) Online SEM investigation of microcrack characteristics of concretes at various temperatures. *Cement and Concrete Research* 35:1385-1390.

Yeong C.L.Y., Torquato S. (1998) Reconstructing random media. II. Three-dimensional media from two-dimensional cuts. *Physical Review E* 58(1):224-233.

Yeong C.L.Y., Torquato S. (1998) Reconstructing random media. *Physical Review E* 57(1):495-506.

CHAPTER 4 NUMERICAL STUDY OF TWO-PHASE FLUID DISTRIBUTIONS IN FRACTURED POROUS MEDIA

Two-phase fluid distributions in fractured porous media is studied using a single-component multiphase (SCMP) lattice Boltzmann method (LBM), which is selected among three commonly used numerical approaches through a comparison against the available results of micro X-ray computed tomography (CT). The influence of the initial configuration and the periodic boundary conditions in the SCMP LBM for the fluid distribution analysis are investigated as well. It is revealed that regular porous media is sensitive to the initial distribution, whereas irregular porous media is insensitive. Moreover, to eliminate the influence of boundaries, the model's buffer size of a SCMP LBM simulation is suggested to be taken as approximately 12.5 times the average particle size. Then, the two-phase fluid distribution of a porous medium is numerically studied using the SCMP LBM. Both detailed distribution patterns and macroscopic morphology parameters are reasonably well captured. Finally, the two-phase fluid distributions in a fractured porous media are investigated. The influence of the degree of saturation, fracture length and fracture width on the fluid distributions and migration are explored.

4.1 INTRODUCTION

The characterization of fluid distributions is of fundamental importance to the accurate modeling of multiphase flow problems, which are related to many industrial applications, e.g., radioactive disposal sites (Jim-Douglas and Spagnuolo 2001), oil/gas extraction (Trivedi and Babadagli 2009), and contaminant transport (Sudicky and Frind

1982). According to a literature review (Or and Tuller 1999, Gray et al. 2002, Culligan et al. 2004, de Gennes et al. 2004, Reynolds and Kueper 2004, German et al. 2006), there are two types of commonly used approaches to characterizing the fluid distribution in porous media: experimental and numerical approaches.

The most popular equipment used to visualize the phase distribution in porous media are scanning electron microscopy (SEM) and micro X-ray computed tomography (CT). Gvirtzman et al. (1987) investigated the water phase distribution within an unsaturated porous medium using SEM. To satisfy the requirement of SEM on a dried specimen, a rapid cooling technique was adopted. However, the cooling process caused a change in the volume of the liquid and lead to most of the samples being destructed. This shortcoming can be overcome using X-ray CT; e.g., Schmitz et al. (1997) conducted a study on the stationary water/air distribution in random and structured packing media using high-resolution micro X-ray CT, and Wildenschild et al. (2004) adopted X-ray CT to measure the saturation, distribution and interfacial characteristics of the fluids within the pore space. In addition to SEM and micro X-ray CT, other techniques, such as nuclear magnetic resonance (NMR) and confocal laser scanning microscopy (CLSM), have also been used by a few researchers; e.g., Liaw et al. (1996) studied the pore structure and fluid phase distribution of sandstone and carbonate samples using NMR, and Krummel et al. (2013) visualized the two immiscible fluids in a 3D porous medium using CLSM.

However, the direct exploration of the underlying microscopic multiphase distribution is time consuming and expensive. Alternatively, numerical approaches provide attractive solutions due to their advantages of low cost, high efficiency and repeatability. Many

numerical methods have been developed to predict multiphase distributions in porous media. There are two popular categories: the Simulated Annealing Method (SAM) and the Lattice Boltzmann Method (LBM). The SAM is a global optimization method proposed by Kirkpatrick et al. (1983), which can be used in the study of multiphase systems, as described in Politis et al. (1998). The SAM was first used to investigate the equilibrium phase distribution by Knight et al. (1990). Later, Silversten and Fort (2000) applied the method to study the fluid distribution in sphere packs, Berkowitz and Hansen (2001) extended the SAM to the water distribution in a partially saturated sandstone, and Lu et al. (2010) investigated the capillarity phenomenon in porous media. Recently, the lattice Boltzmann method (LBM) has become a promising solution for multiphase problems for porous media (Chen and Doolen 1998). Three popular multiphase LBM models have been developed (Huang et al. 2011): the free energy LBM, the Rothman-Keller LBM, and the Shan-Chen LBM. An extensive literature review on these models can be found in the work of Huang et al. (2011). Among those models, the Shan-Chen LBM (Shan and Chen 1993,1994) receives the most popularity because of its well-defined inter-particle potential and straightforward implementation. There are two sub-categories in the Shan-Chen LBM: the multi-component multiphase (MCMP) LBM (Shan and Chen 1993) and the single-component multiphase (SCMP) LBM (Shan and Chen 1994). The MCMP LBM model allows for fluid phases with different wettability, densities, and viscosities. The MCMP LBM was used to study the hysteretic capillary pressure-saturation of a packed sphere system by Pan et al. (2004), the contact angle between the fluid and solid surface by Huang et al. (2007), and the distribution of multiphase fluids in porous media by Sukop et al. (2008). The SCMP LBM focuses on the modeling of one-component fluid systems that obey a non-ideal

gas equation of state and that can undergo a liquid-gas-type phase transition. The SCMP LBM has been successfully applied to investigate the invasion percolation in porous media (Sukop and Or 2003) and the effect of gravity, adhesion, and surface tension on capillary-rise problems (Lu et al. 2013).

The aforementioned studies usually focus on qualitatively describing how the multiphase fluid is distributed in porous media; however, no quantitative study on the multiphase fluid distribution in a fractured porous media has been performed. A fracture in porous media is generally considered as a fast pathway for transports (Zimmerman and Bodvarsson 1996), but the fracture may impede the flow under partial saturation (Wang and Narasimhan 1985). The accurate description of fluid flow in unsaturated fractured porous media requires a clear understanding of the mechanism that produces the multiphase distribution. Moreover, to our knowledge, the accuracy of these numerical methods is still unclear, and a comprehensive verification is strongly required. For example, Lu et al. (2010) verified the prediction results of the SAM against X-ray CT observations, Sukop et al. (2008) compared the MCMP LBM with X-ray CT results, and Sukop and Or (2003) declared that SCMP LBM can produce realistic multiphase distributions. However, no work has been performed toward a quantitative comparison between these numerical approaches against the experimental observations. In this paper, a full comparison of the results predicted by the SAM, SCMP LBM and MCMP LBM with the experimental results of micro X-ray CT (Sukop et al. 2008) is discussed. It was found that the SCMP LBM shows advantages over the other two numerical methods in terms of computational efficiency and multiphase characterization. In addition, the influence of periodic boundary condition and the initial configuration on the fluid distribution predicted by the SCMP LBM were studied. Following this, the

influence of the degree of saturation on the fluid distribution was investigated for an artificial porous medium that was generated using the discrete element method (DEM). Finally, the two-phase fluid distribution in a fractured porous media was studied numerically.

4.2 NUMERICAL METHODS

4.2.1 Simulated Annealing Method (SAM)

The simulated annealing is powerful and algorithmically simple methodology to deal with the multi-parameter global optimization problems. The multiphase distribution problem can be formulated as an optimization problem according to Kirkpatrick et al. (1983).

To represent the fluid distribution of a porous media involving the solid, wetting and non-wetting phases, a three-spin Ising model (1987) is used.

$$I_{\text{sing}}(\mathbf{r}) = \begin{cases} -1 & \text{nonwetting phase} \\ 0 & \text{solid phase} \\ 1 & \text{wetting phase} \end{cases} \quad (4.1)$$

where \mathbf{r} is the spatial location of a pixel (voxel).

The geometry of the solid phase is represented as a group of pixels (voxels) that are assigned to be 0. The wetting phase and non-wetting phase are randomly introduced in the pore space to satisfy the desirable degree of saturation.

The phase distribution of the porous media is governed by the interfacial energy. The equilibrium configuration corresponds to the system of minimum global interfacial energy. The global interfacial energy E of the system can be calculated as

$$E = \sum_{i,j} \sum_{k,\bar{k}} J_{k\bar{k}} n_i^k n_j^{\bar{k}} \quad (4.2)$$

which is the interfacial energy between the pixel site i and all its nearest neighbor sites j , with phases of k and \bar{k} that span all the sites, where $n_i^k=1$ if the pixel site is in phase k and 0 otherwise. $J_{k,\bar{k}}$ is the interfacial free energy of the contact surface between different phases and is defined as

$$J_{k,\bar{k}} = \begin{cases} -1 & (k=1, \bar{k}=1) \\ 1 & (k=1, \bar{k}=-1) \\ -2 & (k=1, \bar{k}=0) \\ 0 & else \end{cases} \quad (4.3)$$

which reproduces the perfect wetting condition (Lu et al. 2010).

During the simulation, two randomly selected pixels of different fluid phases in the pore space will try to exchange their positions, which will result in a variation in the interfacial energy of the system ΔE . To minimize the system energy, the system is updated with a probability p to accept the pixel exchange according to the Metropolis algorithm.

$$p = \begin{cases} 1 & \Delta E \leq 0 \\ e^{-\Delta E/E_{ref}} & \Delta E > 0 \end{cases} \quad (4.4)$$

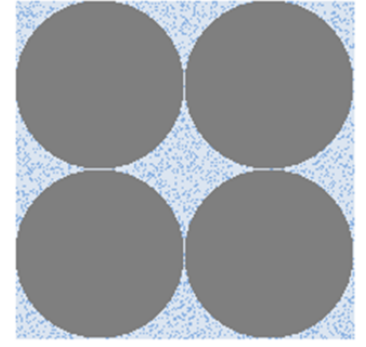
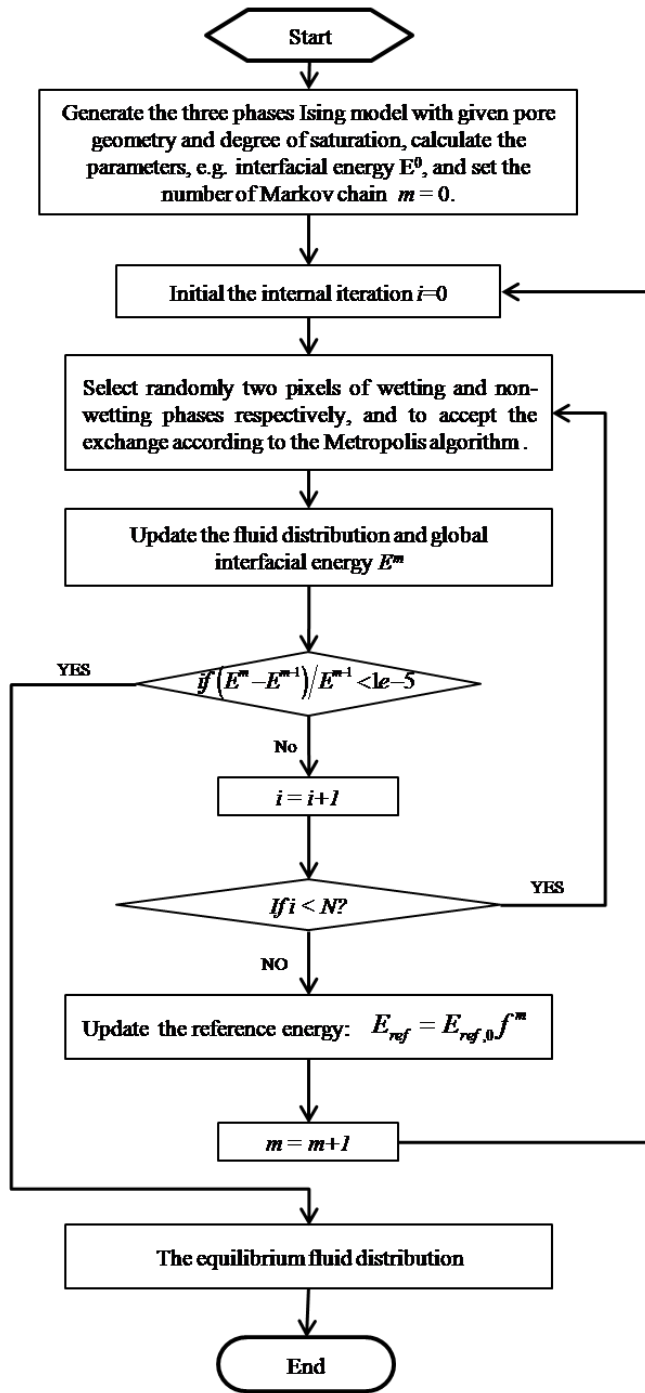
where E_{ref} is the reference energy given by a 'cooling schedule' as

$$E_{ref} = f^m \cdot E_{ref,0} \quad (4.5)$$

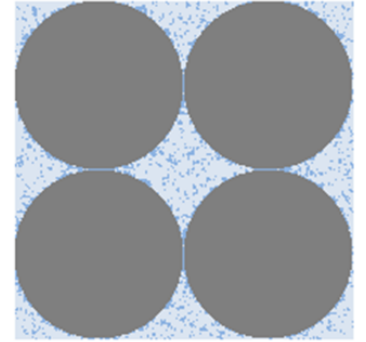
in which f is the reduction parameter, m is the number of the Markov chain, and $E_{ref,0}$ is the initial value of E_{ref} . The value of f is significant in the simulation and must satisfy $0 < f < 1$. A small f indicates fast converge but a high risk of local minima trapping. The physically sound configuration appears when f approaches 1. Meanwhile, the value of E_{ref} should be sufficiently large so that the system can approach the optimal distribution, which is chosen as approximately 30 times the highest value of $J_{k,\bar{k}}$, as shown in Politis et al. (1998). Therefore, $f = 0.95$ and $E_{ref,0} = 30$ were used in this paper.

The detailed procedure of the SAM is shown in Figure 4.1. It is necessary to mention that, the length of Markov chain is chosen as $N=200$ in all simulations, where N is the number of iterations that required to update the system reference energy. The system approaches equilibrium (Figure 4.1c) when the energy change between two Markov chains satisfies $(E^m - E^{m-1}) / E^{m-1} < 10^{-5}$. After reaching equilibrium, another 200 Markov chains are performed, and the profiles generated from each of the Markov chains are averaged to create a smooth curve of the interface, which is called anti-aliasing (Lu et al. 2010) (see Figure 4.2d).

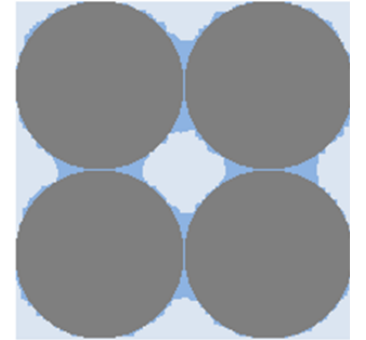
In term of methodology and algorithm, there are three main shortcomings of the SAM: a) the calculation of interaction force between different phases is not clear; b) the substantial computational requirement due to the global optimization; c) the deficiency in parallel computation.



$E = 3766$
(1) The initial model



$E = -104$
(2) The intermediate model



$E = -4439$
(3) The final model

Figure 4.1 Flowchart of the simulated annealing method for modeling two-phase distributions.

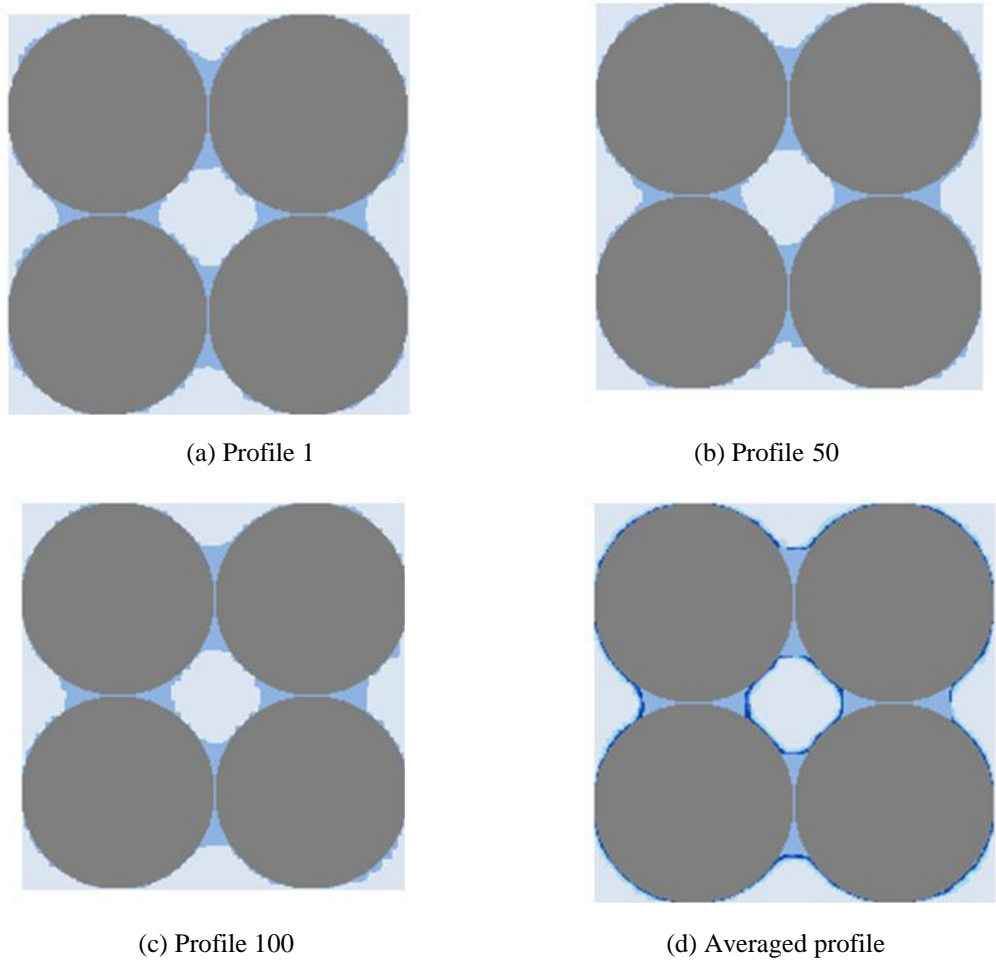


Figure 4.2 Anti-aliasing to produce a smooth interface after equilibrium is obtained.

4.2.2 Lattice Boltzmann method (LBM)

4.2.2.1 Theory background

The lattice Boltzmann method is based on microscopic models and mesoscopic kinetic equations. It is the “bottom-up” method for simulation of fluid flow which is quite distinctive from molecular dynamics (MD) on the one hand and “top-down” methods based on the discretization of partial differential equations on the other hand. The fundamental idea of lattice Boltzmann method is to construct the kinetic model with the

essential physics of microscopic processes incorporated so that the macroscopic averaged properties can be derived directly (Chen and Doolen 1998).

The LBM is originated from the lattice gas automata where the space, time, and particle velocities are all discrete. It can also be viewed as a special finite difference scheme for the kinetic equation of the discrete-velocity distribution function. The particles are residing on the nodes of a regular lattice, and particle distribution functions $f_i(x,t)$ is defined as the particle occupation. Two sub-steps are included in one time step, which refer to the propagation and collision. Propagation means particle moves to the nearest or neighbor node in the direction of its velocity. Collision means particles arrive at a node interact and change their velocity direction according to scattering rules. When the particle arrive at a node that resigned as solid, then the bounce back algorithm would be applied, which means that the particle get back to where it was. It becomes more complicated in term of solid node treatment in the two phase problems, the solid-fluid interfacial force will also be included, which will be discussed later on.

In recent years, it has developed into an promising numerical scheme to simulate single and multiphase fluids for its remarkable ability in dealing with interfacial dynamics and complex boundaries. In this part, the two sub categories of the Shan-Chen LBM model are used to investigate multiphase distribution problems.

4.2.2.2 Multi-component multiphase (MCMP) LBM

In the MCMP LBM, the two-phase system is represented as two indissolvable components. For each of the two fluid components, a distribution function is introduced that satisfies the following evolution function:

$$f_a^k(\mathbf{x} + \mathbf{e}_a \Delta t, t + \Delta t) = f_a^k(\mathbf{x}, t) - \frac{\Delta t}{\tau_k} [f_a^k(\mathbf{x}, t) - f_a^{k,eq}(\mathbf{x}, t)] \quad (4.6)$$

where $f_a^k(\mathbf{x}, t)$ is the k -th component density distribution function in the a -th velocity direction at site \mathbf{x} and at time t , Δt is time step for each iteration, and τ_k is a relaxation time. $f_a^{k,eq}(\mathbf{x}, t)$ is the equilibrium distribution function calculated as

$$f_a^{k,eq}(\mathbf{x}, t) = w_a \rho_k \left[1 + \frac{\mathbf{e}_a \cdot \mathbf{u}_k^{eq}}{c_s^2} + \frac{(\mathbf{e}_a \cdot \mathbf{u}_k^{eq})^2}{2c_s^4} - \frac{(u_k^{eq})^2}{2c_s^2} \right] \quad (4.7)$$

where $c_s = \Delta x / (\sqrt{3}\Delta t)$, with Δx defined as the lattice spacing. \mathbf{e}_a are the discrete velocities in the two dimensional case and are given by

$$[e_0, e_1, e_2, e_3, e_4, e_5, e_6, e_7, e_8] = \begin{bmatrix} 0 & 1 & 0 & -1 & 0 & 1 & -1 & -1 & 1 \\ 0 & 0 & 1 & 0 & -1 & 1 & 1 & -1 & -1 \end{bmatrix} \quad (4.8)$$

ω_a are weight indexes defined as

$$\omega_a = \begin{cases} \frac{4}{9} & (a = 0) \\ \frac{1}{9} & (a = 1, 2, 3, 4) \\ \frac{1}{36} & (a = 5, 6, 7, 8) \end{cases} \quad (4.9)$$

u_k^{eq} is the macroscopic velocity in the equilibrium distribution given by

$$u_k^{eq} = u' + \frac{\tau_k \mathbf{F}_k}{\rho_k} \quad (4.10)$$

where u' is the composite macroscopic velocity, which is expressed as

$$u' = \frac{\sum_k \frac{1}{\tau_k} \sum f_a^i e_a}{\sum_k \frac{1}{\tau_k} \rho_k} \quad (4.11)$$

\mathbf{F}_k is the interaction force acting on the k -th component involving the fluid-fluid cohesion force $\mathbf{F}_{c,k}$, fluid-solid adhesion force $\mathbf{F}_{ads,k}$ and external force \mathbf{F}_{ext} , which is expressed as,

$$\mathbf{F}_k = \mathbf{F}_{c,k} + \mathbf{F}_{ads,k} + \mathbf{F}_{ext} \quad (4.12)$$

The cohesion force acting on the k -th component is

$$\mathbf{F}_{c,k}(\mathbf{x}, t) = -G_c \psi_k(\mathbf{x}, t) \sum_a w_a \psi_{\bar{k}}(\mathbf{x} + \mathbf{e}_a \Delta t, t) \mathbf{e}_a \quad (4.13)$$

where G_c is the parameter that controls the strength of the cohesion force, and ψ_k and $\psi_{\bar{k}}$ are the interaction potential for the components k and \bar{k} , respectively, which can be taken as the density of each component.

The adhesion force acting on the k -th component is calculated as

$$\mathbf{F}_{ads,k}(\mathbf{x}, t) = -G_{ads,k} \psi_k(\mathbf{x}, t) \sum_a w_a s(\mathbf{x} + \mathbf{e}_a \Delta t) \mathbf{e}_a \quad (4.14)$$

where $G_{ads,k}$ is a parameter that adjusts the interaction strength between the k -th fluid component and the solid surface and $s(\mathbf{x} + \mathbf{e}_a \Delta t)$ is an indicator function equal to 1 for solid nodes and 0 for fluid nodes.

The external force \mathbf{F}_{ext} acting on the k -th component is defined as the body force on the particles, such as gravity, which is set as 0 for all simulations.

After every iteration, the distribution function can conveniently be thought of as a typical histogram representing a frequency of occurrence. The frequencies can be considered to be direction-specific fluid densities. Accordingly, the macroscopic density and velocity of the k -th component can be obtained as

$$\rho_k = \sum_a f_a^k \quad (4.15)$$

$$u_k = \sum_a f_a^k e_a / \rho_k \quad (4.16)$$

4.2.2.3 Single component multiphase (SCMP) LBM

The basic components of the SCMP LBM, such as the evolution function, equilibrium distribution function, macroscopic velocity and density are the same as in the MCMP Shan-Chen model. Instead of two distribution functions for each component, only one distribution function is used in the SCMP LBM. The principal distinguishing characteristic of the SCMP LBM is the incorporation of the equation of state. In this paper, we employ the following equation of state proposed by Shan and Chen (1994):

$$\varphi(\rho) = \varphi_0 \exp(-\rho_0 / \rho) \quad (4.17)$$

where φ_0 and ρ_0 are arbitrary constants that dominant the characteristics of the equation of state.

The cohesion force of gas/water and the adhesion force of fluid/surface in the SCMP LBM are defined as follows:

$$\mathbf{F}_c(\mathbf{x}, t) = -G_c \psi(\mathbf{x}, t) \sum_a w_a \psi(\mathbf{x} + \mathbf{e}_a \Delta t, t) \mathbf{e}_a \quad (4.18)$$

$$\mathbf{F}_{ads}(\mathbf{x}, t) = -G_{ads} \psi(\mathbf{x}, t) \sum_a w_a s(\mathbf{x} + \mathbf{e}_a \Delta t) \mathbf{e}_a \quad (4.19)$$

where G_c controls the strength of the cohesion force between two phases and G_{ads} adjusts the interaction strength between the fluids and the solid surfaces.

4.2.2.4 The Palabos library

The Palabos library (www.palabos.org) is an open-source numerical framework based on the LBM, which was developed by Jonas Latt and co-workers (2008). The Palabos library utilizes generic programming, which means that it allows for the intuitive implementation of LBM models with almost no loss of efficiency and with the ease of further development. Parallel computation is another feature of the Palabos library for the algorithm nature of LBM. In this paper, all computations were performed on Leonardi, which is a medium-sized high-performance computing cluster designed to be used for post-graduate and research purposes within the Faculty of Engineering at UNSW. It currently consists of 2,944 AMD Opteron 6174 2.20GHz processor cores, with a total of 5.8TB of physical memory (essentially, 2GB of memory per core) and 100TB of usable disk storage. Leonardi runs the Rocks clustering platform on top of CentOS Linux. The parallelization is performed with the message-passing paradigm of the MPI library, which works well on distributed-memory platforms (e.g., clusters).

For the study of fluid distributions in a fractured porous medium, both the fluid-fluid and fluid-solid interfacial forces are necessary to determine the contact behavior and the interface characteristics. However, in the current release of Palabos library (May 16

2013), only the fluid-fluid interface force was provided in the Shan-Chen LBM. It is essential to modify the code so as to involve the fluid-solid interfacial forces. The codes that deal with the fluid-fluid interfacial force can be found in the "ShanChenprocessor" from the directory of "multiphysics", which corresponds to the implementation of equation (4.13) and (4.18). To include the solid-fluid interfacial forces, equation (4.14) and (4.19) should be programmed in the code. According to equation (4.14), three additional parameters are required in the MCMP LBM model: $G_{ads,1}$, $G_{ads,2}$, and *Solid Index*, where $G_{ads,1}$ and $G_{ads,2}$ are the parameters that determine the fluid-solid adhesive force for each of the fluid components and the *Solid Index* is used to indicate the solid nodes. Similarly, two parameters are added in the SCMP LBM model according to equation (4.19): G_{ads} and *Solid Index*. In both codes, the contributions of the fluid-solid on the interfacial forces are calculated if any neighbors of the fluid node are recognized as solid nodes. Then, these adhesive forces are added to the original force contributed by fluid-fluid forces according to equation (4.12).

To validate the modified code and present the ability of LBM in dealing with multiphase contact and interaction problems, the complete range of contact angle is numerically simulated using both methods.

For a three-phase system, as shown in Figure 4.3(a), the wettability of a solid surface (grey) by a liquid (blue) can be characterized by Young's equation (Admson and Cast 1997):

$$\cos \theta_1 = \frac{\sigma_{2s} - \sigma_{1s}}{\sigma_{12}} \quad (4.20)$$

where θ_1 is the contact angle between fluid 1 and the solid surface; σ_{1s} and σ_{2s} are the interfacial tensions between fluids 1 and 2 and the solid surface, respectively; and σ_{12} is the interfacial tension between fluid 1 and fluid 2.

In the MCMP LBM, the interfacial tensions are controlled by the parameters G_c and $G_{ads,k}$. The relation between the contact angle and these parameters is given by Sukop (2006) as

$$G_c \cos \theta_1 = G_{ads,2} - G_{ads,1} \quad (4.21)$$

which was further improved by Huang et al. (2007) into

$$\cos \theta_1 = \frac{G_{ads,2} - G_{ads,1}}{G_c \frac{\rho_1 - \rho_2}{2}} \quad (4.22)$$

where ρ_1 is the equilibrium main density and ρ_2 is the associated dissolved density.

For the SCMP LBM, the contact angle between the wetting phase and the solid surface can be estimated according to Lu et al. (2013) using equation (4.23)

$$\theta = 210.75 + 0.647 G_{ads} \quad (4.23)$$

To simulate the multiphase contact phenomenon, the simulation domain was selected as 200×100 lattice units (l.u.), and the wetting component was initialized as a square with sides of 40 l.u., whereby the wetting component contacts the solid surface. In the simulation using the MCMP LBM, $\rho_1 = 2.0$ and $\rho_2 = 0.06$ were selected for the sake of stability (Huang et al. 2008). $G_{ads,1}$ and $G_{ads,2}$ were chosen in the manner reported by

Huang et al. (2008), i.e., $G_{ads,1}$ varies from -0.4 to 0.4, with $G_{ads,2} = -G_{ads,1}$. Figure 4.3 shows the complete range of contact angles predicted by the modified *Palabos library*.

The same simulations were conducted using the SCMP LBM, in which the parameters φ_0 and ρ_0 in equation (5.16) were selected as 200 and 4, respectively, G_c was fixed as -120, and G_{ads} varied between -327 and -40. The initial configuration was set in the same manner as was in the MCMPLBM, and the density of the wetting and non-wetting phases were chosen as 524 and 85, respectively. Figure 4.4 shows the simulation results predicted by the SCMP LBM (Lu et la. 2013). It is clear that, the modified code can properly include the solid-fluid interfacial forces and can simulate the complete range of contact angles within multiphase systems.

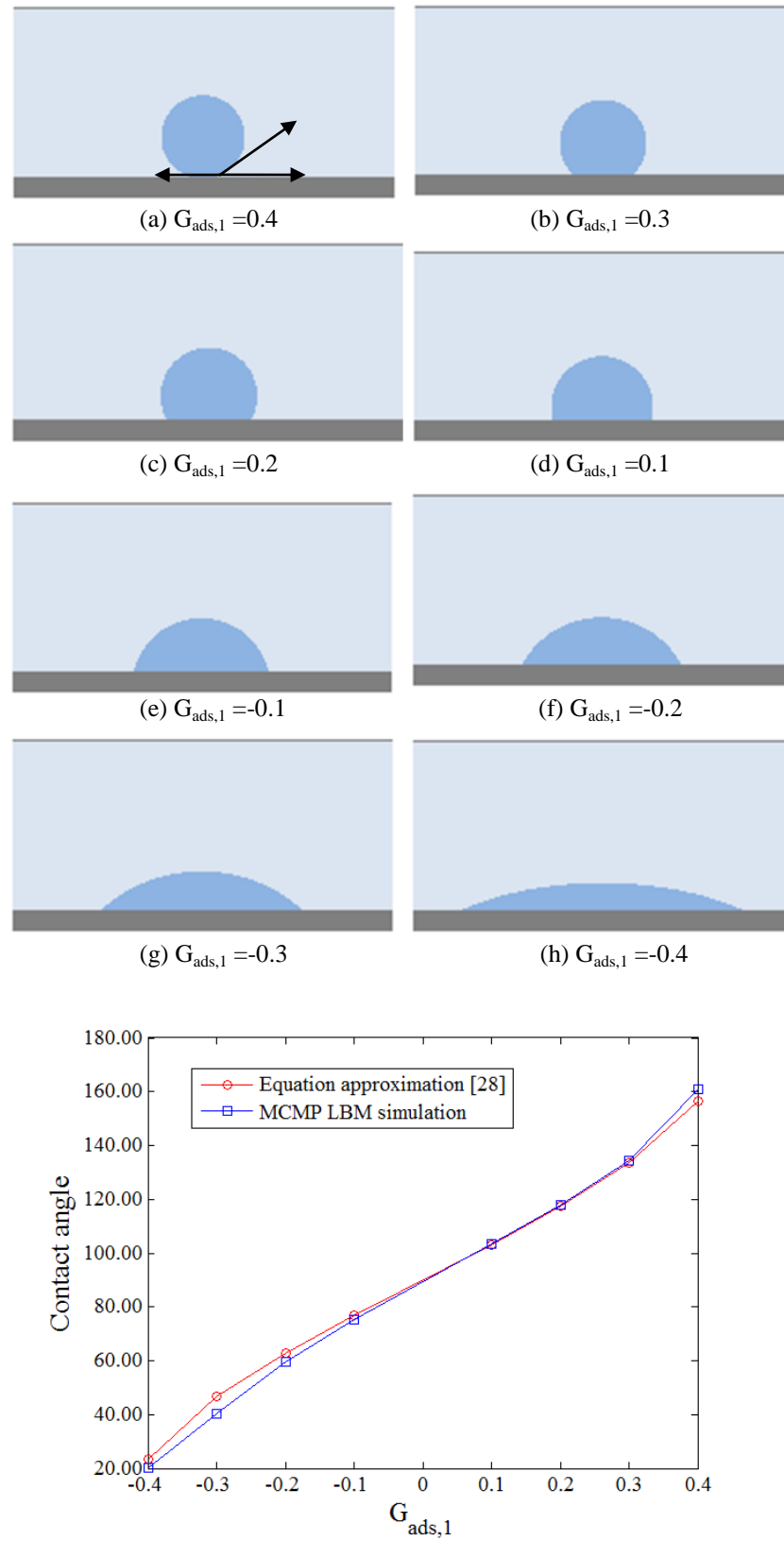


Figure 4.3 Correlation between $G_{ads,\sigma}$ and the contact angle in the MCMP LBM ($G=0.9$; $G_{ads,2}=-G_{ads,1}$).

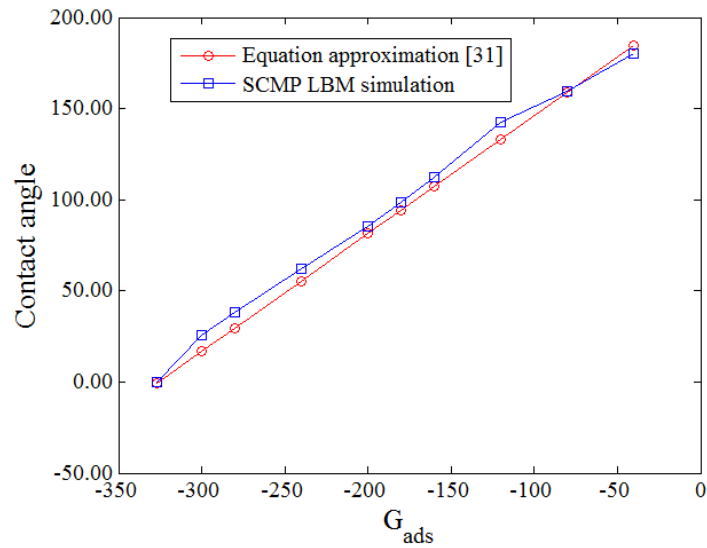
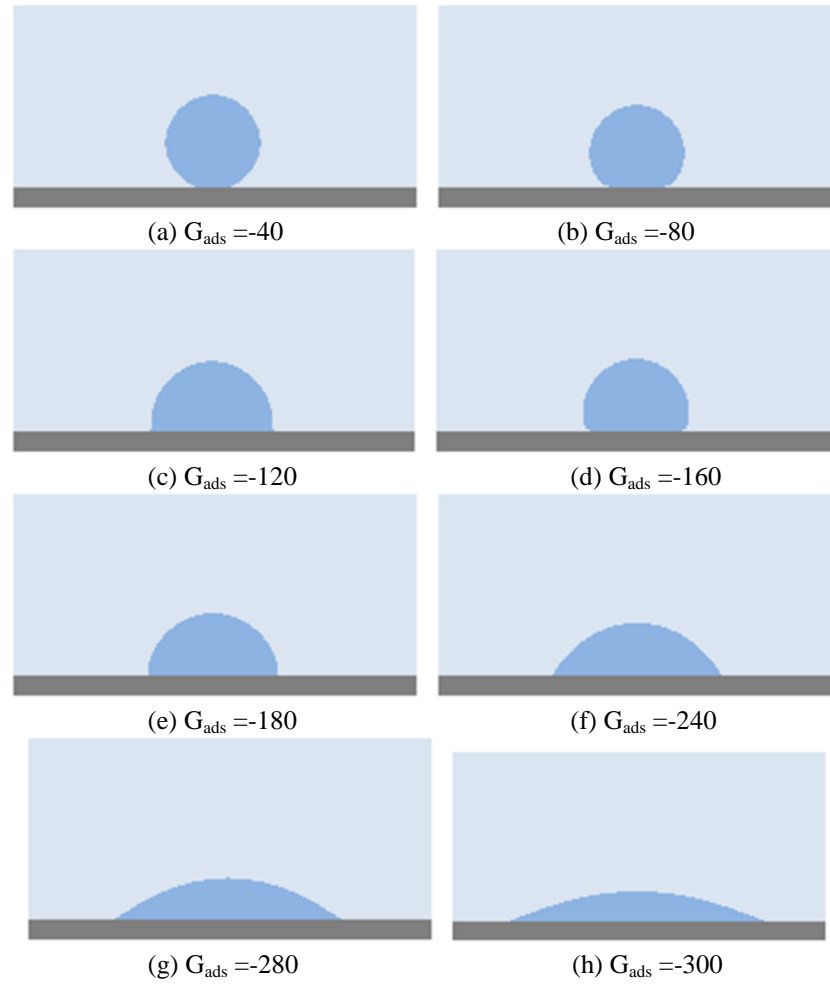


Figure 4.4 Correlation between G_{ads} and the contact angle in the SCMP LBM ($G=-120$)

4.3 VERIFICATION

In this section, numerical simulations using three numerical methods, i.e., the SAM, MCMP LBM, and SCMP LBM, were conducted for the two-phase fluid distribution problem by Sukop et al. (2008). According to the work by Sukop et al. (2008), the contact angle of the wetting phase approaches to 0 which corresponding to the nearly perfect wetting. Therefore, the parameters that control the interaction behaviors in the three methods are chosen in the way reported in the previous part so as to produce 0 contact angle.

The solid phase was taken from the micro X-ray CT image (see Figure 4.5a). All the simulations (except Figure 4.5 (d)) were initialized with a random distribution of wetting and non-wetting phases in the pore space (e.g. Figure 4.1(1)). To remove the initial effect on the final configuration of the MCMP LBM, the model in Figure 4.5(d) was initialized to be the same as one slice of the 3D model shown in Figure 4.5(b).

In all of these simulations, the degree of saturation was set as 0.67 with respect to the wetting phase, and the parameters were selected to produce a zero contact angle (Sukop et al. 2008). The equilibrium condition is approached when the stored energy converged. To obtain the relatively accurate results, the distribution is considered as equilibrium if the ratio between the deviation and average energy less than 10^{-4} .

The simulation results using different numerical methods are shown in Figures 4.5 (c) to (f). In order to visualize the effectiveness of the numerical results, the air phase in the red circle is highlighted in each image which is compared with the x-ray CT. To produce a quantitative comparison of the different numerical methods, the lineal-path function (Hilfer 2000) was adopted to compare the numerical simulation results to the

X-ray micro CT result. The lineal-path function is defined as the probability of finding a line segment that lies entirely in one phase, which contains connectivity information along a lineal path and reflects certain long-range information about the multiphase system. The wetting-phase linear path functions of the fluid configuration from different methods are illustrated in Figure 4.6. It can be observed that the numerical simulation results are in good agreement with the experimental data in terms of the stochastic morphological description. However, different conclusions will be obtained when a detailed comparison between the fluid distribution patterns of the center area (see Figure 4.5a) is performed. The reason that we only want to compare with the center area is that the influence of periodic boundary conditions is minimal in the central area which will be further discussed in part 4.1. It is apparent that the results using the MCMP LBM with random initial configurations (Figure 4.5(c)) is very different compared to the corresponding X-ray results (Figure 4.5(a)). The best fits are those results using the SAM and the SCMP LBM (see Figures 4.5 (e) and (f)). It should be mentioned that the MCMP LBM is sensitive to the initial configuration. For example, when a suitable initial configuration is used, a better result can be generated (see Figure 4.5 (d)).

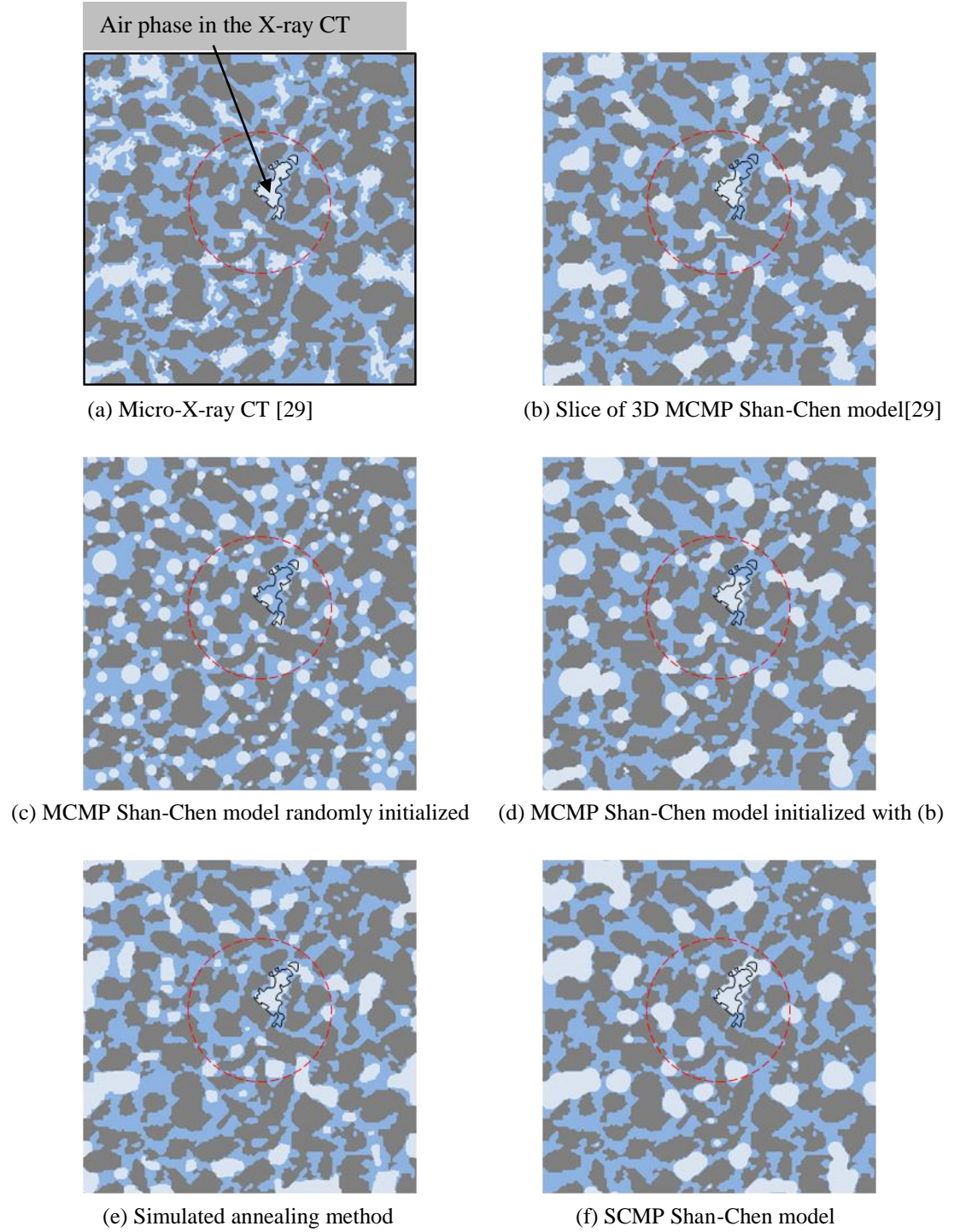


Figure 4.5 Comparison between micro X-ray CT and three numerical methods.

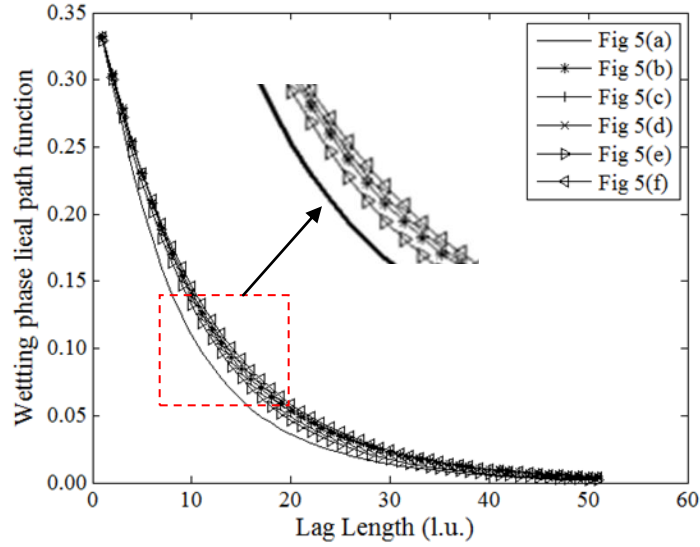


Figure 4.6 Wetting-phase linear-path functions of different fluid distributions by the different methods in Figure 4.5.

This difference comes from the dependence on the initial configuration. To verify this, we set a initial configuration as the square wetting phase with a non-wetting hole of different radius inside which is shown in Figure 4.7(a, b) and Figure 4.8 (a, b). From Figure 4.7(d), it is clear that, in the MCMP LBM, the wetting phase (blue part) splits up once the hole is sufficiently large. In contrast, for the SCMP LBM, only one droplet is generated regardless of how large the hole is (see Figure 4.8 (c, d)).

Based on the comparison between the numerical results and experimental observations as presented in Figure 4.7, it can also be revealed that the mechanism of the MCMP LBM is the kinematic movement of the fluids, whereas the SCMP LBM involves phase transitions. Meanwhile, the SAM is the optimization approach to obtain the equilibrium distribution as the minimum system energy. Both the SCMP LBM and the SAM can produce the very desirable results compared to the experimental observation. This indicates that the process of two-phase fluid distribution within porous media is

controlled by both the phase transition and kinematic movement. Therefore, in terms of computational efficiency and mechanism explanation, the SCMP LBM is the most suitable solution. It can simulate a multiphase system with a complete range of contact angles and phase transition. Moreover, its high computational efficiency is another advantage, e.g. the MPI parallel computation.

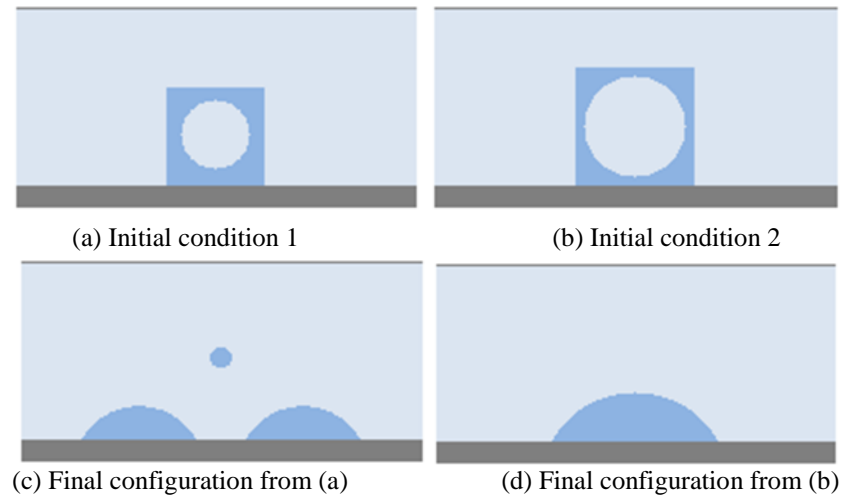


Figure 4.7 Dependence on the initial configuration in the MCMP Shan-Chen model.

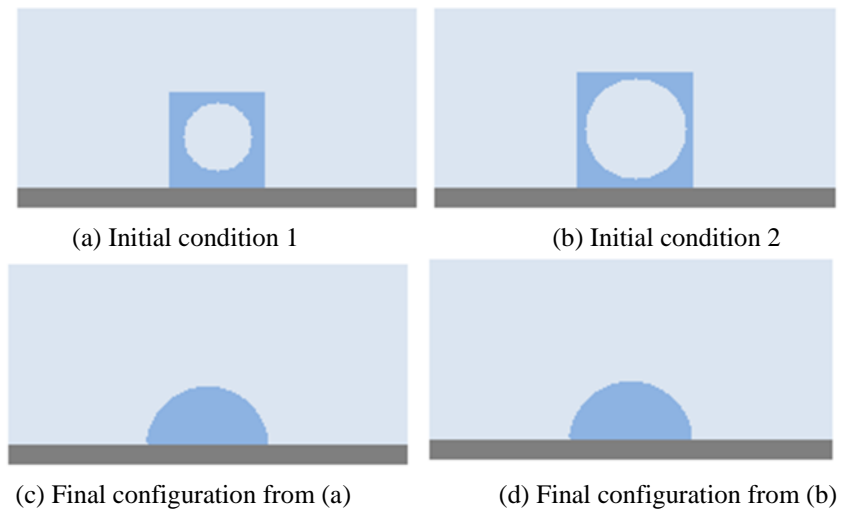


Figure 4.8 Dependence on the initial configuration in the SCMP Shan-Chen model.

4.4 TWO-PHASE FLUID DISTRIBUTION IN FRACTURED POROUS MEDIA

To keep all the simulation consistent, the details of the SCMP LBM parameters are presented in Table 4.1 for reference.

Table 4.1 Parameters used in the SCMP LBM simulations.

Boundary condition at open ends	Periodic
Boundary condition at the solid nodes	Bounce back
Contact angle	0 (perfect wetting)
φ_0	200
ρ_0	4
G_c	-120
G_{ads}	-327
Density of wetting phase	524
Density of non-wetting phase	85
Relaxation time (τ)	1
Time step	1
Lattice space	1

4.4.1 Periodic boundary effect and initial configurations

Various boundary conditions in the LBM have been proposed and evaluated (Jonas et al. 2008, Ziegler 1993, Inamuro et al. 1995, Zou and He 1997). The 'periodic' boundary condition has usually been applied at the model's edges for the sake of simplicity (Pan et al. 2004). However, this will introduce some errors because porous media are not geometrically 'periodic' under most conditions. In this paper, the influence of periodic boundary conditions on the simulation results of the SCMP LBM on fluid distribution problems is investigated. The porous media is generated through the compaction of randomly sized particles using the DEM code PFC^{2D} (Cundall and Strack 1979). A total of 557 particles with radii 30~50 l.u. are generated in the 2000×2000 l.u. domain. In order to produce the hydraulic aperture and create well connected pore space in the random compaction system, the radii of the particles are reduced to 80% of its original

size but keep the centers the same as the initial position. The final geometry of the porous media is shown in Figure 4.9(a), with radii of 24~40 and porosity of 0.552. During the SCMP LBM simulation, all the parameters are set in the way that follows Table 4.1.

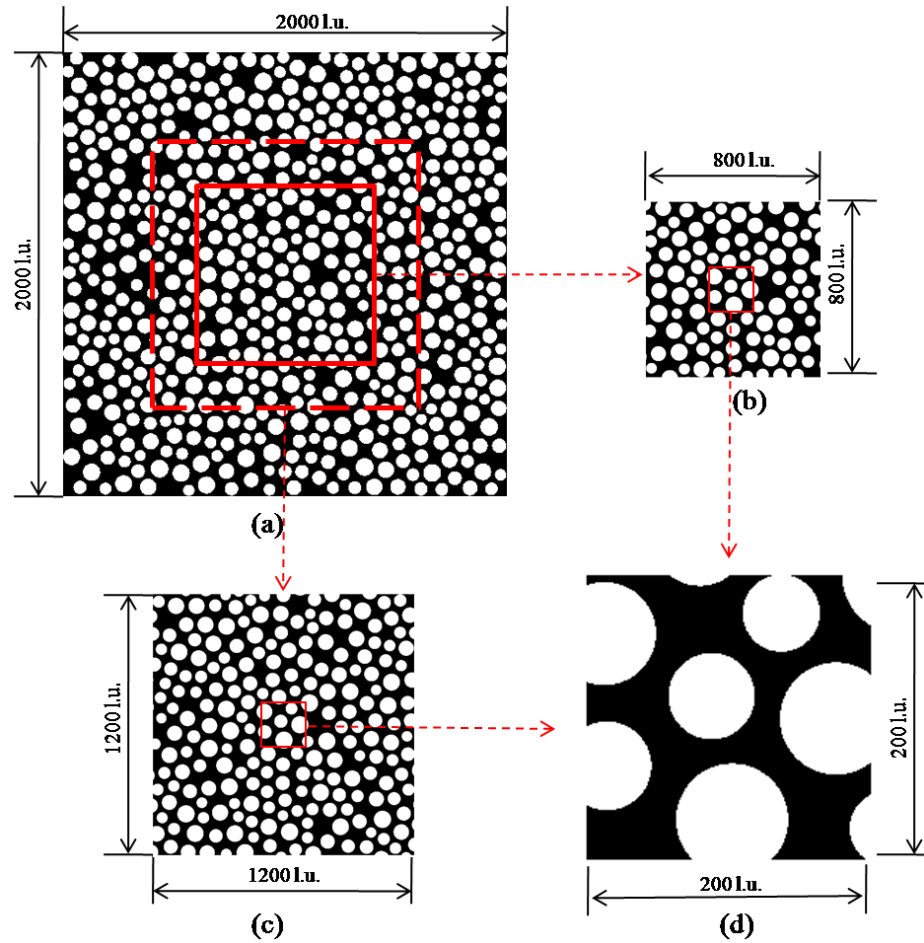


Figure 4.9 Geometry of a porous medium generated from DEM.

(a) is the whole region of the porous medium, (b) and (c) are two examples of different buffer sizes, and (d) is the region of interest

A number of sub-models with different sizes were cropped from the original model (e.g., Figures 4.9(b) and (c)). The purpose is to find a suitable model size to minimize the influence of the 'periodic' boundary' over the region of interest (see Figure 4.9 (d)). The

macroscopic properties, degree of saturation and specific surface area (SSA) of the two-phase fluid interface of the region of interest are shown in Figure 4.10. In Figure 4.10, “*” presents the different results at different buffer size, “_” shows the boundary of the simulation results and the solid line “_” gives the average results from 5 simulation results at each buffer size. It can be found that the macroscopic properties of the numerical simulation are only slightly influenced by the 'periodic' boundary' when the model size is sufficiently large, which confirms its applicability to fluid distribution simulations. It should be mentioned that the simulations are conducted in the same geometry for five runs to reduce the stochastic effects of the random initial configurations, which will be addressed later. Moreover, the difference in the fluid configuration in the region of interest is also slight with increased model size (Figure 4.11). However, when the 'periodic boundary' is directly applied to the region of interest, an apparent difference will be generated (see Figure 4.11a); therefore, a buffer area is recommended. From Figures 4.10 and 4.11, it is found that if the buffer size is large than 400 l.u., the degree of saturation and the SSA of water-air interface become relatively stable. By considering the average particle size in the generated porous media is 32 l.u., the minimum simulation size is suggested taken as about 12.5 times of the average particle radii so as to reduce the periodic boundary effect and obtain accurate distribution.

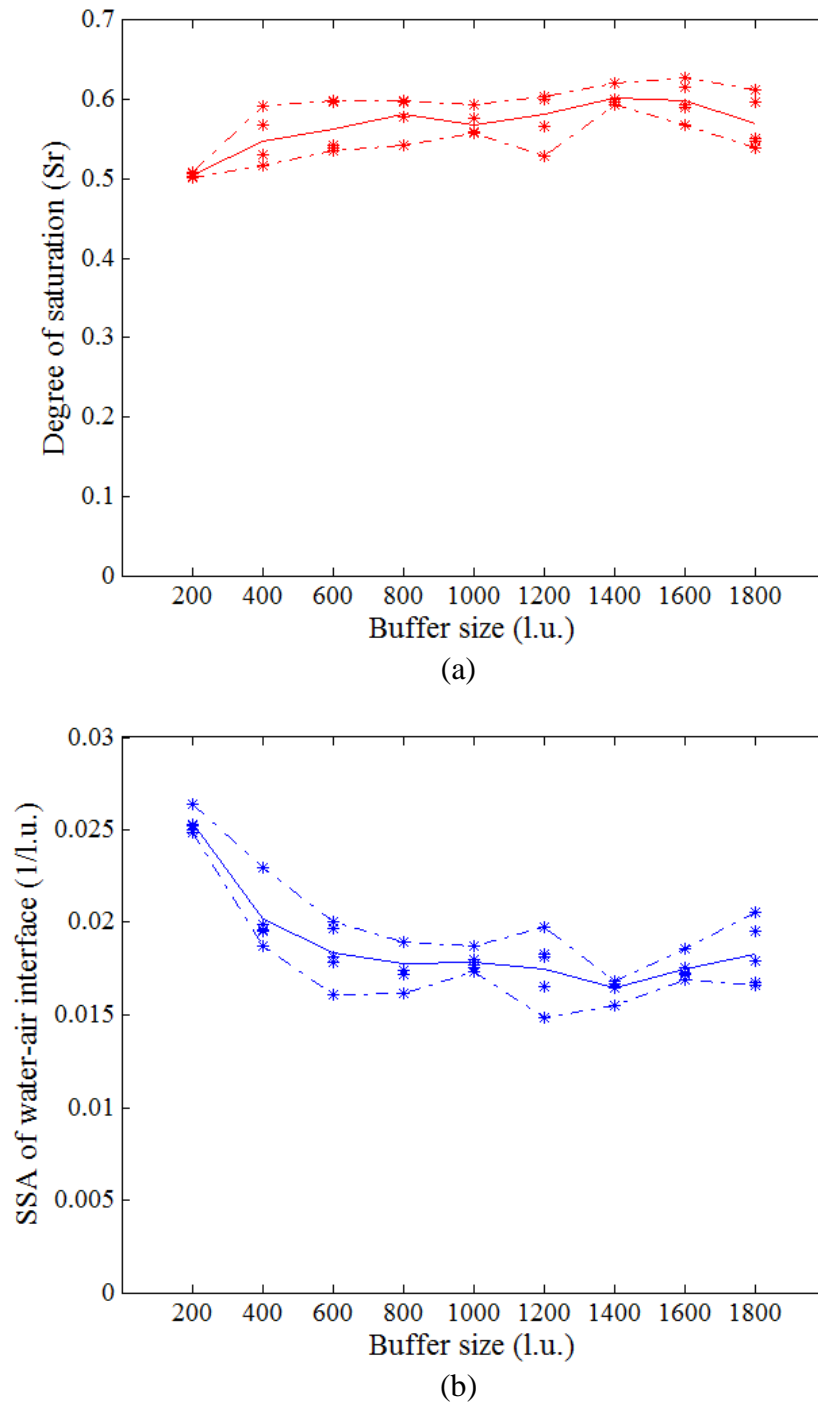


Figure 4.10 Influence of buffer size on the macroscopic properties in the region of interest.

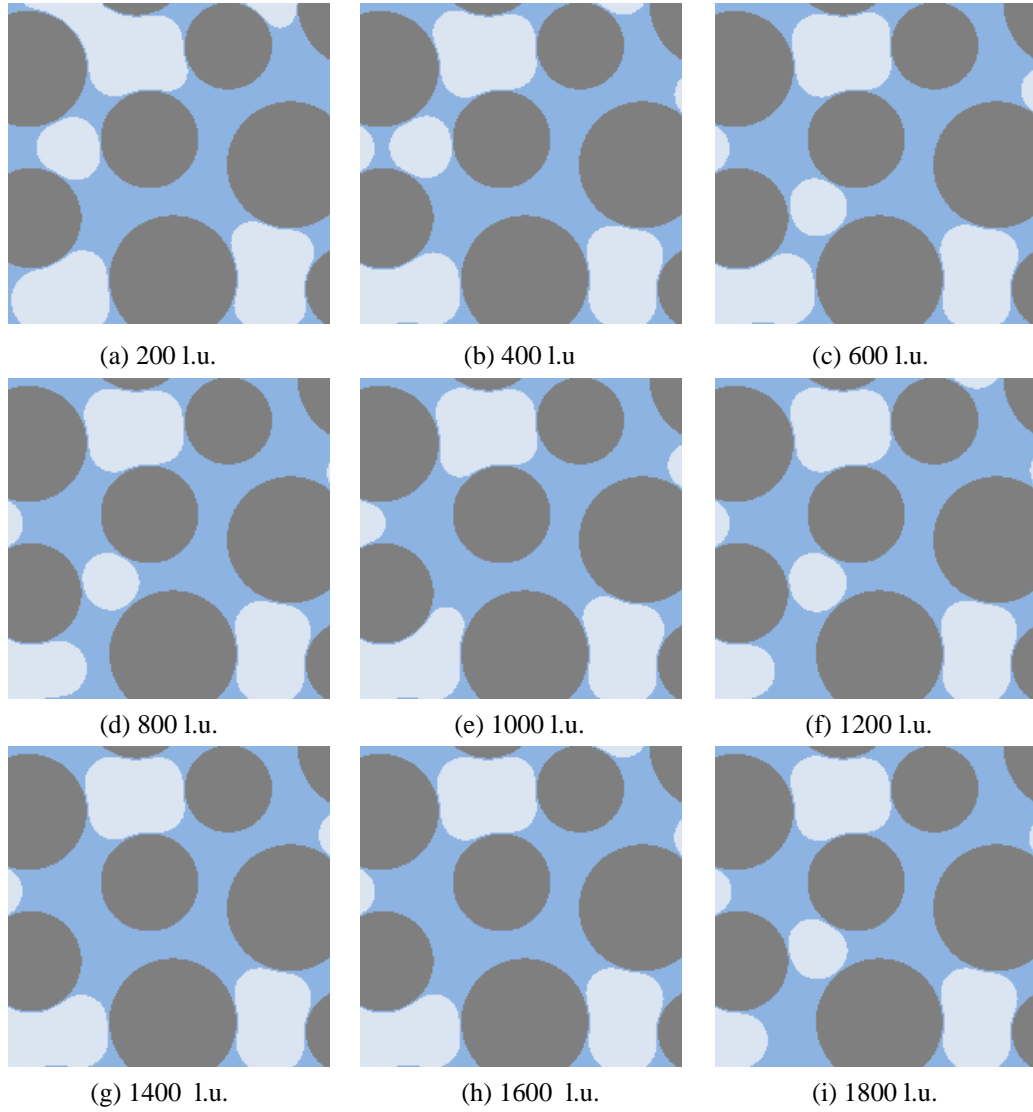


Figure 4.11 Fluid distributions in the region of interest from simulations of different buffer sizes.

To study the influence of the initial fluid distribution, a model with regular solid squares enveloped by a water film with the same thickness is first simulated (see Figure 4.12a). Because the model geometry is perfectly 'periodic', the boundary condition will not introduce any error, which can be confirmed from the modeling results shown in Figure 4.12b, where a perfect homogenous fluid distribution pattern is obtained. In the following, the middle part of the regular configuration is replaced by a random distribution for the initial configuration (Figure 4.12(c)); for this case, the periodic

boundary condition is still fulfilled. However, a clearly different distribution pattern is obtained compared to Figure 4.12(b). Therefore, it can be concluded that for regular porous media, the initial distribution will significantly influence the fluid distribution patterns. For example, all the models are randomly initialized in the middle part and simulated four times, and Figure 4.13 shows the final distributions, where a large difference in the distribution patterns is presented in the regular system. The same simulation is performed for irregular porous media (see Figure 4.14), where only slight differences can be observed. For the two phase system, the wetting phase has the preference to get into the smaller pores whereas the non-wetting phase always occupies the larger pore spaces. It is easy to draw the conclusion that the initial distribution is less sensitive to irregular porous media (e.g. geomaterials) compared to regular media.

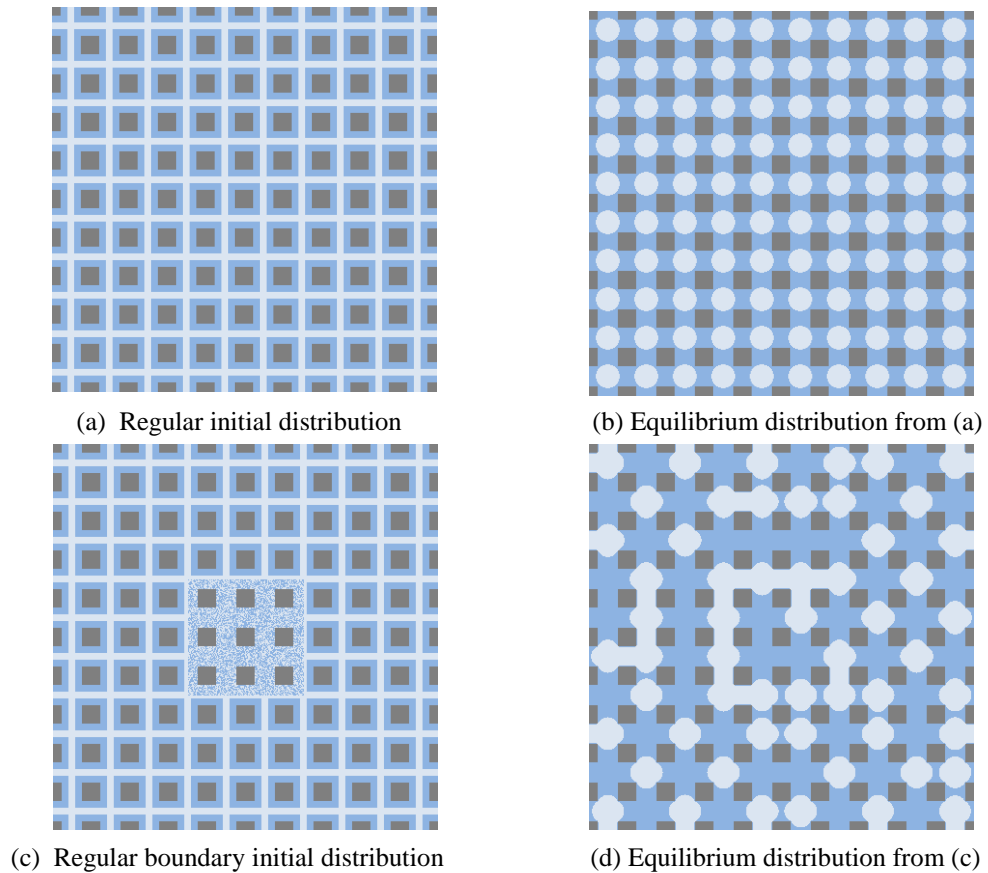


Figure 4.12 Investigation of the boundary conditions and the initial configuration.

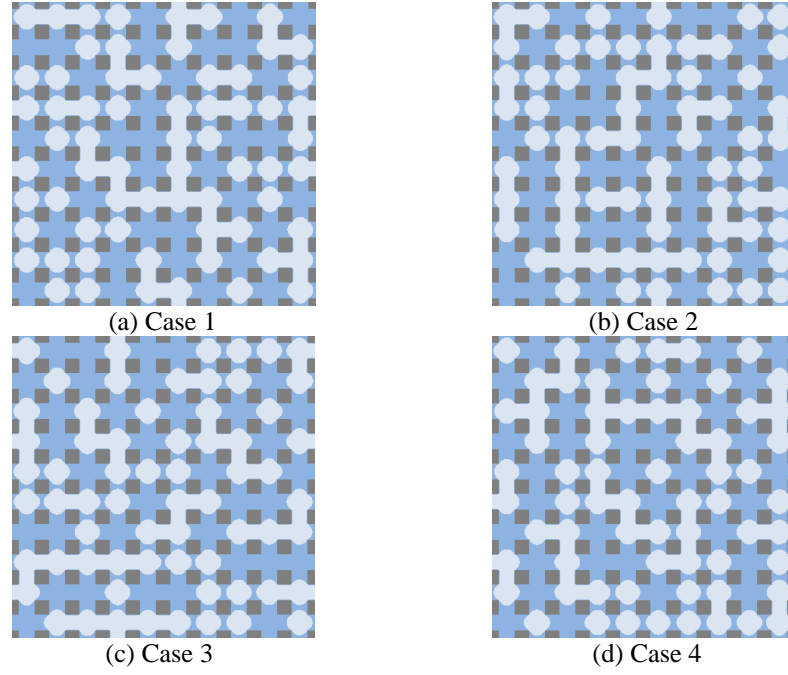


Figure 4.13 Fluid distributions in regular geometry from different random initializations.

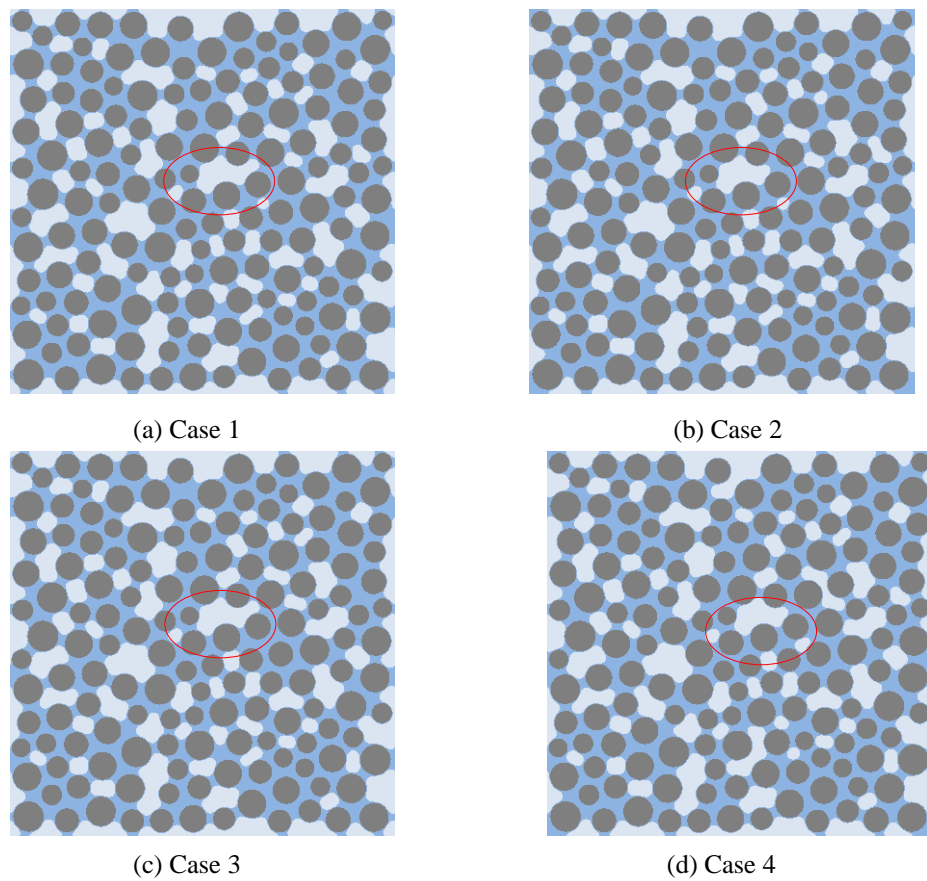


Figure 4.14 Fluid distributions in irregular geometry from different random initializations.

4.4.2 Fluid distribution in porous media

In this section, the influence of saturation on the fluid configuration in porous media is studied using the SCMP LBM. The solid part of the system remains the same as in Figure 4.9(a); the parameters are chosen to produce 0 contact angle for the wetting phase, as reported in the last section; and the degree of saturation of the wetting phase varies from 0.1 to 0.75.

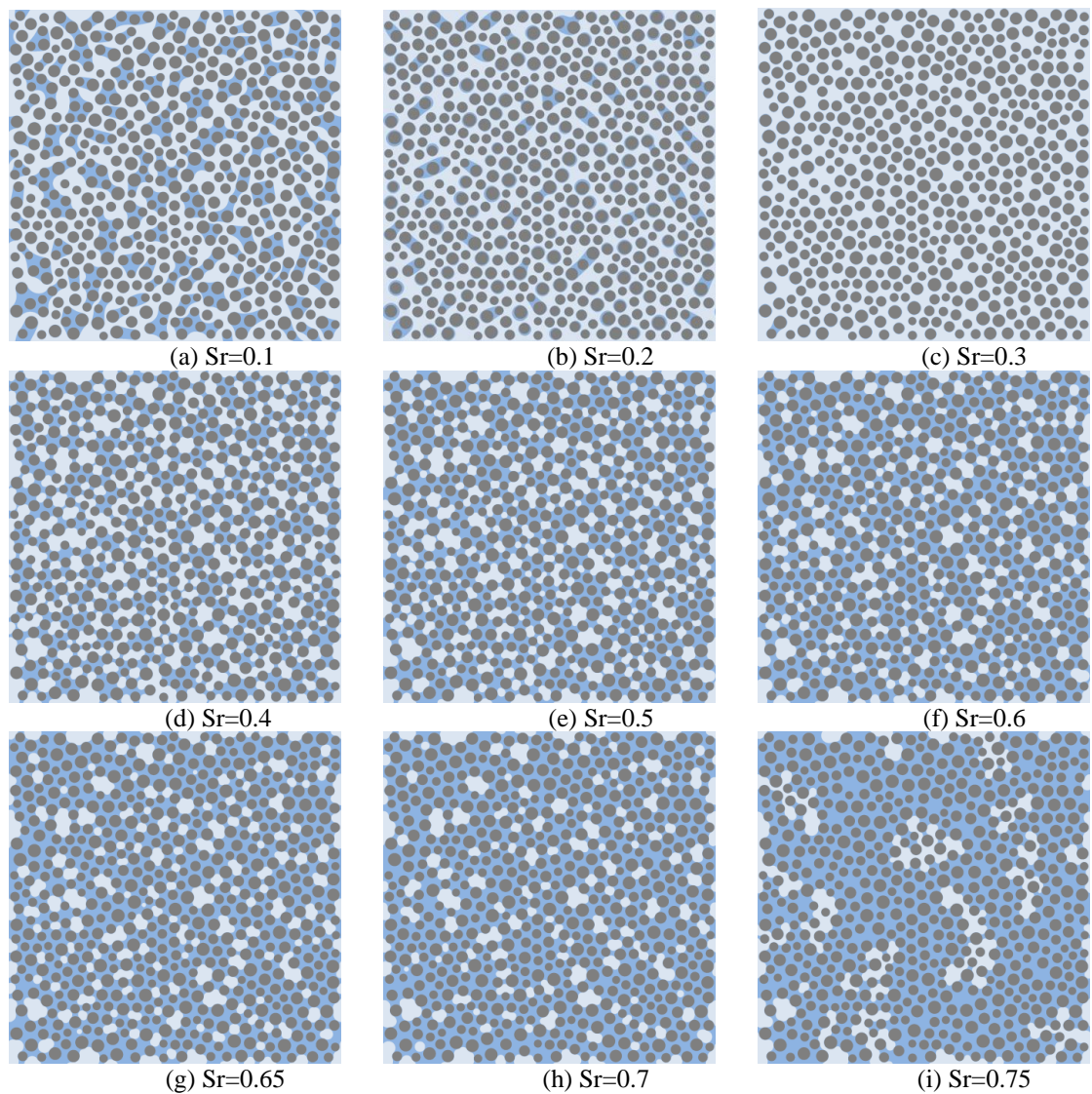


Figure 4.151 Multiphase distributions at different degrees of saturation in a porous medium.

The simulated distribution patterns are shown in Figure 4.15. It is clear that, at very low degrees of saturation (Figure 4.15(a)), the solid phase is enveloped by the wetting films.

The wetting films become thicker as the saturation increases, and capillary condensation between particles is produced (Figure 4.15(b)). A connected network of the wetting phase can be obtained at certain degrees of saturation (Figure 4.15(e)). When the degree of saturation continues increasing, large portions of the porous medium becomes occupied by the wetting phase, and most of the non-wetting phase is trapped in the large pores, as observed in Figure 4.15(i). The simulated results are in agreement with the experimental observations from the X-ray CT images in both the assembling glass beads and Ottawa sand under different degrees of saturation from Lu et al. (2010). Moreover, the specific surface areas of the fluid interfaces are calculated at different degrees of saturation (see Figure 4.16). The specific surface area of the interfaces increase as the degree of saturation becomes less than 0.2, and the opposite phenomenon is observed when the degree of saturation becomes larger than 0.2. The overall trend, first increasing and subsequently decreasing, also agrees well with the experimental observations in Lu et al. (2010).

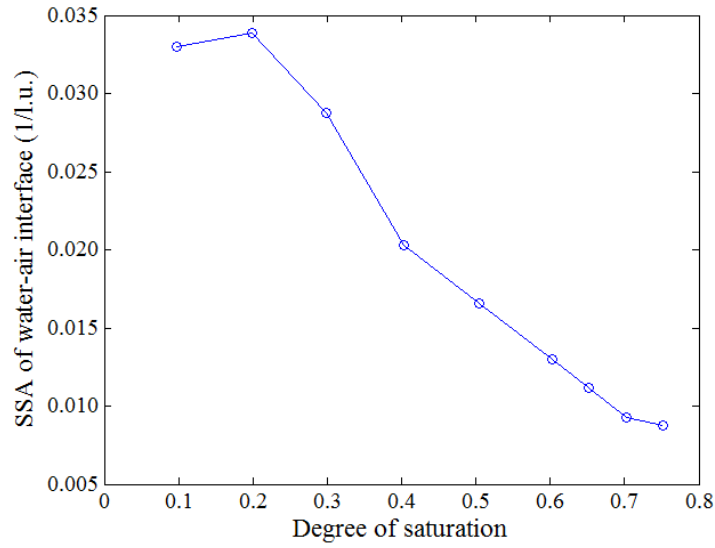


Figure 4.16 Correlation between the degree of saturation and the specific surface area of the fluid interface.

4.4.3 Fluid distribution in fractured porous media

For a porous medium with a static fluid distribution, by introducing fractures, the fluid distribution will evolve to a new equilibrium condition. In this section, the influence of the fracture length and width on the fluid changes in the porous media under different degrees of saturations (S_r) will be investigated using the SCMP LBM. During the simulation, the fluid distribution of the porous medium under given S_r is first calculated. Then, a fracture with a given length and width is inserted into the model (Figure 4.17a). To implement this in the LBM model, all the nodes including the solid, wetting and non-wetting phases in the range of fracture are converted to the non-wetting phase (e.g. air). The model will not be at equilibrium, and the fluid will migrate. Using the SCMP LBM, the final equilibrium condition can be obtained (see Figure 4.17b).

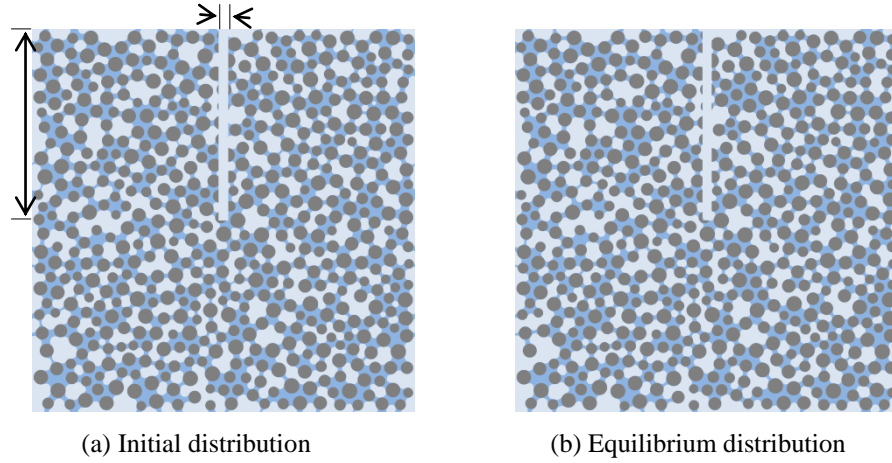


Figure 4.17 Influence of fractures on multiphase distributions ($S_r = 0.4$, Fracture width = 100 l.u., Fracture length = 1000 l.u.).

By conducting a large number of simulations, the influence of fractures on the fluid distribution can be observed using the numerical results. In this paper, the parameters are chosen as follows: S_r with respect to the wetting phase = 0.2, 0.4, 0.6, and 0.75; the fracture width = 25, 50, 75, and 100 l.u.; and the fracture length = 500, 1000, 1500, and 2000 l.u..

It should be mentioned that the fluid flow distribution in fractured porous media is geometrically irregular and unsuitable for direct analysis, e.g., it is difficult to find the fluid migration using Figure 4.17. To obtain a more quantitative analysis, the simulation domain is further divided into $N_{sub} \times N_{sub}$ sub-regions. In this paper, the size of sub-region is selected as squares with side lengths of 40×40 l.u. Therefore, total numbers of 50×50 sub-regions are divided.

The coincident ratio at sub-region i is defined as

$$\text{Coincident ratio}_{(i)} = \frac{N_{co(i)}}{N_{wetting(i)}} \quad (4.24)$$

where $N_{co(i)}$ and $N_{wetting(i)}$ are the number of coincident wetting phases (two pixels of the original porous medium and the fractured porous medium at the same location were both wetting) and the number of pixels in the wetting phase at sub-region i of the original porous medium, respectively. This index can represent the disturbance of the wetting phase, i.e., if it is equal to one, then there is no disturbance, and if it is equal to zero, then the wetting phase is completely disturbed (migrated). Another index, the water migration number, is defined as the amount of change in the wetting phase at the sub-region and is given as

$$\text{Water migration number}_{(i)} = N'_{wetting(i)} - N_{wetting(i)} \quad (4.25)$$

where $N'_{wetting(i)}$ and $N_{wetting(i)}$ are the numbers of wetting phase pixels in the wetting phase at sub-region i of the fractured and initial porous media. It is a positive value for flowing in and a negative value for flowing out.

The changes in the two-phase distribution induced by the fracture expressed as the coincident ratio and water migration number in each sub-region is shown in Figure 4.18. It can be found that the fracture can apparently be reflected from the contour map of the coincident ratio calculated at each sub-region (see Figure 4.18a); in contrast, it is unable to be distinguished using the water migration number (see Figure 4.18b). Therefore, the coincident ratio is used as the post-processing for the simulation results.

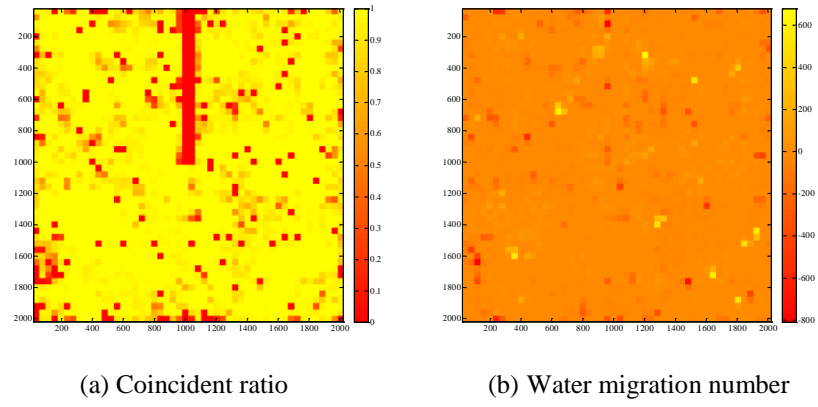


Figure 4.18 Macroscopic description of differences between Figures 17(a) and 17(b) ($S_r = 0.4$, Fracture width = 100 l.u., Fracture length = 1000 l.u.)

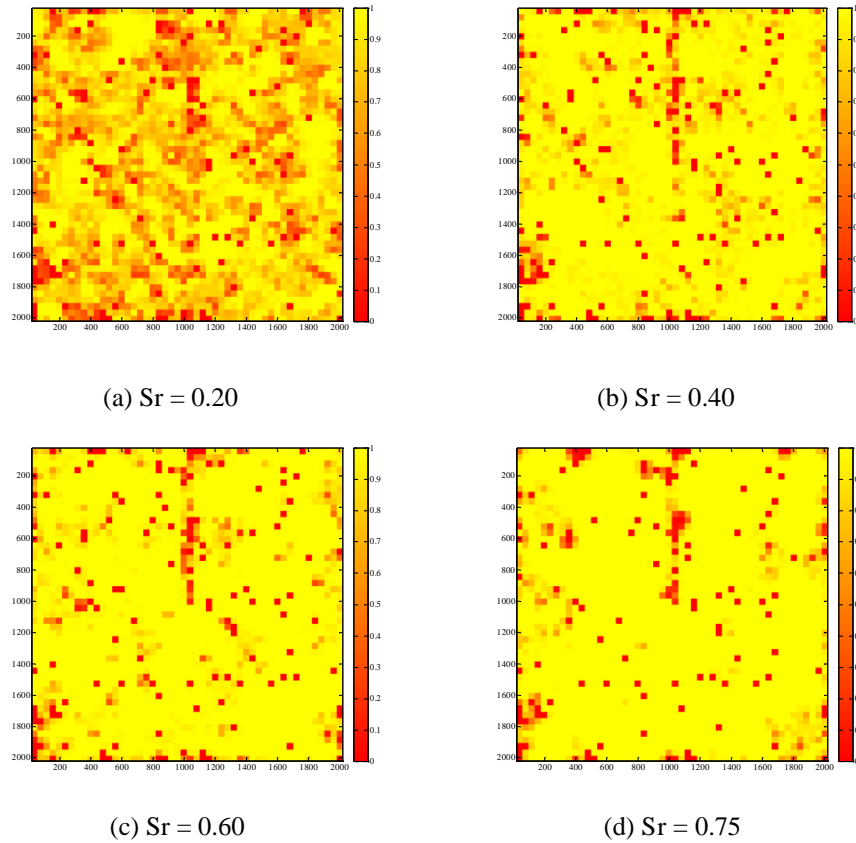


Figure 4.19 Influence of the degrees of saturation on the coincident ratio (Fracture width = 50 l.u.; Fracture length = 1000 l.u.).

The influences of saturation, fracture width and fracture length on the two-phase fluid distributions are diagramed in Figures 4.19, 4.20, and 4.21, respectively. A large part of the system is disturbed at low degrees of saturation (Figure 4.19(a)), and the disturbance area decreases as the degree of saturation increases (Figure 4.19(b, c, d)). The disturbance area increases with increasing width and length of the fracture, with most of the disturbance occurring around the fracture, as illustrated in Figures 4.20 and 4.21.

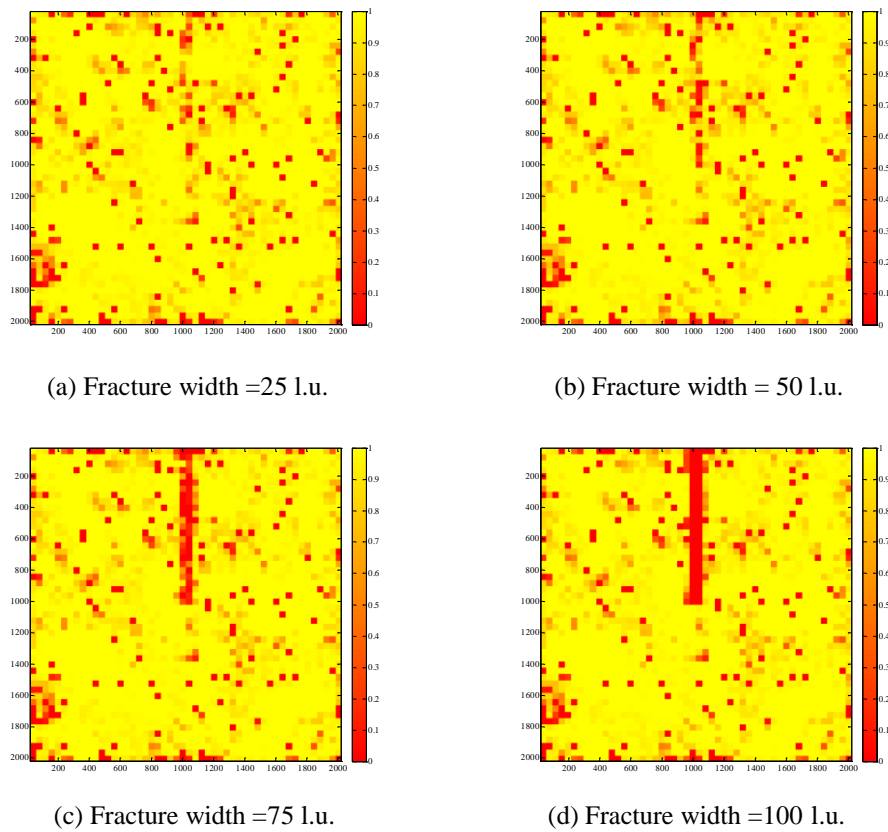
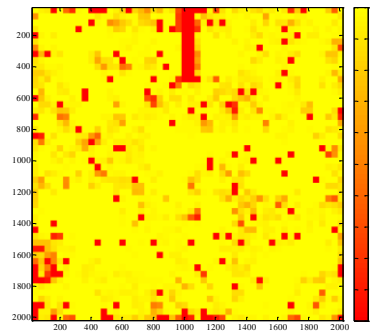


Figure 4.20 Influence of the fracture widths on the coincident ratio ($S_r = 0.4$; Fracture length = 1000 l.u.).

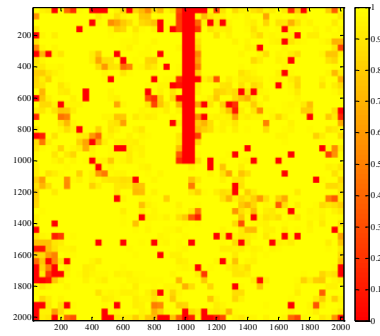
To quantify the disturbed region of the whole model due to the induced fracture, a disturbance ratio Ω is introduced as follows:

$$\Omega = 1 - \frac{\sum N_{co(i)}}{\sum N_{wetting(i)}} \quad (4.26)$$

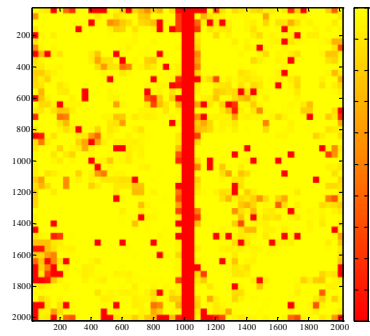
The influences of the fracture length, fracture width, and degree of saturation on the disturbance ratio are summarized in Figure 4.22. It can be observed that, the disturbance ratio increase with the fracture length. Meanwhile, it is also found that the disturbance ratio decreases as the degree of saturation increases. A possible application of these numerical findings is to explore fractures (which might be too small to be observed through X-ray CT due to the limitation of resolution) by indirectly investigating the fluid distribution. Furthermore, it is widely accepted that, the fluid distribution will influence the flow behaviors within a multiphase system. However, it is not practical to obtain the fluid distribution with limited information. Therefore, it is of high value to provide a relative new and powerful approach that could predict the multiphase distribution, which can be employed as the initial configuration in the multiphase flow problems.



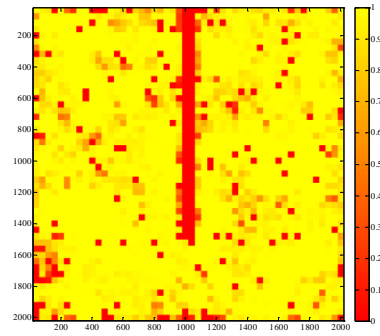
(a) Fracture length = 500 l.u.



(b) Fracture length = 1000 l.u.

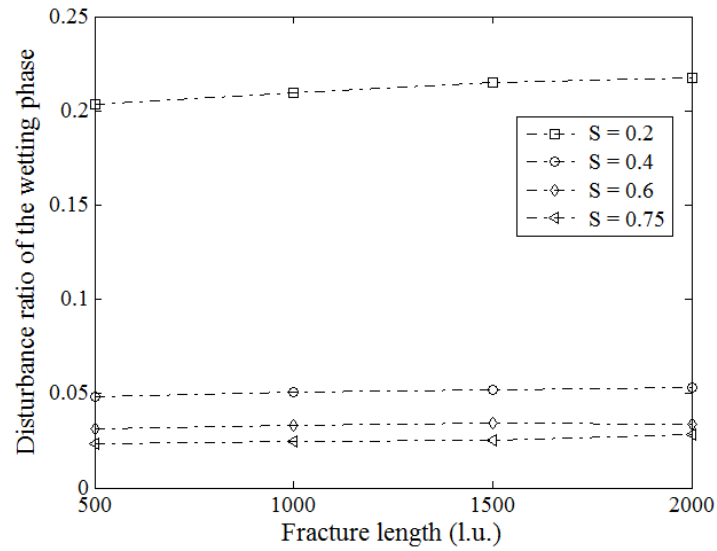


(c) Fracture length = 1500 l.u.

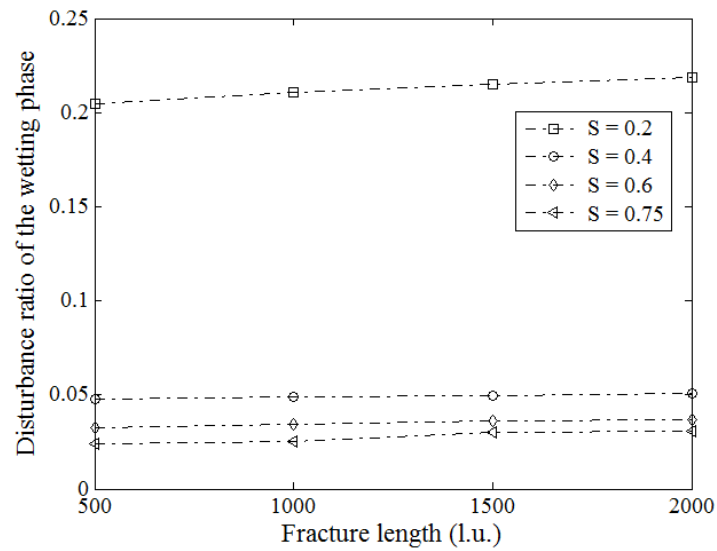


(d) Fracture length = 2000 l.u.

Figure 4.21 Influence of fracture lengths on the coincident ratio ($S_r = 0.4$; Fracture width = 100 l.u.).



(a) Fracture width = 25 l.u.



(b) Fracture width = 100 l.u.

Figure 4.22 Influence of the fracture length on the disturbance ratio at different degrees of saturation.

4.5 CONCLUDING REMARKS

To sum up, the SCMP LBM is found to be the best method in predicting the fluid distribution in partially saturated porous media compared with two other methods (the

SAM and the MCMP LBM). The effect of periodic boundary conditions and the initial configuration are also tested. It is found that a buffer size of approximately 12.5 times the average particle size is suggested to reduce the error resulting from the periodic boundary conditions. Moreover, the initial distribution of the SCMP LBM is less sensitive for an irregular porous medium than that of a regular medium; therefore, it is more suitable for natural porous media, such as rock and soil. The influence of the degree of saturation on the two-phase fluid distribution was investigated using this method. The fluid distribution patterns and the quantitative evaluation at different degrees of saturation were investigated, which is consistent with experimental results from the literature. Finally, the influence of fractures on the two-phase fluid distribution was also studied. The disturbance ratio is introduced to evaluate the change in the two-phase system due to the induced fracture. It was found that more fluids are disturbed as the fracture length and width increase, and the disturbance ratio decreases as the degree of saturation increases.

4.6 REFERENCES

- Adamson A.W., Cast A.P. (1997) Physical chemistry of surfaces. John Wiley & Sons, Inc New York
- Berkowiz B., Hansen D.P. (2001) A numerical study of the distribution of water in partially saturated porous rock. *Transport in Porous Media* 45:303-319.
- Chen S., Doolen G.D. (1998) Lattice Boltzmann method for fluid flows. *Annual Review of Fluid Mechanics* 30:329-364.

Cipra B. (1987) An introduction to the Ising model. *American Mathematics Monthly* 94:937–959.

Culligan K.A., Wildenschild D., Christensen B.S.B., Gray W.G., Rivers M.L., Thompson A.F.B. (2004) Interfacial area measurements for unsaturated flow through a porous medium. *Water Resources Research* 40: W12413.

Cundall P.A., Strack O.D.L. (1979) A discrete numerical model for granular assemblies. *Géotechnique* 29(1):47-65.

de Gennes P.G., Brochard-Wyart F., Quere D. *Capillary and wetting phenomena*. 291 pp, Springer, New York

German E.R., Akin S., Castanier L. (2006) Multiphase flow properties of fracture porous media. *Journal of Petroleum Science and Engineering* 51: 197-213.

Gray W.G., Thompson A.F.B., Soll W.E. (2002) Closure condition for two-fluid flow in porous media. *Transport in Porous Media* 47:29-65.

Gvirtzman H., Magaritz M., Klein E., Nadler A. (1987) A scanning electron microscopy study of water in soils. *Transport in Porous Media* 2:83–93.

Hilfer R. (2000) Local porosity theory and stochastic reconstruction for porous media. *Statistical Physics and Spatial Statistics*. K. Mecke and D. Stoyan, Springer Berlin Heidelberg. 554: 203-241.

<http://leonardi.unsw.wikispaces.net/home>

<http://www.palabos.org/>

Huang H.B., Thorne D.T., Schaap M.G., Sukop M.C. (2007) Proposed approximation for contact angles in Shan-and-Chen-type multicomponent multiphase lattice Boltzmann models. *Physical Review E* 76: 066701.

Huang H.B., Wang L., Lu X. (2011) Evaluation of three lattice Boltzmann models for multiphase flows in porous media. *Computers and Mathematics with Applications* 61:3606-3617.

Inamuro T., Yoshino M., Ogino F. (1995) A non-slip boundary condition for lattice Boltzmann simulations. *Physics of Fluids* 7:2928-2930.

Jim-Douglas J.R., Spagnuolo A.M. (2001) The transport of nuclear contamination in fractured porous media. *Journal of the Korean Mathematical Society* 38(4): 7263-764.

Kirkpatrick S., Gelatt C.D., Vecchi M.P. (1998) Optimization by simulated annealing. *Science, New Series* 220(4598):671-680

Knight R., Chapman A., Knoll M.. (1990) Numerical modeling of microscopic fluid distribution in porous media. *Journal of Applied Physics* 68(3):994-1001.

Krummel A., Datta S.S., Münster S., Weitz D.A. (2013) Visualizing multiphase flow and trapped fluid configurations in a model three-dimensional porous medium. *AIChE J* 59:1022.

Latt J., Chopard B., Malaspinas O., Deville M., Michler A. (2008) Straight velocity boundaries in the lattice Boltzmann method. *Physical Review E* 77(5): 056703.

Liaw H.K., Kulkarni R., Chen S., Watson A.T. (1996) Characterization of fluid distribution in porous media by NMR techniques. *AIChE Journal* 42(2):538-546.

Lu G., Wang X.D., Duan Y.Y. (2013) Study on initial stage of capillary rise dynamics. *Colloids and Surfaces A: Physicochemical and Engineering Aspects* 433:95-103.

Lu N., Zeidman B.D., Lusk M.T., Willson C.S., Wu D.T. (2010) A Monte Carlo paradigm for capillarity in porous media. *Geophysical Research Letters* 37:L23402.

Or D., Tuller M. (1999) Liquid retention and interfacial area in variably saturated porous media: Upscaling from single-pore to sample-scale model. *Water Resources Research* 35(12):3591-3605.

Pan C., Hilpert M., Miller C.T. (2004) Lattice Boltzmann simulation of two phase flow in porous media. *Water Resources Research* 40:W01501.

Politis M.G., Kainourgiakis M.E., Kikkinides E.S., Stubos A.K. (1998) Application of simulated annealing on the study of multiphase systems, *Simulated Annealing*, Cher Ming Tan (Ed.), ISBN: 978-953-7619-07-7, InTech, DOI: 10.5772/5565.

Reynolds D.A., Kueper B.H. (2004) Multiphase flow and transport through fractured heterogeneous porous media. *Journal of Contaminant Hydrology* 71(1-4):89-110.

Schmitz D., Reinecke N., Petritsch G., Mewes D. (1997) High resolution X-ray tomography for stationary multiphase flows. *OECD/CSNI Specialist Meeting on Advanced Instrumentation and Measurement Techniques*. Santa Barbara

Schmitz D., Reinecke N., Petritsch G., Mewes D. (1997) X-ray computed tomography for stationary multiphase flow in random and structured packings. *Conference Proceedings: Frontiers in Industrial Process Tomography II*. Delft.

Shan X., Chen H. (1993) Lattice Boltzmann model for simulating flows with multiple phases and components. *Physical Review E* 47:3

Shan X., Chen H. (1994) Simulation of nonideal gases and liquid-gas phase transitions by the lattice Boltzmann equation. *Physical Review E* 49:4

Silverstein D.L., Fort T. (2000) Prediction of air-water interfacial area in wet unsaturated porous media. *Langmuir* 16:829-834.

Silverstein D.L., Fort T. (2000) Prediction of water configuration in wet unsaturated porous media. *Langmuir* 16:839-844.

Sudicky E.A., Frind E.O. (1982) Contaminant transport in fractured porous media: analytical solutions for a system of parallel fractures. *Water Resources Research* 18(6): 1634-1642.

Sukop M.C., Huang H.B., Lin C.L., Deo M.D., Oh K., Miller J.D. (2008) Distribution of multiphase fluids in porous media: Comparison between lattice Boltzmann modeling and micro-x-ray tomography. *Physical Review E* 77: 026710.

Sukop M.C., Or D. (2003) Invasion percolation of single component, multiphase fluids with lattice Boltzmann models. *Physica B* 338:298-303.

Sukop M.C., Thorne D.T. (2006) Lattice Boltzmann modeling: an introduction for geoscientists and engineers. Springer-Verlag Berlin/Heidelberg

Trivedi J., Babadagli T. (2009) Experimental and numerical modeling of the mass transfer between rock matrix and fracture. *Chemical Engineering Journal* 146: 194-204.

Wang J.S.Y., Narasimhan T.N. (1985) Hydrologic mechanisms governing fluid flow in partially saturated, fractured, porous medium. *Water Resources Research* 21(12): 1861-1874.

Wildenschild D., Culligan K.A., Christensen B.S.B. (2004) Application of X-ray microtomography to environmental fluid flow problems. *Proceeding SPIE 5535, Developments in X-Ray Tomography IV*, 432

Ziegler D.P. (1993) Boundary conditions for lattice Boltzmann simulations. *Journal of Statistical Physics* 71:1171-1177.

Zimmerman R.W., Bodvarsson G.S. (1996) Hydraulic conductivity of rock fractures. *Transport in Porous Media* 23:1-30.

Zou Q., He X. (1997) On pressure and velocity boundary conditions for the lattice Boltzmann BGK model. *Physics of Fluids* 9:1591-1598.

CHAPTER 5 NUMERICAL FLUID FLOW THROUGH DEFORMABLE NATURAL FRACTURE NETWORK

In this Chapter, fluid flow through natural fracture network is studied using Computational Fluid Dynamics (CFD). To investigate the influence of fracture roughness, normal deformation and shear deformation on the fracture transmissivity/permeability, numerical tests of fluid flow through 3D rock fracture are conducted using the Lattice Boltzmann Method (LBM) in a middle size cluster. An empirical equation was obtained from the numerical results. Following this, natural fracture networks are built for fluid dynamics simulation of fluid flow through rock fracture network. It is found that the pipe network model enriched with the derived empirical equation can produce similar results compared with the LBM simulation which further confirm its applicability. Finally, influences of fracture length, fracture density, and deformation of the fracture network on the fluid flow are studied preliminarily from coupling LBM with the Discrete Fracture Network (DFN) model and Discrete Element Model (DEM).

5.1 INTRODUCTION

The flow behavior in fracture networks has been a research focus over the past half century. The discrete fracture network model (DFN) model has become the most widely used method since the work by Long et al. (1982). A DFN model typically combines deterministic and stochastic discrete fractures, which presents the same geological statistics properties as observations, such as fracture density, distribution of location, orientation, size and hydraulic aperture. Numerous works were conducted to investigate

the fluid flow behaviors in rock fractures using DFN model (e.g. Long and Witherspoon 1985, Chen et al. 1999, Dershowitz et al 2004, Kim et al. 2007, Parker et al. 2007, Liu et al. 2014). However, in DFN, the fluid flow was calculated based on the cubic law under the assumption that the fractures are plate surfaces. In practice, the fractures are rough with variety of profiles and aperture distribution which can be changed dynamically under normal and shear deformation. An accurate prediction of hydraulic behavior in fracture network requires a clear understanding of fluid flow through single fracture under these coupled conditions.

Comprehensive works have been conducted to investigate the flow behavior in single fractures including experimental investigation, theoretical analysis and numerical simulation. The early work on fluid flow in single fracture was conducted experimentally by Lomize (1951). The cubic law was found essentially valid for laminar flow in rock joints based on the assumption of parallel flat surface. However, fracture walls contain irregularities which reduce fluid flow and lead to a local channeling effect of preferential flow. A large number of laboratory studies were carried out, the validation of cubic law was discussed and different empirical corrections of the cubic law were proposed (e.g. Iwai 1976, Witherspoon 1980, Neuzil and Tracy 1981, Tsang 1984, Barton et al. 1985, Brown 1987, Barton and Quadros 1997). Recently, influence of deformation on fluid flow in single fracture receives more attentions. For example, Koyama et al. (2008) conducted the coupled shear-flow tests for rock fractures. Indraratna et al. (2014) investigated the fluid flow through deformable rough rock joints. However, most of the works relate the hydraulic property of fracture to the stress rather than deformation of the fracture. The stress-permeability relationship is complex, which is influenced by lots of factors, such as stress condition and fracture profiles as well as

the deformation. The mechanism of the flow behavior behind these experiments is not clearly understood because the geometry within the fracture is not easy to be controlled and obtained. Paralleling with the experimental study, extensive theoretical analysis was conducted (e.g. Zimmerman and Bodvarsson 1996). Theoretically, the flow of incompressible Newtonian viscous fluid is governed by the Navier-Stokes equation (Batchelor 1967). However, the Navier-Stokes equation cannot be solved in closed form when deal with realistic fracture with rough surfaces. Alternatively, numerical approaches provided the opportunity to obtain the solution of fluid flow though rough surfaces under complex boundary conditions.

There are varieties of traditional methods developed for fluid simulations, which are based on discretized partial differential equations, such as finite differences (e.g. Ames 1977; Morton and Mayers 1994), finite volumes (Bryan 1969) or finite element (e.g. Zienkiewicz and Taylor 1991). For example, Brown (1989) used the finite difference method to calculate the volume flow rate and electric current in simulated fractures composed of rough surfaces generated with a fractal algorithm. Rasouli and Hosseini (2011) used the FEM based software (FLUENT) to develop a correlation to estimate the hydraulic parameters through channel of combined JRC profiles under different minimum closures. Indraratna et al. (2014) adopted the finite-volume method to solve the flow problem in deformable rough rock joints, where the three-dimensional Navier-Stokes equation was converted to an equivalent 2D flow model by considering the hydraulic aperture distribution. However, most of the traditional methods present the drawbacks such as long computation times, poor convergence and numerical instabilities, and the difficulties in dealing with complex boundaries (Wolf-Gladrow 2000).

Alternatively, the "bottom up" approaches, such as lattice Boltzmann method developed in the past two decades received more popularity in characterizing the flow problems. Originating from the kinetic theory, the LBM has the appealing features of programming simplicity, intrinsic parallelism, and straightforward resolution of complex solid boundaries and multiple fluid species (e.g. Succi 2001; Higuera & Jiménez 1989; Inamuro et al. 1995; He & Zou et al. 1997; Guo et al. 2002; Latt et al. 2008; Yan et al. 2011). For example, Eker and Akin (2006) presented studies of flow through two dimensional synthetically created fracture apertures using LBM. The permeability of fracture is found to be related to the mean aperture, fractal dimension and anisotropy factor of the synthetic fracture. However, the aforementioned numerical works are limited or simplified to 2D, the geometry description of the fracture is not accurate and the deformation cannot be involved properly.

According to the literature review, there is still no comprehensive study on fluid flow in single fracture considering both the roughness and deformation. Moreover, the direct investigation of flow in fracture networks with roughness is rarely reported as well. Therefore, it is important to explore the mechanism of fluid flow in the natural fracture and fracture network. This chapter is structured as follows. Firstly, the fluid flow behavior in rough fracture is investigated considering the fracture's deformation. The fracture was characterized by the mathematical model proposed by Brown (1995) and the fluid flow was simulated through LBM (Succi et al. 1995, Chen et al. 1998). The accurate of LBM for study of fluid flow through rock fracture is firstly verified through the comparison with the Poiseuille's Law. After that, numbers of fluid flow simulations on realistic synthetic 3D rock fractures are conducted. A two parameters equation is developed based on the simulation results to predict the flow in rough fracture. The

proposed equation can be used to characterize the fluid flow in single fracture involving both roughness and deformation. Then, LBM is used to investigate the fluid flow in natural fracture network, in which the roughness effect is directly incorporated. A good agreement is obtained between LBM simulation and the modified pipe network model using the derived empirical equation. Finally, the fluid flow behavior of stochastic discrete fracture network (DFN) under deformation is preliminarily studied using LBM.

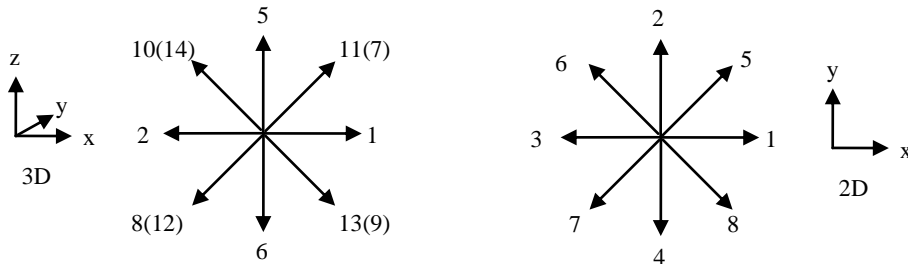
5.2 SINGLE PHASE INCOMPRESSIBLE LBGK MODEL

5.2.1 Basic concept

In the incompressible LBGK model (Guo et al. 2000), the evolution equation of the density distribution function is expressed as

$$f_i(x + c\mathbf{e}_i\Delta t, t + \Delta t) = f_i(x, t) + \Omega_i(f_i(x, t)) \quad (i = 0, 1, \dots, M) \quad (5.1)$$

where $c = \Delta x / \Delta t$. Δx , \mathbf{e}_i and Δt are the lattice grid spacing, discrete velocity direction and time step, respectively. There are two commonly used lattice models for 2D and 3D problems (as illustrated in Figure 5.1).



(a) D3Q15 model

(b) D2Q9 model

Figure 5.1 The D2Q9 model and D3Q15 model.

$\Omega_i(f_i(x, t))$ is the collision operator given by

$$\Omega_i = -\frac{1}{\tau}(f_i - f_i^{eq}) \quad (5.2)$$

where τ is the dimensionless relaxation time, and f_i^{eq} is the equilibrium distribution function defined as

$$f_i^{eq}(x) = \omega_i \rho(x) [1 + s_i(\mathbf{u})] \quad (5.3)$$

in which, ω_i is the weight index, and

$$s_i(\mathbf{u}) = 3 \frac{\mathbf{e}_i \cdot \mathbf{u}}{c^2} + \frac{9}{2} \frac{(\mathbf{e}_i \cdot \mathbf{u})^2}{c^4} - \frac{3}{2} \frac{\mathbf{u}^2}{c^2} \quad (5.4)$$

where \mathbf{u} is the macroscopic velocity.

The macroscopic density and velocity can be obtained as

$$\rho = \sum_{i=1}^M f_i \quad (5.5)$$

$$\mathbf{u} = \frac{\sum_{i=1}^M f_i \mathbf{e}_i}{\rho} \quad (5.6)$$

Detailed explanation of the incompressible LBGK model can be found in the work by Guo et al. (2000), and the corresponding incompressible Navier-Stoke equations were derived through multi-scaling expansion as,

$$\nabla \cdot \mathbf{u} = 0 \quad (5.7)$$

$$\frac{\partial \mathbf{u}}{\partial t} + \nabla \cdot (\mathbf{u}\mathbf{u}) = -\nabla p + \nu \nabla^2 \mathbf{u} \quad (5.8)$$

where $p = c_s^2 \rho$ is the pressure, $c_s = c / \sqrt{3}$ is the sound speed, and $\nu = (2\tau - 1)c^2 \Delta t / 6$ is the kinetic viscosity.

5.2.2 Boundary conditions

There are bunch of boundary conditions have been implemented in LBM. In this Chapter, the boundary conditions are classified in two groups: the boundary condition at the open end (inlet and outlet) and the boundary condition at the solid interface. At the inlet and outlet, pressure boundary is applied to produce the pressure gradient. The no-slip boundary is used at the solid surface (wall), which is implemented through the bounce-back scheme. The so-called bounce-back means that when a fluid particle reaches solid (wall) nodes, the particle will scatter back to the fluid along with its coming direction as shown in Figure 5.2. Both of the boundary conditions are implemented according to the work by Zou and He (1996).

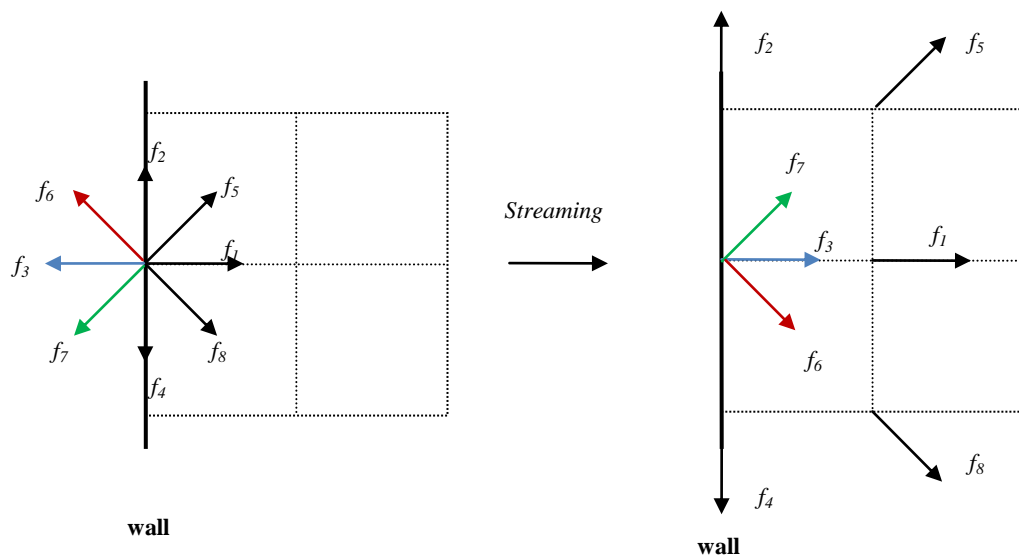


Figure 5.2 Bounce back scheme.

5.2.3 Palabos

The numerical simulations are conducted using the Palabos library (<http://www.palabos.org/>), which is a framework for general-purpose computational fluid dynamics (CFD) with a kernel based on LBM (Jonas Latt 2008). Its programming interface is straightforward, which makes it possible to set up fluid flow simulations with relative ease. Meanwhile, the LBM has the features of intrinsic parallelism. Programs written with Palabos can be automatically parallelized and the parallelization is performed with the message-passing paradigm of the MPI library. The Leonardi (<http://leonardi.unsw.wikispaces.net/>), a middle size cluster, is used to implement the parallel computation of the following numerical simulations.

5.3 FLUID FLOW IN SINGLE FRACTURE

5.3.1 Validation

Firstly, the fluid flow between two parallel plates is simulated so as to verify the accuracy of Palabos. In LBM, it is necessary to convert the physical system to a discrete system so that the LBM simulation can be conducted. The flow domain is set as dimensionless system with length 2 and width 1. The pressure boundary condition is set at the left and right open side so as to produce unit velocity at the center, and the no-slip boundary condition is set at top and bottom. And the parameters used in the simulation are presented in Table 5.1.

Table 5.1 Parameters used in the simulation of fluid flow in single fracture

Parameters	Values
Density (ρ)	1.0
Reynolds number (Re)	1.0
Resolution (N, l.u.)	10~100
δx	1/N
δt	$\sim \delta x^2$

The simulation is considered as converged when the ratio between the standard deviation and average of the velocity is less than 1e-6. The simulations the results are compared with the Poiseuille's Law,

$$u = -\nabla P \cdot \frac{1}{2\rho\nu} ((h/2)^2 - y^2) \quad (5.9)$$

where ∇P is the pressure gradient, ρ is the density, ν is the viscosity, h is the aperture and y is the distance from the center line.

It is necessary to mention that, discrete variables δx and δt are important parameters which have impact on the accuracy and the stability of a simulation, which should follow the relationship $\delta t \sim \delta x^2$ (Jonas Latt 2008) . Once the resolution changes, the times interval should change accordingly. However, the exact relationship has not been reported. In this study, the microscopic parameters are firstly calibrated and the $\delta t = \kappa \delta x^2$ is used to obtain a reasonable value for the choice of δt . The influence of κ on simulation accuracy is investigated at different resolutions and relative error is summarized in Figure 5.3. It is found that, when $\kappa = 1$, stable results are obtained.

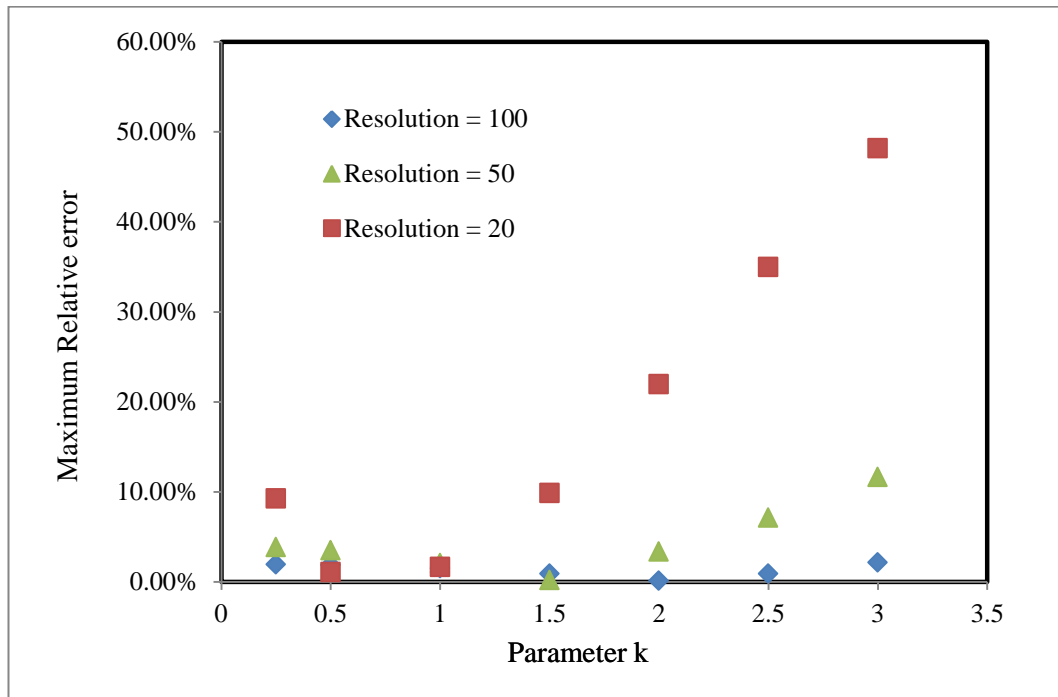
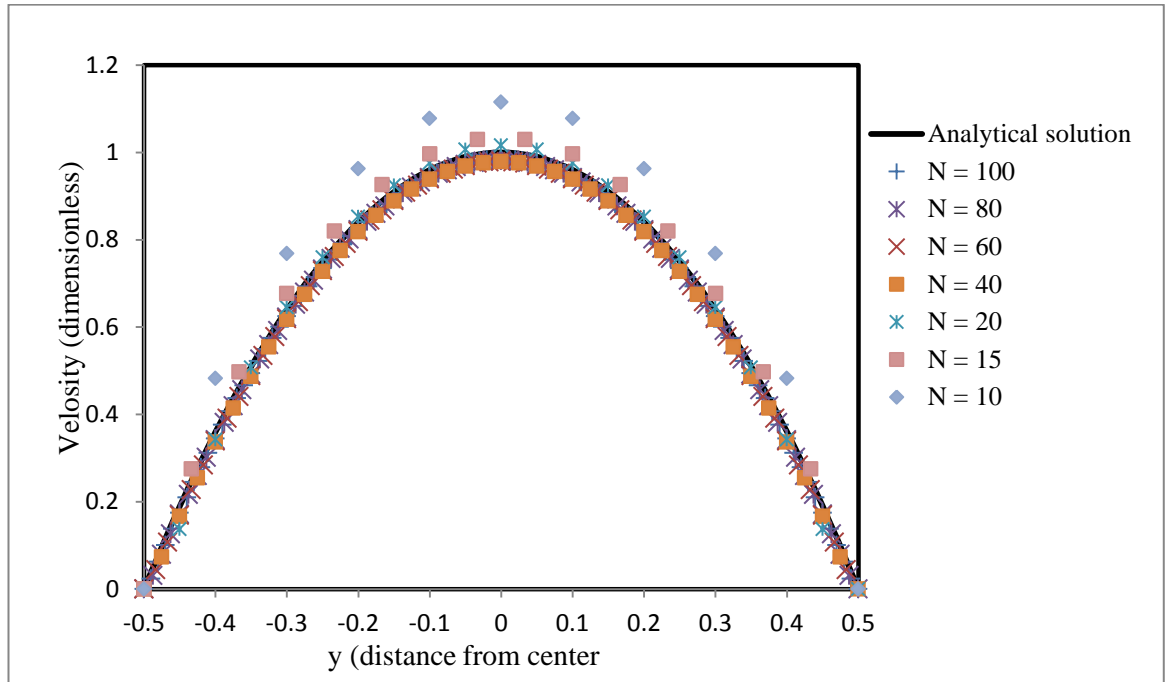
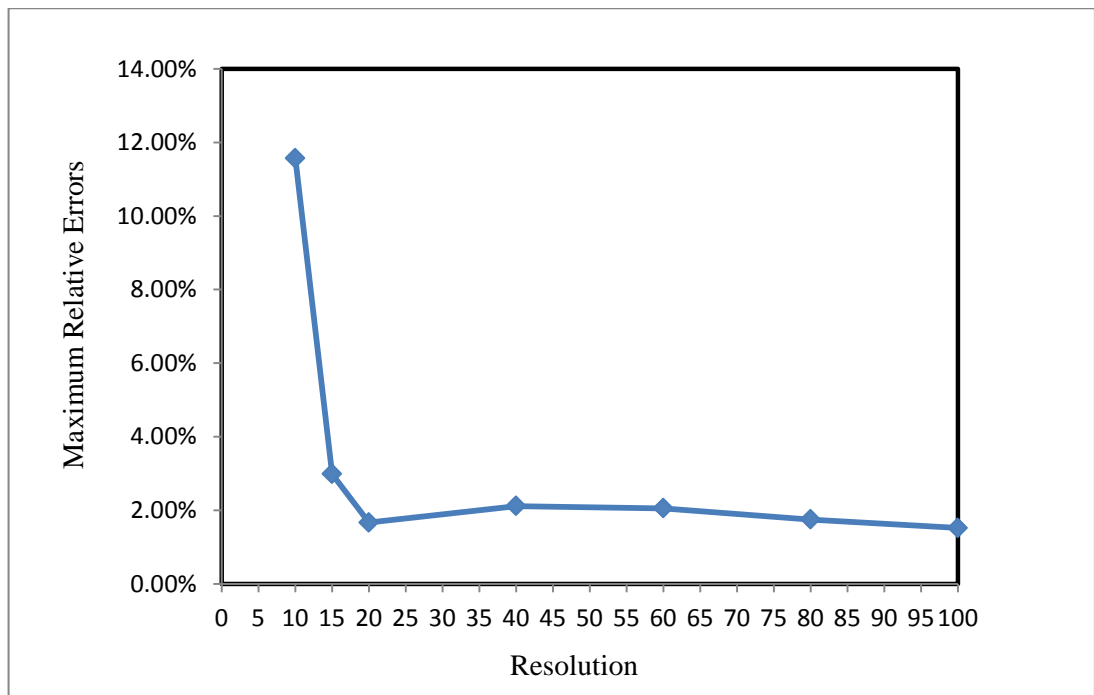


Figure 5.3 Impact of parameter choice.

Based on the calibrated relationship, $\delta t = \delta x^2$, the resolution effect on the simulation accuracy is investigated. The velocity profile at different resolution, which is compared with the analytical solution (5.4a), and relative error is presented in Figure 5.4b.



(a) Velocity profiles at different resolution



(b) Maximum relative errors at different resolution and parameters

Figure 5.4 The simulation results based on the relationship $\delta t = \delta x^2$

The flow rate along the pressure gradient can be obtained through the integration of the analytical solution,

$$Q_x = \int_{-h/2}^{h/2} \left\{ -\frac{dP}{dl} \cdot \frac{1}{2\rho\nu} [(h/2)^2 - y^2] \right\} dy = -\frac{dP}{dl} \cdot \frac{1}{2\rho\nu} \cdot \frac{h^3}{12} \quad (5.10)$$

Therefore, the transmissivity is described as the cubic law,

$$T = \frac{h^3}{12} \quad (5.11)$$

5.3.2 Fluid flow through 3D synthetic fracture

The parallel plate model can only be considered a qualitative description of flow through real fractures. Real fracture surfaces are not smooth parallel plates but are rough and contact each other at discrete points (Brown 1995). There are a number of parameters proposed to characterize the fracture roughness, such as Z_2 (Myers 1962), joint roughness coefficient (Barton 1973), and fractal dimension (Xie 1998). However, it is not always possible to characterize the fracture roughness by single parameter because the roughness of fracture surface in rock depends on the sample size or scale of observation (Bandis et al. 1981; Brown and Scholz 1985).

In this part, a mathematical model developed by Brown (1995) is used to characterize the fracture roughness. In the mathematical model, the rough-walled fractures are dominated by three main parameters: the fracture dimension, the standard deviation of the surface profile, and a length scale describing the degree of mismatch between the two fracture surfaces. The software SynFrac (Ogilvie et al. 2006) is used to generate the synthetic fracture, which shares the same geometrical statistics as the natural fractures.

The GUI of SynFrac is shown in Figure 5.5 and the Brown model is selected among three modules. In this study, the fracture is assumed as two parallel surfaces without considering the mismatch effect. Therefore, there are three parameters to characterize the flow behavior in rough fracture, which are the fractal dimension, the standard deviation and the aperture.

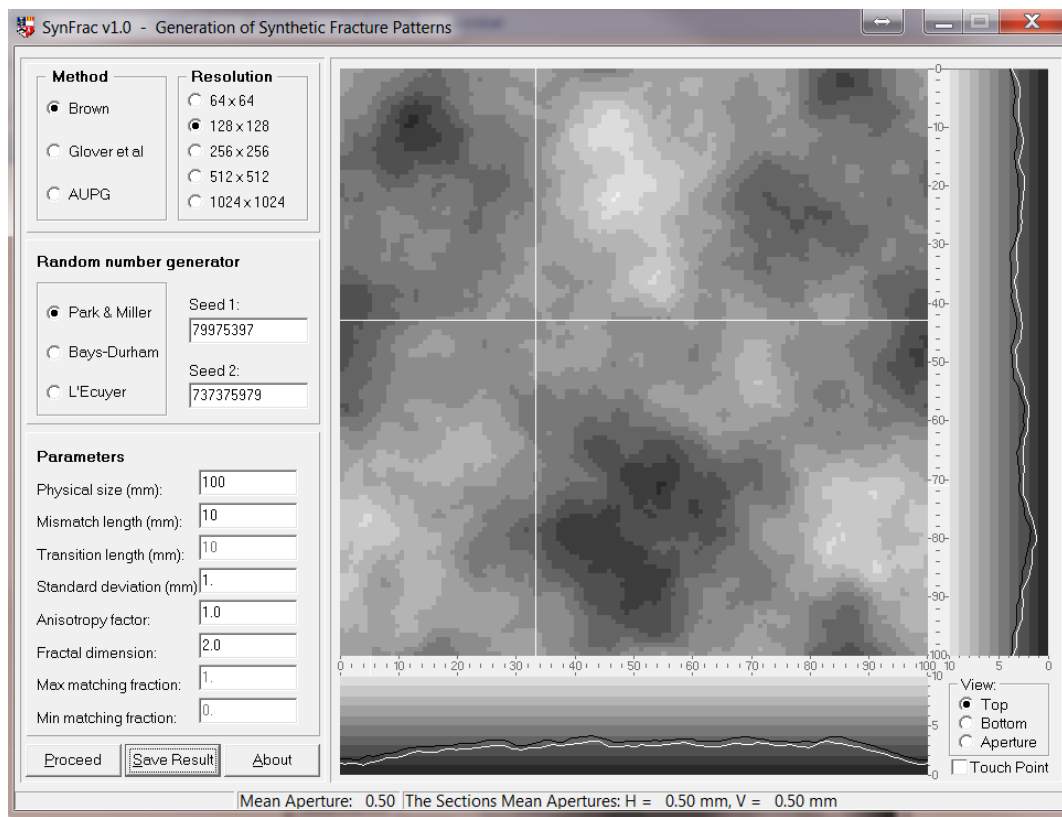
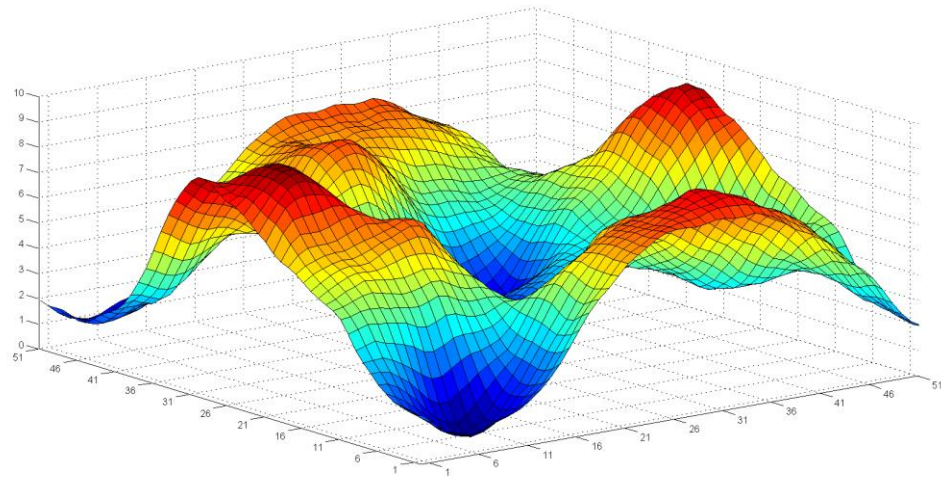


Figure 5.5 Fracture generator (Ogilvie et al. 2006)

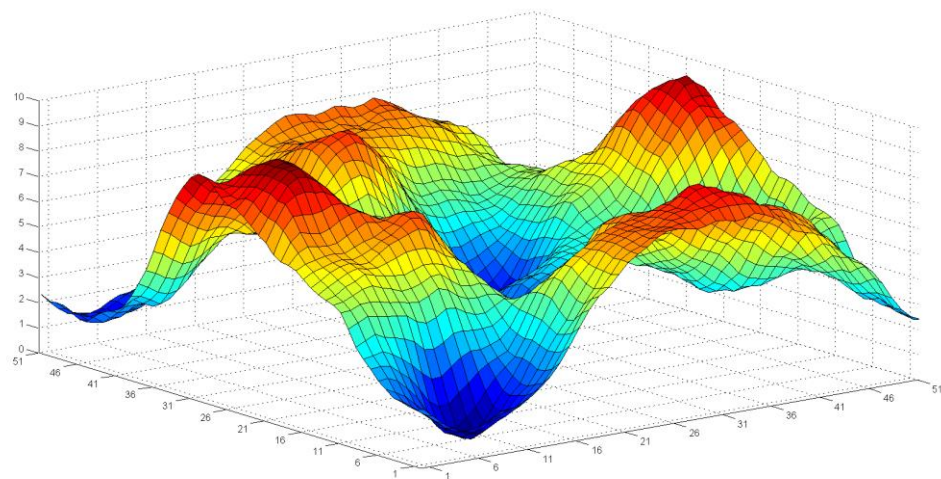
Table 5.2 Parameters used to generate fracture for different fractal dimension, standard deviation and aperture.

Fractal dimension	Standard deviation (mm)	Mean aperture (mm)
1.0; 1.2; 1.4; 1.6; 1.8; 2.0	1; 1.5; 2; 2.5	2; 2.5; 3; 3.5; 4

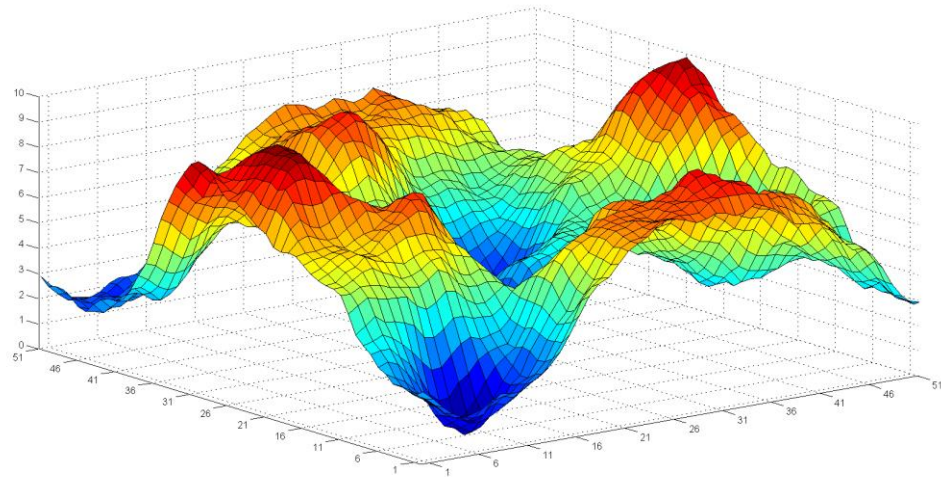
In order to investigate influence of roughness and develop a generic model to characterize the flow behavior in fracture, the physical size is set as 5 cm with resolution of 500×500 , the mismatch length is set as 5 mm for reference only, and the other parameters are presented in Table 5.2. Examples of fracture profiles with different fractal dimension and standard deviation are presented in Figure 5.6 and Figure 5.7.



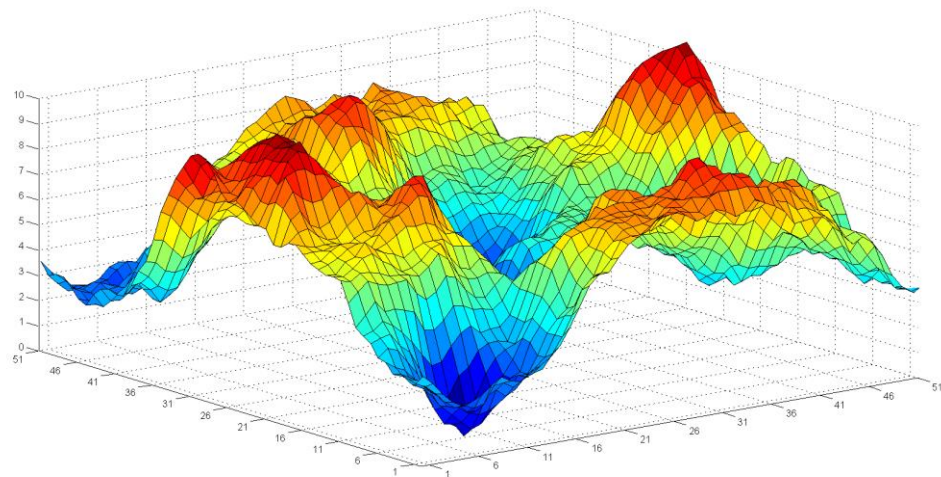
(a) Fractal dimension = 1.2



(b) Fractal dimension = 1.4

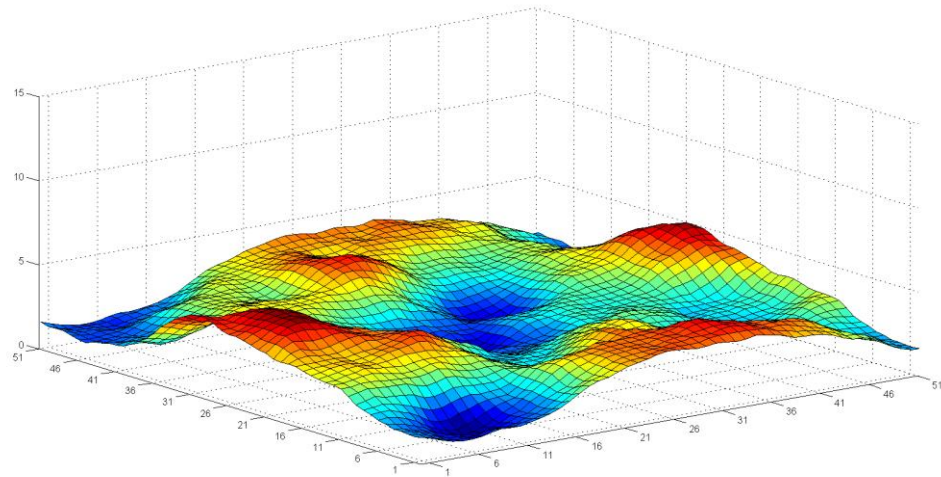


(c) Fractal dimension = 1.6

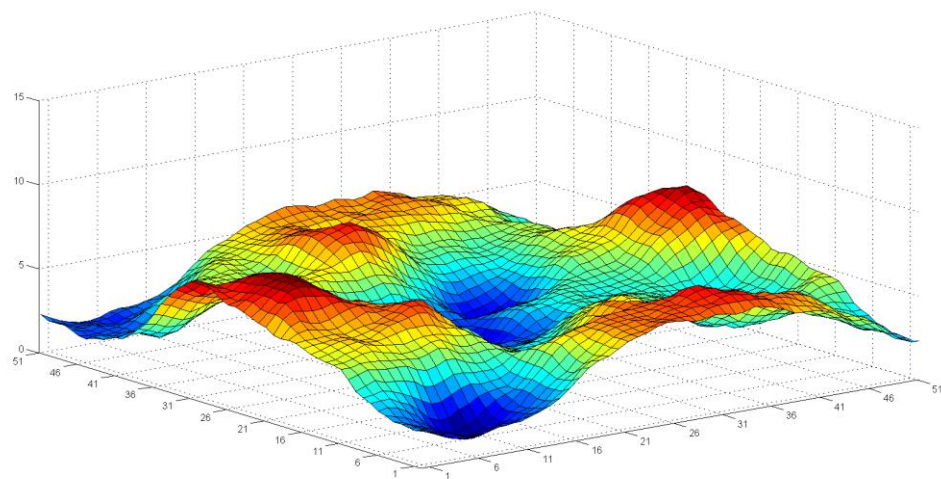


(d) Fractal dimension = 1.8

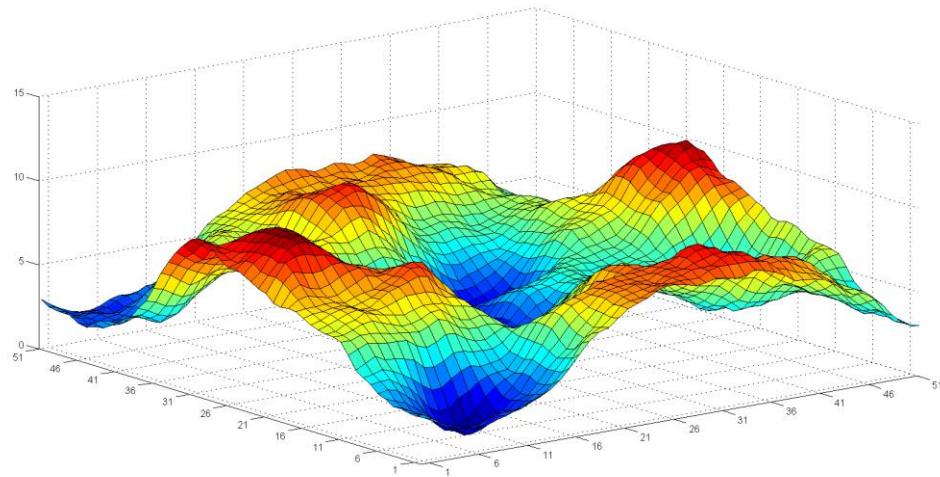
Figure 5.6 Effect of fractal dimension on fracture profile (standard deviation = 2 mm)



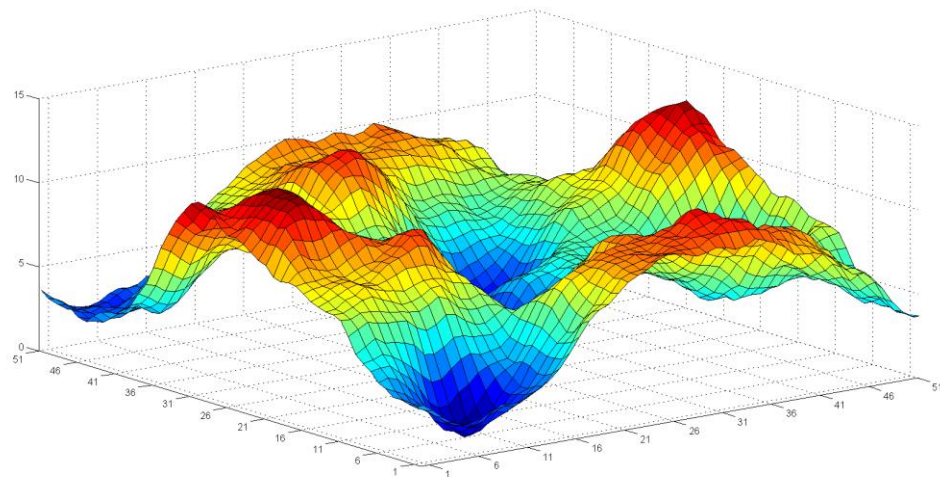
(a) Standard deviation = 1.0 mm



(b) Standard deviation = 1.5 mm



(c) Standard deviation = 2.0 mm



(d) Standard deviation = 2.5 mm

Figure 5.7 Effect of standard deviation on fracture profile (fractal dimension =1.6)

A total number of 120 cases are generated based on the parameters in Table 5.2 which are imported to LBM for fluid dynamics simulation. The geometry of the 3D fracture and velocity profiles are presented in Figure 5.8. The flow rate is calculated through the integration of the velocity at every lattice in the flow domain and the transmissivity of fractures under different profiles is derived. Based on the simulation results, a two coefficients model (Equation 5.12) is developed to describe the fluid flow in a natural fracture. It is found that, the transmissivity decreases with the increase of fractal dimension and standard deviation according to the value of α and the proposed equation. However, the relationship between the coefficient β and fractal dimension is only clear when the standard deviation is larger than 1.5 mm.

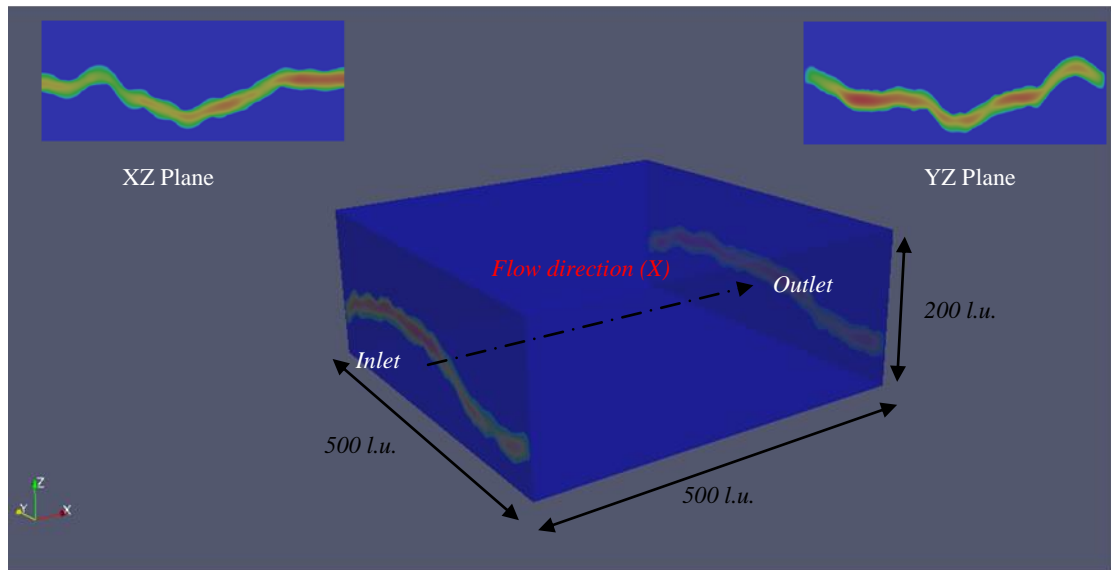
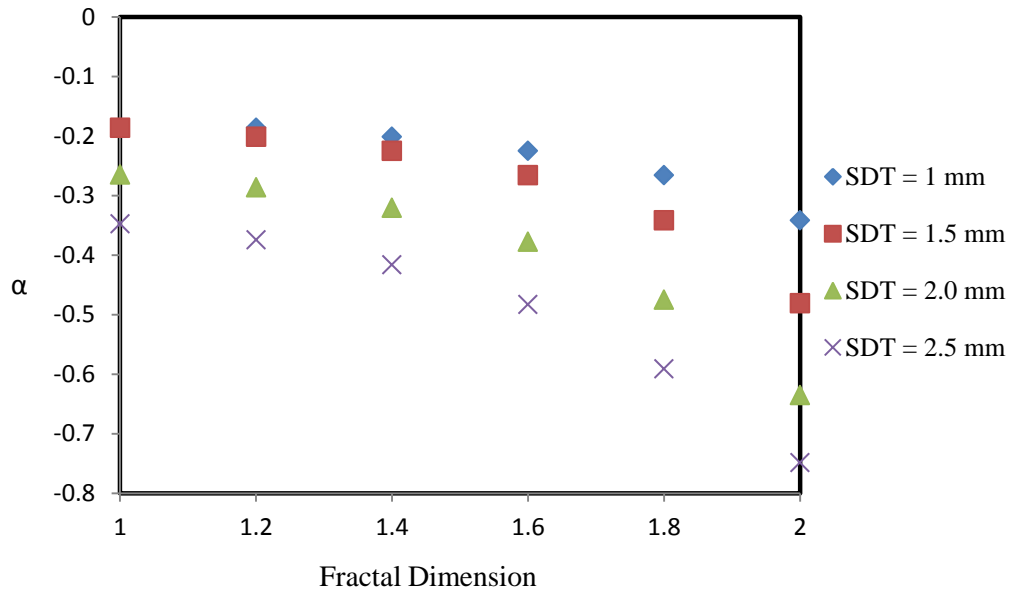
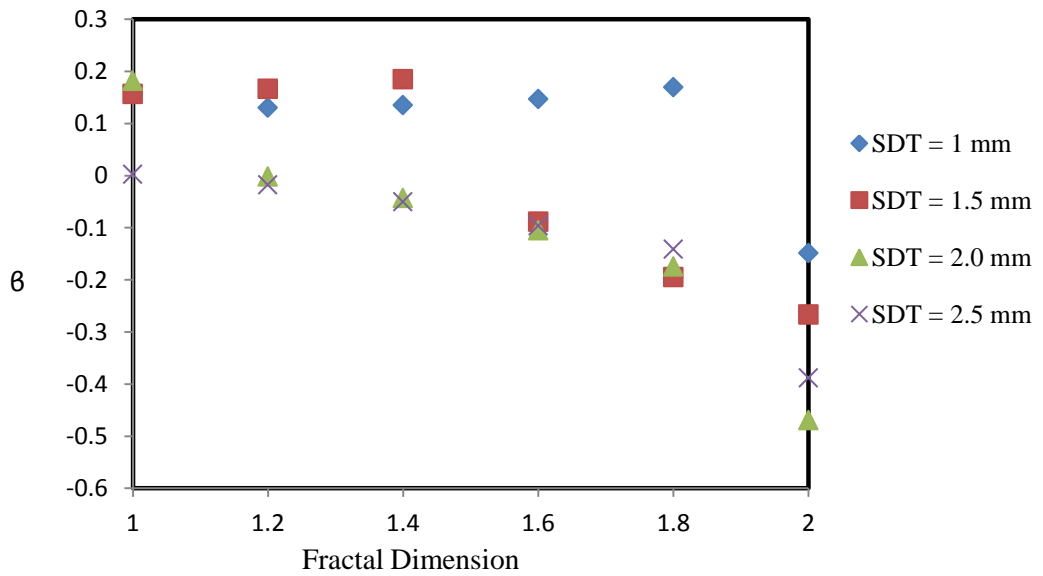


Figure 5.8 Geometry for the fracture and velocity distributions at slices from LBM simulation.



(a) Relation between α and fracture geometry



(b) Relation between β and fracture geometry

Figure 5.9 Dependence of coefficients on fractal dimension and standard deviation of fracture surfaces

$$T = \frac{w(1 + \alpha \cdot e^{\beta h_m})h_m^3}{12} \quad (5.12)$$

where T is the transmissivity, w is the width (equal to 1 in 2D), h_m is the mean aperture, α and β are the coefficients that characterize the fracture roughness.

5.3.3 Effect of displacement

It is notable that the permeability of single fracture depends on fracture geometry and the stress condition (e.g. Pyrak-Nolte and Morris 2000, Koyama et al 2008, Indraratna et al. 2014). Even with extensive studies on stress-flow coupled problem, there is still no existing law or principle to characterize the flow behavior in single fracture under specific fracture deformation. Therefore, it is necessary to investigate the flow behavior involves both the roughness and displacement.

In this study, the fluid flow in single fracture is characterized by the mean aperture, h_m , which is expressed as,

$$h_m = h_0 - \Delta h_n + \Delta h_s \quad (5.13)$$

where h_0 is the initial mechanical aperture, Δh_n is normal displacement and Δh_s is the shear displacement induced aperture change.

The effect of normal displacement is simply to change the mean aperture which has been investigated in the previous part. The following equation is suggested to predict of transmissivity of fracture under normal displacement,

$$T = \frac{w(1 + \alpha \cdot e^{\beta(h_0 - \Delta h_n)})(h_0 - \Delta h_n)^3}{12} \quad (5.14)$$

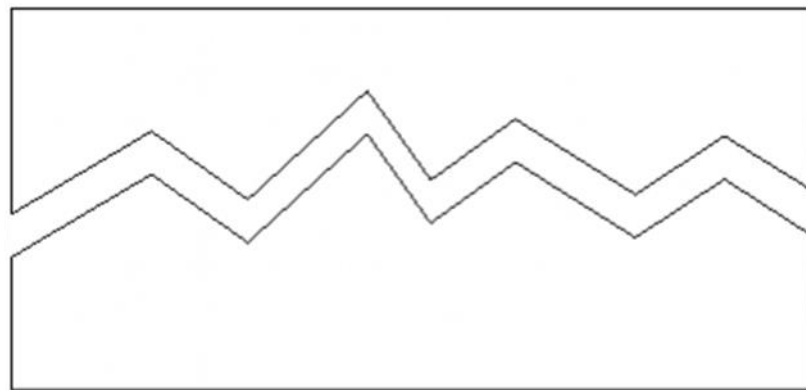
The effect of shear displacement on fluid flow in rough fracture is studied as follows.

The geometry of fracture is set as follows in Table 5.3.

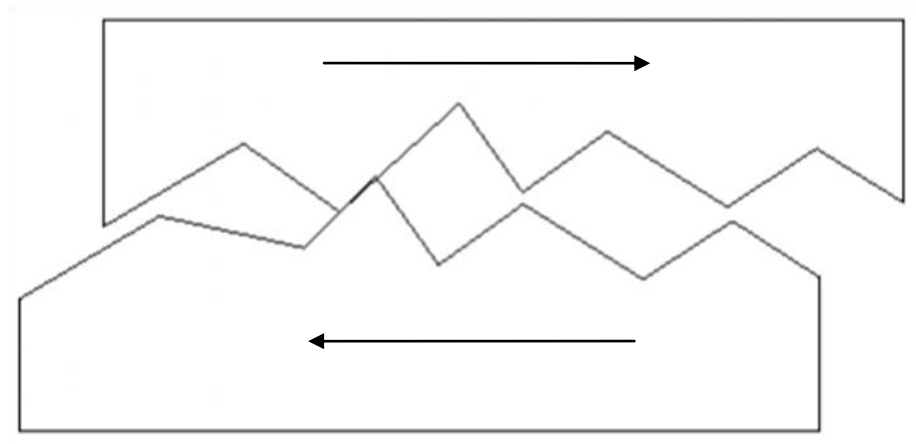
Table 5.3 Parameters in the fluid flow under shear displacement.

Physical size (cm)	5×5
Resolution	500×500
Fractal dimension	2.0
Standard deviation (mm)	2.0
Initial aperture (mm)	5
Normal displacement (mm)	0; 1; 2
Shear displacement (mm)	0~10

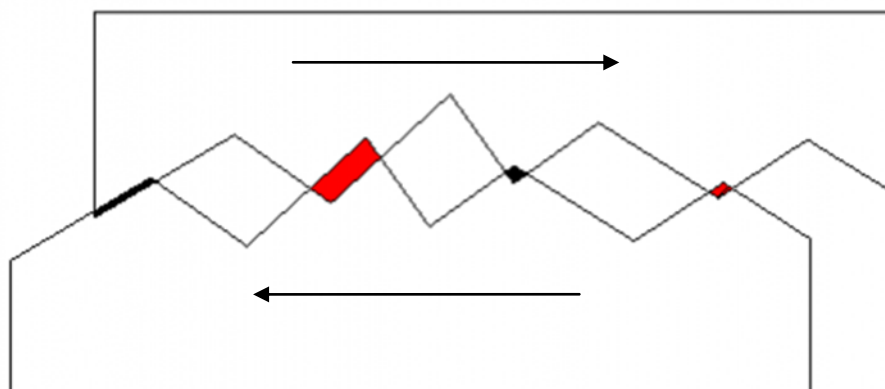
In reality, the two rough surfaces may overlap with each other at some points under shear displacement. However, the degree of overlap is not clear unless the stress-deformation relationship is known. Therefore, two assumptions are made to consider the fracture's deformation. In assumption 1, there is only one contact point between the two surfaces, which means that one of the surfaces may skim over the opposite surface when they get contacted as shown in Figure 5.10(b). In assumption 2, the two surfaces will overlap and generate contact areas (damaged) as shown in Figure 5.10(c). Based on these two assumptions, one example of the generated fracture is demonstrated in Figure 5.11. To visualize the shear displacement induced aperture change, the relationship between the mean aperture change and shear displacement under different normal displacements is summarized in Figure 5.12.



(a) Original model

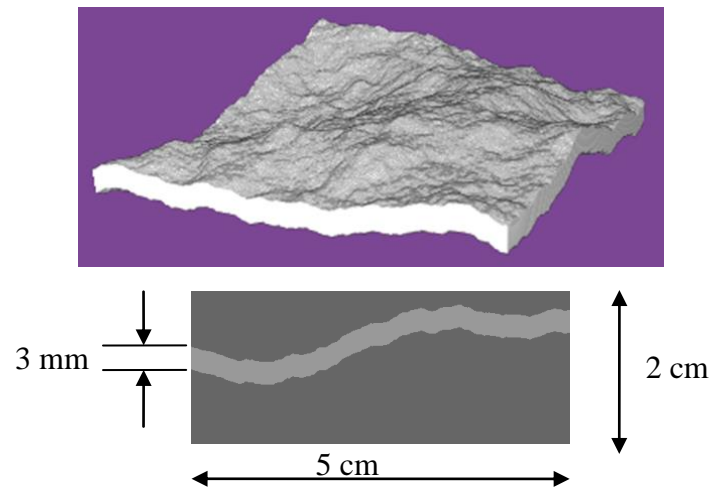


(b) Assumption 1



(c) Assumption 2

Figure 5.10 Assumptions made to implement shear displacement



(a) The original fracture and slice information

Shear displacement

2 mm



4 mm



6 mm



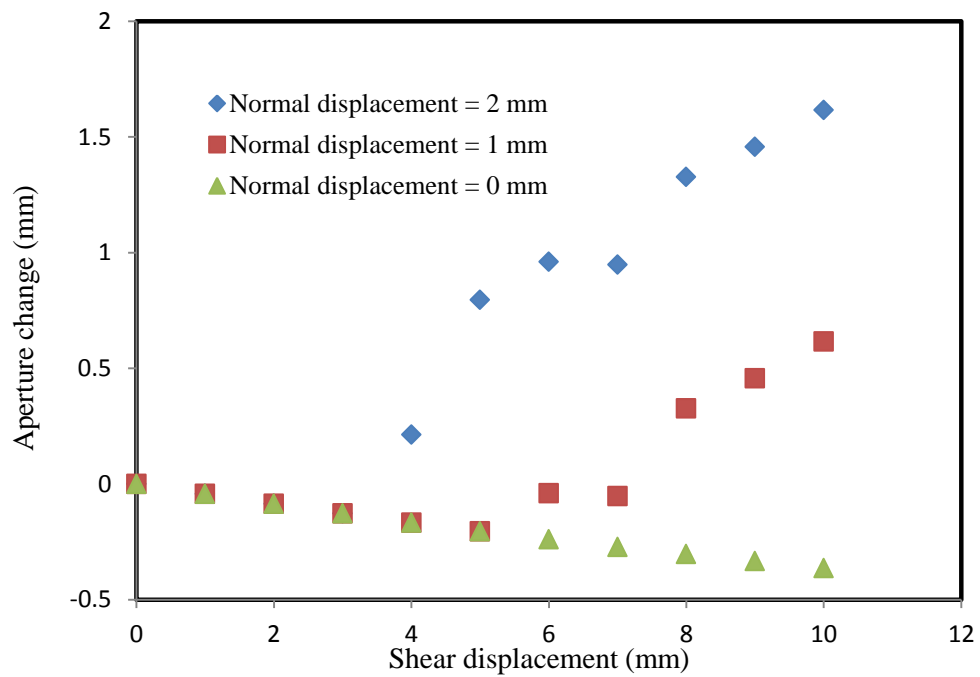
8 mm



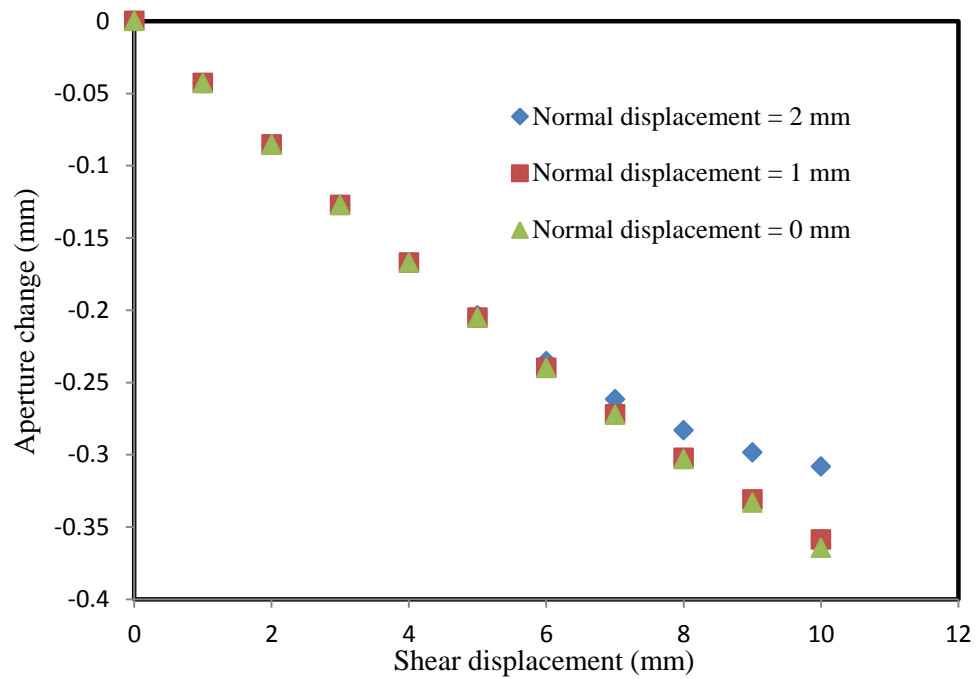
(b) Assumption 1

(c) Assumption 2

Figure 5.11 Geometry of the fracture and the aperture change induced by displacement.



(a) Assumption 1



(b) Assumption 2

Figure 5.12 Relationship between the aperture changes and shear displacement under two assumptions

The flow simulations are conducted in the fracture under different shear displacement and normal displacement. The relationship between the transmissivity and mean aperture is shown in Figure 5.13, which matches the proposed equation 5.15 well.

$$T = \frac{w(1 + \alpha \cdot e^{\beta(h_0 - \Delta h_n - \Delta h_s)})(h_0 - \Delta h_n - \Delta h_s)^3}{12} \quad (5.15)$$

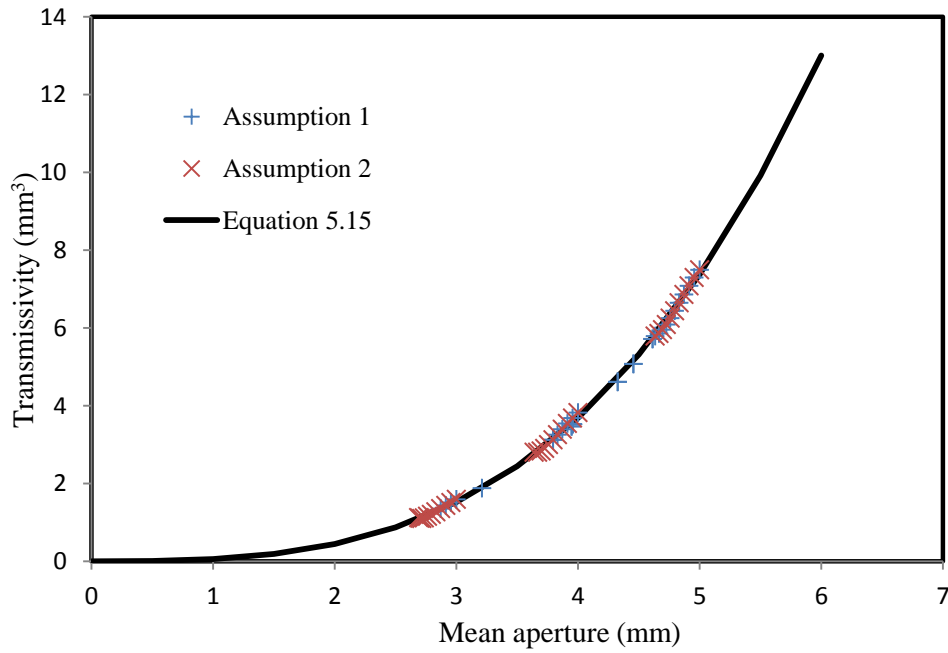


Figure 5.13 Relationship between the transmissivity and mean aperture

5.4 FLUID FLOW THROUGH FRACTURE NETWORK

5.4.1 Pipe network model (PNM)

In the pipe network model, the fluid flow in fracture network is represented by a discrete network made up from bubble and pipes, where the bubbles are the intersection points of the fractures, and the pipes are the links between two bubbles. The fluid flow variables are defined for each bubble as the fluid pressure p and fluid flux q . For each

pipe, the fluid flux and pressure constitutive relationship can be obtained from Darcy's law,

$$\begin{pmatrix} q_i \\ q_j \end{pmatrix} = \mathbf{H}_{pipe} \begin{pmatrix} p_i \\ p_j \end{pmatrix} \quad (5.16)$$

where q_i and p_i are the fluid flux and pressure of the i th bubble, \mathbf{H}_{pipe} is the flux pressure matrix given by

$$\mathbf{H}_{pipe} = -\frac{h_{pipe}^3}{12\mu l_{pipe}} \begin{bmatrix} 1 & -1 \\ -1 & 1 \end{bmatrix} \quad (5.17)$$

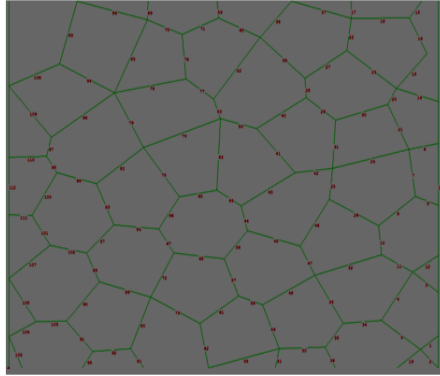
where h_{pipe} is the aperture of the pipe, μ is the dynamic viscosity of the fluid, and l_{pipe} is the length of the pipe.

A global flux pressure matrix is assembled in the way that the flow into a bubble equals the flow out of the bubble, so that the flux pressure relationship can be given as

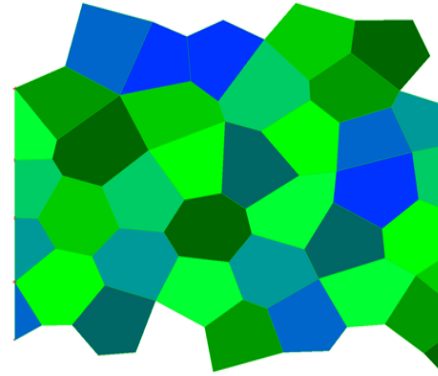
$$\mathbf{Q} = \mathbf{H}_{global} \mathbf{P} \quad (5.18)$$

where \mathbf{Q} is the vector of bubble fluid flux, \mathbf{H}_{global} is the global flux pressure matrix, and \mathbf{P} is the vector of bubble pressure. Similar with classical FEM simulation, the global system matrix can be assembled from each single pipe (fracture) using Equation (5.18). Fluid transmissivity of the fracture network can be obtained from solving the linear system equation together with the prescribed boundary conditions.

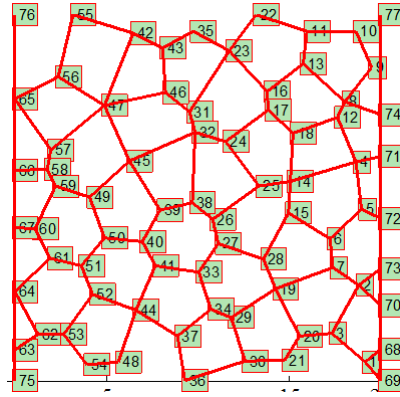
5.4.2 Pipe model generation



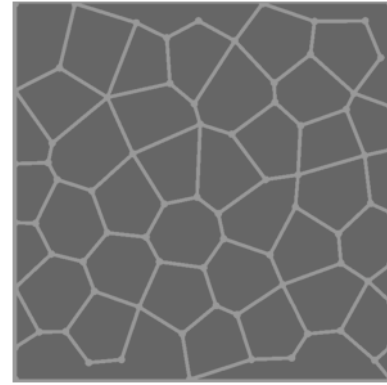
(a) Random fracture network



(b) Block cutting by DC



(c) Pipe network model in Matlab



(d) Geometry used in LBM simulation

Figure 5.14 Process of implement the fracture network in pipe network model and LBM simulation

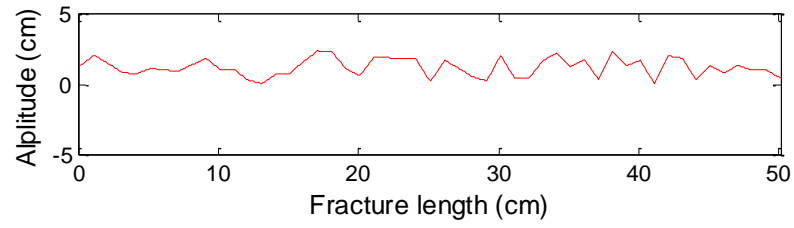
In order to calculate the fluid flow in fracture network through the pipe network model, it needs to identify the location of the bubbles or joints and the links between them. To implement this, we generate the randomly sized polygonal blocks (Figure 5.14(a)) using UDEC. The fractures of blocks are exported to the block cutting code of DDA to obtain the number index of the (bubbles) joints as well as the information of the links (pipes) (Figure 5.14(b)). After that, information is imported to the Matlab program to generate

the pipe network model (Figure 5.14(c)). In order to verify the accuracy of LBM in simulating the fluid flow in fracture network, the corresponding LBM model is generated as shown in Figure 5.14(d).

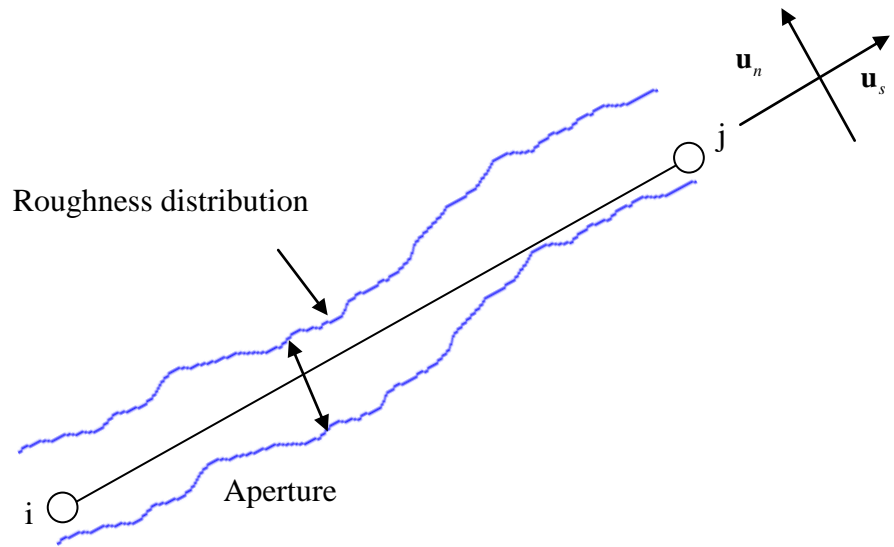
5.4.3 Fluid flow in natural fracture network

As illustrated in the pipe network model, the flow in individual fracture of the fracture network model is characterized by the cubic law. However, the fracture is rough rather than a plate in most circumstances, and the influence of roughness on fluid flow is significant as explained in the previous part. Accordingly, roughness effect on hydraulic behavior of fracture network receives increasing attentions. However, most of studies require the empirical equations that relate the hydraulic aperture to mechanical aperture. For example, Zhao et al. (2013) adopted the dimensionless parameter Z_2 proposed by Myers (1962) to obtain the hydraulic aperture from mechanical aperture. However, the directly investigation on roughness effect on fluid flow through fracture network and the validation of empirical equation is still not reported.

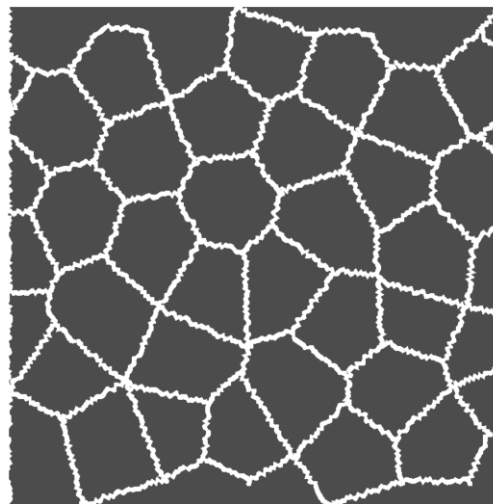
In order to investigate the roughness effect, the individual fracture between two intersection points is simplified as uniform distributed rough surface with constant aperture (Figure 5.15(a)). The rough surface at individual fracture is implemented through the geometrical method illustrated in Figure 5.15(b). There are several parameters that characterize the geometry of fracture between intersection i and j , which includes the direction tensors $(\mathbf{u}_n, \mathbf{u}_s)$, the roughness distribution along \mathbf{u}_s and aperture. The 2D fracture network with roughness is generated by creating the fracture between connected intersections (Figure 5.15(c)).



(a) The geometry of individual fracture roughness



(b) Implementation of roughness at individual fracture



(c) The geometry of fracture network

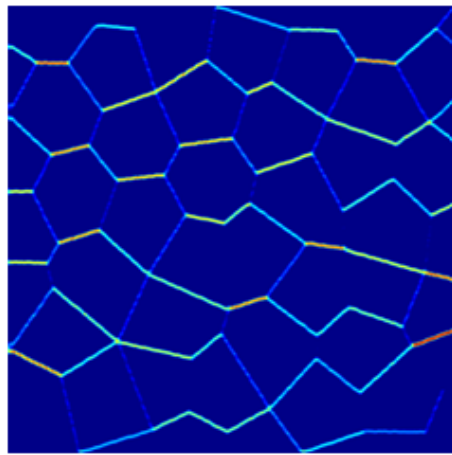
Figure 5.15 Generation of fracture network with roughness.

To obtain the two coefficients that characterize the roughness effect, the fluid flow through single fracture is firstly simulated using LBM. The length of fracture is 5 cm, the maximum amplitude ranges from 0.20 to 0.40 and the aperture ranges from 0.20 to 0.40. The parameters used in the simulation are the same as Table 5.1. The coefficients under different maximum amplitude are derived based on the simulation results which are shown in Table 5.4.

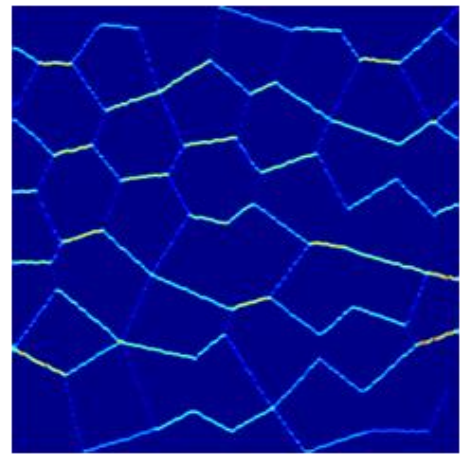
Table 5.4 The coefficients of rough fracture.

Maximum amplitude, cm	Coefficients	
	α	β
0	0	0
0.05	-0.1003	1.7314
0.10	-0.2448	0.1609
0.15	-0.4632	-0.7938
0.20	-0.5610	-0.4510
0.25	-0.7409	-0.6770
0.30	-0.9258	-0.5951

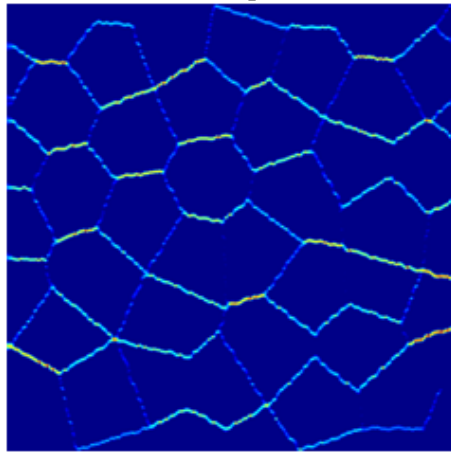
The fluid flow through the fracture network is numerically implemented by using both the modified pipe network model and LBM. In the modified pipe network model, the transmissivity of pipes is calculated based on the proposed equation. In all the simulation, the topology is same as the one shown in Figure 5.14(d) with size of 20 cm×20cm, the resolution in the LBM is set as 100 l.u./cm, and the aperture is set as 0.2 cm for all simulation.



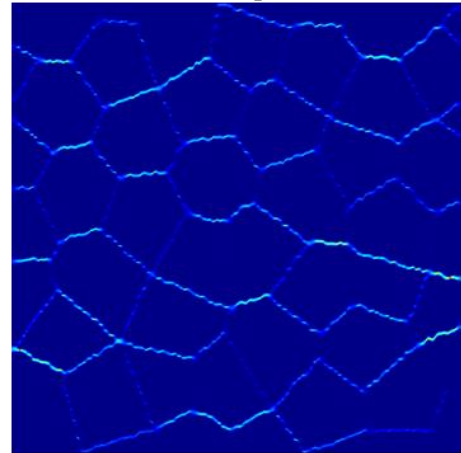
(a) Maximum amplitude = 0.05 cm



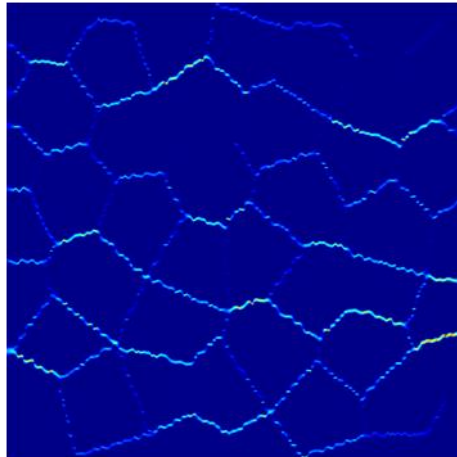
(b) Maximum amplitude = 0.10 cm



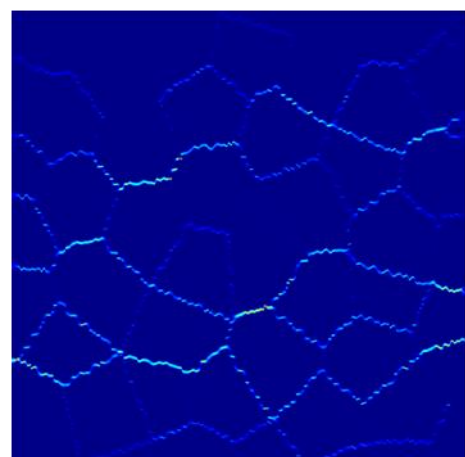
(c) Maximum amplitude = 0.15 cm



(d) Maximum amplitude = 0.20 cm



(e) Maximum amplitude = 0.25 cm



(f) Maximum amplitude = 0.30 cm

Figure 5.16 Velocity distribution of fluid flow in fracture network under different maximum amplitude through LBM simulation.

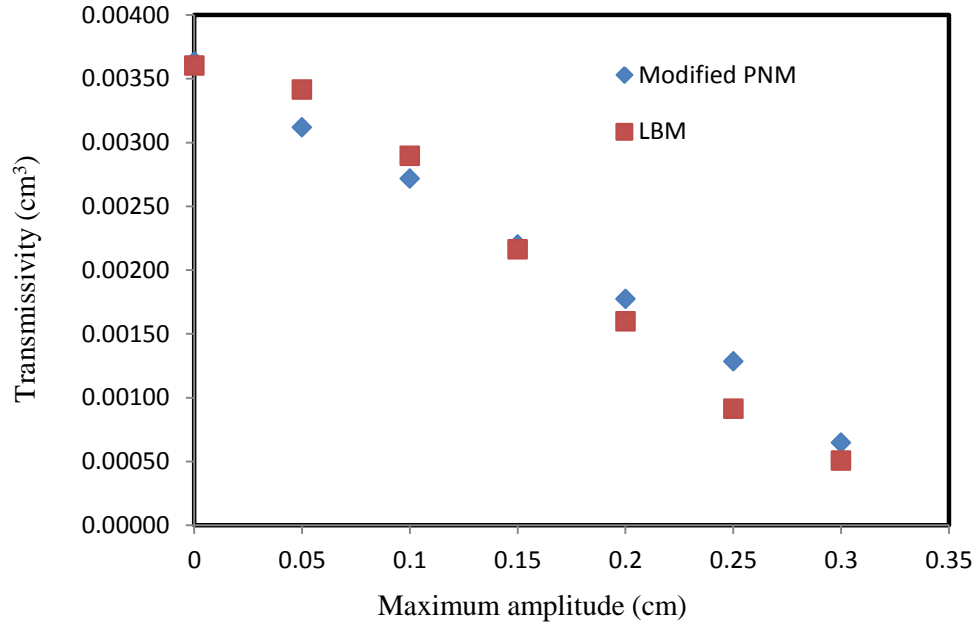


Figure 5.17 Simulation results of fluid flow in fracture network involving roughness.

It is necessary to mention that, the velocity distribution in the single fracture can be simulated directly in the LBM (Figure 5.16), whereas only the flow rate in the pipe network can be obtained for its macroscopic description. The simulation results from both models are summarized in Figure 5.17. Meanwhile, it is found that the simulation result from LBM is close to the computed transmissivity from pipe network model under cubic law assumption when no roughness is presented in the fracture network (amplitude=0), which shows the ability of LBM in dealing with the fracture network flow problems. Furthermore, the proposed two coefficient equation can be employed directly into the pipe network model to represent the roughness effect, which can produce reasonable results through the comparison to the LBM.

5.5 FLUID FLOW IN DISCRETE FRACTURE NETWORK MODEL (DFN) UNDER DEFORMATION

In the conventional methods that involve the discrete fracture network, it is always necessary to implement the block cutting before the flow simulation, the detection of the topology of fracture network as well as the isolated or dead-ends is a complex process. In contrast, the block cutting is not a problem for LBM, the isolated and dead-ends of fractures are naturally detected because they have no contribution to the flow at the micro scale. Meanwhile, it is always difficult or impossible to characterize the flow under large deformation, such as sliding, block rotation, aperture opening or closing, which may change the topology of the fracture network. For example, the existing flow channels may disappear during aperture closing, and the new flow channel may generate, which are not easy to be detected directly by using conventional method. In this section, the interconnectivity of fracture network and the anisotropic flow due to deformation is investigated by using LBM.

5.5.1 Fluid flow in DFN

According to the work conducted by Long et al (1982), the interconnection is dominated by the fracture density and fracture extent or size. To verify this, the fluid flow in the stochastic DFN is numerically simulated by using LBM. The geometry parameters of DFN are presented in Table 5.5. The location of the fracture and the orientation is uniformly distributed, and the aperture is set as 0.3 cm.

Table 5.5 Parameters of DFN models.

Block size, cm	Density, /cm ²	Fracture Length, cm		Aperture, cm	
		Mean	Standard deviation	Mean	Standard deviation
20.0×20.0	0.4;0.6;0.8	4;5;6; 7;8	20% of the mean value	0.3	0

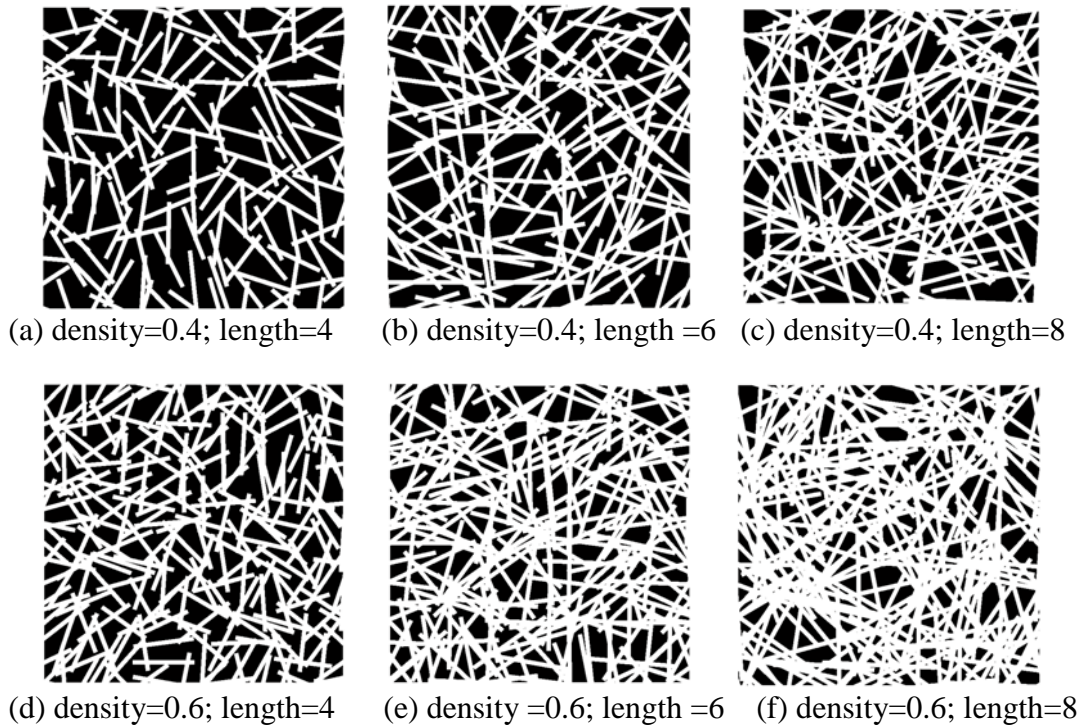


Figure 5.18 DFN models with different fracture densities and lengths.

The generated DFN model is imported LBM with a resolution of 100 l.u./cm so as to obtain relatively accurate results. Examples of the DFN models with different density and fracture length are shown in Figure 5.18, where the black is the solid matrix, and the white is the flow channel. The pressure boundaries are set at the left inlet and right outlet. The velocity distribution is shown in Figure 5.19, it is clear that the there is no flow in the isolated fractures and dead-ends of fractures.

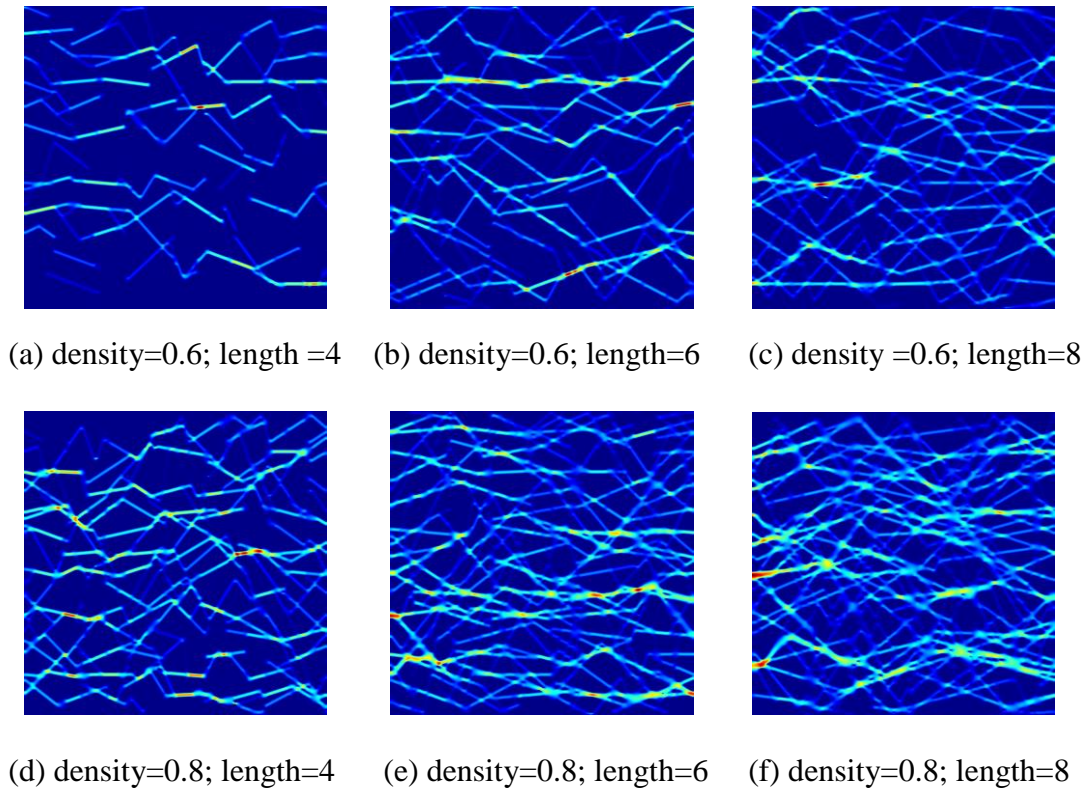


Figure 5.19 Velocity distributions in DFN from LBM simulations.

The flow rate of DFN model under different mean length and density in Table 5.5 is calculated. All the simulation results from LBM are shown in Figure 5.20. It is clear that, the larger density and longer length, the higher flow rate or degree of interconnection of the fracture network. In this part, we adopt the length-density parameter LD introduced by Long et al. (1982) to summarize the results, which is shown in Figure 5.21. The fracture network with larger LD tends to have higher flow rate and degree of interconnection. However, the fracture network have the same LD may behave differently from each other as indicated in the red rectangle in Figure 5.21. Therefore, it is necessary to explore the mechanism behind this. We keep the LD constant as 1.5 cm, 2.0 cm and 2.5 cm, the fracture density varies from 0.1 to 0.8. The simulation results are shown in figure 5.22. It is notable that, under smaller LD, e.g. at LD=1.5 cm, the

fracture network with longer fracture and lower density will have higher flow rate and degree of interconnection. However, at larger LD, e.g. with LD = 2.5 cm, the flow rate increases with the fracture density to certain point and then decrease.

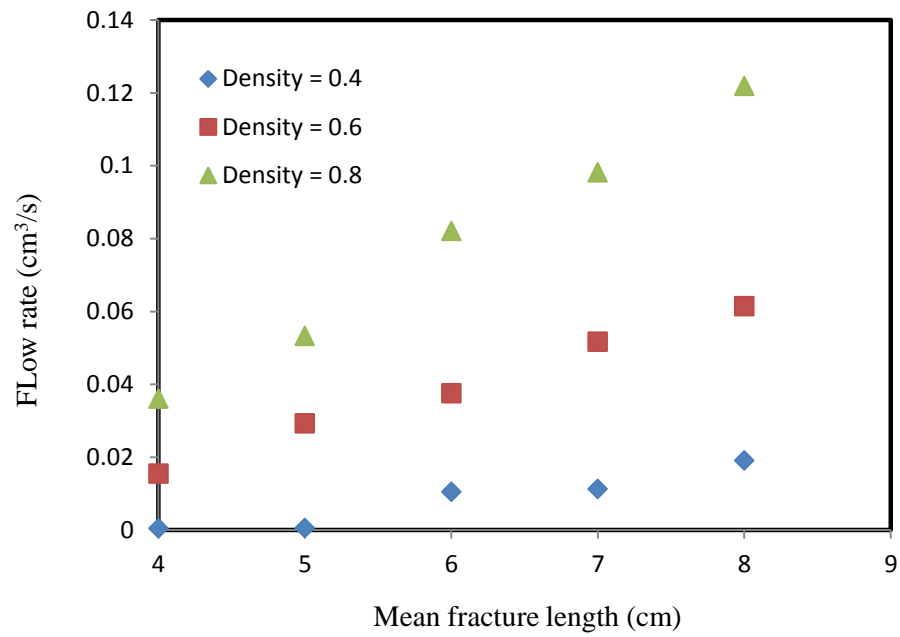


Figure 5.20 Dependence of flow rate on mean fracture length and density.

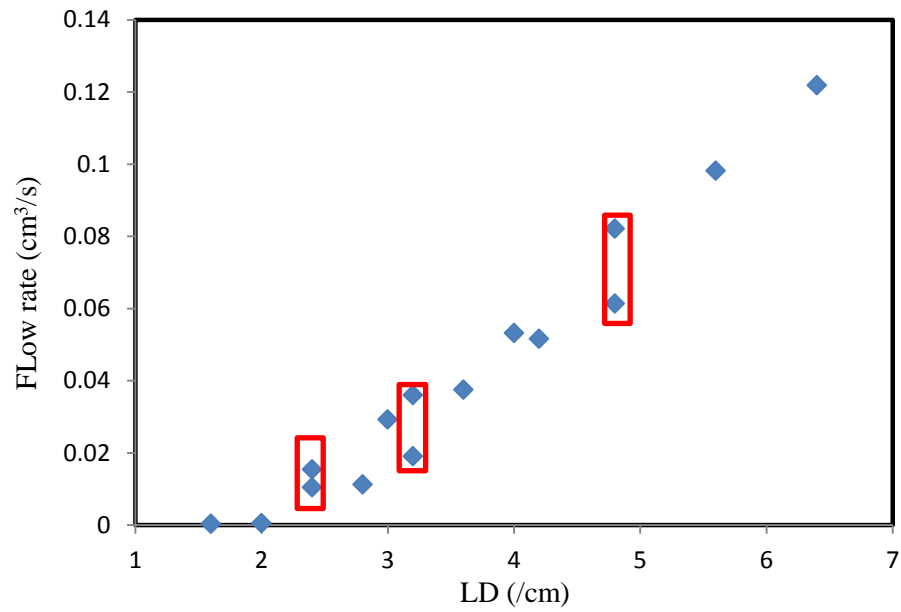


Figure 5.21 Relationship between LD and flow rate.

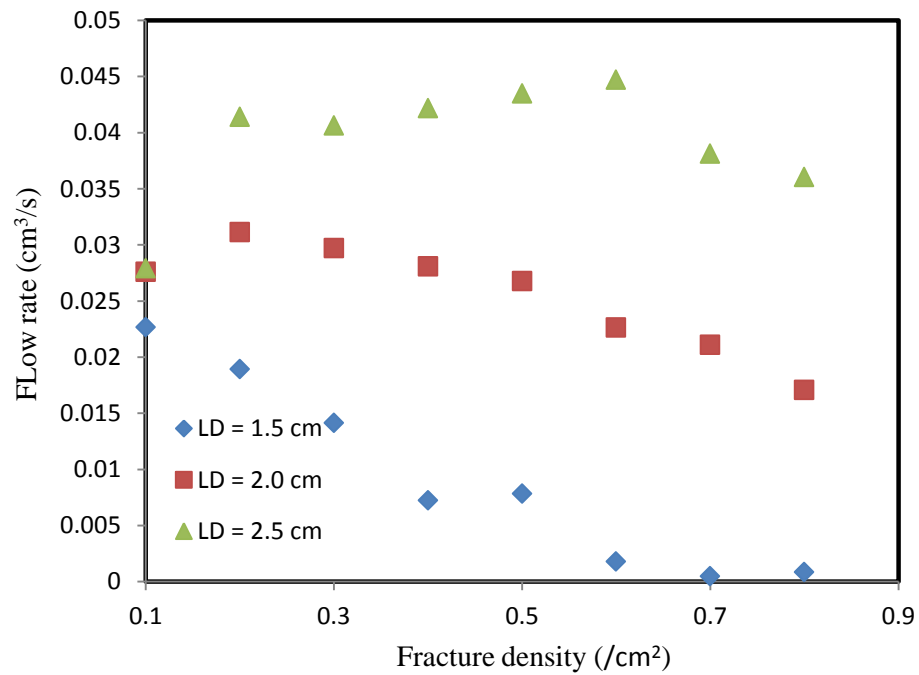


Figure 5.22 Relationship between fracture density and flow rate under different LD.

5.5.2 Indirect coupling between LBM and DEM

Hydro-mechanical coupling is an important consideration in fractured rock mass for rock mechanics and hydrogeology applications. A large number of attempts are conducted to investigate the influence of stresses on permeability of fracture network. The key factors that affect the flow behavior in fracture network include opening, closure, sliding and dilation. For example, Min et al. (2004) conducted the simulation on fluid flow through DFN under stress condition. It is found that, the stress ratio is the main reason for dilation and the permeability of fracture network increases with the stress ratio under certain circumstances.

In this part, an indirect hydro-mechanical coupling is conducted by using DEM and LBM. The "indirect" coupling means that, the applied stress won't produce the change in fluid pressure, and vice versa. Numerous works have been conducted in the study on stress-deformation relationship of the fracture network, which is not our key consideration. This work mainly focuses on the ability and advantage of LBM in characterizing the anisotropic flow behavior of rock masses under uniaxial deformation. To implement this, the stochastic DFN model is firstly generated in rock mass as shown in Figure 5.23(a). The displacement boundaries are set at the top and bottom with constant velocity of 0.01 m/s. Detailed configuration of the mechanical model in UDEC (DEM) can be found in the work by Kazerani and Zhao (2010). The geometry of fracture network is updated under certain axial strains. In order to characterize the anisotropic behavior, the conductivity in fracture network is measured in different directions. Figure 5.23(b) shows the flow region chosen with angle of θ with respect to the horizontal plane.

The LBM simulations are conducted on the deformed DNF models produced by UDEC, and the conductivity is measured relative to the orientation of the flow region. In each of the flow model, the aperture closure and opening due to mechanical displacement is naturally detected, which has shown the advantage of LBM in dealing with the hydro-mechanical coupled problems.

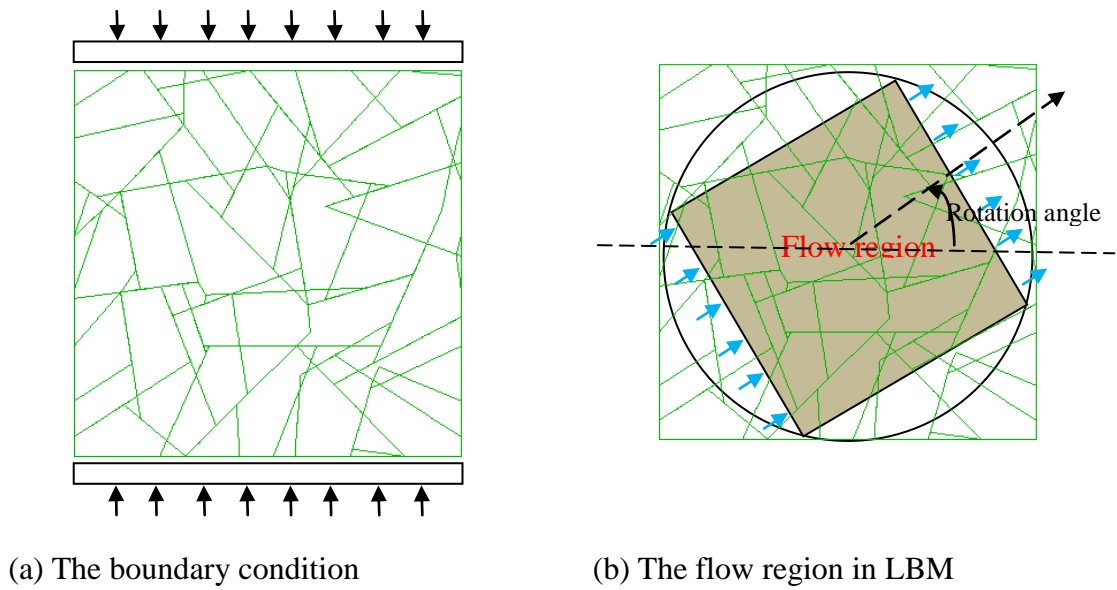


Figure 5.23 Implementation of "indirect" hydro-mechanical coupling.

The simulation results are presented in Figure 5.24 and the velocity distribution of different flow direction and axial strain can be clear observed. The transmissivity of flow regions under different axial strains are calculated, which is presented in Figure 5.25. It is clear that, at the initial state without any displacement, the fracture network behaves as a isotropic media. The anisotropic flow behavior is observed when the vertical displacement is applied on the rock mass. The transmissivity at the horizontal direction decreases with axial strain because of the decrease of aperture due to

compression. On contrary, the transmissivity increase as the axial strain increase which is induced by the aperture opening.

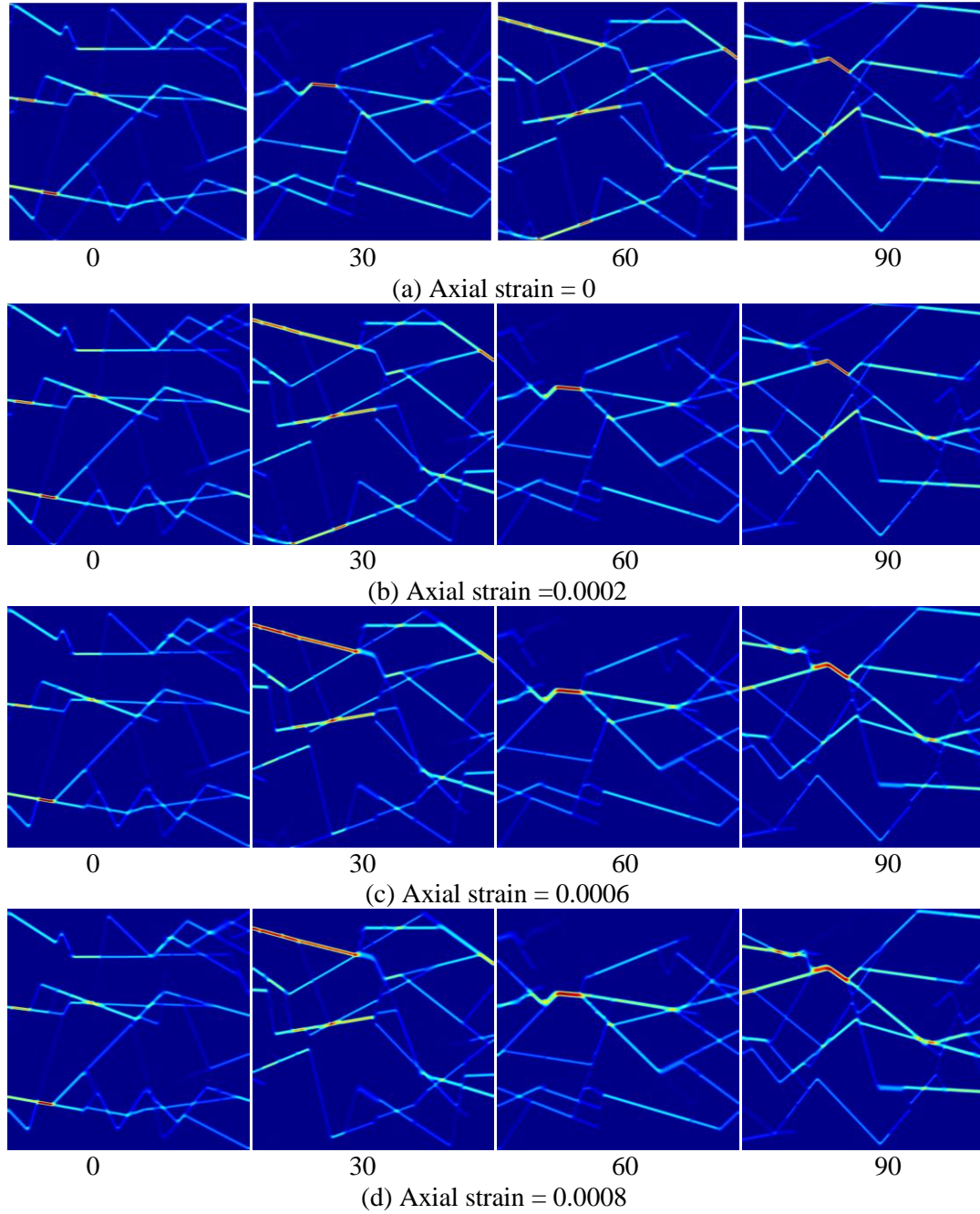


Figure 5.24 Conductivity of flow region with different orientation and axial strain.

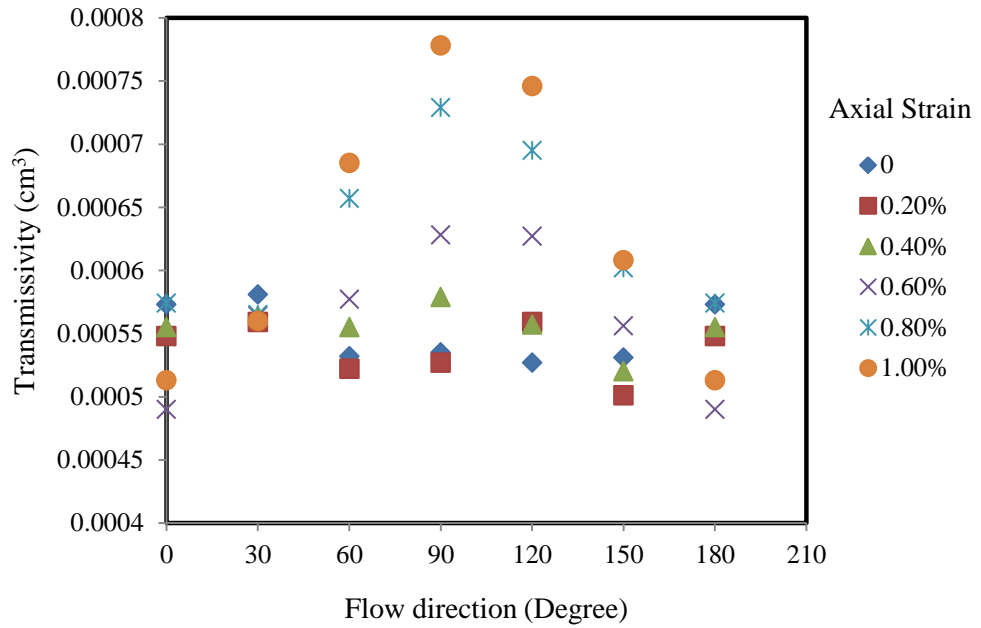


Figure 5.25 Transmissivity of flow region with different orientation and axial strain.

5.6 CONCLUDING REMARKS

The fluid flow through single rough fracture is extensively simulated in 3D through the LBM approach, which shows the ability of LBM in dealing with complex geometries. The two coefficients equation is proposed to characterize the flow behavior by considering both the roughness and displacements. The 2D fluid flows through fracture network are simulated by using LBM and the direct investigation of roughness effect on flow in fracture network is conducted. It is found that, the LBM and modified pipe network model could effectively take into account the roughness effect on fluid flow in fracture networks. Meanwhile, the interconnectivity of fracture network is investigated by LBM, and it is found that interconnectivity is dominant by the length density parameter and the correlation between the DFN parameter and transmissivity is analyzed. The 'indirect' hydro-mechanical coupled problem can be properly simulated

by combining the distinct element method and LBM. The difficulty of flow prediction under large deformation could easily be coped by LBM and the anisotropic flow behavior due to deformation is readily captured by the hydro-mechanical coupled analysis.

5.7 REFERENCES

- Andersson J., Dverstorp B. (1987) Conditional simulations of fluid flow in three-dimensional networks of discrete fractures. *Water Resources Research* 23(10): 1876-1886
- Baecher G.B., Lanney N.A. (1978) Trace length biases in joint survey. *Proceeding of 19th USSymposium on Rock Mechanics* 1:56-65
- Baecher G.B., Lanney N.A., Einstein H.H. (1977) Statistical descriptions of rock properties and sampling. *Proc. U.S. Symp. Rock Mech.*, 18th, SCI-I-SCI-B
- Bai M., Elsworth D., Roegiers J.C. (1993) Multiporosity/multipermeability approach to the simulation of naturally fractured reservoirs. *Water Resources Research* 29(6): 1621-1633
- Bandis S., Lumsden A.C., Barton N.R. (1981) Experimental studies of scale effects on the shear behaviour of rock joints. *International Journal of Rock Mechanics and Mining Sciences & Geomechanics Abstracts* 18(1):1-21
- Barenblatt G.E., Zheltov I.P., Kochina I.N. (1960) Basic concept in the theory of seepage of homogeneous liquids in fissured rocks. *Journal of Applied Mathematics (USSR)* 24(5):1286-1303

Barton N. (1973) Review of a new shear-strength criterion for rock joints. Eng Geol 7:287–332

Barton N.R., Bandis S., Bakhtar K. (1985) Strength, deformation and conductivity coupling of rock joints. International Journal of Rock Mechanics and Mining Sciences & Geomechanics Abstracts 22(3): 121-140

Batchelor G.K. (1967) An Introduction to Fluid Dynamics, Cambridge University Press, New York. 147-150

Batchelor G.K. (1967) An introduction to fluid dynamics. Cambridge University Press, New York

Bear J., Tsang C.F., Marsily G. de (1993) Flow and contaminant transport in fractured rocks. Academic Press, New York

Brown S.R., Scholz C.H. (1985) Broad bandwidth study of the topography of natural rock surfaces. J. Geophys. Res. 90(12): 575-12,582

Brown S.R. (1987) Fluid flow through rock joints: The Effect of Surface Roughness. J Geophys Res 92(B2):1337-1347

Brown S.R. (1989) Transport of fluid and electric current through a single fracture. Journal of Geophysical Research 94(B7):9429-9438

Chen M., Bai M., Roegiers J.C. (1999) Permeability tensors of anisotropic fracture networks. Mathematical Geology 31(4): 335-373

Dershowitz W.S., Einstein H.H. (1988) Characterizing Rock Joint Geometry with Joint System Models. *Rock Mechanics and Rock Engineering* 21: 21-51

Dershowitz W.S., La Pointe P.R., Doe T.W. (2004) Advances in discrete fracture network modeling. In: *Proceedings, US EPA/NGWA fractured rock conference, Portland*, pp 882–894

Eker E., Akin S. (2006) Lattice Boltzmann Simulation of Fluid Flow in Synthetic Fractures. *Transport in Porous Media* 65:363-384

Guo Z., Shi B. and Wang N. (2000) Lattice BGK model for incompressible Navier-Stokes Equation, *Journal of Computational Physics* 165:288-306.

He Y.L., Tao Y.J., Yang L.Z. (2010) Experimental research on hydraulic behaviors in a single joint with various values of JRC. *Chinese Journal of Rock Mechanics and Engineering* 29(Supp.1): 3235-3241

Huyakorn P.S., Lester B.H., Faust C.R. (1983) Finite element techniques for modelling groundwater flow in fractured aquifers. *Water Resources Research* 19(4):1019-1035

Iwai K. (1976) Fundamental studies of fluid flow through a single fracture. Ph.D. dissertation, University of California, Berkeley

Kazerani, T., Zhao, J. (2010) Micromechanical parameters in bonded particle method for modelling of brittle material failure. *International Journal for Numerical and Analytical Methods in Geomechanics* 34(18):1877–1895

Kim H.M., Ryu D.W., Tanaka T., Ando K. (2007) Hydro-geological descriptive model using discrete fracture network (DFN) in a site characterization for subsea tunnels construction. *Chinese Journal of Rock Mechanics and Engineering* 26(11):2217-2225

Koyama T., Li B., Jiang Y., Jing L. (2008) Coupled shear-flow tests for rock fractures with visualization of the fluid flow and their numerical simulations. *International Journal of Geotechnical Engineering* 2(3):215-227

La Pointe P.R., Hudson J.A. (1985) Characterization and interpretation of rock mass joint patterns. *Geological Society of America Special Paper* 199. Geological Society of America, 37pp.

Liu R., Jiang Y., Li B., Wang X., Xu B. (2014) Numerical calculation of directivity of equivalent permeability of fractured rock masses network. *Rock and Soil Mechanics* 35(8): 2394-2400

Lomize G.M. (1951) Flow in fractured rocks. Gosenergoizdat, Moscow (In Russian)

Long J.C.S., Billau D.M. (1987) From field data to fracture network modeling: an example incorporating spatial structure. *Water Resources Research* 23(7):1201-1216

Long J.C.S., Gilmour P., Witherspoon P.A. (1985) A model for steady fluid flow in random three-dimensional networks of disc-shaped fractures. *Water Resources Research* 21(8):1105-1115

Long J.C.S., Remer J.S., Wilson C.R., Witherspoon P.A. (1982) Porous media equivalents for networks of discontinuous fractures. *Water Resources Research* 18(3): 645-658

Long J.C.S., Witherspoon P.A. (1985) The relationship of the degree of interconnection to permeability in fracture networks, *J. Geophys. Res.* 90(B4):3087-3098

Louis C.A. (1969) A study of groundwater flow in jointed rock and its influence on the stability of rock masses. Res Rep 10, Imperial College, London

Min K.B., Rutqvist J., Tsang C.F., Jing L (2004) Stress-dependent permeability of fractured rock masses: a numerical study. *International Journal of Rock Mechanics and Mining Sciences* 41(7) :1191-1210.

Min K.B., Rutqvist J., Tsang C.F., Jing L. (2004) Stress-dependent permeability of fractured rock masses: a numerical study. *International Journal of Rock Mechanics and Mining Sciences* 41(7):1191-1210

Myers N.O. (1962) Characterization of surface roughness. *Wear* 5:182–189

Neuzil C.E., Tracy J.V. (1981) Flow through fractures. *Water Resources Research* 1(3):191-199

Ogilvie S.R., Isakov E., Glover P.W.J. (2006) Fluid flow through rough fractures. II: A new matching model for rough rock fractures. *Earth Planet. Sci. Lett.* 241:454-465

Parker B.L. (2007) Investigating contaminated sites on fractured rock using the DFN approach. In *Proceedings of 2007 U.S. EPA/NGWA Fractured Rock Conference: State of the Science and Measuring Success in Remediation*, September 24-26, Portland, Maine, Westerville, Ohio: National Ground Water Association.

- Pruess K., Wang J.S.Y., Tsang Y.W. (1990) On thermohydrologic conditions near high-level nuclear wastes emplaced in partially saturated fractured tuff: 2. Effective continuum approximation. *Water Resources Research* 26(6):1249-1261
- Quadros E.F. (1982) Determinação das características do fluxo de água em fraturas de rochas. Dissert. De Mestrado. Dept. of Civil Eng., Polytech. School, University of São Paulo
- Rasouli V., Hosseini A. (2011) Correlations developed for estimation of hydraulic parameters of rough fractures through the simulation of JRC flow channels. *Rock Mechanics and Rock Engineering* 44(4):447-461
- Rutqvist J., Stephansson O. (2003) The role of hydromechanical coupling in fractured rock engineering, *Hydrogeology Journal* 11:7-40
- Scesi L. (2007) Roughness control on hydraulic conductivity in fractured rocks. *Hydrogeology Journal* 15(2): 201-211
- Singhal B.B.S., Gupta R.P. (1999) *Applied Hydrogeology of Fractured Rocks*. Kluwer, Dordrecht, 400pp.
- Snow D.T. (1965) A parallel plate model of fractured permeable media. Ph.D. dissertation, 331 pp., Univ. of Calif., Berkeley
- Snow D.T. (1969) Anisotropic permeability of fractured media. *Water Resources Research* 5(6):1273-1289
- Tsang Y.W. (1984) The effect of tortuosity on fluid flow through a single fracture. *Water Resources Research* 20(9):1209-1215

Witherspoon P.A., Wang J.S.Y., Iwai K., Gale J.E. (1980) Validity of Cubic Law for fluid flow in a deformable rock fracture. *Water Resources Research* 16(6):1016-1024.

Xie H., Wang J.A., Stein E. (1998) Direct fractal measurement and multifractal properties of fracture surface. *Phy Lett A* 242(1-2): 41-50

Zhao Z.H., Li B., Jiang Y.J. (2013) Effects of fracture surface roughness on macroscopic fluid flow and solute transport in fracture networks. *Rock Mechanics and Rock Engineering* DOI 10.1007/s00603-013-0497-1

Zimmerman R.W., Bodvarsson G.S. (1996) Hydraulic conductivity of rock fractures. *Transport in Porous Media* 23(1): 1-30

Zou Q., He X. (1996) On pressure and velocity flow boundary conditions for the lattice Boltzmann BGK model. *Physics of Fluids* 9:1591–98

CHAPTER 6 NUMERICAL STUDY OF MULTIPHASE FLOW IN FRACTURED POROUS MEDIA USING LATTICE BOLTZMANN METHOD

In this chapter, the multiphase flow through fractured porous media is studied by using the multiphase LBM model. First of all, the multi-component and single-component Shan-Chen model are compared through the basic multiphase flow simulations, such as the flow patterns in single fracture, co-current flow and bubble flow around solid bar. It is found that the flow pattern is influenced by the degree of saturation and body forces. In the simulation of co-current flow, it is found that the SCMP model is more preferable in the study of two phase flow problem, especially in the water-air system. The MCMP model on the other hand cannot handle the multiphase flow with different viscosity and density. Moreover, the SCMP model produces more reasonable results compared with the MCMP model in the bubble flow problem. Then, the SCMP model is used to investigate the two phase flow in porous media. The body force for the simulation is calibrated and effect of wettability on two phase flow is studied. After that, the influence of fracture on two phase flow is studied. The trial of two phase flow in 3D reconstructed porous media is conducted and some suggestions are given at the end.

6.1 INTRODUCTION

There are variety of applications of multiphase flow in fractured porous media, such as petroleum engineering, mining engineering and geotechnical engineering. The multiphase flow problems have been investigated using various theoretical, numerical, and experimental approaches during the past half century. The early works on

multiphase flow focused on the laboratory measurement (Bear 1972). For example, Persoff and Pruss (1995) conducted the laboratory test to investigate the two phase flow in natural rough-walled rock fractures, the relative permeability was measured and the flow behavior was visualized. Hughes et al. (1996) designed and constructed the experiment on two phase flow in fractured porous media using the CT imaging. However, the experimental works are commonly expensive and time consuming, and it also has several limitations such as complexity of process and uncertainty in measurements. The theoretical analysis on the other hand, can provide the complementary understanding of the complex process in the two phase flow problem. E.g. the relative permeability of multiphase flow can be taken as the empirical function of saturation, but, the close form solution of the theoretical analysis is impossible especially under complex condition.

Alternatively, numerical approaches provide attractive solutions due to their advantages of low cost, high efficiency and repeatability. The numerical methods for multiphase flow can be classified into three groups: macro-scale methods and the micro-scale methods as well as the pore-scale methods. In the macro-scale approach, the continuity equations together with momentum and species balances are solved and constitutive equation such as extension of Darcy's law is utilized. However, the macro-scale approach cannot explain the processes at pore scale, e.g. the pore space geometry and topology as well as fluid property cannot be physically represented. The microscopic methods based on classical molecular dynamics, on the other hand, attempt to consider every atom or molecule within a system. However, the complexity increases rapidly with increasing problem sizes, which cannot be overcome even with today's fastest supercomputers. Apart from the methods at microscopic and macroscopic level, there

are considerable interests in the so-called pore scale methods, in which, the pore network model and lattice Boltzmann method have attracted the most attentions. The popularity of the pore scale method increases rapidly over the past 20 years because of the development of imaging technique, such as Micro X-ray computed tomography (CT) and Nuclear Magnetic Resonance (NMR), which makes the simulation more accurate and realistic. In both of the two models, the flow equation is solved at pore scale, the geometry and topology of the medium can be readily considered.

To be specific, the pore network model idealizes the geometry to some simple geometry, such that the essential features are adequately represented (Celia et al. 1995; Blunt 2001). This simplification allows us to simulate large domains with less computational effort but lead to loss of geometrical and topological information. In contrast, the LBM can solve equations in arbitrary pore space geometry and topology without simplification, for its ability to deal with complex boundary conditions as discussed in last chapter. Meanwhile, the parallel nature of programming and the development of high performance computation make it possible to simulate the fluid flow on a full voxel-based void domain. For example, the imaging data from CT or NMR can be used for the simulation directly, which provides a more scientific way to explain the physical and chemical process at micro scale. In addition, the LBM has the ability to simulate multiphase flow problem, in which, the fluid-surface interactions can be reasonably included and there is no need for the tracking of fluid interfaces. There were various types of LBM had been developed to study the multiphase flow problems (Pan et al. 2004, Huang et al. 2011), in which, the Shan-Chen LBM receives the most popularity because of its well-defined inter-particle potential and straightforward implementation. They are widely used to model the multiphase flow problems such as immiscible

displacement in channel, capillary phenomenon at tubes, fluid distributions as well as unsaturated flow through porous media.

Concerted efforts have been made over the past few decades to arrive at predictive capabilities for multiphase flow behavior of fractured porous media. However, the factors that influence the multiphase flow in fractured porous media are not clear. The objective of this research is to provide a more scientific and more convincing methodology for explanation of the underlying mechanism of multiphase flow in fractured porous medium based on the microstructure and fluid surface interactions. In this part, flow pattern in single fracture is firstly investigated. Then, the ability of LBM in dealing with multiphase process is firstly validated through the comparison with analytical solution of two phase annular flow. After that, the multiphase flow in fractured porous media is numerically studied.

6.2 COMPARISON OF THE SHAN-CHEN SCMP AND MCMP MODEL IN TWO PHASE FLOW PROBLEMS

The theoretical background and basic concept of Shan-Chen model has been introduced in Chapter 4. It was used to realize the complete range of contact angle and to investigate the multiphase static equilibrium distribution. Meanwhile, the influence of geometry and degree of saturation on fluid distribution was investigated. In this section, we focus on the dynamic multiphase flow problems. It is expected to provide a fundamental explanation on how the two phase flow in fractured porous media and investigate how the geometry and fluid-solid interaction influence the two phase flow.

Firstly, the two multiphase modes are compared by implementing basic flow problems, such as flow pattern, co-current flow validation, bubble flow around solid surface.

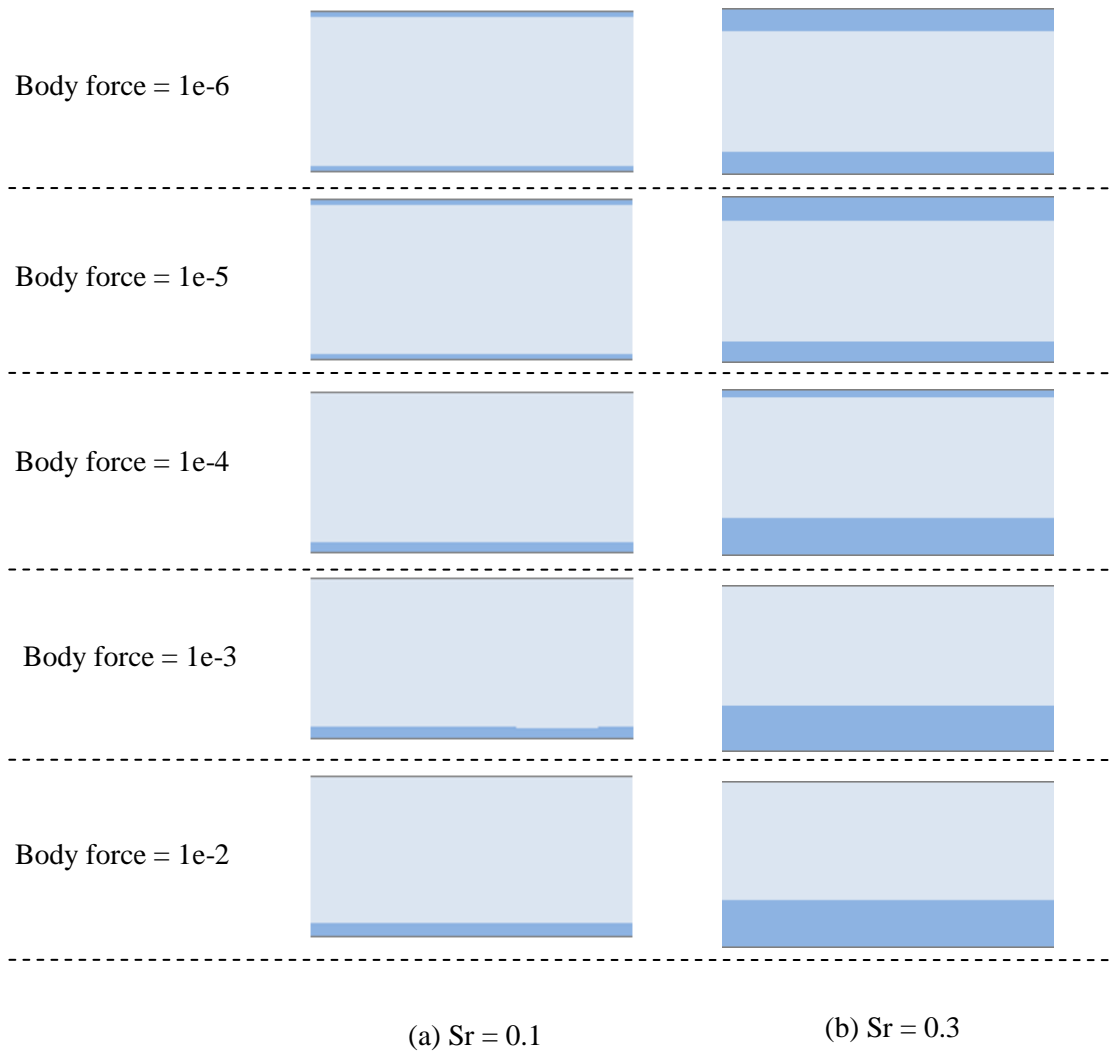
6.2.1 The two phase pattern in single fracture

The analytical solution of the two phase flow is available only if the pattern is known and regular. For example, the analytical solution of co-current two phase flows is readily available if the properties of the fluids are known. Other researchers, for example, Indraratna et al. (2003) assumed that the flow pattern is to be the stratified flow so that the two phase flow problem can be readily simulated. In reality, the two phase flow can be separated or mixed. There is no general equation that could incorporate any types of flow because of the impossibility of direct observation of the flow pattern and the irregularity of the fluid interface. Therefore, it is fairly important to investigate the flow pattern from numerical approach.

The Shan-Chen SCMP model is firstly used to investigate the two phase pattern at different degree of saturation and different body forces. The parameters used in the model are same as introduced in chapter 4. All the simulations are initialized with random distributed two-phases between the solid surfaces. The body force is imposed on both the water and air after the equilibrium distribution is approached. To evaluate effect of body force on two phase pattern in single fracture, periodic boundary is applied at horizontal direction and the body force is applied perpendicular to the flow channel changes from $1e-6$ to $1e-2$. The two phase patterns at different degree of saturation and different body forces are presented in Figure 6.1.

It is obviously that when the body force is less than $1e-4$ and degree of saturation is less than 0.5, the concurrent flow pattern can be observed, in which the wetting phase film is attached to the wall and the non-wetting phase is in between the films. When the body force is larger than $1e-4$ and degree of saturation is less than 0.5, the stratified pattern is obtained with the heavier phase at the bottom and the light phase at the top. However, at high degree of saturation, that is larger than 0.5, the non-wetting bubbles are generated within and the curved interface is produced because the presence of the surface tension. Meanwhile, the shape and location of the bubble is influenced by the magnitude of the body force.

Similar simulations are conducted using the Shan-Chen MCMP model, the simulation results are presented in Figure 6.2. It is clear that the two phase distributions in MCMP model are different from the SCMP model. That is because the Shan-Chen MCMP model is limited to the two components with identical density and viscosity which will be discussed in next section. Therefore, the flow in MCMP model can not classified as two phase flow (e.g. water-air flow), and the effect of body force won't have the same effect as that in the SCMP model. Similar phenomenon can also be observed in the MCMP simulation, that the co-current pattern shows up at low degree of saturation and the bubbles are generated at high degree of saturation.



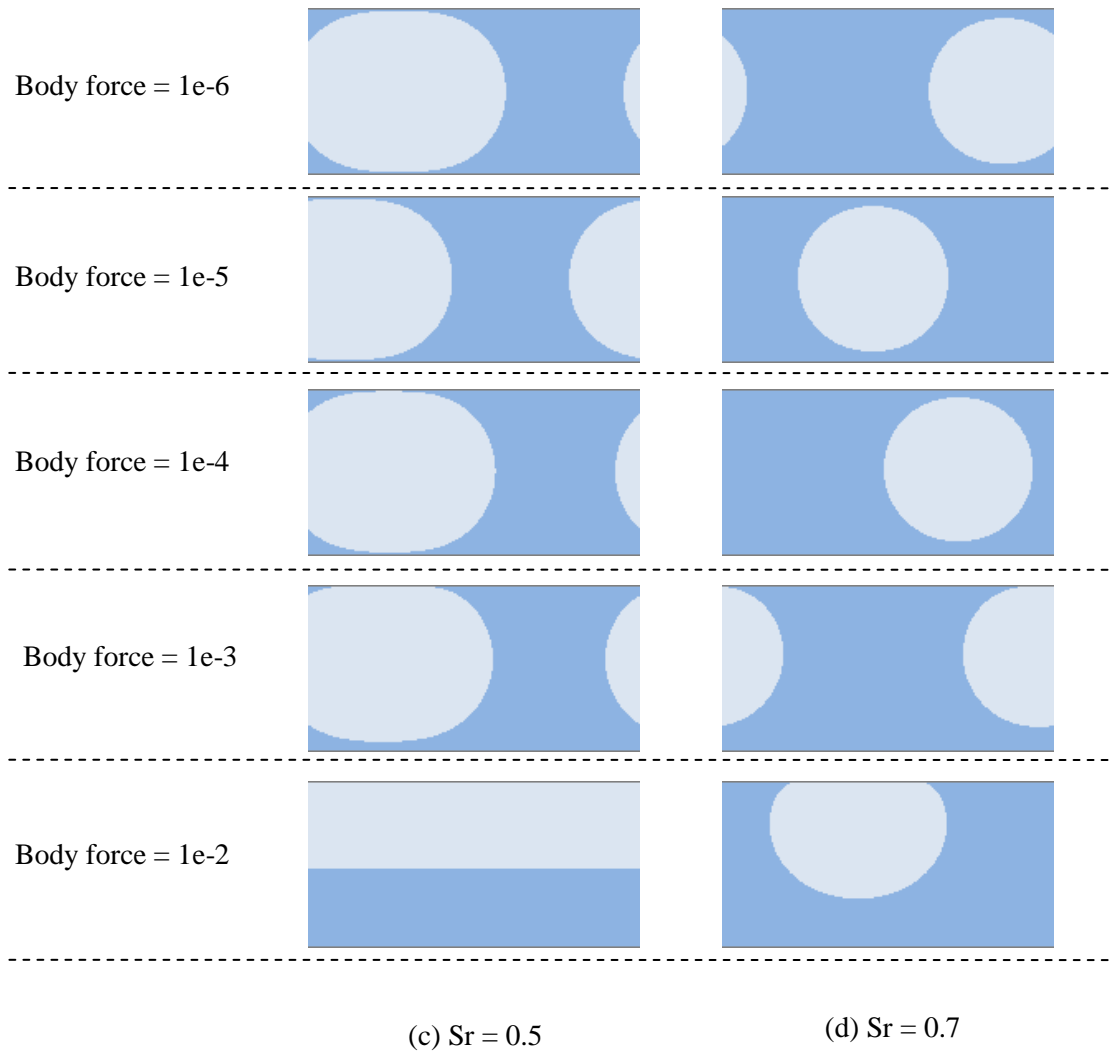


Figure 6.1 Effect of body force on two phase distribution at different degree of saturation using Shan-Chen SCMP model.

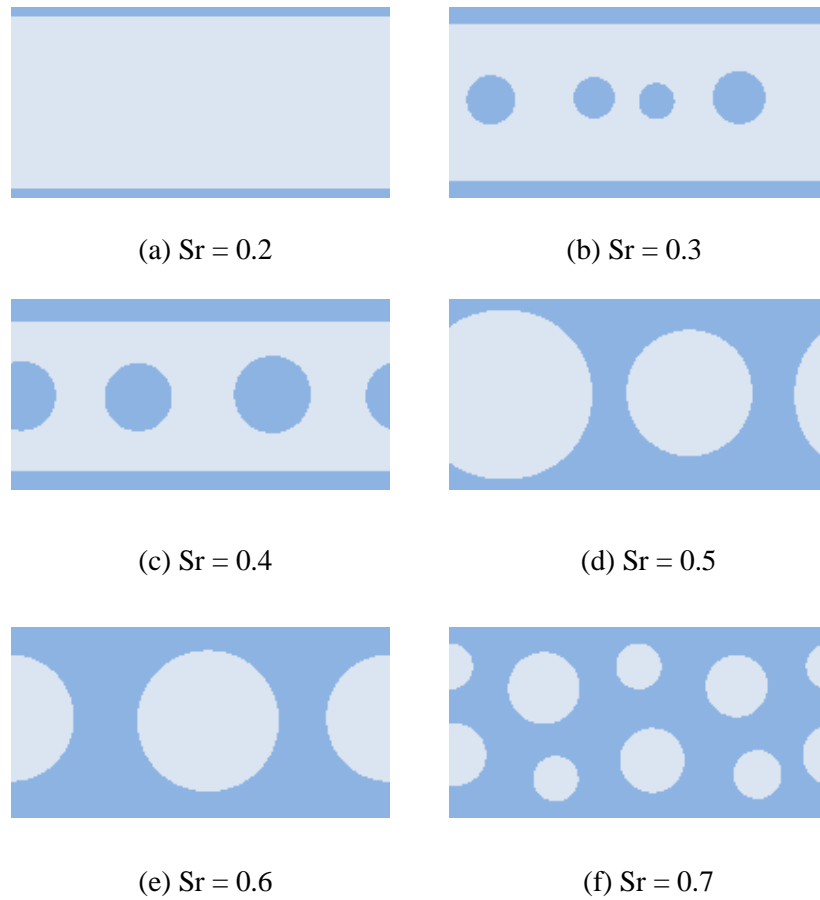


Figure 6.2 Flow patterns at different degree of saturation using Shan-Chen MCMP model.

6.2.2 Validations of co-current flow

It is discussed in last section that, the analytical solution is known if the flow pattern is known and regular. For a typical two phase annular flow, the wetting phase moves along the solid surface and the non-wetting phase flow in the center of the wetting films as shown in Figure 6.3. The analytical solution for the velocity profile is

$$u_x = \begin{cases} \frac{\Delta F}{2\mu_w}(b^2 - y^2) & a < |y| < b \\ \frac{\Delta F}{2\mu_w}(b^2 - a^2) + \frac{\Delta F}{2\mu_{nw}}(a^2 - y^2) & 0 < |y| < a \end{cases} \quad (6.1)$$

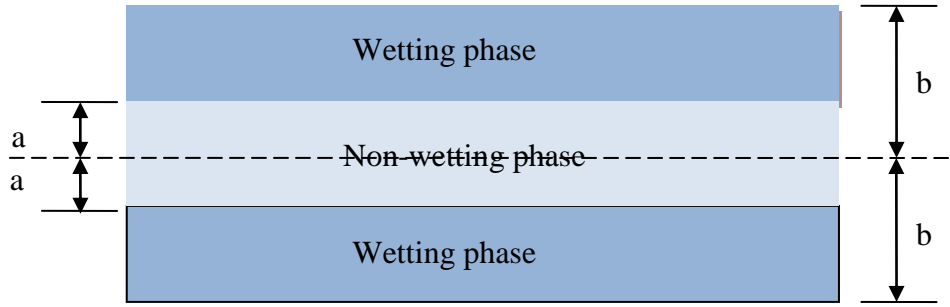


Figure 6.3 Flow pattern of two phase co-current flow.

In this section the two LB models are validated by comparing the simulation results with the analytical solution.

Firstly, the simulation by SCMP model is implemented. In the SCMP Shan-Chen model, the equation of state is essential, which has great influence on the pressure and surface tension. According to He and Doolen (2002), the non-ideal EOS for SCMP model is described as,

$$P = \rho RT + \frac{GRT}{2} [\psi(\rho)]^2 = \frac{\rho}{3} + \frac{G}{6} [\psi(\rho)]^2 \quad (6.2)$$

Different EOS can be incorporated in SCMP model by choosing different interaction potential (Shan and Chen 1993,1994, Qian et al. 1995, Martys and Chen 1996, Yuan and Schaefer 2006). In this simulation, the EOS proposed by Shan and Chen (1994) is used,

$$\psi(\rho) = \psi_0 \exp(-\rho_0 / \rho) \quad (6.3)$$

where ψ_0 and ρ_0 are arbitrary constants.

By using the same parameters as chapter 4, $G = -120$, $\psi_0 = 4$ and $\rho_0 = 200$, and substitute equation 6.3 to equation 6.2, the pressure-density relationship of SC EOS is shown in Figure 6.3. It is clear that, the two phases can coexist in the system at the same pressure, e.g. point A and B.

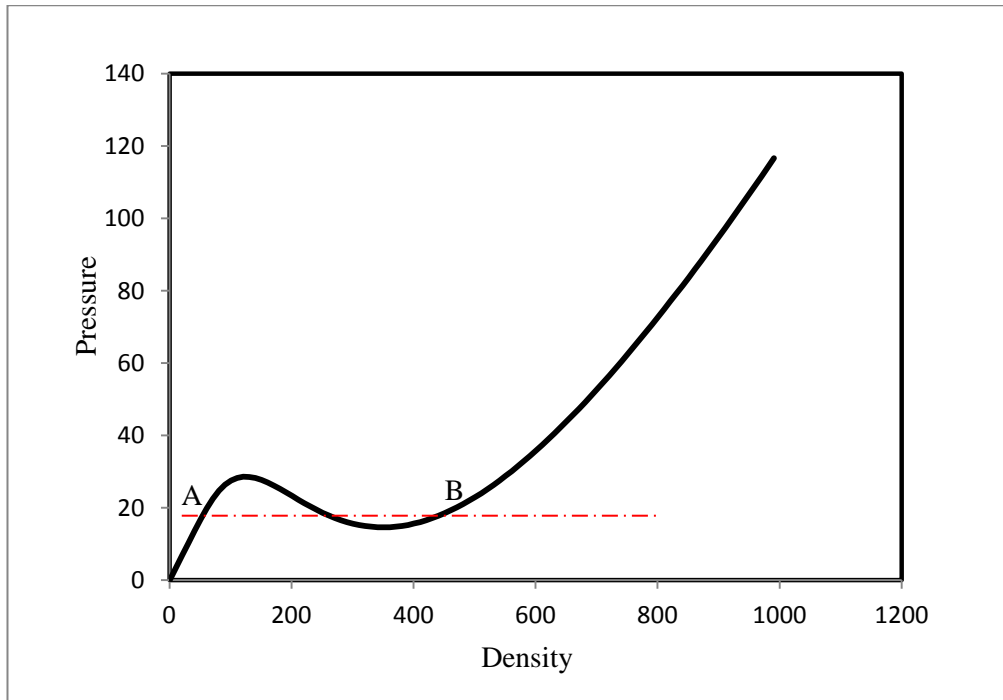


Figure 6.4 Equation of state from Shan and Chen (1994).

This equation of state has been successfully used in the estimation of the surface tension, realization of different contact angle and fluid distribution ((Lu et al. 2008, Yin and Gao 2015).

For the two phase co-current flow (Figure 6.3), there is no surface tension at the fluid interface, which means that the pressures in wetting phase and non-wetting phase are the same. Therefore, the density of wetting phase is chosen as $\rho_w = 524.0$ in the liquid region and the density of non-wetting phase is set as $\rho_{nw} = 85.44$ in the gas regions accordingly.

Meanwhile, in LBM simulation, the relaxation parameter τ is set as 1 for sake of numerical stability and the kinetic viscosity in is calculated as $\nu = (2\tau - 1)/6 = 0.167$ for both phases. Therefore, the viscosity of the wetting phase and non-wetting phase are calculated as $\mu_w = \rho_w \nu$ and $\mu_{nw} = \rho_{nw} \nu$ respectively.

To implement the co-current flow, the length and width of the fracture are set as 100 l.u. and 200 l.u. respectively. The distant from the non-wetting boundary and center line is set as $a = 50$ (Figure 6.5a).

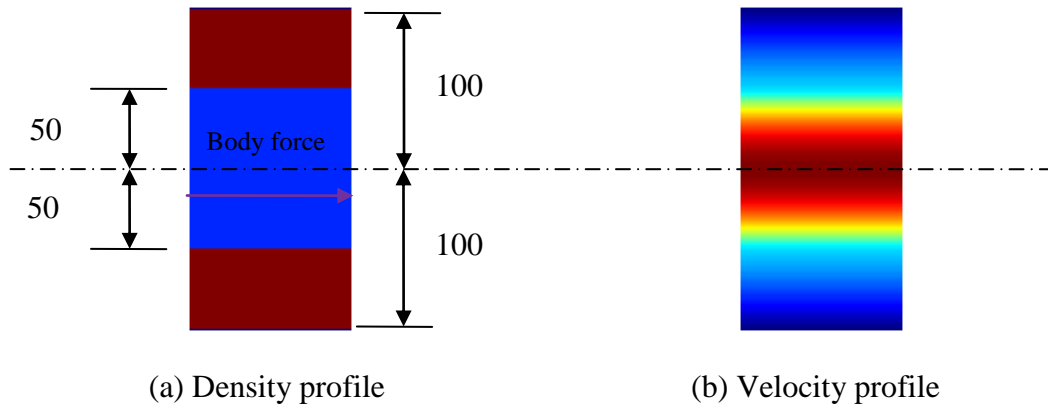


Figure 6.5 Implementation of the co-current flow in SCMP model.

The periodic boundary condition is set at the left inlet and right outlet and the bounce back is set at the top and bottom surface. By introducing the body force of $1e-2$ in the simulation, the steady state flow can be reached (Figure 6.5b) which is compared with the analytical solution as shown in figure 6.6.

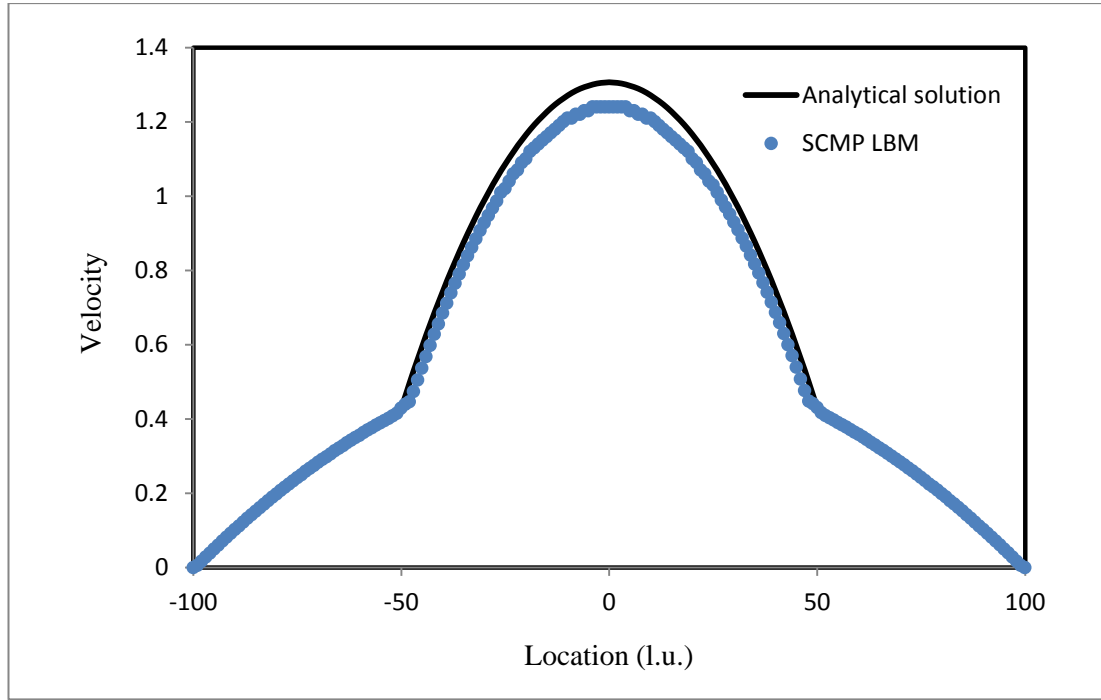


Figure 6.6 Velocity profile from SCMP model.

It is found that, the viscosity coupling of two flow problems can be reasonably simulated. Meanwhile, the velocity profile in the wetting phase matches the analytical solution well, and in the non-wetting part, the velocity is slightly lower than that of the analytical solution with error of 5%, which is acceptable.

Similar simulation is implemented in the MCMP model. The densities are set as 1 for both components, the viscosity ratio is adjusted through the relaxation time τ . In case 1, the relaxation time is set as 1 for both of the fluids. In case 2, the relaxation time is set

as 2 and 1 for wetting and non-wetting respectively, which leads to the viscosity ratio of 3.

It is clear that, the simulation result matches the analytical solution under viscosity ratio of 1 (Figure 6.7). However, in the case of viscosity ratio equals to 3, the large velocity discontinuity is observed at the interface, and the interface moved to the location rather than its original place (Figure 6.8a). Moreover, by analyzing the fluid density of the two components, it is found that, the density of wetting phase become larger and the non-wetting density get smaller with a density ratio around 2 which is different from its original values (Figure 6.8b). Therefore, it is concluded that, the Shan-Chen MCMP model is not suitable for the simulation of the viscosity ratio rather than 1 and it cannot used to simulate the water-air system.

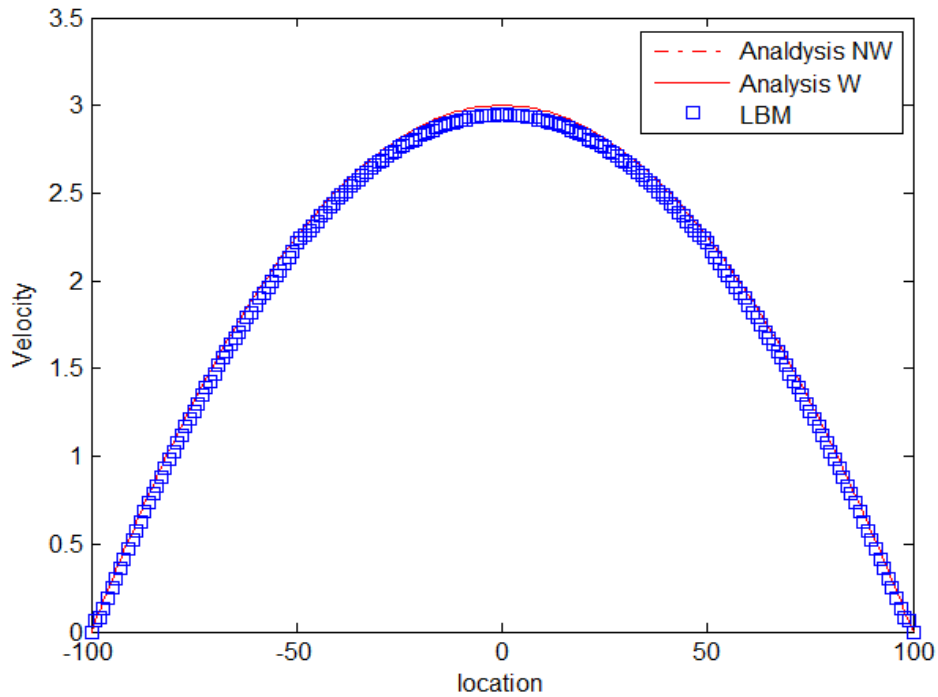
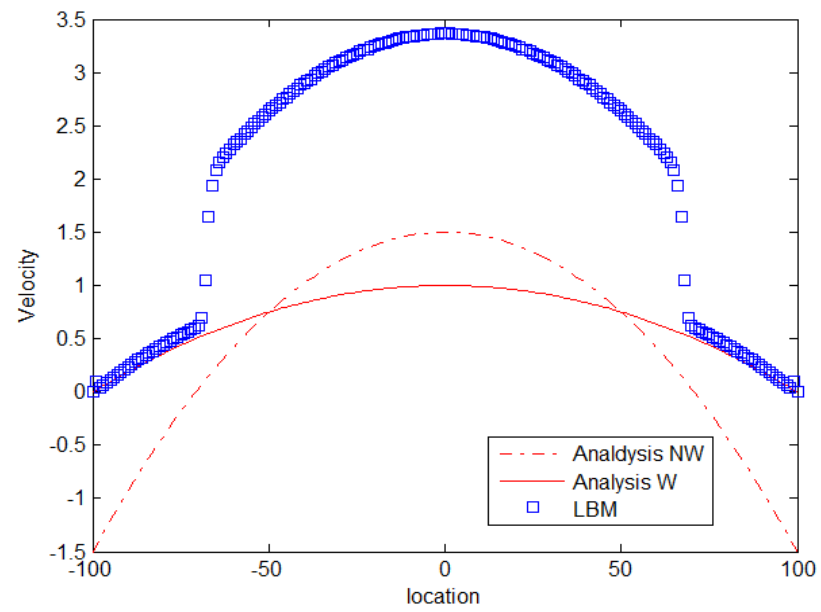
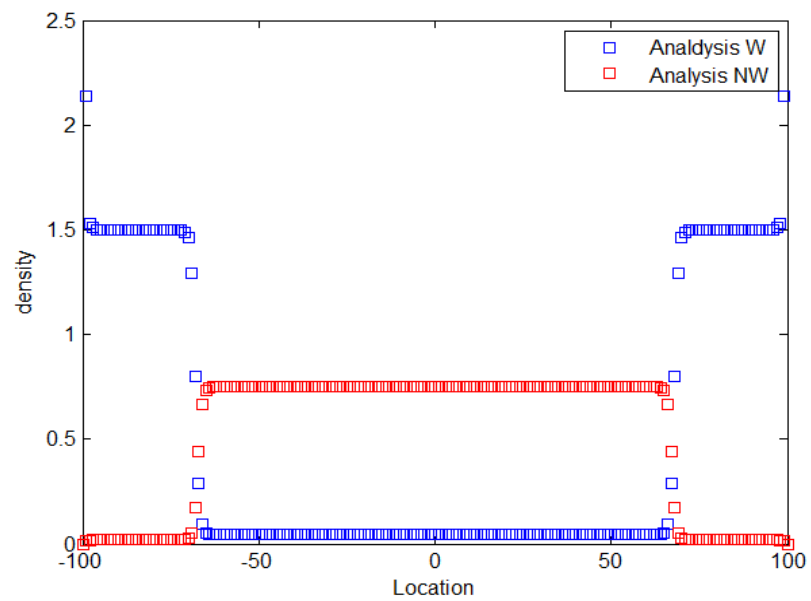


Figure 6.7 Velocity profile from MCMP model with viscosity ratio = 1.



(a) The velocity profile



(b) The density profile

Figure 6.8 Velocity and density distribution from MCMP model with viscosity ratio = 3.

6.2.3 Bubble flow around a solid surface

In this section, we are trying to explore the difference of the two model in simulating two phase flows with solid surface present in the flow region. As shown in Figure 6.9, the non-wetting bubble (blue) is surrounded by the wetting fluid (red), and the solid bar is assigned in front of the bubble. Periodic boundary is set from left to right, and the top and bottom are set as the solid surface as well.

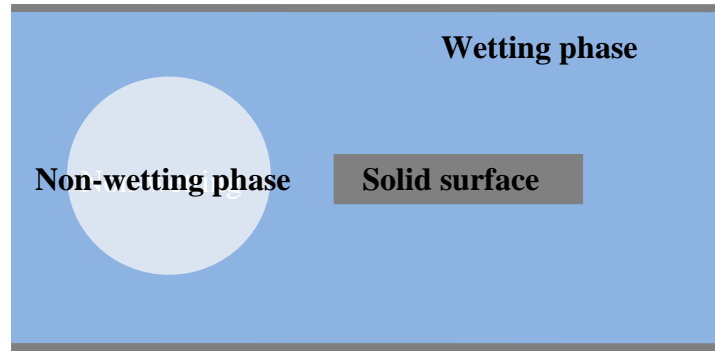


Figure 6.9 Setup of the bubble flow.

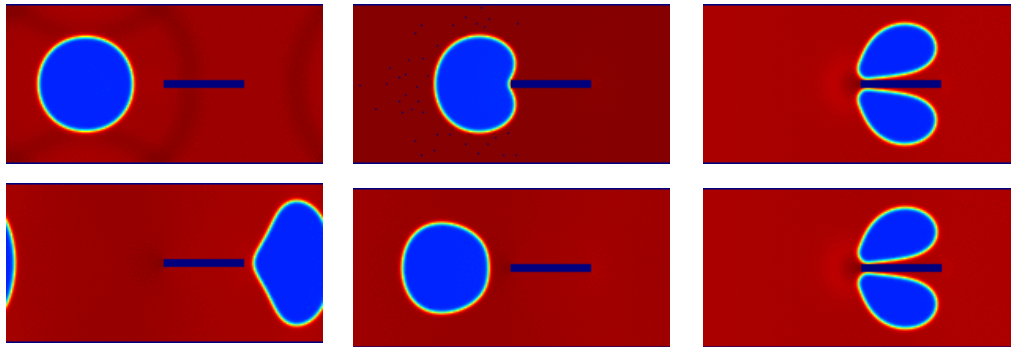
It is found that the two models present different behavior of a bubble flow across a solid bar. In the SCMP model (Figure 6.10a), the bubble separates when across the solid bar, and the separated bubbles merge together to a single bubble after the bar. This phenomenon is consistent with the theory based on the analysis of Yong-Laplace equation,

$$\Delta P = P_{inside} - P_{outside} = \frac{2\gamma}{R} \quad (6.4)$$

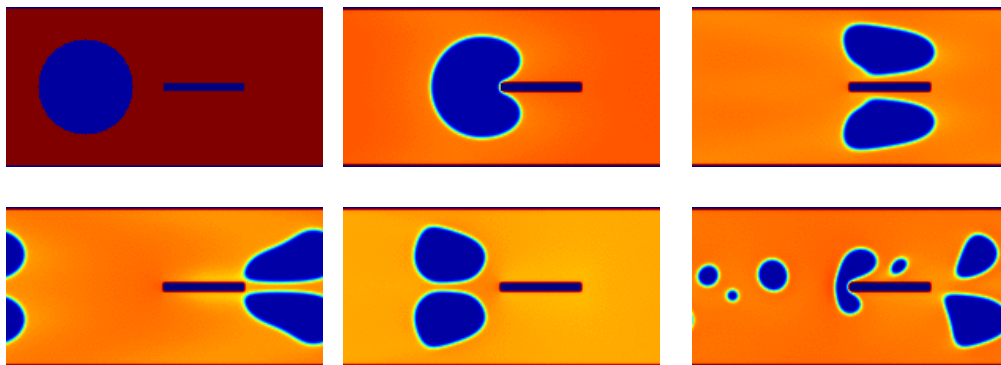
where P_{inside} and $P_{outside}$ is the pressure inside and outside of the bubble respectively, γ is the surface tension and R is the radius of the bubble.

At equilibrium condition, the parameters in equation 6.4 are constant. When the bubble separates, the radius decrease which lead to the non-equilibrium. Therefore, the separated bubble has to be expanded to approach the Yong-Laplace equation, which leads the bubble merge as observed in Figure 6.10a.

However, in the MCMP model (Figure 6.10b), the phenomenon observed is complete different from the SCMP model. At early stage, there are two bubbles generated behind the solid surface, after 60000 steps of iteration, the complex flow pattern is observed, which cannot reasonably explained according to the analysis. That is because in MCMP, the bubble splits when passing around the solid bar. The two bubbles are not symmetry about the center line which will break down and present an instable behavior.



(a) Simulation result from SCMP



(b) Simulation result from MCMP

Figure 6.10 Time evolution of bubble flow across the solid bar.

Based on the simulation results of the basic flow problems, it is found that, the SCMP model is more appropriate for investigation of the multiphase flow problems especially in the water-air co-exist system. Therefore, in the following sections, the SCMP model is used to study the multiphase flow in fractured porous media.

6.3 TWO PHASES FLOW IN POROUS MEDIA

The problem of two phases flow in porous media has been a research topic for half century. The Darcy's extended law is widely used to characterize the two phase flow behavior.

$$q_i = -\frac{k_{ri}k}{\mu_i} \nabla P_i \quad i = \text{wetting phase, nonwetting phase} \quad (6.5)$$

where q_i is the flux, k_{ri} is the relative permeability, μ_i is the viscosity, k is the absolute permeability and ∇P_i is the pressure drop.

However, this macroscopic description has difficulties in accounting the complex process in the microstructure. In this part, the two phase flow in porous media is numerically investigated using the Shan-Chen SCMP model.

6.3.1 Setup of the simulation

In order to have a basic understanding of two phase flow in porous media, the media has to be isotropic and homogeneous so that to reduce the effect of microstructure. Therefore, the ordered particles with radius of 50 l.u. are generated in the regions of 500 l.u.×500 l.u. as shown in Figure 6.11a, where the gray is the particle and white is the

pore space. In order to produce the interconnected porous media, the radius is reduced to half of its original value (Figure 6.11b)

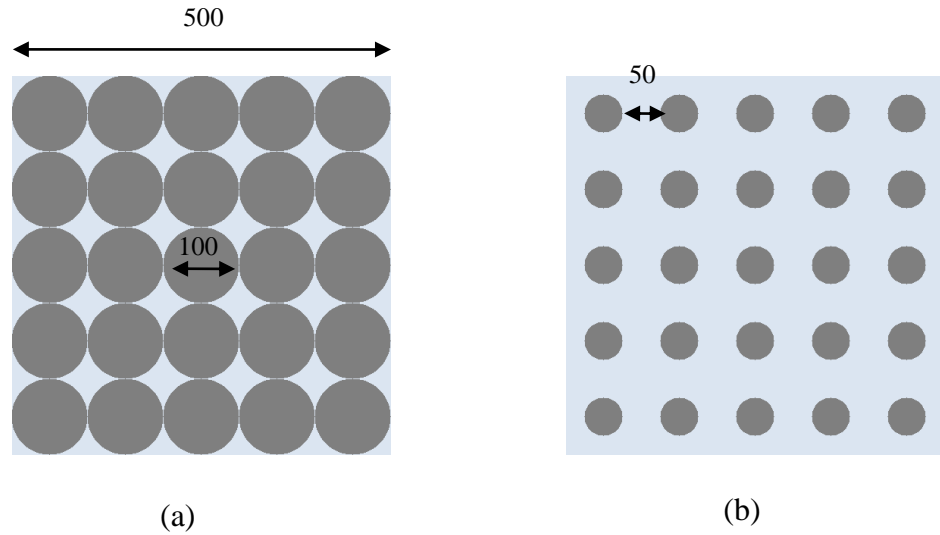


Figure 6.11 The isotropic and homogeneous porous media.

In the simulations, the density and the parameters control the surface tension and contact angle are set the same as Chapter 4. The periodic boundary condition is applied at both the horizontal and vertical direction, and the no-slip (bounceback) boundary is set at the particles. Initially, the liquid phase and gas phase are randomly distributed in the pore space. When the system approaches the equilibrium distribution, the body force is applied along the horizontal direction.

Theoretically, the Shan-Chen model is a diffuse interface model, which imposes the smooth transition between phases, and the interface is diffused over a few lattice units. Therefore, the post-processing of LBM should be taken carefully because of the presence of interface. To explain this, the equilibrium condition at degree saturation of 0.5 is shown in Figure 6.12. It is clear that, there is density transition from the fluid

phase to the gas phase at the interfaces, and the velocity is also produced at interface. Therefore, the value of body force should be chosen with care. Firstly, the body force should be high enough so that the velocity in the two phases has a same or higher order compared with the velocity at interface. Secondly, the body force should keep small to ensure the numerical stability.

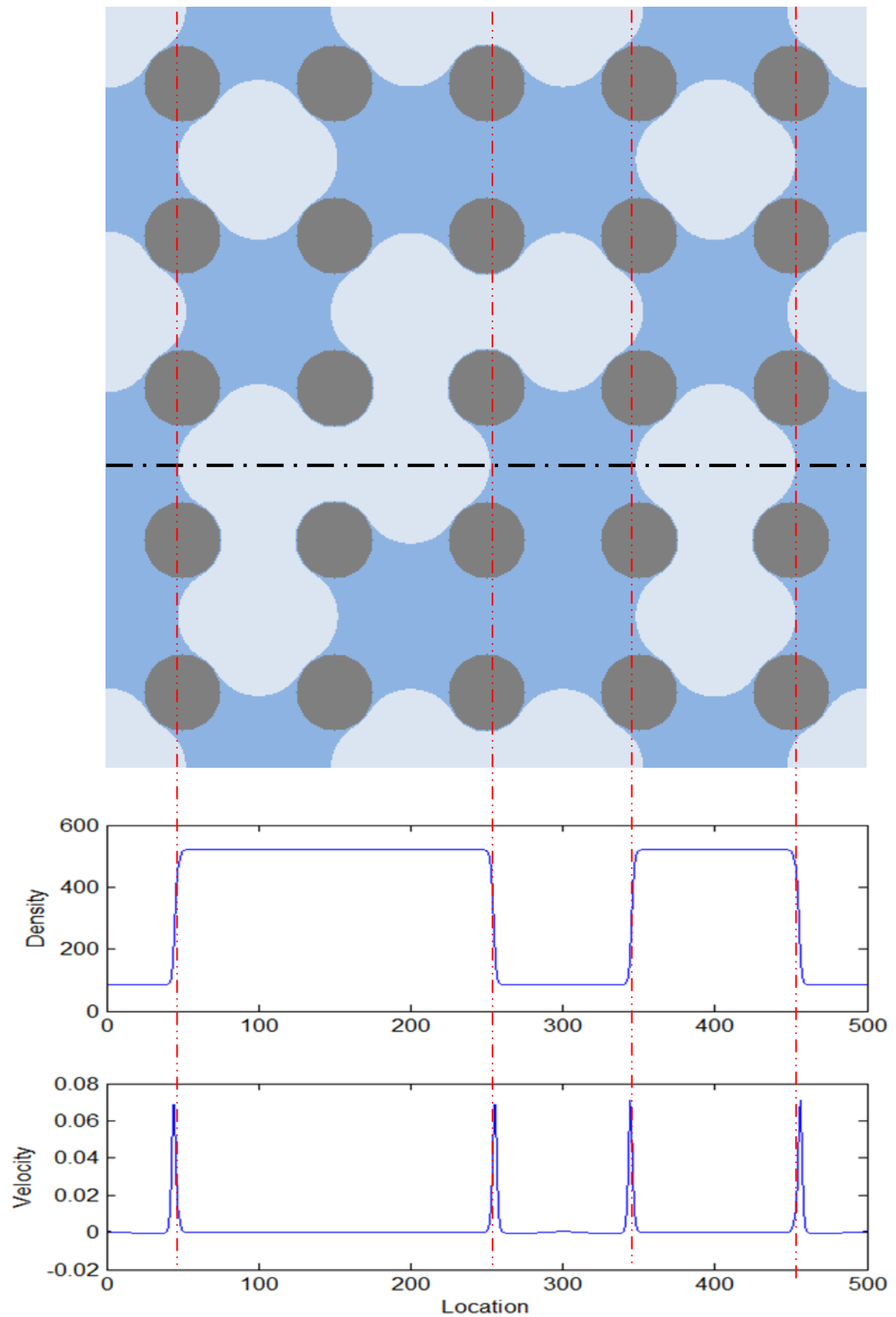
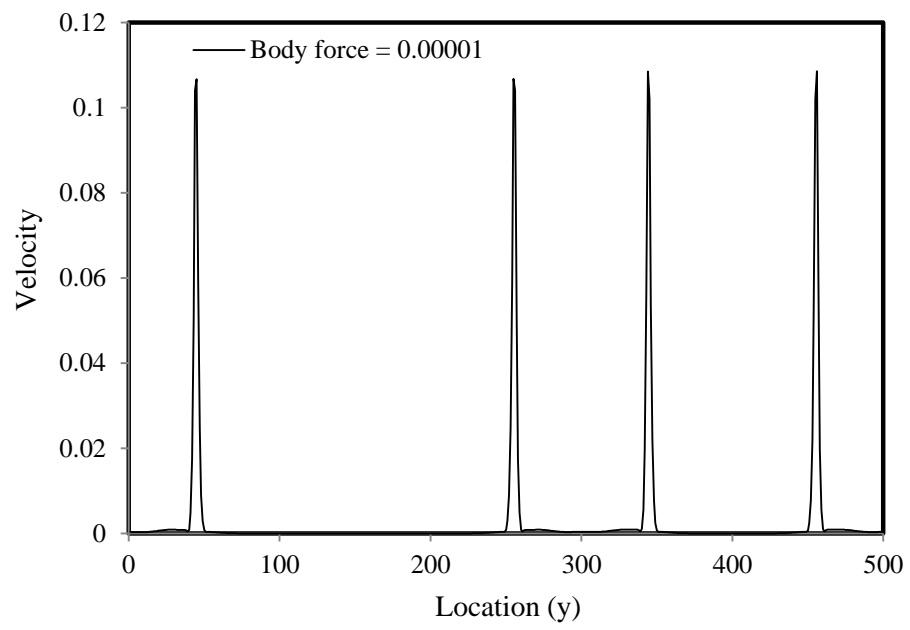
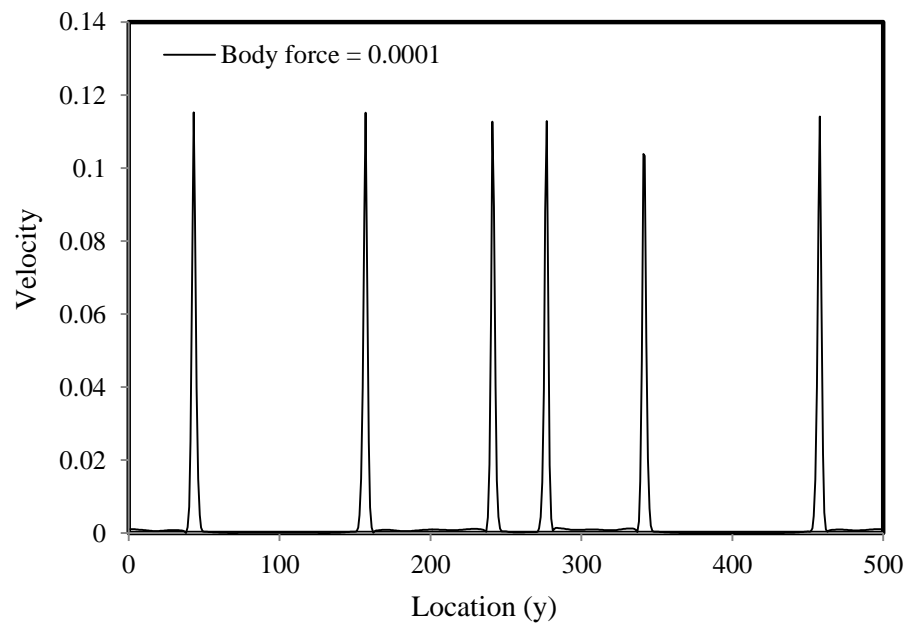


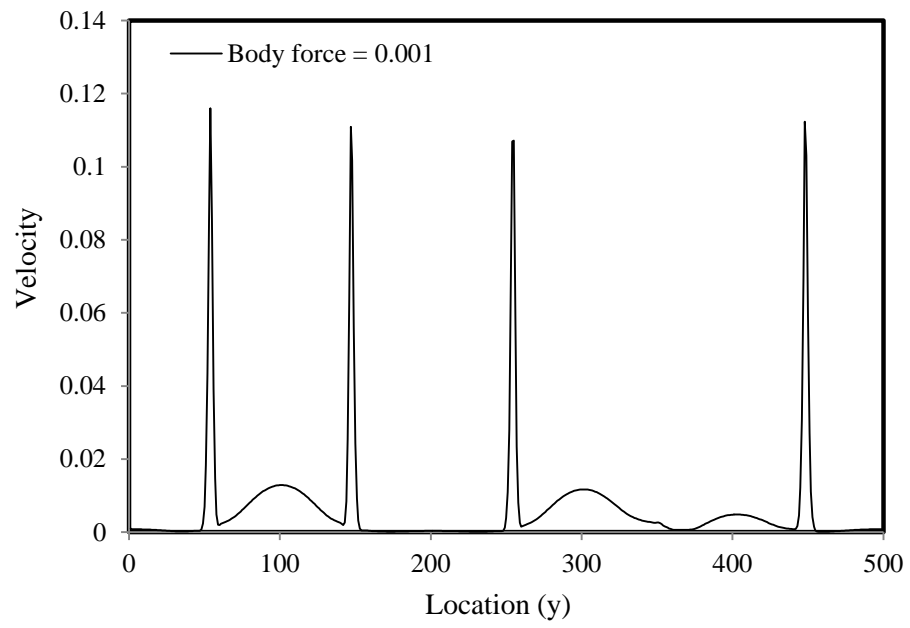
Figure 6.12 Density and velocity profile for the distribution at static condition.



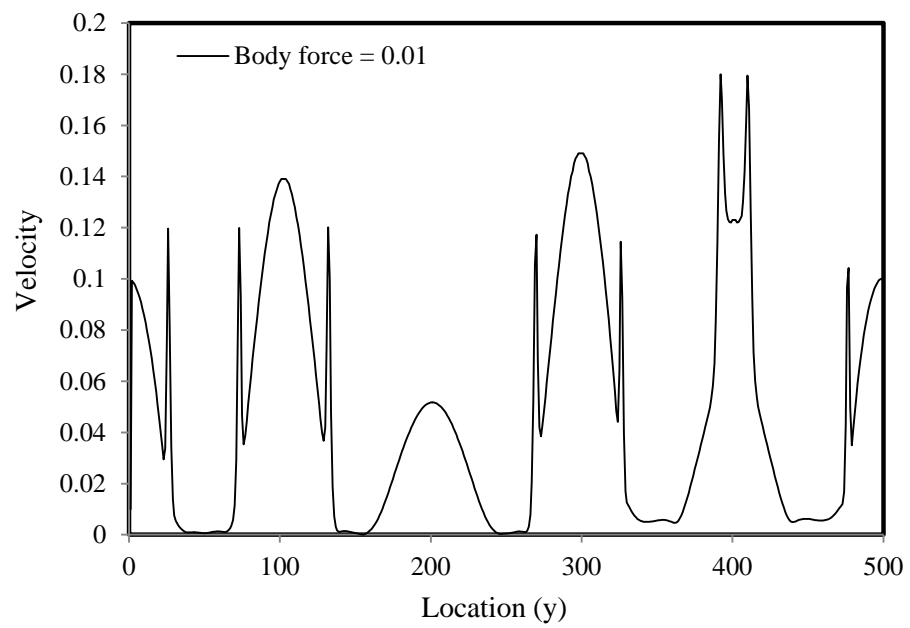
(a)



(b)



(c)



(d)

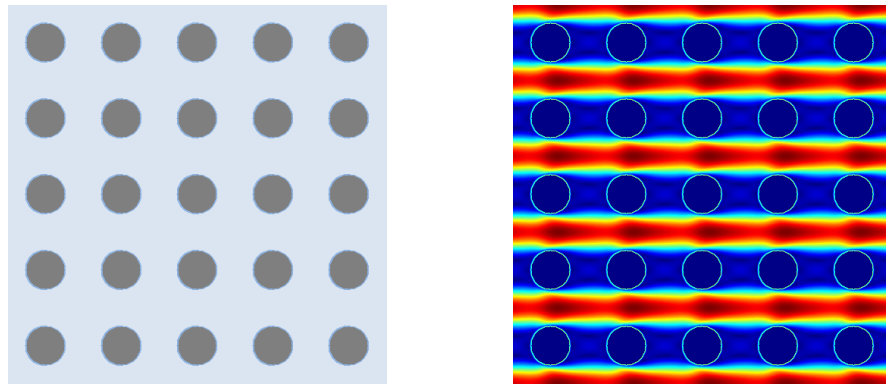
Figure 6.13 Effect of body force on velocity profile at $X = 220$.

In order to find a reasonable value of the body force to implement the two phase flow simulations. The degree of saturation is set as 0.5 and the body force changes from 0.1 to 0.00001. The velocity profile at different body forces are shown in Figure 6.13. It is found that, at low body force, the velocity at the interface is much larger than that of the two phases (Figure 6.13 a,b,c). The velocities at the interface approach to the same order as in the two phases when the body force gets as high as 0.01 (Figure 6.13d). As the body force increase to 0.02, the numerical instability occurs. Therefore, the body force in the following simulations is chosen as 0.01, the flow rate is calculated for both phases according to the density profile, whereas, the velocity at the interface is not considered.

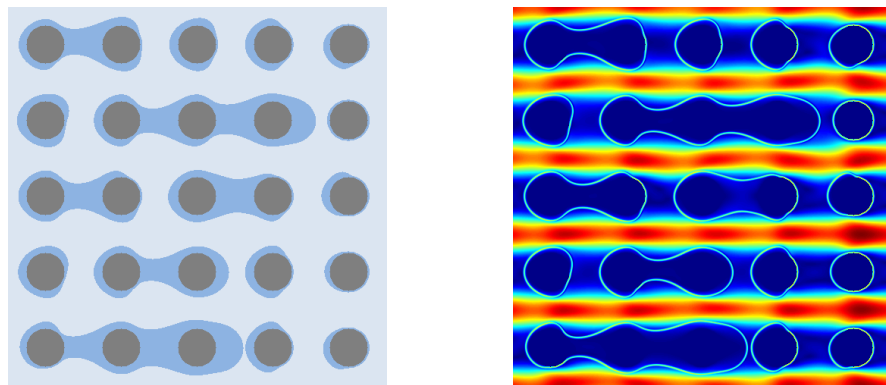
6.3.2 The effect of wettability

It is well known that the absolute permeability in equation 6.6 depends only on the microstructure of the media. However, the relative permeability is more complex, which is influenced by many factors, such as the fluids viscosity ratio, fluid-surface interaction. In this part, the effect of wettability on two phase flow is investigated, which is realized through the adjustment of the contact angle.

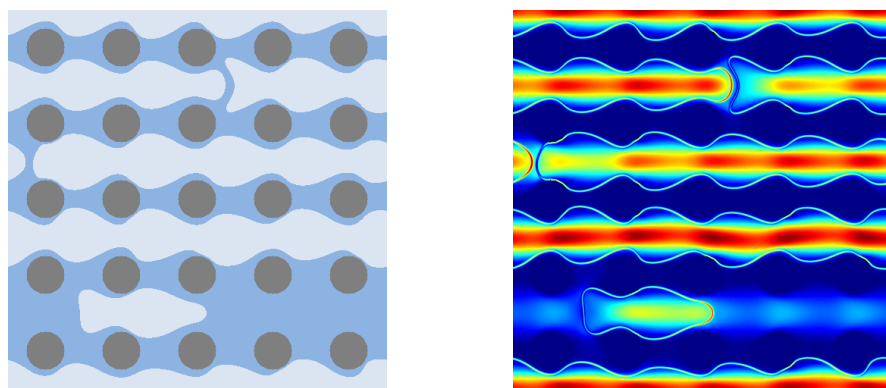
Based on the simulation results from Chapter 4, the complete contact angle can be obtained through the equation $\theta = 210.75 + 0.647G_{ads}$. In this section, the contact angle change from 0 to 90 and its influence on two phase flow behaviors is studied. To illustrate the two phase flow in porous media, the flow pattern at perfect wetting is shown in Figure 6.14. The velocity distributions in all of the figures are normalized to [0,1], where the red represent the maximum velocity and blue represent the minimum velocity. Therefore, the color-bar is not presented.



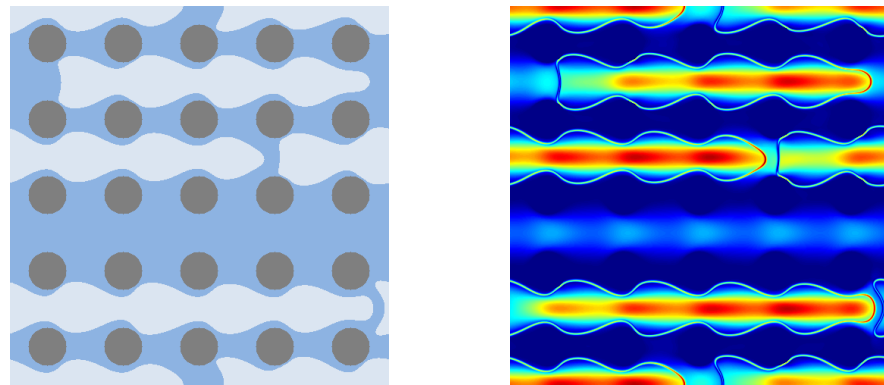
(a) $Sr = 0.0$



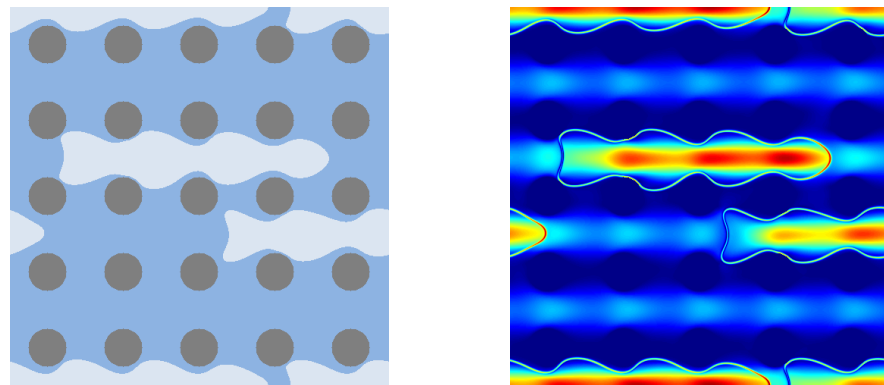
(b) $Sr = 0.2$



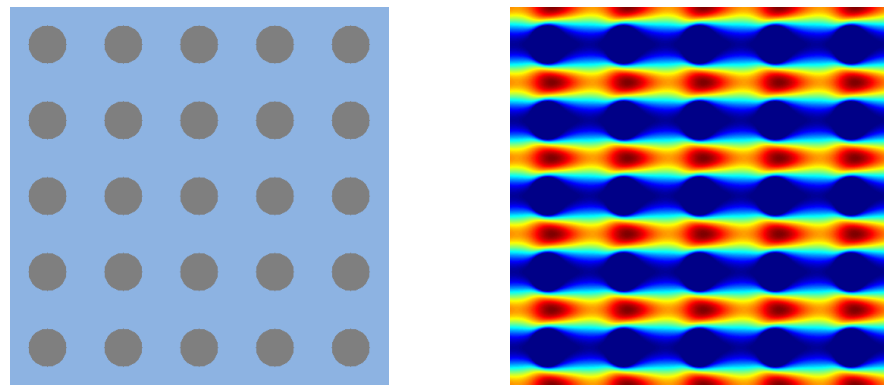
(c) $Sr = 0.4$



(d) $Sr = 0.5$



(e) $Sr = 0.7$



(f) $Sr = 1.0$

Figure 6.14 Two phase in porous media at perfect wetting condition (Left-density distribution; Right-velocity distribution).

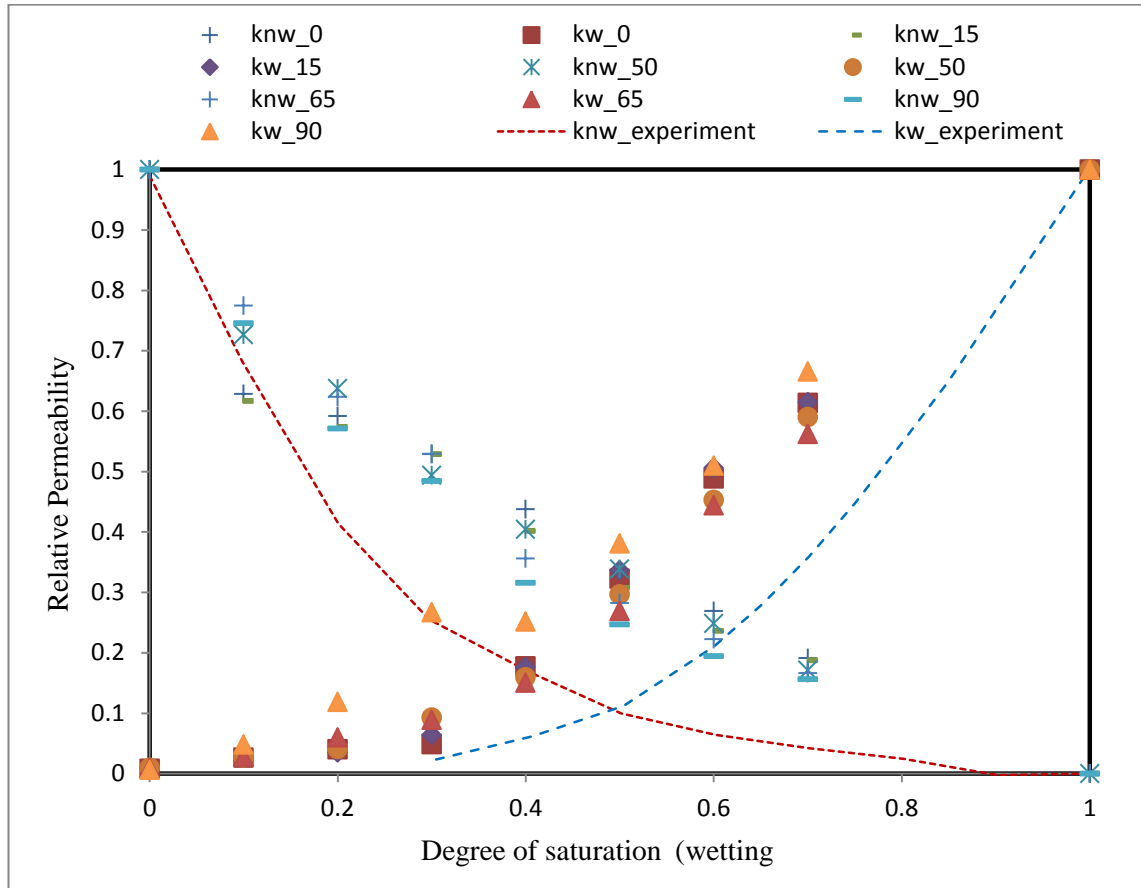


Figure 6.15 Relative permeability-Saturation relationships with different contact angle.

It is obviously that, at low degree of saturation, the non-wetting phase is continuous and the wetting phase is discontinuous which lead to very low flow rate for the wetting phase and low relative permeability. Meanwhile, the velocity of the gas phase is higher than that of liquid phase for its lower viscosity. The relative permeability of different contact angles are summarized in Figure 6.15. It is found that the contact angle has little effect on the multiphase flow behavior at large flow rate, and the relative permeability follows the trend line of $k_{rw} = S^{\gamma_w}$ and $k_{mnw} = (1-S)^{\gamma_{mnw}}$ for wetting phase and non-wetting phase respectively. Meanwhile, the simulation results present the same trend as reported by Bryant and Blunt (1992).

6.3.3 The effect of hydraulic aperture

In this section, the influence of hydraulic aperture on two phase flow is studied. The hydraulic aperture changes from 20 to 60 as illustrated in Figure 6.16. The absolute permeability of the porous media is measured at different hydraulic aperture, which increases with hydraulic aperture as shown in Figure 6.17.

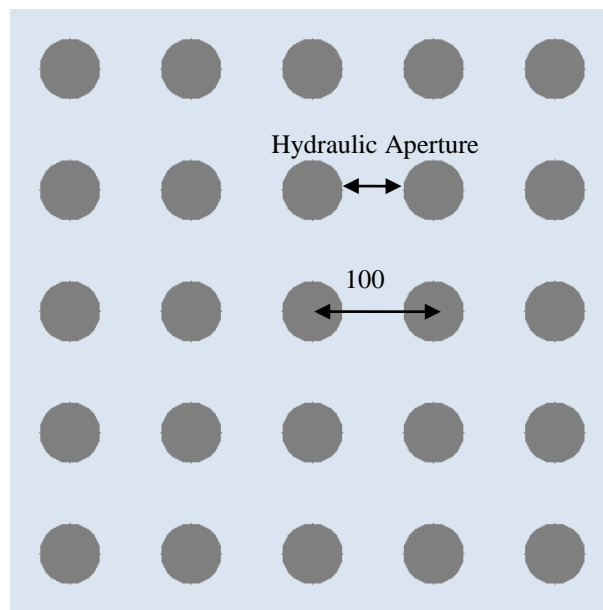


Figure 6.16 Illustration of the change of aperture in the porous media.

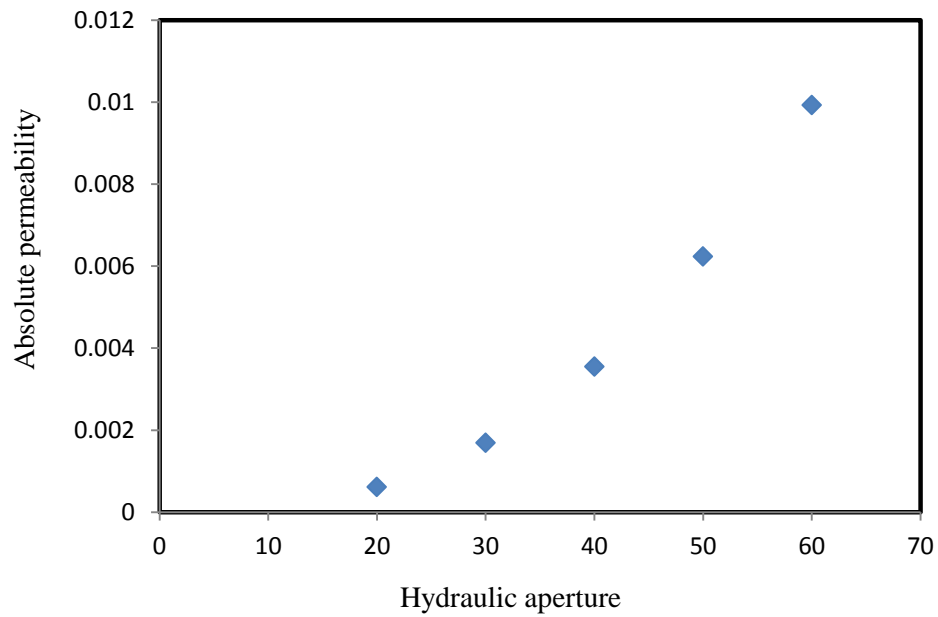
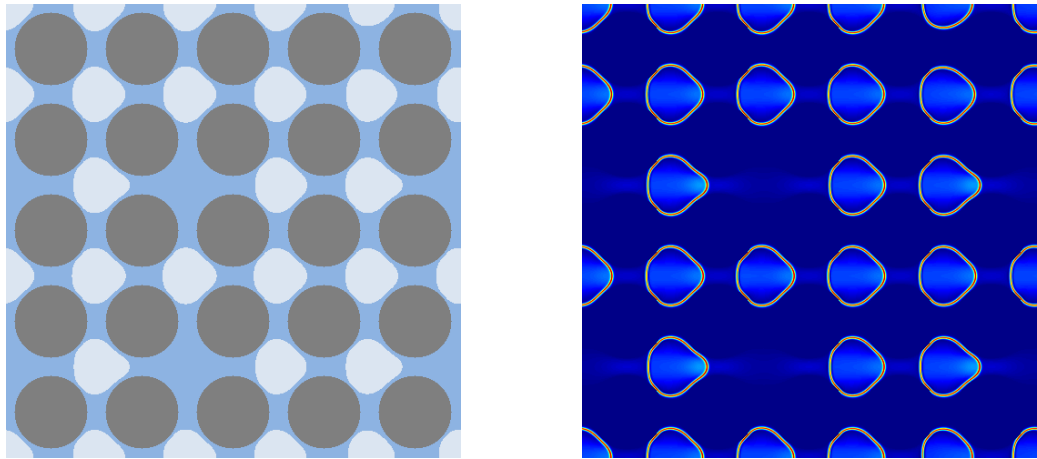
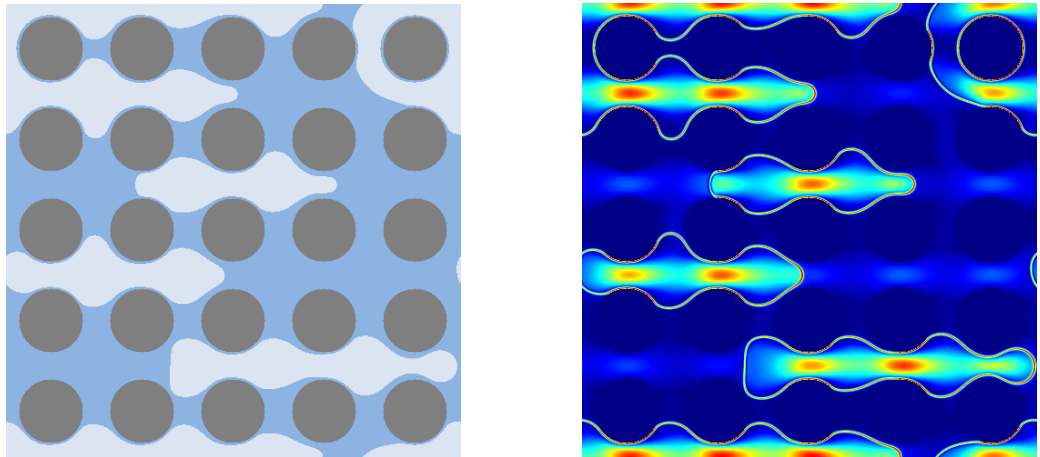


Figure 6.17 Relationship between the hydraulic aperture and absolute permeability.

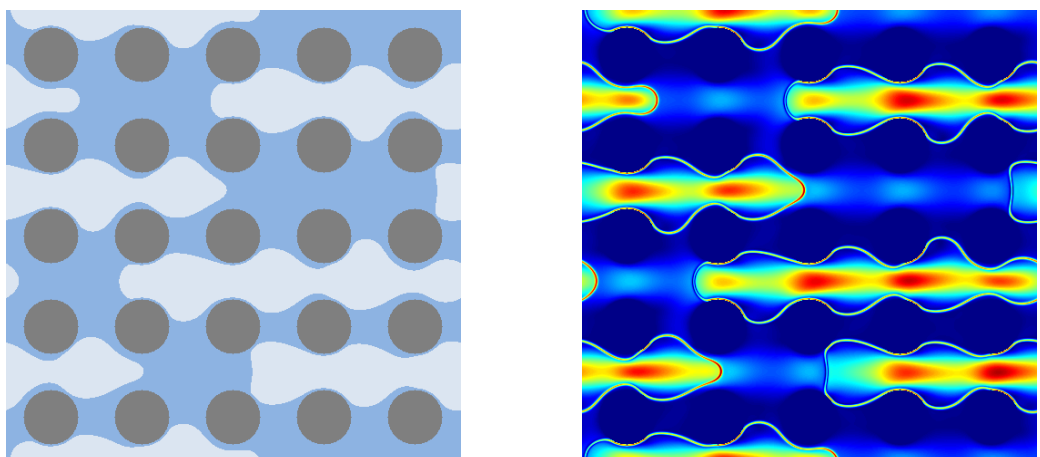
Meanwhile, the two phase flow simulations are conducted at different degree of saturation. To visualize the effect of hydraulic aperture on two phase flow, the fluid distribution and velocity distribution at saturation of 0.5 are presented in Figure 6.18. It is clear that, at small hydraulic aperture, the non-wetting phase are isolated and the velocity is very small. As the hydraulic aperture increases, clusters of non-wetting phase are produced, which have higher velocity than the wetting phase. The relative permeability at different hydraulic aperture is summarized in Figure 6.19.



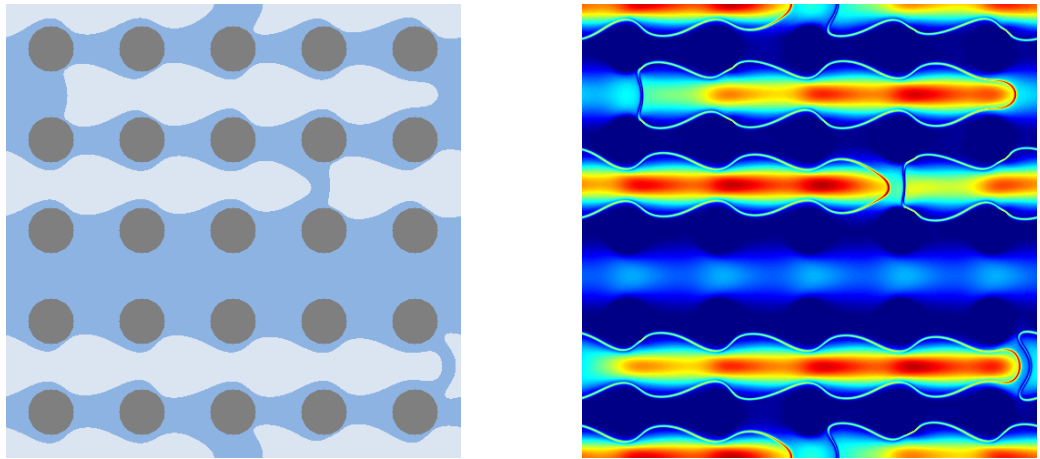
(a) Hydraulic aperture = 20



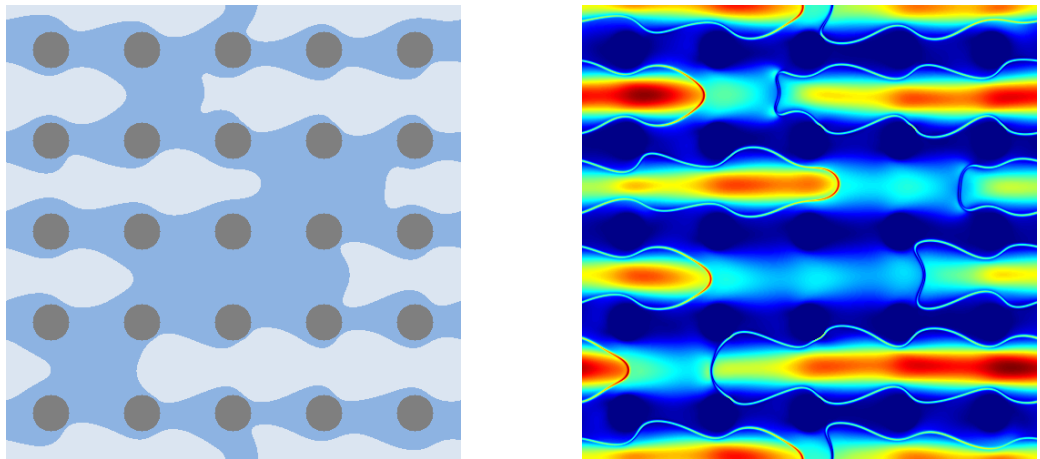
(b) Hydraulic aperture = 30



(c) Hydraulic aperture = 40



(d) Hydraulic aperture = 50



(d) Hydraulic aperture = 60

Figure 6.18 Density and velocities distribution at different hydraulic aperture.

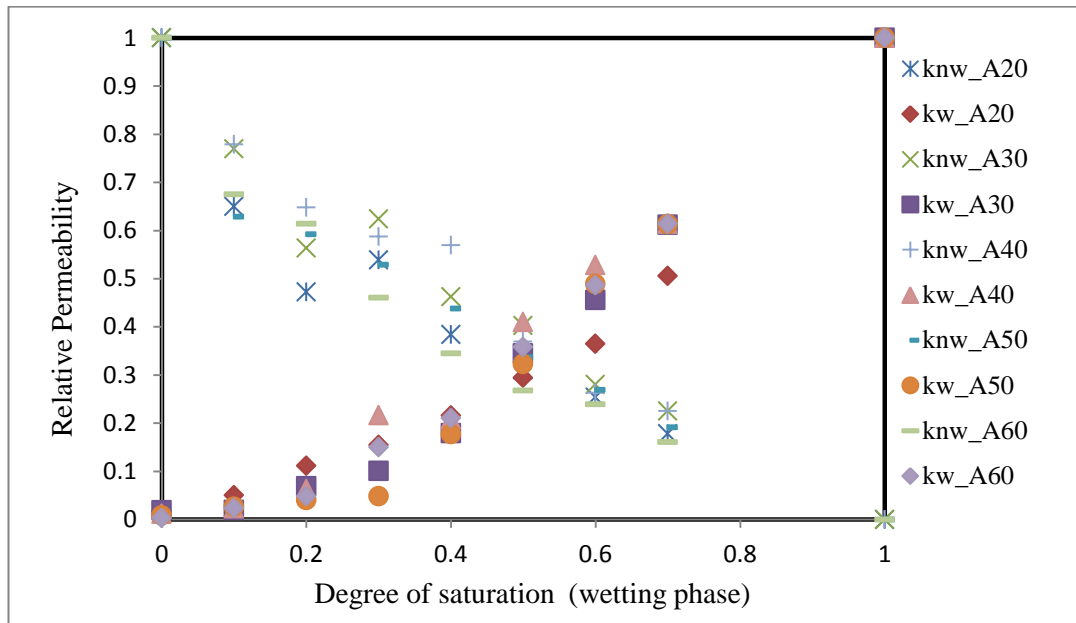


Figure 6.19 Relative permeability-saturation relationships with different hydraulic aperture.

6.4 FLOW IN FRACTURED POROUS MEDIA

It is widely accepted that the fracture is the preferable flow path in single phase problems. However, the fracture behaves differently in the two phase flow, which is not well understood. In this section, the mechanism of two phase flow in fractured porous media is explored and the influence of fracture on two phase flow is numerically investigated.

To this end, a porous media of 1000×1000 is created. The radius of particle and interval are set as 10 and 50 respectively, which leads to a porous media with hydraulic aperture of 30. By considering that the space in the fracture is larger than that in the porous media, the hydraulic aperture in fracture is set as 60 l.u. with different orientation, the vertical and horizontal as well as the inclined direction. The geometry of the porous media with inclined fracture is shown in Figure 6.20.

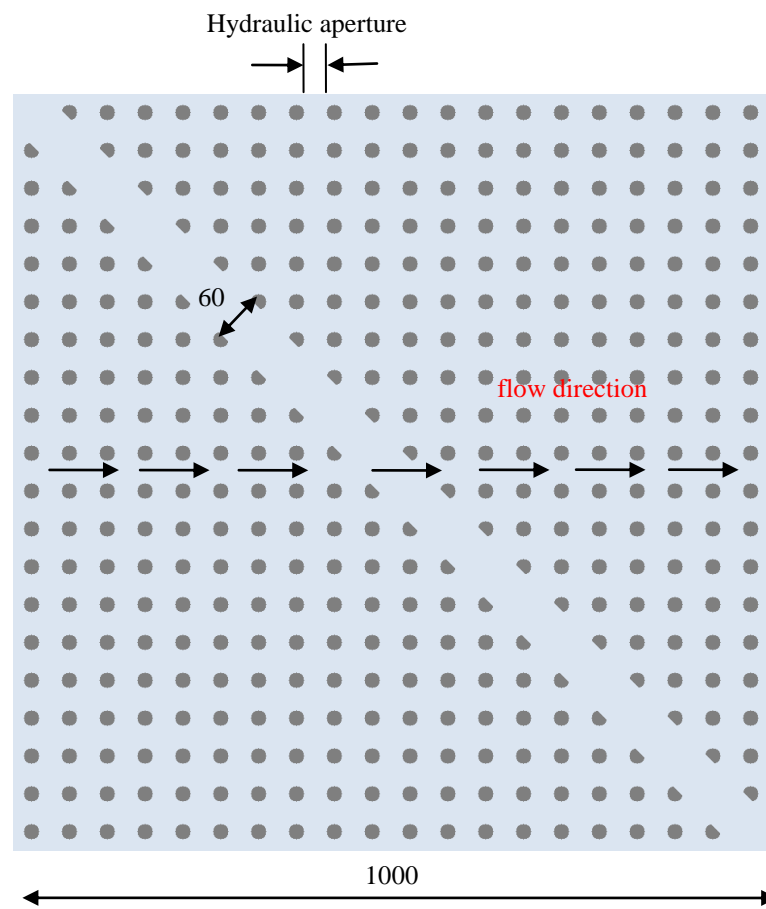
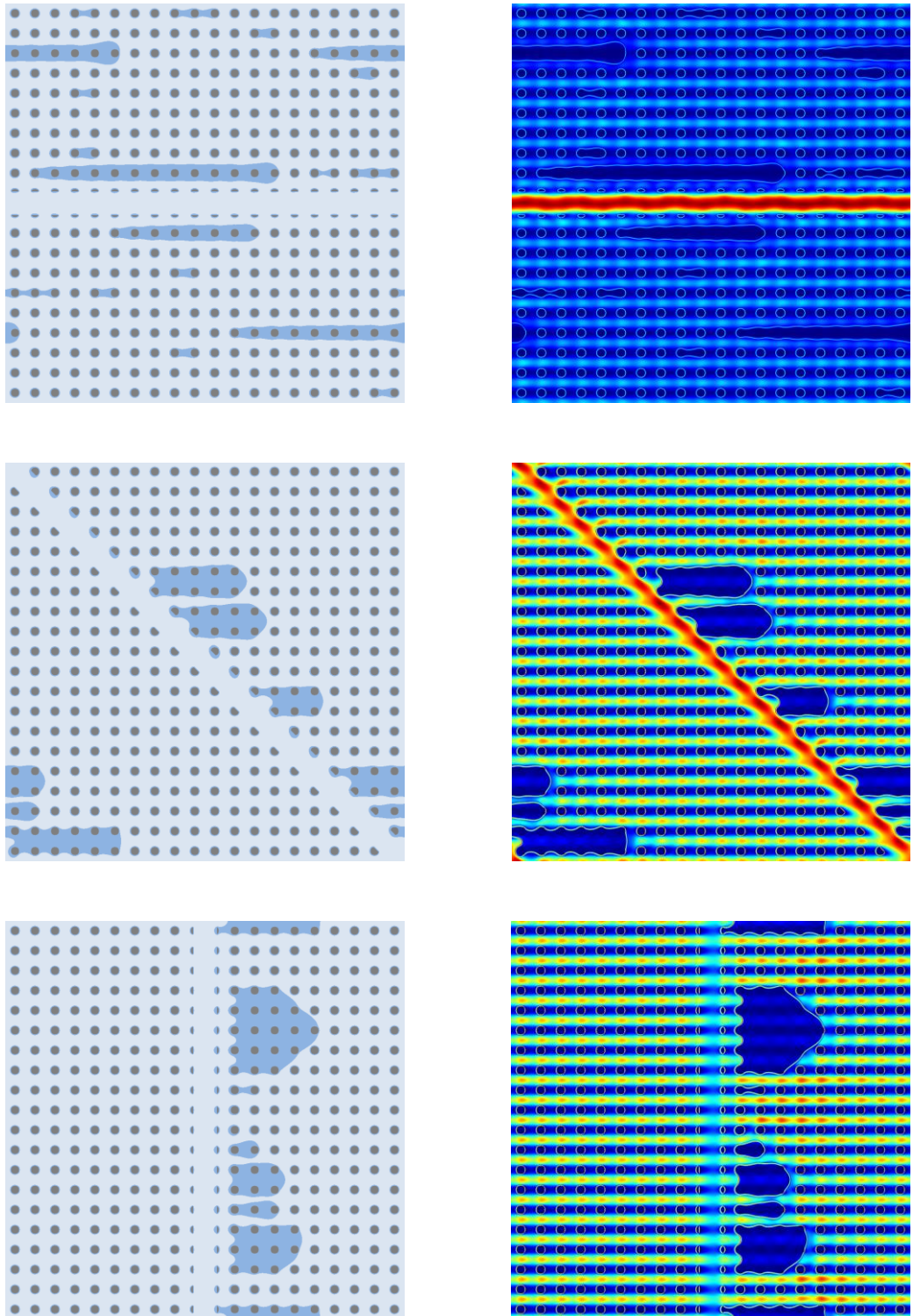
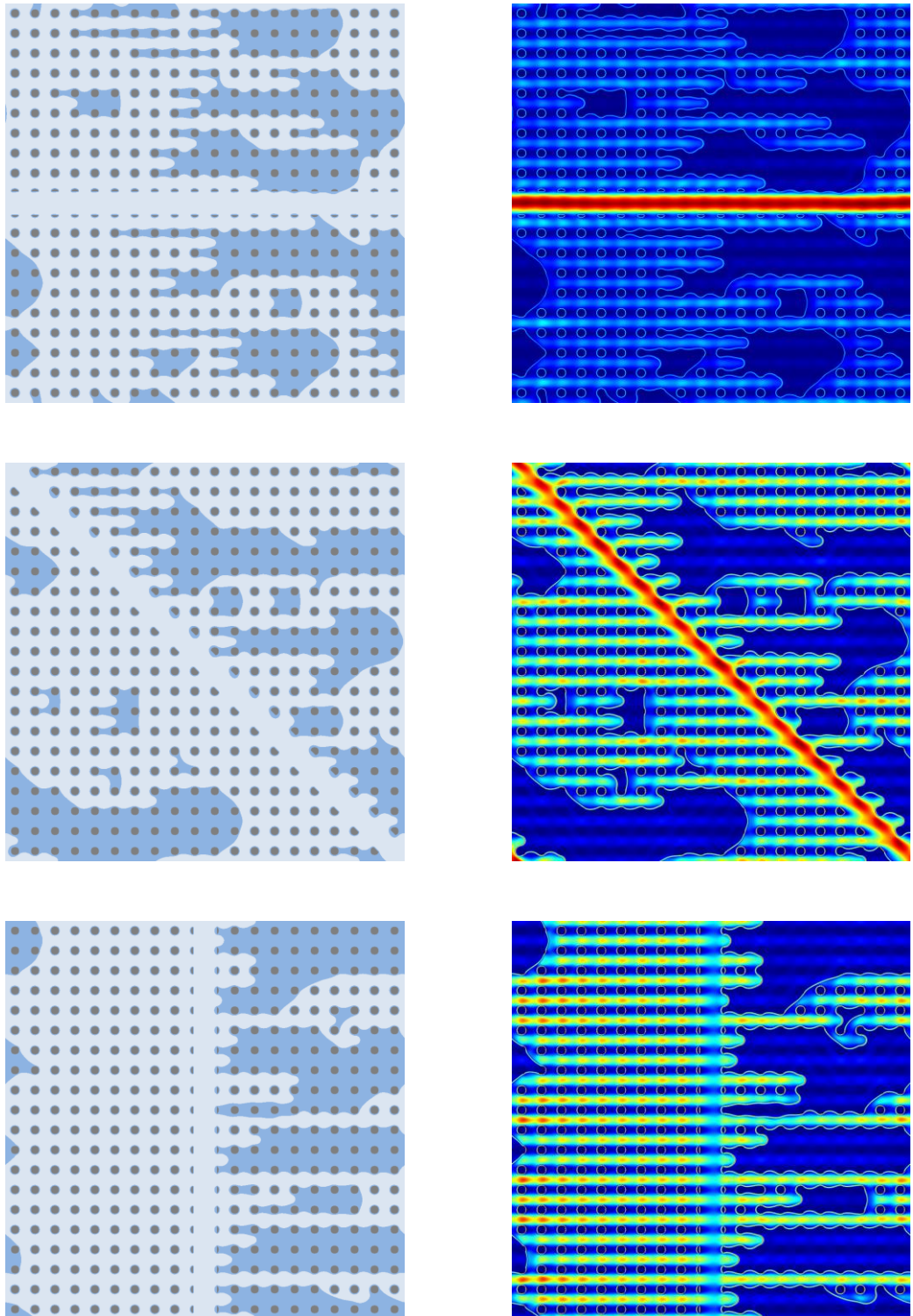


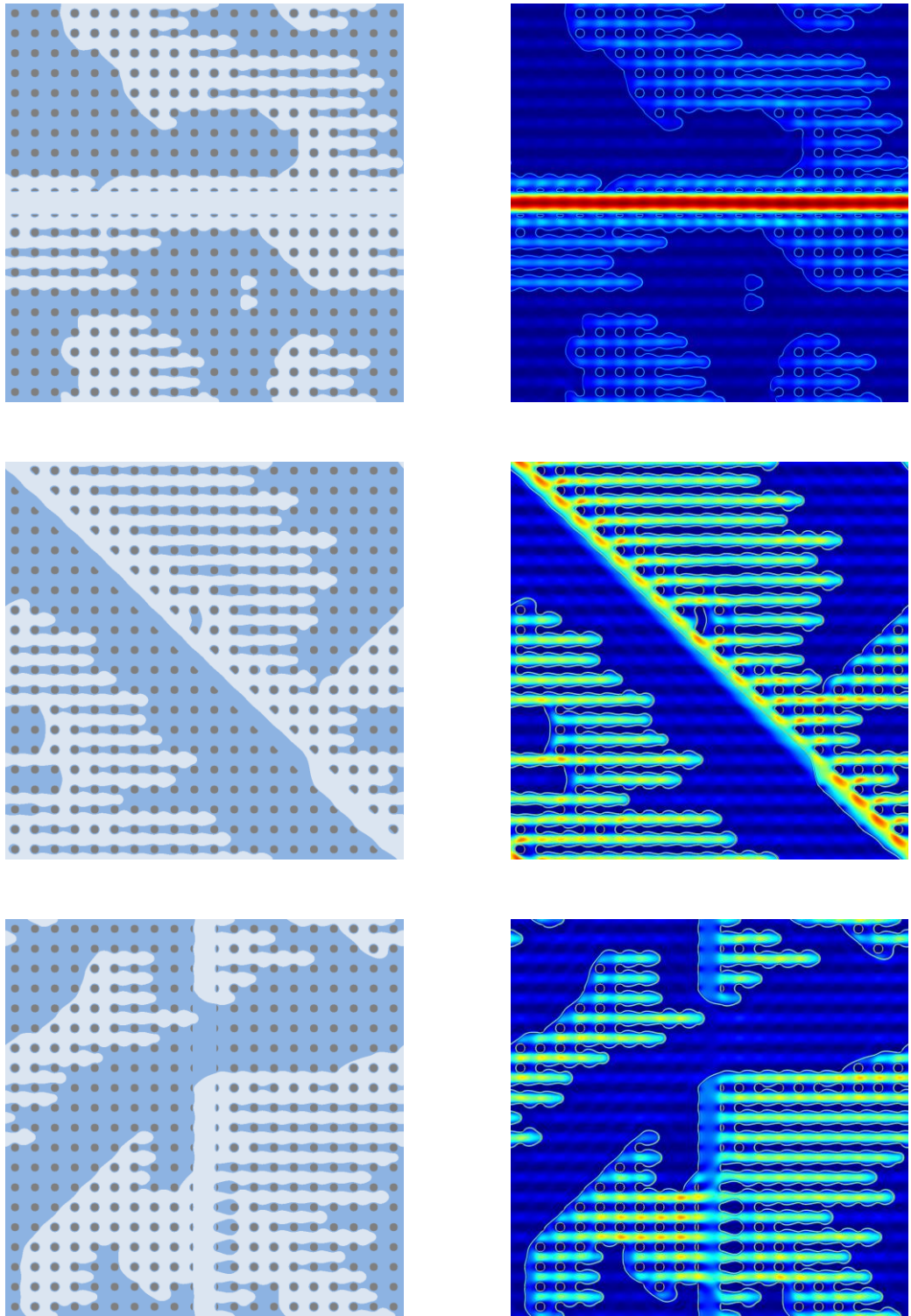
Figure 6.20 Geometry of the fractured porous media.



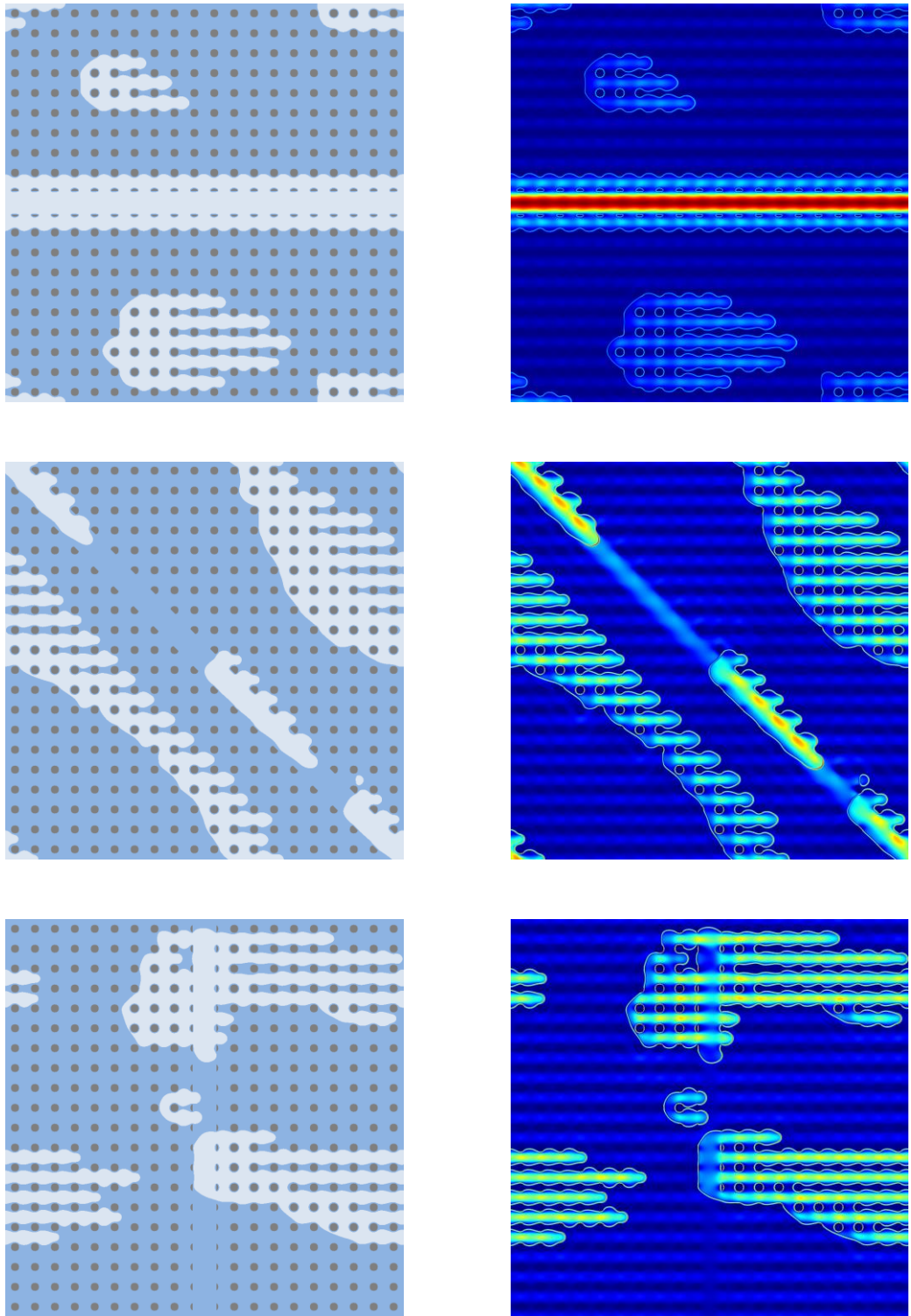
(a) $Sr = 0.1$



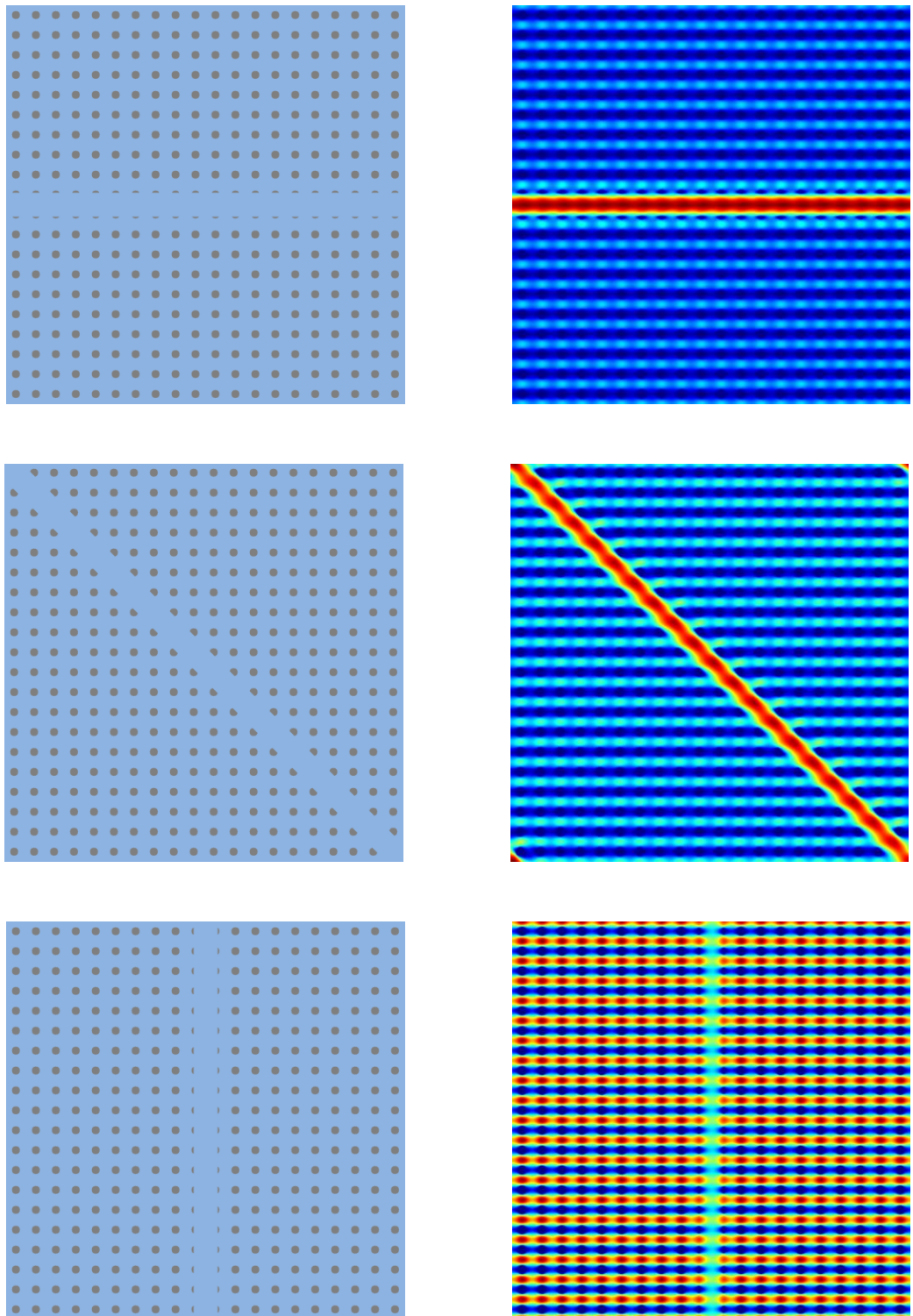
(b) $Sr = 0.3$



(c) $Sr = 0.5$

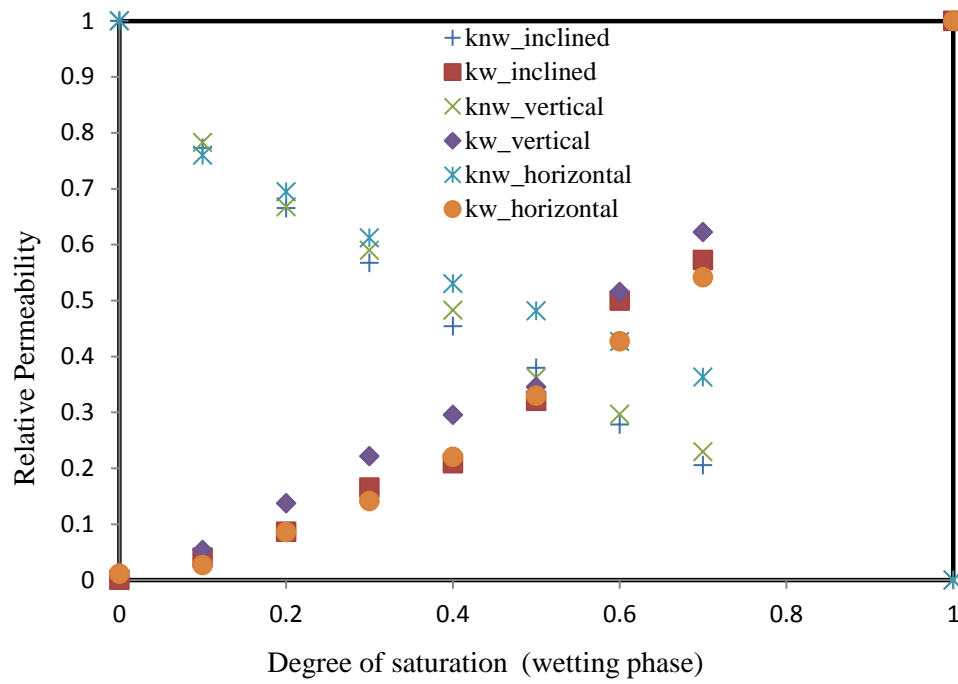


(d) $Sr = 0.7$

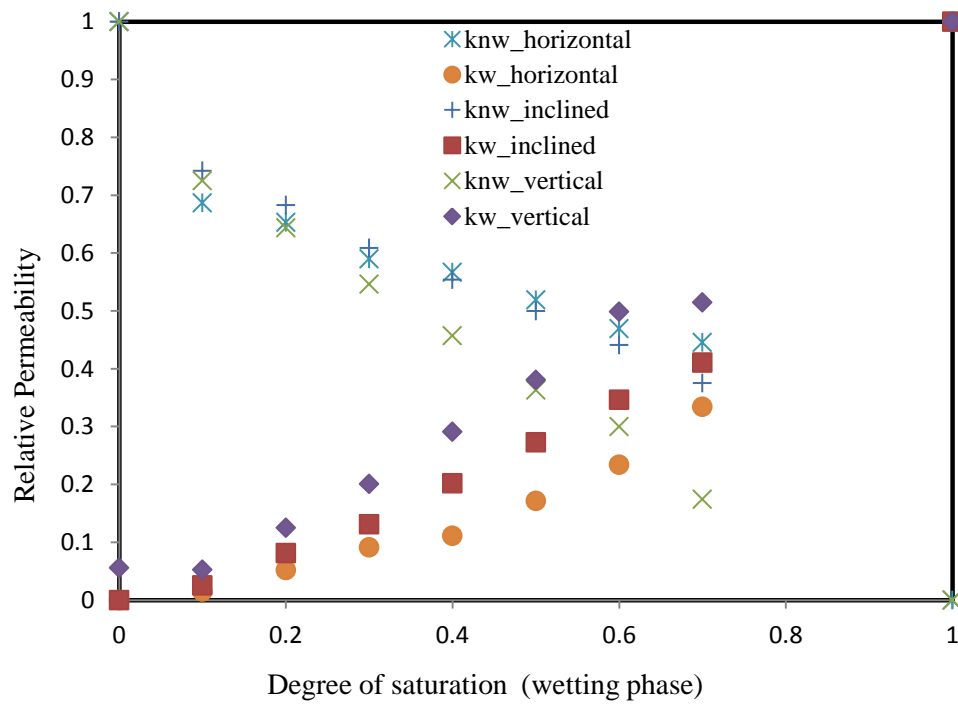


(e) $S_r = 1.0$

Figure 6.21 Density distribution and velocity profile in the fractured porous media at different degree of saturation and different fracture orientation.



(a) Hydraulic aperture = 30



(b) Hydraulic aperture = 20

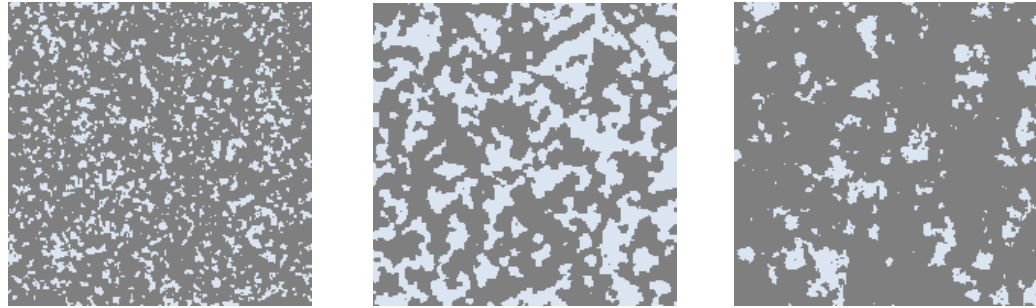
Figure 6.23 Relative permeability-saturation relationships of the fractured porous media.

The two phase flow simulations are conducted in the fractured porous media with different fracture orientation with respect to the flow direction. The density and velocity distribution are presented in Figure 6.21. It is found that, the wetting phase has the preference to flow in porous matrix with small hydraulic aperture. The fracture, on the other hand, is mostly occupied by the non-wetting phase. The same simulations are conducted by reducing the hydraulic aperture to 20 and the relative permeability with different fracture direction and different hydraulic aperture of porous media are summarized in Figure 6.22. It is clear that, for the non-wetting phase, the fractured porous media with horizontal fracture has the higher relatively permeability, whereas, the vertical fracture presents the lower relatively permeability. In contract, for the wetting phase, the opposite phenomenon is observed. It is also observed that, in the fractured porous media, the porous matrix dominated by the wetting phase flow, and the fracture do more contribution on non-wetting phase flow than the wetting phase flow. Moreover, with the decreasing of hydraulic aperture of porous media, influence of fracture becomes more remarkable by comparing the results of Figure 6.22a and Figure 6.22b.

6.5 TRIAL OF TWO PHASE FLOW IN NATURAL MATERIAL

In this part, the multiphase flow in geomaterial is simulated. There are three common materials, the Sandstone, Carbonate and Ceramics (Figure 6.24). However, the porosity of sandstone and Carbonate are very small, which are 0.2 and 0.15 respectively. Meanwhile, the pores are not well connected, which makes two phase flow impossible. The Ceramics, on the other hand, has a very high porosity of 0.4 and the pores have a

higher degree of connectivity. By considering both the efficiency and accuracy of LBM, the Ceramics is used in this study.



(a) Sandstone

(b) Ceramics

(c) Carbonate

Figure 6.24 Geometry of different material from CT.

However, the 2D simulation is impossible because the pore is not interconnected. To cope with this problem, the 3D model with size of $200 \times 200 \times 200$ is generated through the simulated annealing simulation following the work by Yin and Zhao (2014). The 3D reconstructed Ceramics is shown in Figure 6.25, which is imported to the 3D Shan-Chen SCMP model.

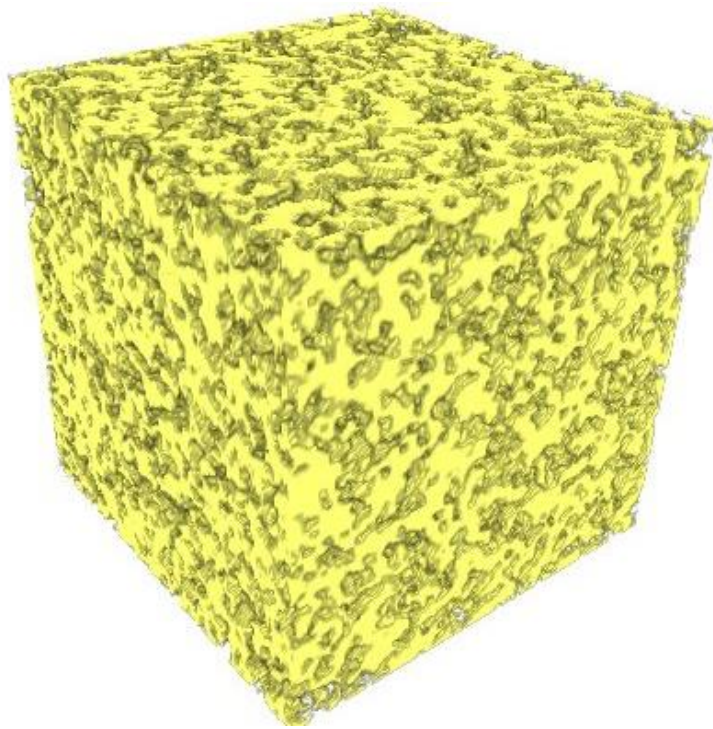


Figure 6.25 3D reconstructed Ceramics.

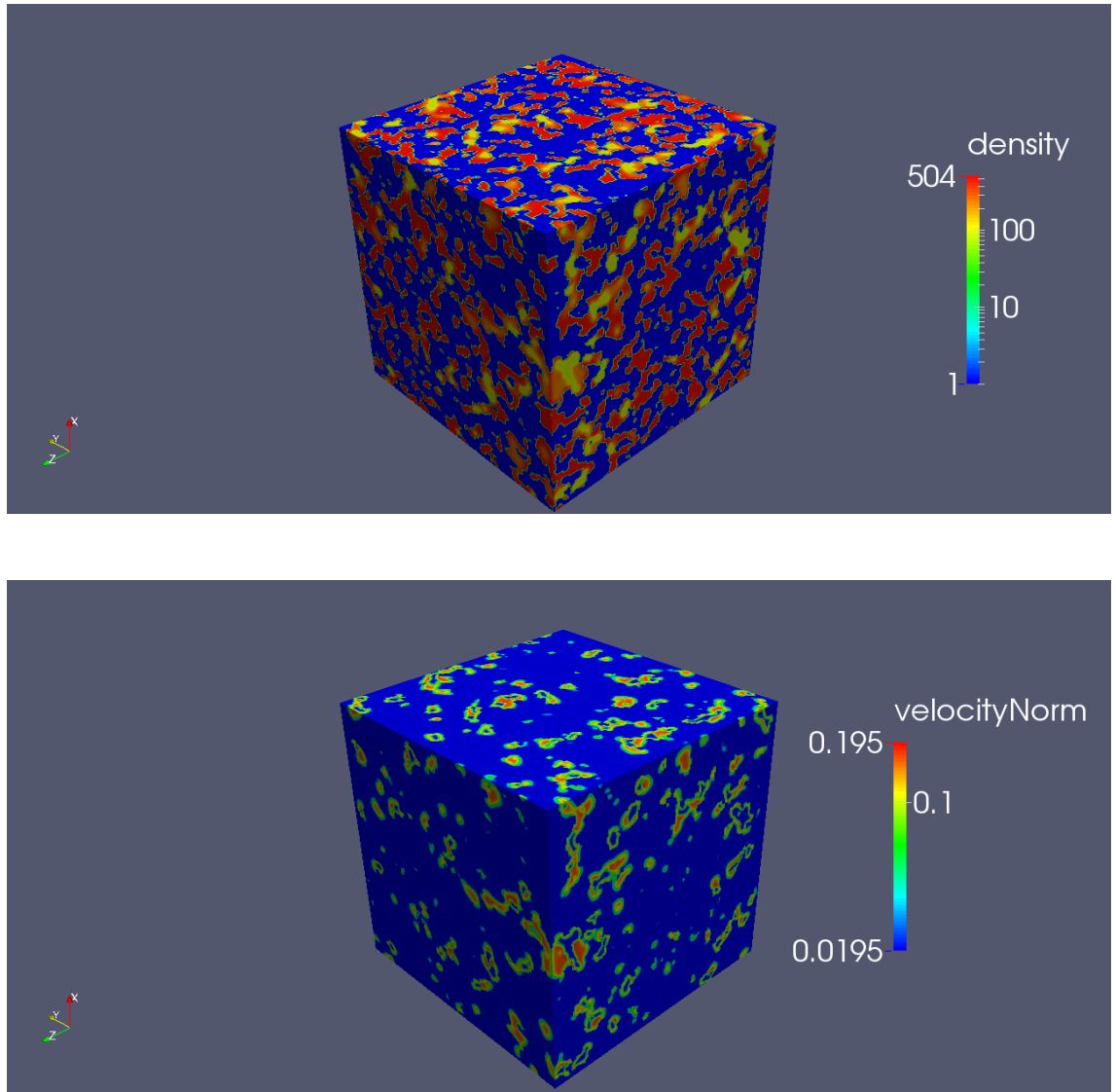


Figure 6.26 Density and velocity distribution of two phase flow in 3D reconstructed porous media.

The density and velocity distribution of the 3D simulation is presented in Figure 6.26. It is found that, the two phase flow can be readily simulated in reconstructed porous media. However, there are some challenges of LBM simulation in natural material. First of all, the size of the sample cannot be too large because of the memory requirement of the simulation. E.g. for a cubic specimen, the increase of length from L to $n \times L$ will increase the computational cost to L^3 to $(n \times L)^3$, the storage of microscopic information will

increase at the same time. Secondly, the size should not be very small so that the simulation conducted is close the representative element volume (REV). E.g. for X-Ray CT test, specimen of several millimeter may not large enough to represent the complete information of the porous media. Thirdly, the resolution should be large enough to obtain stable and accurate results. E.g. based on the simulation in chapter 5, lattice number of 20 is the recommended minimum size of pore space to obtain reasonable results.

6.6 CONCLUDING REMARKS

An extensive study of two phase flow in fractured porous media has been presented. The two Shan-Chen LBM models are compared through the basic flow simulations. It is found that the SCMP is more reasonable for its ability of simulate two phase with different density and viscosity. Meanwhile, the body force used in the simulation is evaluated; the value of 0.01 is suggested in our simulation by considering both the numerical accuracy and stability. In the study of two phase flow in porous media, the effect of wettability and aperture on two phase flow in investigated. The relative permeability is found slightly influenced by the contact angle but significantly influence by the hydraulic aperture. Moreover, the two phase flow in fractured porous media, it is found that the non-wetting phase has preference to flow in fractures and the orientation has significant influence on the relative permeability. The 3D numerical simulation of two phase flow in reconstructed natural material is demonstrated at the end. It is found that the 3D simulation cannot be coped with easily, which requires very high resolution of the porous media so as to obtain accurate results.

6.7 REFERENCES

Bear J. (1972) *Dynamics of Fluids in Porous Media*, Am. Elsevier, New York

Blunt M. (2001) Flow in porous media—pore-network models and multiphase flow. *Current Opinion in Colloid & Interface Science* 6:197–207.

Bryant S., Blunt M. (1992) Prediction of relative permeability in simple porous media. *Physical Review A* 46(4):2004-2011.

Celia M., Reeves P., Ferrand L. (1995) Recent advances in pore scale models for multiphase flow in porous media. *Reviews of Geophysics* 33:1049.

Chen S., Doolen G.D. (1998) Lattice Boltzmann method for fluid flows. *Annual Review of Fluid Mechanics* 30:329-364.

He X., Doolen G.D. (2002) Thermodynamics foundations of kinetic theory and lattice Boltzmann models for multiphase flows. *The Journal of Statistical Physics* 107(1/2):309–328.

<http://leonardi.unsw.wikispaces.net/home>

<http://www.palabos.org/>

Huang H.B., Thorne D.T., Schaap M.G., Sukop M.C. (2007) Proposed approximation for contact angles in Shan-and-Chen-type multi-component multiphase lattice Boltzmann models. *Physical Review E* 76: 066701.

Huang H.B., Wang L., Lu X. (2011) Evaluation of three lattice Boltzmann models for multiphase flows in porous media. *Computers and Mathematics with Applications* 61:3606-3617.

Hughes R.G, Brigham W.E., Castanier L.M. (1995) CT imaging of two phase flow in fractured porous media. *proceedings, Twenty-First Workshop on Geothermal Reservoir Engineering Stanford University, Stanford, California*

Lu G., Wang X.D., Duan Y.Y. (2013) Study on initial stage of capillary rise dynamics. *Colloids and Surfaces A: Physicochemical and Engineering Aspects* 433:95-103.

Pan C., Hilpert M., Miller C.T. (2004) Lattice Boltzmann simulation of two phase flow in porous media. *Water Resources Research* 40:W01501.

Persoff P., Pruess K. (1995) Two-Phase Flow Visualization and Relative Permeability Measurement in Natural Rough-Walled Rock Fractures. *Water Resources Research* 31(5):1175-1186.

Shan X., Chen H. (1993) Lattice Boltzmann model for simulating flows with multiple phases and components. *Physical Review E* 47:3.

Shan X., Chen H. (1994) Simulation of nonideal gases and liquid-gas phase transitions by the lattice Boltzmann equation. *Physical Review E* 49:4.

CHAPTER 7 SUMMERY AND CONCLUSIONS

The micromechanics of multiphase flow in fractured porous media have been investigated extensively from the microstructure characterization to the numerical simulation of single phase and multiphase fluid flows.

In order to characterize the pore geometry of porous media, the stochastic reconstruction of Gosford sandstone from its surface image is conducted. A digital microscope is adopted to capture surface images of the Gosford sandstone specimen where the carbon dust treatment on the surface is introduced. The 3D morphological distribution curve is derived through a porosity adjustment of the 2D surface images. By comparing all the stochastic reconstructed microstructure models with the original X-ray micro CT model, it is shown that the reconstructed models can successfully reflect essential morphological information of the Gosford sandstone. Meanwhile, the single fracture is characterized through the mathematical model proposed by Brown. The fractal dimension and standard deviation is found effectively in describing the fracture roughness. Furthermore, the stochastic reconstruction of fracture network is adopted to characterize the rock fracture statistically.

The single phase fluid flows in fracture and fracture network are investigated using lattice Boltzmann Method (LBM). The fluid flow through 3D rough fracture is extensively simulated, which shows the ability of LBM in dealing with complex geometries. The two coefficients equation is proposed to characterize the flow behavior by considering both the roughness and displacements. The 2D fluid flows through

fracture network are simulated by using LBM and the direct investigation of roughness effect on flow in fracture network is conducted. It is found that, the LBM and modified pipe network model could effectively take into account the roughness effect on fluid flow in fracture networks. Meanwhile, the interconnectivity of fracture network is investigated by LBM, and it is found that interconnectivity is dominant by the length density parameter and the correlation between the DFN parameter and transmissivity is analyzed. The 'indirect' hydro-mechanical coupled problem can be properly simulated by combining the distinct element method and LBM. The difficulty of flow prediction under large deformation could easily be coped by LBM and the anisotropic flow behavior due to deformation is readily captured by the hydro-mechanical coupled analysis.

The transition from single phase flow to the multiphase flow requires the clear understanding of the complex physical process at micro scale. Accordingly, the wettability and the two phase distribution in fractured porous media are investigated. The multiphase LBMs are capable to simulate the two phase system of different wettability or contact angles. Meanwhile, the SCMP LBM is found to be the best method in predicting the fluid distribution in partially saturated porous media compared with two other methods (the SAM and the MCMP LBM). The effect of periodic boundary conditions and the initial configuration are also tested. It is found that a buffer size of approximately 12.5 times the average particle size is suggested to reduce the error resulting from the periodic boundary conditions. Moreover, the initial distribution of the SCMP LBM is less sensitive for an irregular porous medium than that of a regular medium; therefore, it is more suitable for natural porous media, such as rock and soil. The influence of the degree of saturation on the two-phase fluid distribution was investigated using this method. The fluid distribution patterns and the quantitative

evaluation at different degrees of saturation were investigated, which is consistent with experimental results from the literature. Finally, the influence of fractures on the two-phase fluid distribution was also studied. The disturbance ratio is introduced to evaluate the change in the two-phase system due to the induced fracture. It was found that more fluids are disturbed as the fracture length and width increase, and the disturbance ratio decreases as the degree of saturation increases.

A detailed study of two phase flow in fractured porous media has been presented at the end. The two Shan-Chen LBM models are compared through the basic flow simulations. It is found that the SCMP is more reasonable for its ability of simulating two phases with different density and viscosity. Meanwhile, the body force used in the simulation is evaluated and the value of 0.01 is suggested in our simulation by considering both the numerical accuracy and stability. In the study of two phase flow in porous media, the effect of wettability and aperture on two phase flow are investigated. The relative permeability is found slightly influenced by the contact angle but significantly influence by the hydraulic aperture. Moreover, based on the results of the two phase flow in fractured porous media, it is found that the non-wetting phase has preference to flow in fractures and the orientation has significant influence on the relative permeability. The 3D numerical simulation of two phase flow in reconstructed natural material is also demonstrated and it is found that the 3D simulation cannot be coped with easily, which requires very high resolution of the porous media so as to obtain accurate results.

All those findings give clear perspectives on the characterization of fractured porous media and the dependence of macro multiphase flow behaviors on microstructure and micro-physics.